Lorentz Force Evaluation
Novel Forward Solution and Inverse Methods

Dissertation

zur Erlangung des akademischen Grades

Doktor-Ingenieur

(Dr.-Ing.)

vorgelegt der

Fakultät für Informatik und Automatisierung der

Technischen Universität Ilmenau

von

M. Sc. Eva-Maria Dölker (Kowalski)

geboren am 09.02.1991 in Ilmenau

Keep away from people who try to belittle your ambitions. Small people always do that, but the really great make you feel that you, too, can become great. - *Mark Twain*

Acknowledgments

Abstract

The development of new materials, as well as the increasing standards for quality and safety, require high-resolution, nondestructive evaluation methods for manufacturing and maintenance. In a novel method, referred to as Lorentz force evaluation, a permanent magnet is moved relative to a conducting specimen. Owing to this movement, eddy currents are induced inside the conductor. The interaction of the eddy currents with the magnetic field leads to the Lorentz force acting on the conductor. A force of the same magnitude but in opposite direction acts on the permanent magnet, where it is measured. In the presence of a defect, the eddy currents are perturbed. Consequently, the Lorentz force components are also perturbed. The defect properties are determined from the measured Lorentz force components by solving an ill-posed inverse problem.

The thesis aims to develop a novel forward solution, compare different forward solutions, develop new inverse calculation methods and create a method for improving defect depth estimation for Lorentz force evaluation. Further, a qualitative comparison to classical eddy current evaluation was realized.

The existing forward solutions in Lorentz force evaluation: approximate forward solution and the computational more demanding extended area approach were compared regarding their defect reconstruction performance. A goal function scanning method was used as inverse method in order to directly compare the influence of both forward solutions on the defect reconstruction result avoiding the bias of tuning parameters of the inverse methods. The use of the extended area approach as forward solution yielded more accurate defect depth and extensions estimations compared to the approximate forward solution. However, both forward solutions are limited to defects of regular geometry. Thus, a novel forward solution referred to as single voxel approach was developed. It is based on the superposition of force perturbation signals of small elementary defects. For numerical simulations of various defect sizes, depths and shapes, the novel forward solution showed the smallest deviation in comparison to the other two existing forward solutions.

To reconstruct the defect properties, a minimum norm estimation with elastic net regularization was applied to Lorentz force measurement data of an aluminum specimen. The rationale of using the elastic net regularization is given by the *a priori* knowledge of a non-conducting defect surrounded by a conductor with constant conductivity.

The widely used Tikhonov-Phillips-regularization was applied for comparison purposes. With both regularization methods reproducible and correct depth and adequate size estimations were obtained. The same inverse methods have been applied for defect reconstruction of eddy current evaluation measurements of an aluminum specimen. The reconstructed defects where blurred and less stable for deep lying defects in comparison to the Lorentz force evaluation. Conversely, with the eddy current evaluation, the reconstruction of more complex shaped defects was possible.

As another inverse method, the adapted Landweber iteration was introduced for Lorentz force evaluation. The Landweber iteration has been selected due to promising imaging results in the field of electrical capacitance tomography. An adapted Landweber iteration yielded adequate defect size estimations. The positions of deep lying defects were estimated above the correct ones.

The Lorentz force evaluation is characterized by the difficulty that a small defect close to the specimen surface and a larger and deeper defect generate similar force perturbation signals. This aggravates the estimation of the correct defect depth. A novel principle, referred to as velocity dependent Lorentz force evaluation, was introduced to support the defect depth estimation. The Lorentz force perturbation signals are evaluated at a high velocity ($10 \, \text{m/s}$) relative to a low velocity ($0.1 \, \text{m/s}$). Amplitude changes and signal shifts are used to determine the defect depth incorporating the motion-evoked skin effect. The general feasibility of this novel method has been shown for simulated data.

Zusammenfassung

Die Entwicklung neuer Materialien sowie die ansteigenden Anforderungen an Qualität und Sicherheit erfordern die Entwicklung hochauflösender, zerstörungsfreier Werkstoffevaluierungsverfahren für die Produktion und Wartung. Im neuen Lorentzkraftevaluierungsverfahren wird ein Permanentmagnet relativ zu einem elektrisch leitenden Prüfkörper bewegt. Aufgrund der Bewegung werden Wirbelströme im Prüfkörper induziert. Die Wechselwirkung der Wirbelströme mit dem Magnetfeld führt zur Lorentzkraft, welche auf den Prüfkörper wirkt. Eine Kraft derselben Größe aber in entgegengesetzte Richtung wirkt auf den Permanentmagneten, wo sie gemessen wird. Bei Vorliegen eines Defekts sind die Wirbelstromverteilung und entsprechend die Lorentzkraft verändert. Die Defekteigenschaften werden aus den gemessenen Lorentzkraftkomponenten mittels der Lösung eines schlecht gestellten inversen Problems bestimmt.

Die Ziele der Dissertation umfassen die Entwicklung einer neuen Vorwärtslösung, den Vergleich verschiedener Vorwärtslösungen, die Entwicklung neuer inverser Verfahren sowie die Erarbeitung einer Methode zur verbesserten Defekttiefenbestimmung für die Lorentzkraftevaluierung. Des Weiteren wurde ein qualitativer Vergleich mit der klassischen Wirbelstromevaluierung umgesetzt.

Die existierenden Vorwärtslösungen für die Lorentzkraftevaluierung: "Approximate Forward Solution" und "Extended Area Approach" wurden hinsichtlich der Defektrekonstruktionsgüte verglichen. Es wurde ein Zielfunktionsscanningverfahren angewandt um den Einfluss der beiden Vorwärtslösungen direkt zu vergleichen. Damit wurde eine Verzerrung durch die sonst notwendige Parameterwahl bei inversen Methoden vermieden. Die Verwendung der Vorwärtslösung "Extended Area Approach" erzielte genauere Schätzungen der Defekttiefe und -abmessungen im Vergleich zur "Approximate Forward Solution". Die beiden Vorwärtslösungen sind jedoch auf Defekte mit gleichmäßiger Geometrie beschränkt. Aus diesem Grund wurde die neue Vorwärtslösung "Single Voxel Approach" entwickelt. Sie basiert auf der Superposition von Kraftveränderungssignalen von kleinen elementaren Defekten. Bei numerischen Simulationen mit Defekten verschiedener Größen, Tiefen und Formen zeigte der "Single Voxel Approach" die geringste Abweichung im Vergleich zu den beiden existierenden Vorwärtslösungen.

Eine Minimum-Norm-Schätzung mit Elastic-Net-Regularisierung wurde auf die Lorentzkraftmessdaten eines Aluminiumprüfkörpers zur Rekonstruktion der Defekteigen-

schaften angewandt. Die Motivation zur Nutzung der Elastic-Net-Regularisierung stammt aus dem *a priori* Wissen, dass ein nicht-leitender Defekt von einem Prüfstück mit konstanter Leitfähigkeit umgeben ist. Die weit verbreitete Tikhonov-Phillips-Regularisierung wurde zu Vergleichszwecken angewandt. Mit beiden Regularisierungsmethoden konnte reproduzierbar eine korrekte Defekttiefenschätzung und eine adäquate Größenschätzung erzielt werden. Dasselbe inverse Verfahren wurde für die Defektrekonstruktion aus Wirbelstromevaluierungsmessdaten eines Aluminiumprüfkörpers angewandt. Die Defektrekonstruktionsergebnisse stellten sich für tiefer liegende Defekte verschwommen und weniger stabil im Vergleich zur Lorentzkraftevaluierung dar. Im Gegensatz war mit der Wirbelstromevaluierung die Rekonstruktion komplexerer Defektgeometrien möglich.

Als weitere inverse Methode, wurde die adaptierte Landweber-Iteration für die Lorentzkraftevaluierung eingeführt. Die Landweber-Iteration wurde ausgewählt, da sich im Bereich der elektrischen Kapazitätstomographie vielversprechende Rekonstruktionsergebnisse gezeigt haben. Die adaptierte Landweber-Iteration erzielte adäquate Defektgrößenschätzungen. Die Position von tief liegenden Defekten wurde zu hoch rekonstruiert.

Die Lorentzkraftevaluierung ist gekennzeichnet durch die Schwierigkeit, dass ein kleiner Defekt nahe der Prüfkörperoberfläche und ein größerer tiefer liegender Defekt ähnliche Kraftveränderungssignale zeigen. Das erschwert die Bestimmung der korrekten Defekttiefe. Das neue Prinzip der geschwindigkeitsabhängigen Lorentzkraftevaluierung wurde eingeführt um die Defekttiefenbestimmung zu unterstützen. Die Lorentzkraftveränderungssignale werden bei einer hohen Geschwindigkeit ($10\,\mathrm{m/s}$) relativ zu den Signalen bei einer niedrigen Geschwindigkeit ($0.1\,\mathrm{m/s}$) ausgewertet. Amplitudenveränderungen und Signalverschiebungen werden genutzt um die Defekttiefe zu bestimmen. Dabei wird der bewegungsinduzierte Skineffekt ausgenutzt. Die Plausibilität dieser neuen Methode wurde für Simulationsdaten gezeigt.

Table of Contents

1 Introduction

1.1 Motivation

On July 19, 1989 the aircraft McDonnell Douglas DC-10 crashed on the way from Denver to Chicago at the Sioux Gateway Airport [1]. The reason for this crash was a sand grain sized hollow below the titanium surface of the fan disk that lead to a fatigue crack, which has been overlooked during maintenance. The fan disk broke apart and the flying debris destroyed the hydraulic lines thus, leading to a disabled aircraft and subsequently to the crash. This example illustrates the importance of high-resolution, nondestructive evaluation (NDE) methods during manufacturing and maintenance. Further, the development of new materials as well as the increasing standards for quality and safety require high-resolution NDE methods.

NDE aims to characterize a material defect by its location, shape and size in contrast to the nondestructive testing, which offers information about the presence or absence of a defect. In the field of NDE, conducting materials are often evaluated by ultrasonics [2], radiography [3], thermography [4], magnetic induction thermography [5], magnetic flux leakage [6] and eddy current evaluation (ECE) [7].

In the frequently used ECE, a coil is excited with a time-changing current leading to a time-varying magnetic field that induces eddy currents in a conducting material under test according to Faraday's induction law [8]. The induced eddy currents generate a secondary magnetic field that is quantified by a magnetic field sensor, e.g. a pick-up coil. In presence of a defect, the eddy currents are perturbed and in consequence the secondary magnetic field is also perturbed. The ECE is limited by the skin effect. An increasing excitation frequency f_e increases the eddy current amplitudes as well as the corresponding magnetic field response, but it decreases the penetration depth at the same time. In consequence, the ECE is preferably used to characterize defects that are located close to the upper surface of a specimen [9].

To reduce this limitation, the Lorentz force evaluation (LFE) has been introduced in 2013 [10]. In LFE, a permanent magnet is moved relative to a conducting specimen under test. Owing to this movement, eddy currents are induced inside the conductor. The interaction of the eddy currents with the magnetic field leads to the Lorentz force. A force

of the same magnitude but in opposite direction acts on the permanent magnet, where it is measured. In presence of a defect, the eddy currents are perturbed. Consequently, the Lorentz force components are also perturbed. The force perturbation signal, referred to as defect response signal (DRS), acts as input signal for defect reconstruction algorithms. The LFE belongs to the motion-induced eddy current evaluation methods. Instead of measuring the Lorentz force, another research group uses the secondary magnetic field from the induced eddy currents to detect defects in conducting specimen [11–14].

In order to determine defect properties in NDE (Fig. 1.1) from a measured variable, an inverse problem has to be solved. For that purpose a forward solution that projects the setup with the defect onto the measurement data is needed. One class of inverse methods starts with an initial guess of the defect. The variable corresponding to the measured one is forward calculated and the deviation is determined. The new parameters of the defect are estimated by the inverse method. Then, a new forward calculation is performed and the deviation to the measured variable is computed again. This process is repeated until defect parameters are found that give a minimal deviation between the forward calculated and the measured variable.
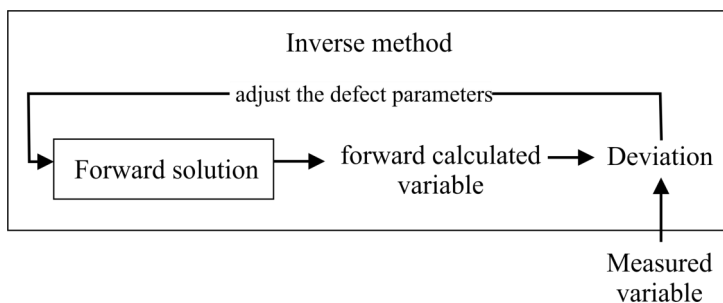
Figure 1.1: Principle of an inverse problem in NDE: An inverse method adjusts the defect parameters such that they minimize the deviation between the measured variable and the forward calculated one. For LFE, the measured variable is the Lorentz force DRS.

In 2013, the approximate forward solution (AFS) [10] was introduced for LFE, where the permanent magnet was modeled by a single magnetic dipole. In this study [10], the inverse problem was solved by reconstruction of a conductivity distribution using the truncated singular value decomposition (TSVD). The defect parameters where derived from the reconstructed conductivity distribution. For the first time, the feasibility of LFE was shown. An aluminum specimen with cuboidal defects at the defect depth of 2 mm were investigated. The difficulty of depth estimation in LFE was pointed out, as it could not be estimated accurately.

Spherical permanent magnets are difficult to align in the desired direction. Thus, cuboidal and cylindrical permanent magnets are used in the experimental setups [15]. The single magnetic dipole model is only appropriate for spherical permanent magnets.

In 2015, the multiple dipoles method (MDM) was introduced as novel permanent magnet model [16]. Contrary to analytical models for these types of permanent magnets, the MDM can be integrated easily into the forward solution AFS. Also in 2015, the differential evolution algorithm [17] was used to reconstruct the conductivity distribution from the measured Lorentz force signals of an ALUCUBOND® specimen. ALUCUBOND is made of two aluminum alloy layers with an isolating interface layer of polyethylene. A cylindrical shaped defect was located at the bottom aluminum layer at the depth of 3.5 mm. The evolutionary algorithm achieved an appropriate defect size and position estimation and a correct depth estimation.

Up until then, the AFS was the only used forward solution for LFE, but it only works optimal for uniformly shaped defects with equal extensions, like defects with circular or quadratic cross-sections. The DRS calculation by the AFS is based only on the defect. The extended area approach (EAA) [18], introduced in 2015, also takes the area around the defect into account. It leads to more accurate estimations of the DRS, especially for uniformly shaped defects with non-equal extensions, like defects with ellipsoidal or rectangular cross-sections [18]. The EAA is computational more demanding than the AFS. The defect reconstruction performance of both forward solutions has not been compared up to now. Both forward solutions are defined for a setup with a single defect with high *compactness of shape* located far away from the specimen edges.

In 2016, the current density reconstruction [19] was introduced as inverse method for LFE. It assumes that the defect depth is known beforehand by another method. The size and position estimation errors were in a good range but worse compared to the differential evolution method [15,17]. In the same year, a glass-fiber reinforced aluminum laminate (GLARE) specimen, containing a cuboidal defect in the second aluminum layer at depth of 0.75 mm was investigated by LFE [15]. The defect could be detected. The evaluation of the specimen by a length-width-depth scanning method that used the EAA as forward solution, did not yield the correct defect extensions and depth.

To summarize the open challenges of the LFE, the first point that needs to be addressed is the reconstruction of defects located deeper than 4 mm from the top layer of the conducting specimen, as previous work only investigated defects of depths between 0 and 4 mm. The second important topic deals with the defect depth estimation. In LFE, a small defect close to the surface and a deeper and larger one generate similar DRS. That aggravates the estimation of the correct defect depth. Novel inverse methods and novel principles need to be developed that achieve more accurate and stable defect depth estimation results. It should be investigated, whether the use of the computational more demanding forward solution EAA is justified by an improved defect reconstruction performance in comparison to the use of AFS. Further, a novel forward solution should be developed that overcomes the limits of AFS and EAA in terms of defect shape and location. Moreover, up to now it has not been investigated, whether the LFE shows

reproducibility of defect reconstruction results for repeated measurements. Additionally, only the defect detection limits have been compared for Lorentz force eddy current testing and classical eddy current testing [20]. Thus, the defect evaluation should be compared qualitatively between LFE and ECE.

Thus, the aims of the thesis are:

1. Development of novel inverse methods that incorporate *a priori* knowledge by regularization methods and are also able to reconstruct deep lying defects using the forward solution AFS.

2. Investigation of the reproducibility of defect reconstruction results in LFE.

3. Qualitative comparison of LFE and ECE.

4. Comparison of the forward solutions AFS and EAA of LFE regarding the defect reconstruction performance.

5. Development a novel forward solution that overcomes the limitations of AFS and EAA regarding defect shape and location.

6. Development of a novel principle that supports the defect depth estimation.

1.2 Structure and Contribution of the Thesis

Chapter 2 contains the fundamentals of LFE (section 2.1) and ECE (section 2.2). The principle, the numerical simulations, the measurement setup and the used forward solutions are described for both NDE methods. The inverse problem is examined in section 2.3 regarding its properties. Further, an overview over selected inverse calculation methods is given.

Chapter 3 is divided into four sections. It addresses the first aim of the thesis. The principle idea is to use a regularization method to incorporate the *a priori* knowledge that a non-conducting defect is surrounded by a conductor with constant conductivity. For that purpose, the first section 3.1 introduces the elastic net regularization (ENR) as regularization technique for inverse problems. In section 3.2, the minimum norm estimation (MNE) with ENR in comparison to the commonly used Tikhonov-Phillips-regularization (TPR) is applied for the defect reconstruction in LFE. This section contains methods and results that have been presented in [21] and are published in [22]. The following sections 3.3 and 3.4 address the third aim of the thesis. Section 3.3 contains the MNE with ENR in comparison to TPR applied to defect reconstruction in ECE. A qualitative comparison between the LFE and the ECE is drawn in section 3.4.

Chapter 4 also addresses the first aim of the thesis. It introduces an adapted Landweber algorithm for the determination of defect properties from Lorentz force data. The

Landweber iteration has been selected due to promising imaging results in the field of electrical capacitance tomography which showed a comparable situation of the inverse problem. Parameter studies based on simulation data are performed in order to obtain the crucial parameters of the Landweber algorithm, e.g. the number of iterations. The results are also presented for measurement data. This Chapter contains methods and results that were presented in [23].

Chapter 5 contains the approach of the fourth aim. A comparison between two forward solutions of LFE, the AFS and the EAA, is implemented regarding the defect reconstruction performance. For this purpose, data sets from simulations and measurements with varying defect shapes and depths are investigated. Goal function scans are applied to determine the defect properties directly. With the goal function scan a comparison between AFS and EAA regarding the defect reconstruction performance is possible without a bias from parameter selection for the inverse calculation method. Parts of the methods and results of this Chapter have been published in [24] and presented at [25–27].

Chapters 3-5 additionally address the first aim as defect depths up to 8 mm are investigated within aluminum specimens. Further, the second thesis aim is addressed by these Chapters as repeated Lorentz force measurements are investigated.

A novel forward solution for LFE, referred to as single voxel approach (SVA), is introduced in Chapter 6. It addresses the fifth thesis aim. This novel approach is based on the idea to calculate the defect response signal for a small cuboidal defect at varying positions using methods of numerical simulations. The DRS of an arbitrary shaped defect is then calculated as a superposition of single DRSs from the small cuboidal defects that belong to this defect. The DRSs are calculated for various defect shapes at different depths and compared to DRSs obtained by finite element method (FEM) simulations. The results are compared to the previous forward solutions AFS and EAA. This Chapter contains methods and results that have been presented at [28] and are published in [29].

Chapter 7 addresses the difficulty in LFE to determine the defect depth from the 2D Lorentz force measurement and with that the sixth thesis aim. A novel principle is derived that uses a low (0.1 m/s) and a high (10 m/s) velocity for the relative movement between the permanent magnet and the specimen under test. Due to the motion-evoked skin effect, the DRSs at the high velocity in relation to the DRSs at the low velocity change for varying defect depths such that parameters for the depth estimation can be extracted. A simulation study is performed for defects of varying sizes and depths to determine the depth estimation parameters. This Chapter contains methods and results that have been presented at [30] and are published in [31].

2 Fundamentals

2.1 Lorentz Force Evaluation

2.1.1 Principle

In the LFE, a conducting specimen under investigation is moved relative to a fixed permanent magnet with a velocity $\vec{v}$ (Fig. 2.1). Due to this movement eddy currents are induced inside the specimen that counteract with the magnetic field $\vec{B}$. This counteraction leads to the Lorentz force $\vec{F}_{\mathrm{L}}$. The Lorentz force acts on the conducting specimen as
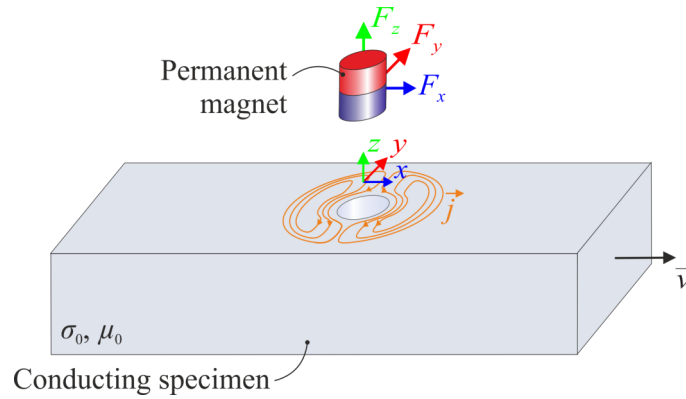
Figure 2.1: Principle of Lorentz force evaluation: A conducting specimen is moved relative to a fixed permanent magnet. The induced eddy currents counteract with the magnetic field and thus lead to Lorentz forces. In presence of a defect the eddy currents are perturbed and so are the Lorentz force components.

a braking force. Due to Newton's third axiom, a force $\vec{F} = -\vec{F}_{\mathrm{L}}$ with the same magnitude but in opposite direction acts on the permanent magnet, where it can be measured. The force $\vec{F}$ that acts on the permanent magnet at the position $\vec{r}_0 = [x_0 \ y_0 \ z_0]^{\mathrm{T}}$ is defined as

$$\vec{F} = \begin{bmatrix} F_x \\ F_y \\ F_z \end{bmatrix} = \int_V -\vec{j} \times \vec{B} \ dV, \tag{2.1}$$

where $\vec{j}$ denotes the eddy current density within the conducting specimen of volume V. In the framework of this thesis, this force $\vec{F}$ is also referred to as Lorentz force

for simplification. The magnetic flux density $\vec{B} = \vec{B}_{\mathrm{p}} + \vec{b}_{\mathrm{s}}$ consists of the magnetic flux density $\vec{B}_{\mathrm{p}}$ of the permanent magnet and the secondary magnetic flux density $\vec{b}_{\mathrm{s}}$ originating from the induced eddy currents $\vec{j}$. In presence of a defect, the eddy currents are perturbed. In consequence, the Lorentz force components are perturbed as well.

   For the estimation of defect properties, the Lorentz force components have to be measured at several positions. The movement of the conducting specimen relative to the fixed permanent magnet can be viewed just as the permanent magnet moves over the fixed conducting specimen under test. From that point of view, the permanent magnet moves in parallel scanning lines (Fig. 2.2) above the specimen with the velocity $\vec{v}$. The force acting on the permanent magnet during the scanning process is measured.
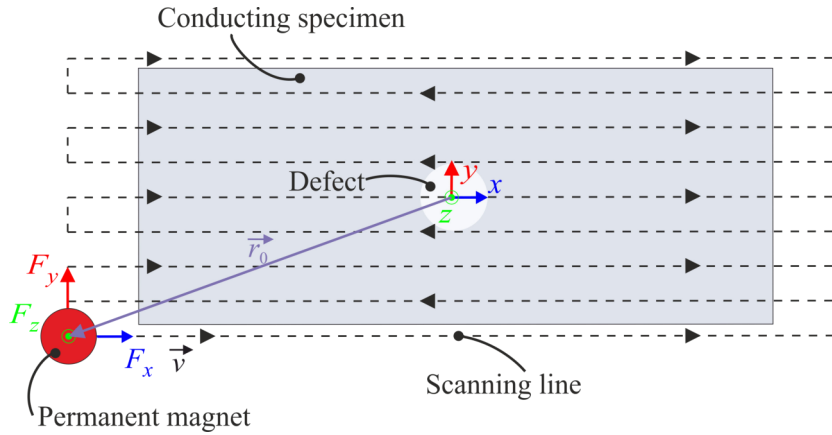
Figure 2.2: Principle of Lorentz force evaluation scanning: The movement of the specimen relative to the fixed permanent magnet can be viewed just as the permanent magnet moves above a fixed specimen. The permanent magnet "scans" the specimen in multiple parallel scanning lines.

Fig. 2.3 c shows exemplary force components $F_{0,x}$ and $F_{0,z}$ along one scanning line ($y = 0$) for a specimen without a defect obtained by FEM simulations. The signal deflections at the beginning and end of the signal occur due to the edges of the specimen. The force components F_x and F_z for the same specimen but containing a subsurface defect are shown in Fig. 2.3 b. The force components F_y and $F_{0,y}$ for the specimen with and without a defect vanish at this scanning line ($y = 0$) due to symmetry.

The information about the defect is encoded in the perturbation of the force signal (Fig. 2.3 b, arrows). To extract this perturbation, the DRS at one permanent magnet position $\vec{r}_0$ (Fig. 2.2) is defined as

$$\Delta \vec{F} = \begin{bmatrix} \Delta F_x \\ \Delta F_y \\ \Delta F_z \end{bmatrix} = \vec{F} - \vec{F}_0 = \int_V -\vec{j} \times \vec{B} \; dV - \int_V -\vec{j}_0 \times \vec{B} \; dV, \qquad (2.2)$$

describing the difference of the force $\vec{F}$ acting on the permanent magnet with the spec-

imen containing a defect and the force $\vec{F}_0$ for the same specimen without a defect. The eddy current densities $\vec{j}$ and $\vec{j}_0$ describe the defect and the defect free case, respectively. Fig. 2.3 a shows the DRS components ΔF_x and ΔF_z along one scanning line ($y = 0$) for the given example. The DRS obtained along multiple parallel scanning lines (Fig. 2.2) acts as input signal for the reconstruction of defect properties. Fig. 2.4 shows an example of the DRS components. In order to determine the defect properties from the DRS components like shown in Fig. 2.4, an inverse problem has to be solved.
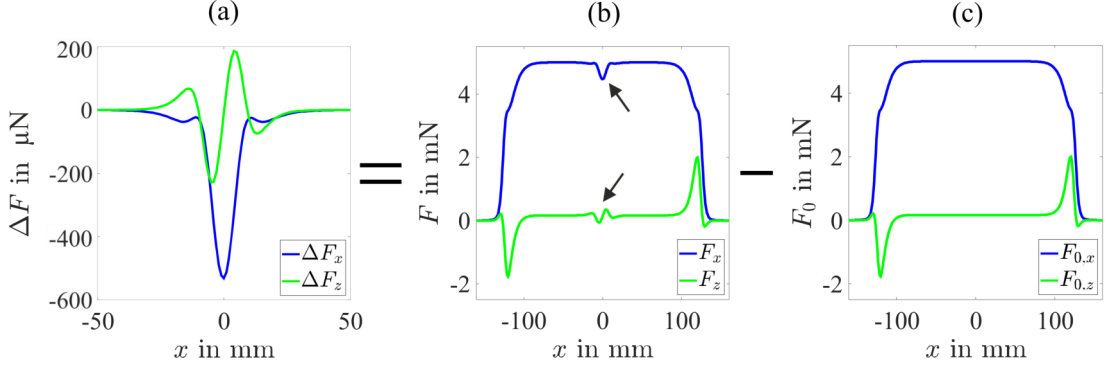
Figure 2.3: Principle of DRS: DRS components ΔF_x and ΔF_z (a) are determined by the difference of force components F_x and F_z from a specimen containing a defect (b) and $F_{0,x}$ and $F_{0,z}$ of the same specimen without a defect (c). The force components are shown along the symmetry line ($y = 0$), where the y-component vanishes. Note the different scale for ΔF_x and ΔF_z in (a).
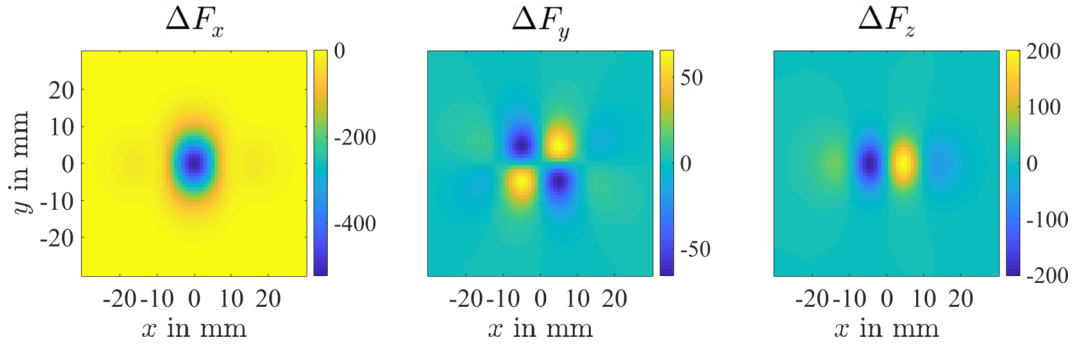
Figure 2.4: DRS components ΔF_x, ΔF_y and ΔF_z in µN obtained by FEM simulations.

2.1.2 Numerical Simulations

2.1.2.1 Overview

Numerical simulations in LFE provide noise-free benchmark signals to develop new forward solutions, investigate novel inverse methods, examine new principles or conduct

parameter studies. Thus, the general properties of a novel method can be assessed before the application to measurement data. The data sets obtained by FEM simulations act as reference data sets in this thesis.

The selected principle of a numerical simulation depends on the relative velocity $\vec{v} = v\vec{e}_x$ between the permanent magnet and the specimen as well as the conductivity σ_0 and the magnetic permeability μ of the material. The selection is based on the magnetic Reynolds number

$$R_{\mathrm{m}} = \mu\sigma_0 l_{\mathrm{c}} v, \tag{2.3}$$

where l_{c} denotes the characteristic length of the problem. In the framework of LFE, the magnetic permeability of the investigated non-magnetic conducting materials equal the vacuum permeability $\mu = \mu_0$. The magnetic Reynolds number R_{m} is a measure to decide, if the secondary magnetic field $\vec{b}_{\mathrm{s}}$ of the induced eddy currents and the skin effect are negligible. In consequence, also the numerical simulation method can be selected according to the magnetic Reynolds number R_{m}. According to [32], the type of numerical simulation method can be roughly chosen by

$$R_{\mathrm{m}} = \begin{cases} & R_{\mathrm{m}} < 1 \;\; \rightarrow \;\; \text{Weak Reaction Approach} \\ 1 \leq & R_{\mathrm{m}} < 10 \rightarrow \;\; \text{Quasi-stationary Approach} \\ & R_{\mathrm{m}} \geq 10 \rightarrow \;\; \text{Transient Approaches} \end{cases} \tag{2.4}$$

In LFE, the characteristic length l_{c} can be chosen as half of the height H of the specimen [33], thus $l_{\mathrm{c}} = {}^H\!/_2$. According to [33], for an aluminum specimen with $H \leq 50\,\mathrm{mm}$ and a conductivity of $\sigma_0 = 30.61\,\mathrm{MS/m}$, the weak reaction approach can be applied for velocities $v < 0.5\,\mathrm{m/s}$. In this thesis, specimens with two different σ_0-H-configurations are investigated. The approximate velocity boundaries for the selection of the numerical simulation methods are derived from the described rule of [33] and are shown in Table 2.1.

Table 2.1: Investigated configurations of conductivity σ_0 and specimen height H and the consequence for selection of the numerical simulation method.

Config.	σ_0 in MS/m	H in mm	Weak Reaction Approach	Quasi-stationary Approach	Transient Approaches
A	30.61	100	$v < 0.25\,\mathrm{m/s}$	$0.25\,\mathrm{m/s} \leq v \leq 2.5\,\mathrm{m/s}$	$v > 2.5\,\mathrm{m/s}$
B	21	50	$v < 0.7\,\mathrm{m/s}$	$0.7\,\mathrm{m/s} \leq v \leq 7\,\mathrm{m/s}$	$v > 7\,\mathrm{m/s}$

In order to determine the DRS components $\Delta\vec{F}$ according to (2.2), the numerical simulations have to be done for the specimen with the defect to calculate $\vec{F}$ and for the same specimen without a defect in order to obtain $\vec{F}_0$. For the calculation of a

whole scan, like shown in Fig. 2.4, the underlying problem of the numerical simulation method has to be solved for each relative permanent magnet position separately. If the specimen has large extensions in x- and y-direction such that force plateaus are present as shown in Fig. 2.3, the DRS components can be obtained more easily. The influences of the specimen edges (Fig. 2.3) are cut away and the offsets of the scanning lines are subtracted in order to obtain ΔF_x, ΔF_y and ΔF_z.

2.1.2.2 Weak Reaction Approach

In general, the LFE uses small velocities, e.g. $v = 0.1\,\text{m/s}$, to reduce the skin effect [34] and mechanical oscillations [17]. The secondary magnetic field $\vec{b}_s$ and the motion-evoked skin effect are negligible as the magnetic Reynolds number $R_\text{m} < 1$. Thus, according to the weak reaction approach [33], the eddy current density within the conductor can be calculated directly by Ohm's law for moving conductors as

$$\vec{j} = [\sigma_0]\left(-\nabla\varphi + \vec{v} \times \vec{B}_\text{p}\right),\qquad(2.5)$$

where $\vec{B}_\text{p}$ denotes the magnetic flux density of the permanent magnet and φ the electric scalar potential. The conductivity is expressed as a tensor $[\sigma_0] = \text{diag}\left(\sigma_{xx},\ \sigma_{yy},\ \sigma_{zz}\right)$ which allows the definition of anisotropic and isotropic materials. The drawback of the weak reaction approach is that the calculation of the unperturbed part $F_{z,0}$ of the force component F_z equals zero due to the neglection of the secondary magnetic field which imposes a symmetry in the eddy current density distribution [33]. This symmetry is suppressed in presence of a defect such that the DRS component ΔF_z is determined correctly.

Finite Element Method   The continuity's equation is used to derive the Laplace equation for the electric scalar potential φ:

$$\nabla \cdot \vec{j} = 0 \text{ with } \vec{n} \cdot \vec{j} = 0\Big|_{\Gamma_c \cup \Gamma_d} \rightarrow \nabla^2\varphi = 0 \text{ with } \frac{\partial\varphi}{\partial n} = \vec{n} \cdot \left(\vec{v} \times \vec{B}_\text{p}\right)\Big|_{\Gamma_c \cup \Gamma_d},\qquad(2.6)$$

where $\vec{n}$ is the unit vector normal to the conductor (Γ_c) and the defect surfaces (Γ_d) [32]. For ensuring the solution's uniqueness of (2.6) with Neumann boundary condition $\vec{n} \cdot \vec{j} = 0$, a grounding condition has to be added. The potential φ is set to zero at one of the upper corners of the specimen. In the case of a defect inside the specimen, Ohm's law for moving conductors (2.5) also takes into account the conductivity's jump at the internal boundary between the conductor and the defect including both contributions to $\vec{j}$ based on the electric scalar potential φ and the product $\vec{v} \times \vec{B}_\text{p}$. The problem (2.6) is implemented in COMSOL Multiphysics® Version 5.2a (COMSOL Inc., Burlington, USA). Only the specimen and the defect are discretized by tetrahedral elements. The

magnetic flux density $\vec{B}_\mathrm{p}$ is imported from previous calculations, which depend on the used permanent magnet. If a spherical permanent magnet is used, it is modeled by a single magnetic dipole (see also section 2.1.4.1) and $\vec{B}_\mathrm{p}$ is calculated analytically as shown in [8]. In case of a cylindrical permanent magnet, the magnetic flux density is calculated by the analytic current model [35]. The corresponding elliptic integrals are approximated by the mid-point rule [36] and the arithmetic geometric mean method [32, 37].

After solving (2.6) by FEM, the eddy current density values are determined by (2.5) with the obtained values for φ and $\vec{B}_\mathrm{p}$. The Lorentz force components for one permanent magnet position are calculated according to (2.1). For the calculation of a whole scan, problem (2.6) has to be solved for each relative permanent magnet position separately.

Boundary Element Source Method   The boundary element source method (BESM) [38] is a variant of the boundary element method. In order to calculate the Lorentz force components according to (2.1) using the weak reaction approach, the electrical scalar potential φ has to be determined for the calculation of the eddy current density distribution according to (2.5). The key concept of the BESM is the presence of surface charges, which occur at the interfaces that separate mediums of different conductivity, i.e. the specimen surface and the defect surface, like illustrated in Fig. 2.5.

The electric scalar potential φ within the conducting specimen can be calculated by a superposition of the unknown surface charges. The surface charges are determined

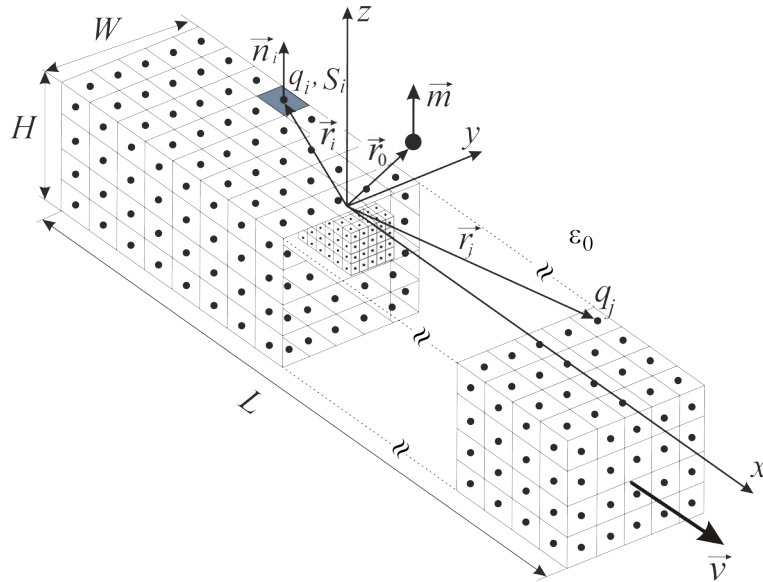Figure 2.5: Principle of BESM: Surface charges occur at the interfaces that separate mediums of different conductivity, i.e. specimen and defect surfaces (small cuboid). The surface charges are assumed to be constant at each boundary element (squares) and placed at the centroids of the elements (dots in each square) in order to calculate the electric scalar potential φ by fulfilling the boundary conditions at the interfaces.

by fulfilling the boundary condition $\vec{j} \cdot \vec{n} = 0$ at the surfaces. Ohm's law for moving conductors (2.5) is inserted into the boundary condition that leads to

$$\left(-\nabla\varphi_i + \vec{v} \times \vec{B}_i\right) \cdot \vec{n}_i = 0, \tag{2.7}$$

which has to be fulfilled at the i-th surface charge element (Fig. 2.5). The gradient of the electric scalar potential $\nabla\varphi_i$ at the i-th surface charge element is calculated as a superposition of the surface charges q_j by Coulomb's potential [38]. The contribution from the surface charge q_i itself is added as described in [38]. As a consequence, a system of linear equations is built from (2.7) as

$$[A]_{(S+D)\times(S+D)} \cdot \vec{q}_{(S+D)\times 1} = \vec{c}_{(S+D)\times 1}$$

$$\text{with } a_{i,j} = \begin{cases} -\dfrac{1}{2S_i\varepsilon_0}, & i = j \\[2mm] \dfrac{(\vec{r}_i - \vec{r}_j) \cdot \vec{n}_i}{4\pi\varepsilon_0 \left|\vec{r}_i - \vec{r}_j\right|^3}, & i \neq j \end{cases}$$

$$\text{and } c_i = -\left(\vec{v} \times \vec{B}_i\right) \cdot \vec{n}_i \tag{2.8}$$

where S and D denote the numbers of surface charge elements at the specimen and defect surfaces, respectively. A diagonal element $a_{i,i}$ of the matrix $[A]$ depends on the size S_i of the i-th surface charge element. The vectors $\vec{r}_i$ and $\vec{r}_j$ belong to the centers of the observed surface charge element i and the source surface charge element j, respectively. Eqn. (2.8) is valid for normal vectors $\vec{n}_i$ pointing in positive directions of the coordinate system (Fig. 2.5). In case of normal vectors $\vec{n}_i$ in negative direction, the signs of $a_{i,i}$ and c_i are flipped. The calculation of the magnetic flux density $\vec{B}_i$ at the center of the i-th surface charge element depends on the used permanent magnet. A spherical permanent magnet is modeled by a single magnetic dipole (Fig. 2.5, see also section 2.1.4.1) and $\vec{B}_i$ is calculated analytically as shown in [8]. It is also possible to import the magnetic flux density distribution calculated by another numerical simulation method. The system of linear equations (2.8) is solved to determine the unknown charges q_j of $\vec{q}$.

In order to calculate the Lorentz force components according to (2.1), the specimen is discretized into M volume elements (voxels) of volume V_{E} and the eddy current density $\vec{j}_m$ in the center $\vec{r}_m = [x_m\ y_m\ z_m]^{\mathrm{T}}$ of the m-th voxel is calculated by Ohm's law of moving conductors (2.5). The electric scalar potential φ_m is calculated by

$$\varphi_m = \frac{1}{4\pi\varepsilon_0} \sum_{j=1}^{S+D} \frac{q_j}{|\vec{r}_m - \vec{r}_j|}. \tag{2.9}$$

In order to determine the DRS components according to (2.2), the Lorentz force

components $\vec{F}_0$ have to be calculated for the defect free specimen. For that purpose, the system of linear equations (2.8) is reformulated containing only the S surface charge elements on the specimen surface. The calculation of φ_m (2.9) changes accordingly.

If the scans of the Lorentz force components for the specimen with a defect should be calculated, the surface charge distribution $\vec{q}$ has to be calculated for each relative position of the permanent magnet. However, the change of the magnet position only influences the right-hand side $\vec{c}$ of the system of linear equations (2.8). The matrix $[A]$ does not change and its inversion has to be done only once. The determination of the charges requires just a multiplication of the inverted matrix $[A]^{-1}$ and a right-hand side $\vec{c}$ of a system of linear equations. This procedure has to be repeated for the defect free specimen in order to obtain the DRS component scans. The BESM methodology is implemented in MATLAB® R2018a (The MathWorks, Inc., Natick, Massachusetts, USA).

2.1.2.3   Quasi-stationary Approach

In case of the LFE, the quasi-stationary approach (QSA) is used roughly for magnetic Reynolds numbers R_m between 1 and 10 [32]. The QSA takes the stationary part of the secondary magnetic field $\vec{b}_s$ into account but neglects any time-dependency of the total magnetic field $\vec{B} = \vec{B}_p + \vec{b}_s$. The governing equations are

$$\triangledown \times \left(\frac{1}{\mu_0} \triangledown \times \vec{A} - \vec{M} \right) = [\sigma] \left(-\triangledown \varphi + \vec{v} \times \triangledown \times \vec{A} \right)$$
$$\triangledown \cdot \left([\sigma] \left(-\triangledown \varphi + \vec{v} \times \triangledown \times \vec{A} \right) \right) = 0 \text{ with } \vec{n} \cdot \vec{j} = 0 \Big|_{\Gamma_c}, \tag{2.10}$$

where $\vec{A}$ denotes the magnetic vector potential with $\vec{B} = \triangledown \times \vec{A}$ and $\vec{M}$ the magnetization of the permanent magnet, respectively. The stationary part of the secondary magnetic field $\vec{b}_s$ is incorporated in the term $\vec{v} \times \triangledown \times \vec{A}$. The problem described in (2.10) is solved by FEM implemented in COMSOL Multiphysics® Version 5.2a. The determined φ and $\vec{A}$ are used to calculate the eddy current density within the specimen by

$$\vec{j} = [\sigma] \left(-\triangledown \varphi + \vec{v} \times \triangledown \times \vec{A} \right) \tag{2.11}$$

and further the Lorentz force according to (2.1). For the determination of a scan, a new finite element mesh has to be generated and (2.10) has to be solved for each relative permanent magnet position individually. One advantage of the QSA is that due to the neglection of the time dependence each solution is treated individually. In consequence, the numbers of finite elements and degrees of freedoms are reduced in comparison to transient approaches. The QSA is flexible in positioning of a defect and able to model the defect geometry in detail, especially for defects with curvatures, like spheres, ellipsoids

or cylinders [32].

2.1.2.4 Transient Approaches: Moving Defect and Moving Magnet Approach

The two methods of transient numerical simulation of the Lorentz force in LFE are the moving defect approach (MDA) and the moving magnet approach (MMA). They differ in terms of the frames of reference where the calculations are performed and for which part of the system the movement is implemented. Both methods are implemented in COMSOL Multiphysics® Version 5.2a using FEM [32].

Moving defect approach   In the MDA, the electromagnetic fields are calculated in the laboratory frame of reference [32]. It means that the observer is located in the fixed permanent magnet and looks at the movement of the conducting specimen below. Instead of moving the specimen together with the defect, which would lead to time consuming re-meshing, the MDA realizes a moving of the defect within the conductor. For that purpose, a volume in movement direction is defined within the specimen, referred to as defect-domain Ω_{d}. This volume is discretized into hexahedral elements. The movement of the defect within Ω_{d} is realized by a time-dependent conductivity distribution using logical expressions as

$$[\sigma(\vec{r}, t)] = (1 - LE(\vec{r}, t)) [\sigma_0] + LE(\vec{r}, t) [\sigma_{\mathrm{d}}], \qquad (2.12)$$

where $\vec{r}$ denotes the position vector within the conductor. The logical expressions $LE(\cdot)$ realize the modeling of the spatial coordinates of moving parts on a fixed computational grid by application of Boolean algebra [39]. The conductivity tensors of the specimen and the defect are denoted by $[\sigma_0]$ and $[\sigma_{\mathrm{d}}]$, respectively. The movement of the defect or an assemble of multiple defects is realized by redefining the logical expression at every time step [32].

At each time step, the following governing equations have to be solved

$$\nabla \times \left(\frac{1}{\mu_0} \nabla \times \vec{A}^* - \vec{M} \right) = [\sigma] \left(-\frac{\partial \vec{A}^*}{\partial t} + \vec{v} \times \nabla \times \vec{A}^* \right)$$

$$\nabla \cdot \left([\sigma] \left(-\frac{\partial \vec{A}^*}{\partial t} + \vec{v} \times \nabla \times \vec{A}^* \right) \right) = 0 \text{ with } \vec{n} \cdot \vec{j} = 0 \Big|_{\Gamma_{\mathrm{c}}}, \qquad (2.13)$$

where $\vec{A}^*$ denotes the modified magnetic vector potential $\vec{A}^* = \vec{A} + \int_0^t \nabla \varphi \, dt$ [40] that is used to solve the field more effectively as the degrees of freedom are reduced. The problem (2.13) is solved by using fixed time steps to avoid time consuming re-meshing. The determined $\vec{A}^*$ is used to calculate the eddy current density within the specimen by

$$\vec{j} = [\sigma] \left(-\frac{\partial \vec{A}^*}{\partial t} + \vec{v} \times \nabla \times \vec{A}^* \right) \tag{2.14}$$

and in consequence the Lorentz force according to (2.1).

The advantage of MDA is that complicated magnet geometries such as Halbach arrays combined with ferromagnetic materials can be considered, due to the used frame of reference [32]. The drawbacks of MDA are that the defect has to be located far away from the front and the rear end of the specimen. Thus, not the whole Lorentz force profile including the specimen edges can be calculated. Additionally for complex defect shapes, a very fine discretization and sophisticated logical expressions are necessary [32].

Moving magnet approach   In the MMA, the electromagnetic field problem is solved in the rest frame of reference [32]. It means that the observer is located in the fixed specimen and looks at the movement of the magnet system in negative direction. For that purpose, a volume in negative movement direction is defined around the magnet system, referred to as magnet-domain Ω_m. This volume is discretized into hexahedral elements. The movement of the magnet system within Ω_m is realized by a time-dependent magnetic remanence distribution using logical expressions as

$$\vec{B}_r(\vec{r}, t) = [LE_x(\vec{r}, t), LE_y(\vec{r}, t), LE_z(\vec{r}, t)]^{\mathrm{T}} B_r. \tag{2.15}$$

The parts of the magnet system are assumed to be made of the same material with a nominal magnetic remanence B_r. At each time step, the following governing equations have to be solved

$$\nabla \times \left(\frac{1}{\mu_0} \nabla \times \vec{A}^* - \vec{M} \right) = [\sigma] \left(-\frac{\partial \vec{A}^*}{\partial t} \right)$$

$$\nabla \cdot \left([\sigma] \left(-\frac{\partial \vec{A}^*}{\partial t} \right) \right) = 0 \text{ with } \vec{n} \cdot \vec{j} = 0 \Big|_{\Gamma_c}. \tag{2.16}$$

The velocity term is omitted in the MMA. The determined $\vec{A}^*$ is used to calculate the eddy current density within the specimen by

$$\vec{j} = [\sigma] \left(-\frac{\partial \vec{A}^*}{\partial t} \right) \tag{2.17}$$

and in consequence the Lorentz force according to (2.1). The MMA is able to model the complete force signal including the specimen edges, but is currently restricted to relatively simple magnet geometries without ferromagnetic materials [32].

2.1.3 Measurement Setup

The BASALT-C MMP-15 (TETRA GmbH, Ilmenau, Germany, 2015) with a mechanical system and a control cabinet builds the measurement setup for the LFE. The specimen, a set of stacked aluminum alloy (EN AW-5754) sheets (Fig. 2.6), is mounted on the direct drive of the mechanical system. One of the aluminum sheets contains a defect. The direct drive accelerates the specimen to the desired velocity. It is moved relative to the permanent magnet in x-direction. A desired constant velocity up to $4\,\mathrm{m/s}$ can be achieved with a negligible standard deviation of $2.19 \cdot 10^{-10}\,\mathrm{mm/s}$. The direct drive provides an acceleration up to $50\,\mathrm{m/s}^2$ [20].

A granite positioning portal is installed above the direct drive. It carries spindle drives in y- and z-direction to position the mount that carries the 3D force sensor and the cylindrical permanent magnet (Fig. 2.6) above the top surface of the specimen [20]. The NdFeB permanent magnet of material grade N52 is characterized by a diameter of $D_\mathrm{m} = 22.5\,\mathrm{mm}$ and height of $H_\mathrm{m} = 17.6\,\mathrm{mm}$ with the homogeneous magnetization $\vec{M} = {}^{B_\mathrm{r}}\!/\mu_0\ \vec{e}_z\ B_\mathrm{r} = 1.43\,\mathrm{T}$, where B_r denotes the remanence. This permanent magnet configuration is optimized for the detection of deep lying defects [41]. The force acting on the permanent magnet is measured by the strain gauge force sensor K3D40 (ME-Meßsysteme GmbH, Hennigsdorf, Germany, 2014). The nominal force in x-, y- and z-direction of the force sensor equals $\pm2\,\mathrm{N}$. The mechanical system is set on a granite block in to reduce external mechanical oscillations acting on the 3D force sensor (Fig. 2.6) [20].

A scan of the specimen under test is done by moving it relative to the permanent magnet in x-direction with a constant velocity along several parallel scanning lines in y-direction. The y-position of the specimen is changed by changing the y-position of the direct drive. The PC of the control cabinet records the signal from the force sensor and positional data from the drives with a sampling rate of $f_\mathrm{s} = 1000\,\mathrm{s}^{-1}$. The measurement setup is controlled by a panel PC in the control cabinet.
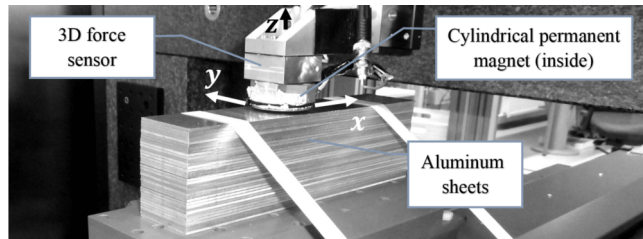

Figure 2.6: Measurement setup of Lorentz force evaluation.

2.1.4 Forward Solutions

2.1.4.1 Permanent Magnet Modeling

Spherical permanent magnet   The spherical permanent magnet acts as a simple reference magnet shape for simulation setups. It is used to generate reference setups for the testing of new forward solutions or inverse methods.

A spherical permanent magnet can be modeled by a single magnetic dipole located in the center of the sphere. The magnetic flux density $\vec{B}_k$ at a point $\vec{r}_k = [x_k\ y_k\ z_k]^{\mathrm{T}}$ with the magnetic dipole located at $\vec{r}_0 = [x_0\ y_0\ z_0]^{\mathrm{T}}$ is defined as

$$\vec{B}_k = \frac{\mu_0}{4\pi}\left(3\frac{\vec{m}\cdot(\vec{r}_k - \vec{r}_0)}{|\vec{r}_k - \vec{r}_0|^5}\,(\vec{r}_k - \vec{r}_0) - \frac{\vec{m}}{|\vec{r}_k - \vec{r}_0|^3}\right), \tag{2.18}$$

where $\vec{m} = V_{\mathrm{m}}\vec{M}$ denotes the equivalent magnetic dipole moment of the spherical permanent magnet with the magnetization $\vec{M}$ and the volume V_{m}. The spherical permanent magnet is homogeneously magnetized in z-direction. Thus, the magnetization can be written as $\vec{M} = {}^{B_{\mathrm{r}}}/_{\mu_0}\,\vec{e}_z$, where B_{r} describes the remanence.

Cylindrical permanent magnet   The measurement setup uses a cylindrical permanent magnet as a spherical permanent magnet can not be mounted easily such that the magnetization is aligned to the z-direction of the setup.

A cylindrical permanent magnet could be modeled e.g. by the analytic current model that represents the permanent magnet by an infinite thin cylindrical solenoid (Fig. 2.7 a). The axially magnetized cylindrical permanent magnet is replaced by an equivalent surface current flowing in azimuthal direction on the lateral cylinder surface. The magnetic flux density is calculated using the Biot-Savart law [35].

Another possible method is a semi-analytical one [35, 42], where the magnet is represented by a set of elementary circular current loops (Fig. 2.7 b). The magnetic flux density is determined as a linear superposition of the magnetic flux densities of the single current loops [35, 42].

Alternatively, the magnetic field of a cylindrical permanent magnet can be calculated with the help of artificial magnetic surface charges also referred to as monopoles. Positive and negative magnetic charges are placed at the upper and lower surface of the cylindrical permanent magnet (Fig. 2.7 c). The magnetic flux density is calculated as a superposition of the magnetic fields produced by the charges using Dirac's equations for magnetic monopoles [43].

However, these described methods are not capable for direct integration into the forward solutions used in LFE. For that reason, the multiple dipoles method (MDM) [16] is used to model the cylindrical permanent magnet. The general idea is to represent a

(a) Surface Current Model   (b) Semi-Analytic Model   (c) Surface Magnetic Charge Model
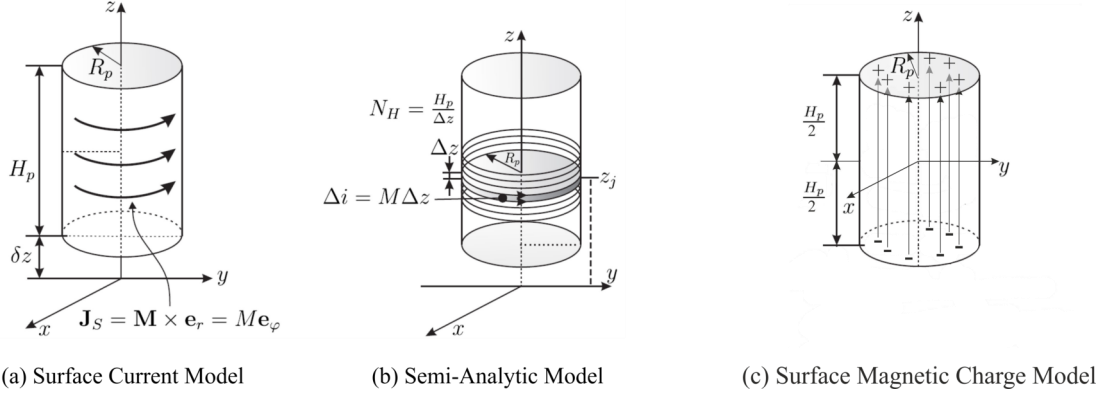
Figure 2.7: Models of a cylindrical permanent magnet [15,43]. Figure adapted from [15].

permanent magnet of arbitrary shape by a superposition of magnetic dipoles that are optimized in number and position.

For that purpose, the cylindrical permanent magnet is divided into layers (Fig. 2.8). Each slice is divided into rings and each ring is divided into voxels. The central voxels are of cylindrical shape (Fig. 2.8, left). The surrounding ring voxels are hollow cylinder segments (Fig. 2.8, right). Each voxel contains a magnetic dipole.

The number of layers N_{h}, the number of rings N_{r} and the corresponding number of magnetic dipoles N_{d} are optimized by testing different N_{h}-N_{r}-combinations. For each combination, the z-position, represented by parameter α, and the radial position, represented by parameter β, of the magnetic dipole within a voxel are optimized globally for all voxels using the simplex search method [44]. For the central voxels, the position of the magnetic dipole is fixed to the central line in z-direction, and only α is varied. The optimization procedure uses the normalized root mean square error (NRMSE) between
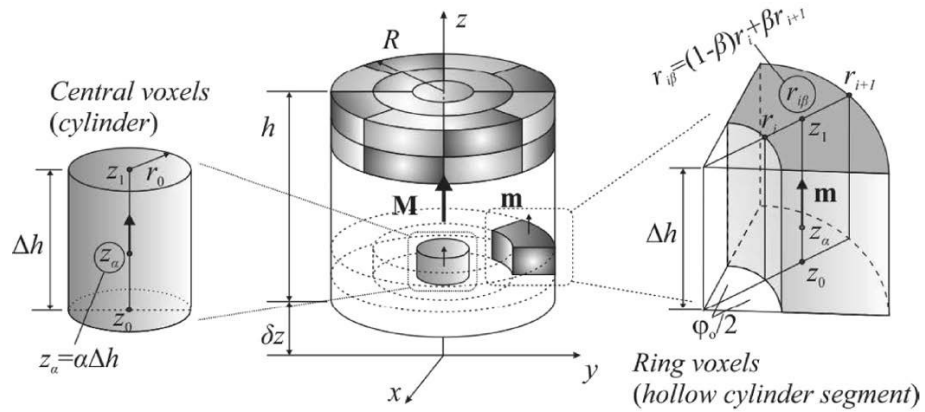
Figure 2.8: Principle of magnetic dipoles model of a cylindrical permanent magnet: The cylinder is divided into central and ring voxels, a magnetic dipole is placed within each voxel [16].

the magnetic flux density calculated by the MDM and magnetic flux density calculated by the reference analytical surface current model. The parameter configurations that offer the minimal NRMSE are used for the modeling of the cylindrical permanent magnet [16].

The measurement setup uses a cylindrical permanent magnet with diameter of $D_{\mathrm{m}} = 22.5\,\mathrm{mm}$ and height of $H_{\mathrm{m}} = 17.6\,\mathrm{mm}$ with the homogeneous magnetization $\vec{M} = {}^{B_{\mathrm{r}}}\!/_{\mu_0}\,\vec{e}_z$ ($B_{\mathrm{r}} = 1.43\,\mathrm{T}$), where B_{r} denotes the remanence. The optimization procedure leads to a discretization of the magnet in $N_{\mathrm{h}} = 23$ layers with $N_{\mathrm{r}} = 7$ rings. The parameters α and β are determined as $\alpha = 0.5075$ and $\beta = 0.5003$ describing the z-position and the radial position of each single magnetic dipole within the $N_{\mathrm{d}} = 3335$ voxels. The magnetic flux density at the center $\vec{r}_k$ outside of the permanent magnet is calculated as a superposition of the magnetic flux densities of the N_{d} single magnetic dipoles by

$$\vec{B}_k = \frac{\mu_0}{4\pi} \sum_{p=1}^{N_{\mathrm{d}}} \left(\frac{3\,[\vec{m}_p \cdot (\vec{r}_k - \vec{r}_p)]}{|\vec{r}_k - \vec{r}_p|^5}\,(\vec{r}_k - \vec{r}_p) - \frac{\vec{m}_p}{|\vec{r}_k - \vec{r}_p|^3} \right). \qquad (2.19)$$

The magnetic moment $\vec{m}_p$ of a single magnetic dipole is calculated as $\vec{m}_p = {}^{V_{\mathrm{m}}}\!/_{N_{\mathrm{d}}}\,\vec{M}$, where V_{m} denotes the volume of the permanent magnet. This calculation is validated by the fact that all voxels of the permanent magnet are of equal volume. One single magnetic dipole is located at $\vec{r}_p = [x_p\ y_p\ z_p]^{\mathrm{T}}$.

2.1.4.2 Approximate Forward Solution

The approximate forward solution (AFS) [10] is a linear method for modeling the DRS. It is based on the weak reaction approach (section 2.1.2.2) and assumes a single defect located far away from the specimen edges. The shape of the defect is assumed to be uniform, e.g. of cylindrical or cuboidal shape with low extension in z-direction, where the cuboid has equal edge lengths in x- and y-direction. The defect is characterized by a conductivity of $\sigma_{\mathrm{d}} = 0$. Thus, the DRS of (2.2) for one permanent magnet position $\vec{r}_0$ changes to

$$\Delta \vec{F} = \int_{V - V_{\mathrm{d}}} -\vec{j} \times \vec{B}\ dV - \int_{V} -\vec{j}_0 \times \vec{B}\ dV \qquad (2.20)$$

as no eddy currents flow through the defect volume V_{d}. This can be reformulated to

$$\Delta \vec{F} = \int_{V - V_{\mathrm{d}}} -\vec{j} \times \vec{B}\ dV - \left(\int_{V - V_{\mathrm{d}}} -\vec{j}_0 \times \vec{B}\ dV + \int_{V_{\mathrm{d}}} -\vec{j}_0 \times \vec{B}\ dV \right) \qquad (2.21)$$

$$= -\int_{V - V_{\mathrm{d}}} \left(\vec{j} - \vec{j}_0 \right) \times \vec{B}\ dV - \int_{V_{\mathrm{d}}} -\vec{j}_0 \times \vec{B}\ dV. \qquad (2.22)$$

The AFS neglects the first term of (2.22). As a result, only the defect volume V_{d} contributes to the DRS $\Delta \vec{F}^{\mathrm{AFS}}$. If a region of interest at which the defect is expected

is discretized into K voxels of volume V_{E}, each voxel gets a defect identification value θ_k. If the voxel belongs to the defect and contributes to $\Delta \vec{F}^{\mathrm{AFS}}$, then $\theta_k = 1$; otherwise $\theta_k = 0$. As a result, $\Delta \vec{F}^{\mathrm{AFS}}$ for one observation point $\vec{r}_0$ is defined as

$$\Delta \vec{F}^{\mathrm{AFS}} = \begin{bmatrix} \Delta F_x^{\mathrm{AFS}} \\ \Delta F_y^{\mathrm{AFS}} \\ \Delta F_z^{\mathrm{AFS}} \end{bmatrix} = V_{\mathrm{E}} \sum_{k=1}^{K} \theta_k \left(\vec{j}_{0,k} \times \vec{B}_k \right). \tag{2.23}$$

The eddy current density $\vec{j}_{0,k}$ is calculated from Ohm's law for moving conductors according to (2.5) as

$$\vec{j}_{0,k} = \sigma_0 \left(-\nabla \varphi_k + \vec{v} \times \vec{B}_k \right), \tag{2.24}$$

where φ_k and $\vec{B}_k$ describe the electric scalar potential and the magnetic flux density at the center of the k-th voxel, respectively. The magnetic flux density $\vec{B}_k$ is calculated using a single magnetic dipole (2.18) or the MDM (2.19) depending on the used permanent magnet.

The eddy currents of the defect-free specimen flow perpendicular to the magnetic flux, e.g. circulate in x-y-planes. Thus, the eddy current density component $j_{0,k,z}$ is negligible for points far away from the specimen edges. Further, the laminated structure of the specimen (section 2.1.3) with insulating layers between the aluminum sheets leads to the same assumption that $j_{0,k,z}$ is negligible, i.e. $j_{0,k,z} = 0$. In consequence, the partial differential equation $\partial \varphi_k / \partial z = v B_{k,y}$ is derived from (2.24) and can be solved by direct integration [10].

If a single magnetic dipole is used to model a spherical permanent magnet (2.18), the electric scalar potential φ_k within the center $\vec{r}_k = [x_k \ y_k \ z_k]^{\mathrm{T}}$ of the k-th voxel for one permanent magnet position $\vec{r}_0 = [x_0 \ y_0 \ z_0]^{\mathrm{T}}$ is then derived as according to [10]

$$\varphi_k = -vm \frac{\mu_0}{4\pi} \frac{y_k - y_0}{\left[(x_k - x_0)^2 + (y_k - y_0)^2 + (z_k - z_0)^2 \right]^{3/2}}, \tag{2.25}$$

where v denotes the magnitude of the velocity. The magnetic moment amplitude m of the permanent magnet is defined as $m = V_{\mathrm{m}} M$, where V_{m} describes the volume of the permanent magnet and $M = {}^{B_{\mathrm{r}}}/\mu_0$ the amplitude of the magnetization.

If the permanent magnet, e.g. of cylindrical shape, is modeled by the superposition of N_{d} magnetic dipoles according to the MDM (section 2.1.4.1), the calculation of φ_k for one permanent magnet position changes to

$$\varphi_k = -vm \frac{\mu_0}{4\pi N_{\mathrm{d}}} \sum_{p=1}^{N_{\mathrm{d}}} \left(\frac{y_k - y_p}{\left[(x_k - x_p)^2 + (y_k - y_p)^2 + (z_k - z_p)^2 \right]^{3/2}} \right), \tag{2.26}$$

where $\vec{r}_p = [x_p \ y_p \ z_p]^{\mathrm{T}}$ describes the position of the p-th magnetic dipole.

In order to consider the multiple observation points in LFE, a vector-matrix-form is build from (2.23). The subscript '0' of $\vec{j}_{0,k}$ will be omitted in the following paragraphs. The superscript 'AFS' is left out for better readability. The vector-matrix-form of AFS is defined as

$$
\underbrace{\begin{bmatrix} \Delta F_x^1 \\ \Delta F_y^1 \\ \Delta F_z^1 \\ \vdots \\ \Delta F_x^n \\ \Delta F_y^n \\ \Delta F_z^n \\ \vdots \\ \Delta F_x^N \\ \Delta F_y^N \\ \Delta F_z^N \end{bmatrix}}_{\Delta \vec{F}^{\mathrm{AFS}}} = V_{\mathrm{E}} \underbrace{\begin{bmatrix} j_{1,y}^1 B_{1,z}^1 & \cdots & j_{K,y}^1 B_{K,z}^1 \\ -j_{1,x}^1 B_{1,z}^1 & \cdots & -j_{K,x}^1 B_{K,z}^1 \\ j_{1,x}^1 B_{1,y}^1 - j_{1,y}^1 B_{1,x}^1 & \cdots & j_{K,x}^1 B_{K,y}^1 - j_{K,y}^1 B_{K,x}^1 \\ \vdots & \vdots & \vdots \\ j_{1,y}^n B_{1,z}^n & \cdots & j_{K,y}^n B_{K,z}^n \\ -j_{1,x}^n B_{1,z}^n & \cdots & -j_{K,x}^n B_{K,z}^n \\ j_{1,x}^n B_{1,y}^n - j_{1,y}^n B_{1,x}^n & \cdots & j_{K,x}^n B_{K,y}^n - j_{K,y}^n B_{K,x}^n \\ \vdots & \vdots & \vdots \\ j_{1,y}^N B_{1,z}^N & \cdots & j_{K,y}^N B_{K,z}^N \\ -j_{1,x}^N B_{1,z}^N & \cdots & -j_{K,x}^M B_{K,z}^N \\ j_{1,x}^N B_{1,y}^N - j_{1,y}^N B_{1,x}^N & \cdots & j_{K,x}^N B_{K,y}^N - j_{K,y}^N B_{K,x}^N \end{bmatrix}}_{[L]} \underbrace{\begin{bmatrix} \theta_1 \\ \vdots \\ \theta_k \\ \vdots \\ \theta_K \end{bmatrix}}_{\vec{\theta}} . \qquad (2.27)
$$

The superscript n denotes the n-th out of N observation points. The subscripts characterize the Cartesian direction and the index of the related voxel, respectively. The resulting $\Delta \vec{F}^{\mathrm{AFS}}$ is a vector that covers the x-, y- and z-DRS components at the observation points. It is calculated as a product of the lead field matrix $[L]$ and the defect identification vector $\vec{\theta}$.

2.1.4.3 Extended Area Approach

The extended area approach (EAA) [18] is an extension of the AFS. It assumes a single defect far away from the specimen edges. In order to model the DRS more accurately, the first term of (2.22) is taken into consideration. For that purpose, an extended area around the defect is discretized into E voxels of volume V_{E}.

Anisotropic conductor   In case of an anisotropic conducting specimen, the eddy currents in z-direction are neglected. The extension is performed in x- and y-direction only (Fig. 2.9).
The DRS in EAA is approximated by

$$
\Delta \vec{F}^{\mathrm{EAA}} = \begin{bmatrix} \Delta F_x^{\mathrm{EAA}} \\ \Delta F_y^{\mathrm{EAA}} \\ \Delta F_z^{\mathrm{EAA}} \end{bmatrix} = -V_{\mathrm{E}} \sum_{e=1}^{E} \left(\vec{j}_e \times \vec{B}_e \right) + \Delta \vec{F}^{\mathrm{AFS}}, \qquad (2.28)
$$

where $\vec{B}_e$ denotes the magnetic flux density at the center of the e-th voxel of the extended
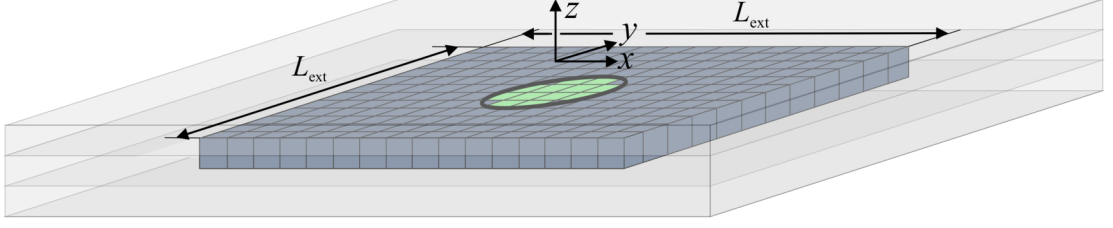
defect voxel   voxel of extended area

Figure 2.9: Principle of extended area approach for an anisotropic conducting specimen, represented by three metal layers: The defect (black circle), discretized by the green voxels and an extended area, discretized by the gray voxels, are considered for the calculation of the DRS.

area. It is calculated using a single magnetic dipole (2.18) or the MDM (2.19), depending on the used permanent magnet. The distortion eddy current density $\vec{j}_e \approx \vec{j} - \vec{j}_0$ (see (2.22)) [18] at the the center of the e-th voxel of the extended area is determined by

$$\vec{j}_e \cong C_\mathrm{d} \frac{V_\mathrm{E}}{2\pi\Delta z} \sum_{k=1}^{K} \left[2\frac{-\vec{j}_{0,k}\cdot(\vec{r}_e - \vec{r}_k)}{|\vec{r}_e - \vec{r}_k|^4}(\vec{r}_e - \vec{r}_k) - \frac{-\vec{j}_{0,k}}{|\vec{r}_e - \vec{r}_k|^2} \right], \qquad (2.29)$$

where Δz denotes the height of the e-th voxel within the extended area. The distortion eddy current density $\vec{j}_e$ is calculated from the eddy current density values $\vec{j}_{0,k}$ of the K voxels of the defect according to (2.24). The position vectors of the voxels' centroids in the defect and the extended region are denoted by $\vec{r}_k = [x_k\ y_k\ z_k]^\mathrm{T}$ and $\vec{r}_e = [x_e\ y_e\ z_e]^\mathrm{T}$, respectively. The dipolar correction factor C_d is defined as

$$C_\mathrm{d} = \begin{cases} 1 + \dfrac{c_x}{c_y} & \text{for elliptical shaped defects} \\ 1 + \dfrac{\pi}{4}\dfrac{c_x}{c_y} & \text{for rectangular shaped defects} \end{cases} \qquad (2.30)$$

where the shape is described by the cross-section of the defect in the x-y-plane. The parameters c_x and c_y describe the axes lengths of the ellipse in x- and y-direction and the length and width in x- and y-direction of the rectangular shaped defect, respectively. The defect is assumed to have the height of the metal layer.

The selection of an appropriate extension is an important aspect of the EAA. In order to find a sufficient size of the extended region for the particular analyzed setup, the DRS components are calculated by FEM simulations (section 2.1.2.2) for a reference case that contains a defect with elliptical or rectangular shape at a reasonable depth. The DRS components are calculated by EAA for increasing extension factors ε and the

NRMSE between the DRS by FEM and by EAA is calculated by

$$\text{NRMSE} = \frac{1}{3} \sum_{i=x,y,z} \frac{\sqrt{\frac{1}{N} \sum_{n=1}^{N} \left(\Delta F_{n,i}^{\text{EAA}} - \Delta F_{n,i}^{\text{FEM}} \right)^2}}{\min\left[R^{\text{EAA}}, R^{\text{FEM}} \right]}$$

$$\text{with } R^{\text{EAA}} = \max\left(\Delta \vec{F}_i^{\text{EAA}} \right) - \min\left(\Delta \vec{F}_i^{\text{EAA}} \right)$$
$$\text{and } R^{\text{FEM}} = \max\left(\Delta \vec{F}_i^{\text{FEM}} \right) - \min\left(\Delta \vec{F}_i^{\text{FEM}} \right), \tag{2.31}$$

where n indicates the current position of the permanent magnet. An extension factor of $\varepsilon = 0$ means that no extension is applied and the DRS is calculated by AFS only. If $\varepsilon \geq 1$ the area used for the calculation equals [18]

$$A_{\text{ext}} = L_{\text{ext}} \times L_{\text{ext}} = \left((1 + \varepsilon) \cdot \max\left(c_x, c_y \right) \right)^2. \tag{2.32}$$

That means, if for example a cuboidal defect with $c_x = 12\,\text{mm}$ and $c_y = 2\,\text{mm}$ with the height of the metal plate and and extension factor of $\varepsilon = 2$ is considered, an area of $A_{\text{ext}} = 36\,\text{mm} \times 36\,\text{mm}$ is taken into account for EAA.

The extension factor ε should be chosen such that the NRMSE does not decrease further. Additionally, it should be taken into account that the numbers of voxels E within the extended area increase according to

$$E = \left(\max\left(c_x, c_y \right)^2 \right) \varepsilon^2 + 2 \cdot \max\left(c_x, c_y \right)^2 \varepsilon + \max\left(c_x, c_y \right)^2 - K, \tag{2.33}$$

where K denotes the number of voxels within the defect. The number of voxels E in the extended area depends quadratic on the defect extension and the extension factor ε. The computational time increases according to the number of voxels E without considering methods of parallel computing. This is the reason why the smallest possible extension factor ε should be chosen in order to avoid a huge increase in computational time while only gathering a small further decrease of the NRMSE.

Isotropic conductor   For an isotropic conducting specimen, the extension is applied in x-, y- and z-direction as the distortion eddy currents $\vec{j}_{\text{e}}$ flow not only in x-y-planes but around the entire defect [18]. The DRS components are calculated according to (2.28). The calculation of the part $\Delta \vec{F}^{\text{AFS}}$ remains the same as the eddy current density values in the defect voxels $\vec{j}_{0,k}$ are similar for anisotropic and isotropic conducting specimens as $j_{0,k,z} = 0$ holds for both [18].

The calculation of $\vec{j}_e$ changes according to [18] as

$$
\begin{aligned}
\vec{j}_e \cong C_{\mathrm{d}}\frac{V_{\mathrm{E}}}{4\pi}\Bigg(&\sum_{k=1}^{K}\left[3\frac{-\vec{j}_{0,k}\cdot(\vec{r}_e-\vec{r}_k)}{|\vec{r}_e-\vec{r}_k|^5}(\vec{r}_e-\vec{r}_k)-\frac{-\vec{j}_{0,k}}{|\vec{r}_e-\vec{r}_k|^3}\right]\\
&+\sum_{k=1}^{K}\left[3\frac{-\vec{j}_{\mathrm{M},k}\cdot(\vec{r}_e-\vec{r}_{\mathrm{M},k})}{|\vec{r}_e-\vec{r}_{\mathrm{M},k}|^5}(\vec{r}_e-\vec{r}_{\mathrm{M},k})-\frac{-\vec{j}_{\mathrm{M},k}}{|\vec{r}_e-\vec{r}_{\mathrm{M},k}|^3}\right]\Bigg).
\end{aligned}
\tag{2.34}
$$

The first sum of (2.34) is calculated from the K eddy current densities $\vec{j}_{0,k}$ within the defect voxels. The centroids of the defect voxels are denoted by $\vec{r}_k$. In order to fulfill the boundary condition $\vec{j}_e\cdot\vec{n}=0$ at the top surface of the specimen, the eddy current densities $\vec{j}_{0,k}$ are mirrored against the plane $z=0\,\mathrm{mm}$ [18]. The "mirrored" eddy current densities are taken into account as $\vec{j}_{\mathrm{M},k}$ in the second sum of (2.34), with $\vec{j}_{\mathrm{M},k}=\vec{j}_{0,k}$. The influences of the other specimen boundaries, which are more far away from the defect, are neglected.

The dipolar correction factor C_{d} for the isotropic conductor is defined as [18]

$$
C_{\mathrm{d}}=1+\frac{1}{4}\left(\frac{c_x}{c_y}+\frac{c_z}{c_y}\right).
\tag{2.35}
$$

The choice of the extension factor ε is done in the same way as described for the anisotropic conductor. The size of the extended volume equals

$$
V_{\mathrm{ext}}=L_{\mathrm{ext}}\times L_{\mathrm{ext}}\times L_{\mathrm{ext}}=\left((1+\varepsilon)\cdot\max\left(c_x,c_y,c_z\right)\right)^3,
\tag{2.36}
$$

where now also the extension c_z of the defect in z-direction is taken into account. Also the number E of voxels in the extended area changes to

$$
\begin{aligned}
E=\left(\max\left(c_x,c_y,c_z\right)\right)^3\varepsilon^3&+3\cdot\left(\max\left(c_x,c_y,c_z\right)\right)^3\varepsilon^2\\
&+3\cdot\left(\max\left(c_x,c_y,c_z\right)\right)^3\varepsilon+\cdot\left(\max\left(c_x,c_y,c_z\right)\right)^3-K.
\end{aligned}
\tag{2.37}
$$

2.2 Eddy Current Evaluation

2.2.1 Principle

The ECE in this study uses a planar coil that is excited with a sinusoidal current. The corresponding primary time-dependent magnetic field $\vec{B}_{\mathrm{p}}(t)$ induces eddy currents $\vec{j}$ in the conducting specimen under test (Fig. 2.10) according to Faraday's law. The induced eddy currents generate a secondary magnetic field $\vec{b}_{\mathrm{s}}(t)$ as stated by Ampere's law. In the presence of a defect, the eddy currents and the corresponding secondary magnetic field are perturbed. The magnetic field variations can be measured by magnetic sensors [45] such as pick-up coils, fluxgate sensors [46], superconducting quantum interference
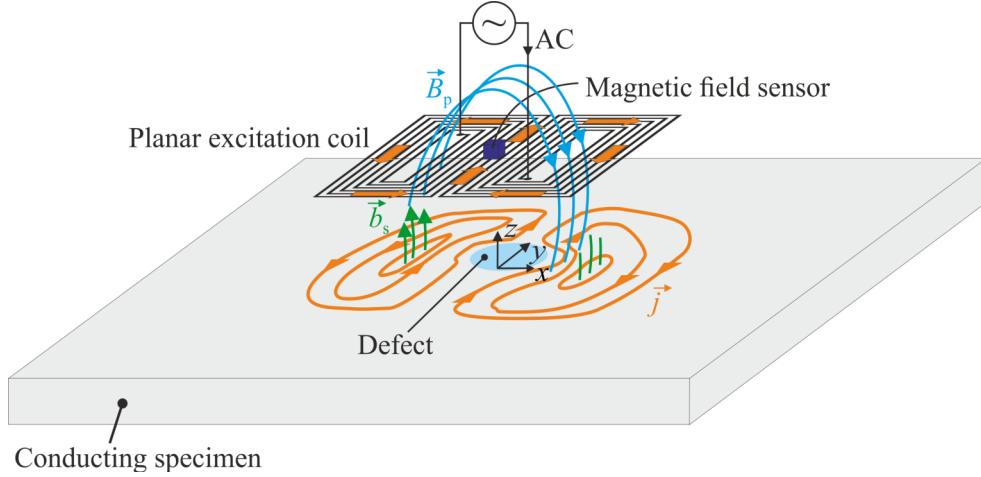
Figure 2.10: Principle of eddy current evaluation: An excitation coil is excited with an alternating current (AC) that generates a time-dependent magnetic field $\vec{B}_{\mathrm{p}}(t)$. This leads to induced eddy currents $\vec{j}$ in the conducting specimen under test that create a secondary magnetic field $\vec{b}_{\mathrm{s}}(t)$. In presence of a defect the eddy currents and the corresponding secondary magnetic field are perturbed. The magnetic field variations are measured by a magnetic field sensor.

devices (SQUIDs) [47], Hall sensors and magnetoresistive sensors [48, 49].

If the specimen is scanned by the probe (planar excitation coil + magnetic field sensor), the excitation field remains invariant in the scanning region. This is the case if the scanned region is smaller than the central region of the coil. If no defect is present, the induced currents flow in lines parallel to the excitation current in a region below the center of the coil.

The magnetic field sensor measures the flux density in x-direction. The time dependent magnetic flux density component $B_x(t)$ at the magnetic field sensor consists of

$$B_x(t) = B_{\mathrm{p},x}(t) + b_{\mathrm{s},x}(t), \tag{2.38}$$

Similarly to LFE, only the magnetic field perturbation (MFP) $\Delta b_x(t)$ is of interest for the reconstruction of the defect properties. It is defined as

$$\Delta b_x(t) = B_x(t) - B_{x,0}(t) = (B_{\mathrm{p},x}(t) + b_{\mathrm{s},x}(t)) - (B_{\mathrm{p},x}(t) + b_{\mathrm{s},x,0}(t))$$
$$= b_{\mathrm{s},x}(t) - b_{\mathrm{s},x,0}(t), \tag{2.39}$$

where $B_x(t)$ and $B_{x,0}(t)$ denote the total magnetic flux density component in x-direction for a specimen with and without a defect, respectively. As the primary magnetic flux density is similar for the defect and the defect free case, the MFP only depends on the secondary magnetic flux density components $b_{\mathrm{s},x}(t)$ and $b_{\mathrm{s},x,0}(t)$. Due to the sinusoidal
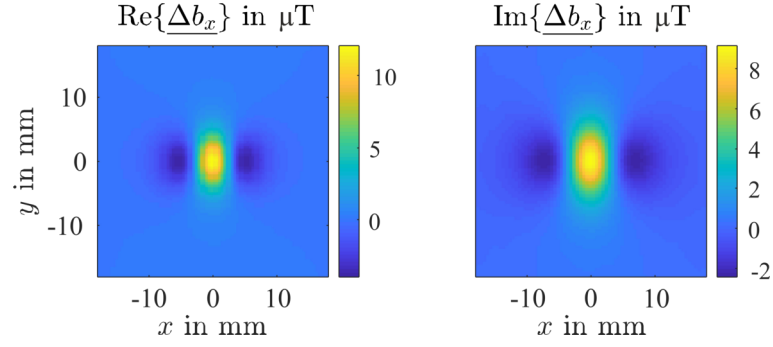
Figure 2.11: Real (left) and imaginary (right) part of MFP $\underline{\Delta b_x}$ obtained by FEM simulations in the vicinity of a cylindrical shaped defect.

excitation current, the MFP can be described by complex numbers as

$$\underline{\Delta b_x}(\mathrm{i}\omega t) = \left|\underline{\Delta b_x}(\mathrm{i}\omega t)\right| e^{\mathrm{i}(\omega t - \Phi)} = \mathrm{Re}\left\{\underline{\Delta b_x}(\mathrm{i}\omega t)\right\} + \mathrm{iIm}\left\{\underline{\Delta b_x}(\mathrm{i}\omega t)\right\} \qquad (2.40)$$

where i denotes the imaginary unit. The angular frequency $\omega = 2\pi f_e$ contains the excitation frequency f_e. The variable Φ denotes the phase shift of the MFP. Fig. 2.11 shows an example of a MFP with $\mathrm{Re}\left\{\underline{\Delta b_x}\right\}$ and $\mathrm{Im}\left\{\underline{\Delta b_x}\right\}$ for different probe positions. In order to determine the defect properties from the MFP an inverse problem has to be solved.

The difficulty that occurs is that defects located parallel to the induced eddy currents do not generate a disturbed eddy current flow (Fig. 2.12 a). The disturbance is maximal if the defect is perpendicular to the induced eddy currents (Fig. 2.12 b). This is the reason why the MFP has to be obtained for at least two perpendicular uniform excitation directions as the defect orientation is not known in advance. According to [50,51], the inverse problem is solved separately for each MFP of the varying excitation directions. The obtained current density norm maps are combined afterwards.
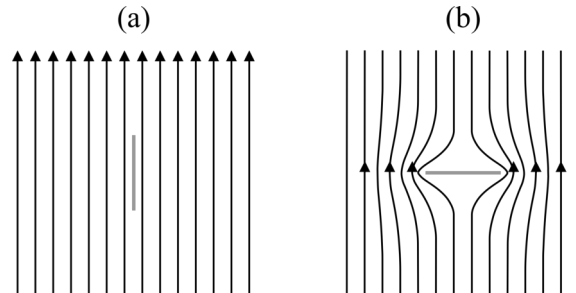

Figure 2.12: Representation of the eddy current flow with: (a) a defect (gray) parallel to the current flow and (b) perpendicular to the current flow.

2.2.2 Numerical Simulations

Numerical simulations in ECE provide noise-free benchmark signals to investigate the properties of inverse methods before the application to measurement data. In order to calculate the MFP, the governing equations represented in complex numbers are

$$i\omega\sigma\underline{\vec{A}} + \nabla \times \left(\frac{1}{\mu_0}\nabla \times \underline{\vec{A}}\right) = \underline{\vec{J_e}} \text{ with } \nabla \cdot \underline{\vec{A}} = 0$$
$$\nabla \cdot \left(\sigma\left(-i\omega\underline{\vec{A}} + \underline{\vec{J_e}}\right)\right) = 0 \text{ with } \vec{n} \cdot \underline{\vec{j}} = 0\Big|_{\Gamma_c} \text{ and } \vec{n} \times \underline{\vec{A}} = \vec{0}\Big|_{\Gamma_a}. \qquad (2.41)$$

The external eddy current density from the excitation coil is represented by $\underline{\vec{J}}_e$. The electrical conductivity is denoted by σ. The gauge is selected such that the electric scalar potential φ vanishes and only the magnetic vector potential $\underline{\vec{A}}$ has to be considered [52]. In this study, the investigated specimens are made of the aluminum and the used excitation frequencies are maximal at $2\,\mathrm{kHz}$. Thus, the displacement current density $\partial\vec{D}/\partial t$ is neglected in (2.41). The problem described in (2.41) is solved by FEM implemented in COMSOL Multiphysics® Version 4.3b. For that purpose, the conducting specimen with the defect, the excitation coil and a surrounding air box are discretized by hexahedral elements. The boundary conditions have to be fulfilled at the conductor and the air box surface Γ_c and Γ_a, respectively. The total magnetic flux density at the observation points is determined from the obtained magnetic vector potential $\underline{\vec{A}}$ by $\underline{\vec{B}} = \nabla \times \underline{\vec{A}}$. The complex x-component $\underline{B_x}$ is extracted.

In order to get the MFP $\underline{\Delta b_x}$, an observation point is chosen where no influence of the defect is visible (e.g. $x = y = 10\,\mathrm{mm}$, Fig. 2.11). This point contains the magnetic flux density of the specimen without a defect $\underline{B_{x,0}}$ (2.40) in complex form. Due to the uniform excitation, the calculated magnetic flux densities at the observation points just have to subtracted by the extracted $\underline{B_{x,0}}$.

2.2.3 Measurement Setup

The principle of the measurement setup [50,53] is shown in Fig. 2.13. It is controlled by a MATLAB program running on a PC connected via R232 interface to the PXI Chassis. The desired current amplitude and excitation frequency of the sinusoidal current are set at the PC and sent to the current generator controlled by a General Purpose Interface Bus (GPIB). The current generator consists of a function generator (AFG3102 from Tektronix) and transadmittance amplifiers to generate the desired current wave form. The excitation current is monitored and the voltage output is adjusted to the limits of the data aquistion (DAQ) unit by the signal conditioning unit. The scanning process is implemented at the PC and sent to an XY-Positioning system via R232. The voltage signal from the magnetic field sensor is converted back into T units at the PC. Two

different probes have been used in this thesis where both use giant magnetoresistive (GMR) sensors to measure the magnetic field.

Giant magnetoresistive sensor GMR sensors are based on the giant magnetoresistivity phenomenon. A giant magnetoresistor is made of several layers of ferromagnetic metal separated by non-magnetic metal layers. The ferromagnetic layers are magnetized in alternating direction, such that electrons cannot pass easily through. If an external magnetic field is present, all ferromagnetic parts are magnetized in the direction of the external field. In consequence, electrons can pass more easily as the resistance of the GMR is reduced. A GMR sensor (A002-02, Non-Volatile Electronics) is used in this thesis. It consists of four giant magnetoresistors that are arranged in a Wheatstone bridge with two sensing elements and two shielded resistors. The A002-02 is powered by a $\pm$ 12 V power supply. If the GMR sensor is located in the vicinity of a magnetic field, the resistance ratios of both potential dividers are not equal any more due to the giant magnetoresistivity phenomenon resulting in a voltage difference in the bridge output. A small magnet is placed close to the sensor to obtain a linear behavior of the sensor [51]. The sensor has a sensitivity of 3.6 V/mT per V of the power supply [53]. The GMR sensor is used because of the high sensitivity and large frequency range (DC - 1 MHz) [51].

Single coil planar probe Fig. 2.14 shows the scheme (a) and a photo (b) of the planar probe with a single coil [53]. The coil with 50 turns is built on a printed circuit board (PCB) with the GMR sensor A002-02. The GMR sensor is characterized by a sensitivity axis in x-direction perpendicular to the direction of the uniform excitation currents. A sinusoidal excitation current with an amplitude up to 2.4 A is applied to the coil. The planar probe keeps a constant distance to the plate reducing variations in the sensed magnetic field due to lift-off variations [53]. In order to achieve different excitation directions, the probe has to be rotated.
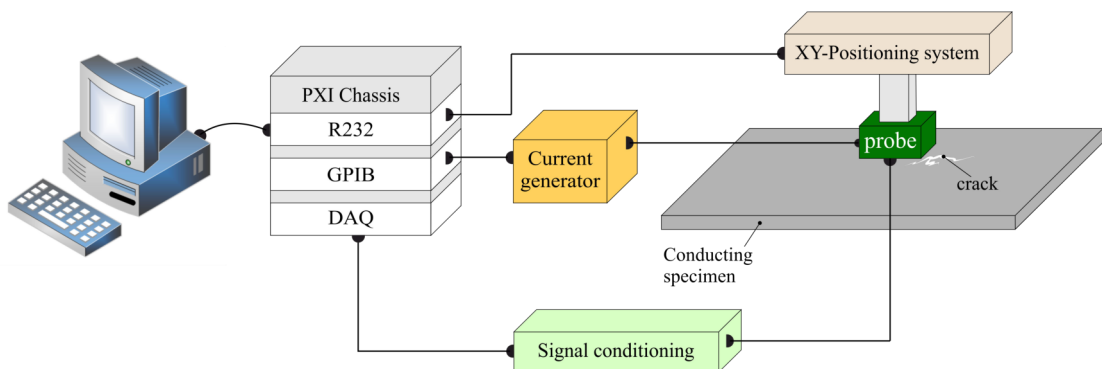

Figure 2.13: Measurement setup for eddy current evaluation.

Double coil planar probe   The second probe, introduced in [50], consists of two perpendicular arranged planar excitation coils (Fig. 2.15 a) and two GMR sensors with sensitive axes in x- and y-direction (Fig. 2.15 b). The GMR sensors are located $2\,\mathrm{mm}$ above the top surface of the specimen. At each scanning point, two synchronized sinusoidal excitation currents are applied to the two planar coils. The coils have a distance of $1\,\mathrm{mm}$. In order to compensate for this distance, a calibration procedure obtained that the top coil has to be excited with a 1.36 larger current amplitude than the bottom one [50]. The excitation modes (Fig. 2.15 c) lead to uniform excitation currents at angles of 0°, 45°, 90° and 135° without the need of rotating the probe. The currents of the top and the bottom coil are in phase for 45°-excitation and have a phase shift of 180° for 135°-excitation. The double coil planar probe is more complicated to operate than the single coil planar probe. It also enables a constant lift-off distance to the specimen under investigation.

2.2.4 Forward Solution

In order to calculate the MFP Δb_x according to (2.39), a closer look is taken on the underlying induced eddy current density distributions (Fig. 2.16). It is assumed that the eddy current component in z-direction is negligible. Further, it is assumed that the investigated specimen is thin such that the eddy currents circulate only in one x-y-plane and can be viewed as two-dimensional. Fig. 2.16 shows a representation of the eddy current flow for a specimen with a defect (Fig. 2.16, center) that generates the secondary magnetic field with the x-component $b_{\mathrm{s},x}$. The uniform eddy current flow for the same specimen without a defect (Fig. 2.16, right) generates the secondary magnetic field with the x-component $b_{\mathrm{s},x,0}$. Due to the superposition principle, the MFP Δb_x can be generated by the perturbation eddy current density $\Delta \vec{j} = \vec{j} - \vec{j}_0$.

The perturbation eddy current density distribution $\Delta \vec{j}$ can be represented by discretizing the area into a set of unitary square current loops (Fig. 2.17 a) according to [51]. Thus,

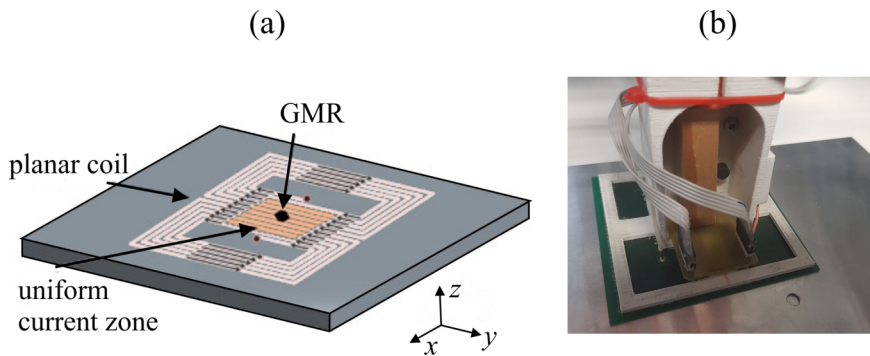(a)   (b)

Figure 2.14: Single coil planar probe with GMR sensor: (a) scheme [53] and (b) photo.
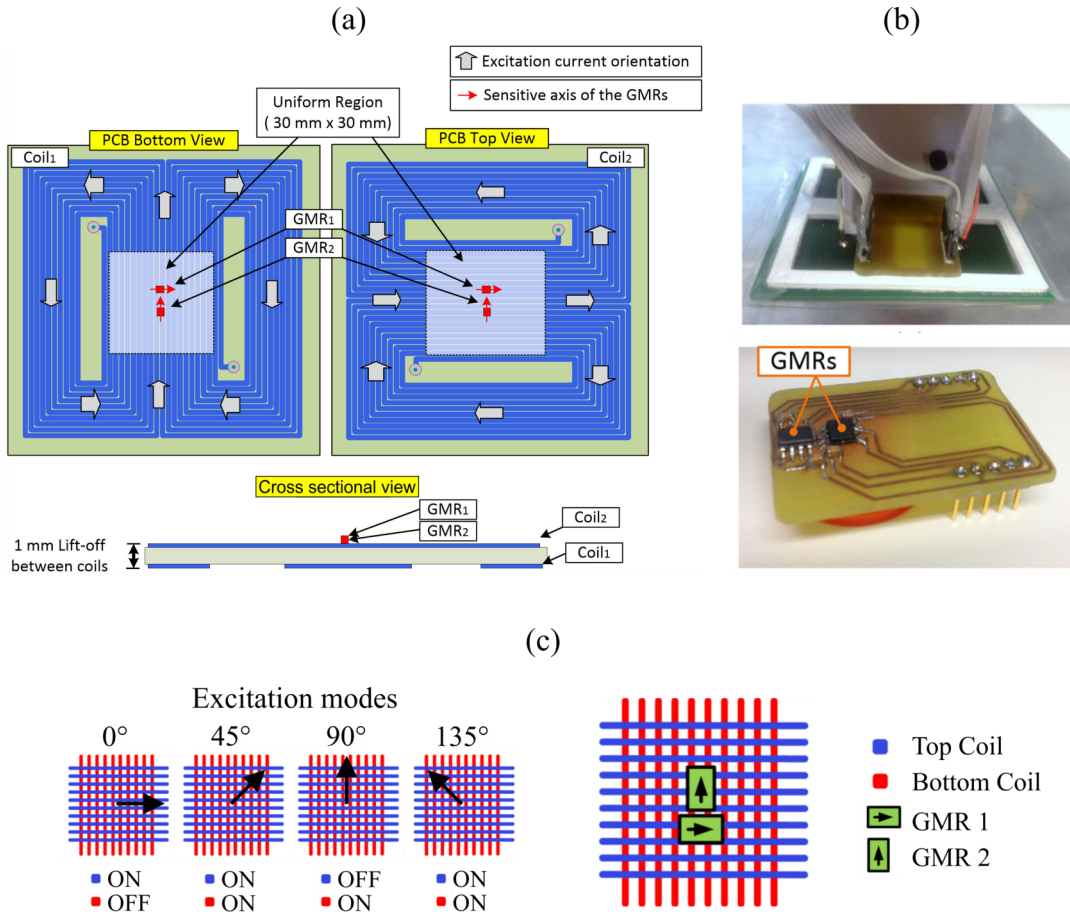
Figure 2.15: Double coil planar probe with two GMR sensors: (a) Scheme: Two coils are arranged perpendicular on a PCB, (b) photo of the probe and the GMR sensors and (c) excitation modes. Figure rearranged from [50].
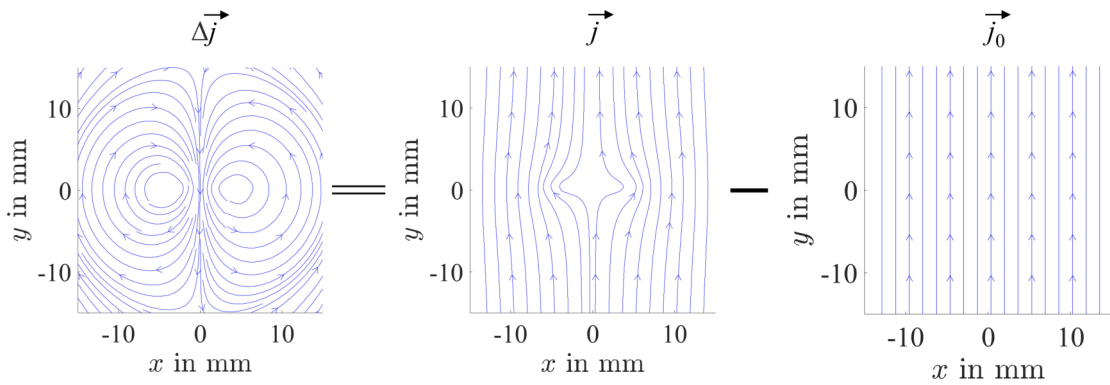

Figure 2.16: Representation of the perturbation eddy current density distribution $\Delta\vec{j}$ of a linear defect of $10\,\mathrm{mm}$ length by the difference of the eddy current density distribution $\vec{j}$ for the specimen with a defect minus the eddy current density distribution $\vec{j}_0$ for the same specimen without a defect.

the degrees of freedom of the forward and corresponding inverse problem are reduced by factor 2. Each square current loop is characterized by a current $I_\mathrm{d}(i,j)$. A square loop

(a) Discretization of the perturbation eddy current density into square current loops [51].

(b) Perturbation magnetic flux density component $\Delta \widetilde{b}_x$ in µT of one unitary square current loop located at $x = y = 0$ with $I_\mathrm{d} = 1\,\mathrm{A}$.
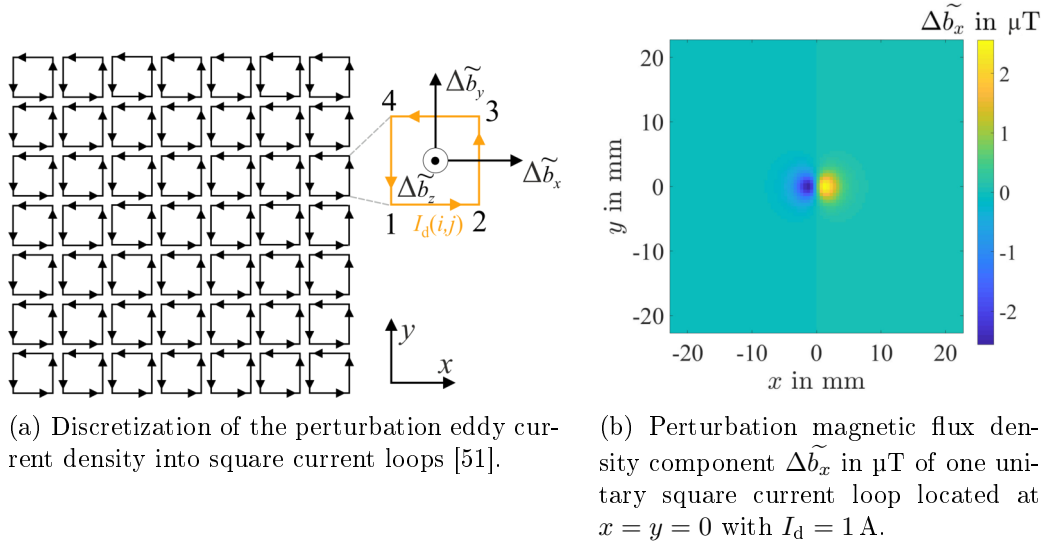
Figure 2.17: Forward solution principle of ECE.

generates a part of the MFP according to the Biot-Savart law at one observation point $\vec{r} = [x\ y\ z]^\mathrm{T}$

$$
\begin{bmatrix} \Delta \widetilde{b}_x \\ \Delta \widetilde{b}_y \\ \Delta \widetilde{b}_z \end{bmatrix} = \frac{\mu_0}{4\pi} \oint I_\mathrm{d}(i,j) d\vec{l} \times \frac{\vec{r} - \vec{r}\,'}{|\vec{r} - \vec{r}\,'|^3},
\tag{2.42}
$$

where $\vec{r}\,' = [x'\ y'\ z']^\mathrm{T}$ denotes the location of the current flow at the infinitesimal short part $d\vec{l}$. As only the x-component $\Delta \widetilde{b}_x$ is of interest in this work (2.42) reduces to (Fig. 2.17 a)

$$
\Delta \widetilde{b}_x = \frac{\mu_0}{4\pi} I_\mathrm{d}(i,j) \left[\int_2^3 \frac{dl(z - z')}{|\vec{r} - \vec{r}\,'|^3} - \int_4^1 \frac{dl(z - z')}{|\vec{r} - \vec{r}\,'|^3} \right].
\tag{2.43}
$$

Fig. 2.17 b shows an exemplary $[\Delta \widetilde{b}_x]_{N \times M}$ for $N \times M$ observation points for one unitary current loop with $I_\mathrm{d} = 1\,\mathrm{A}$ located at $x = y = 0$. The z-distance δz to the observation points is chosen exemplary as $\delta z = 2.5\,\mathrm{mm}$. This mirrors the z-distance of the GMR sensor to the center of a $1\,\mathrm{mm}$ thick conducting plate under investigation. The total MFP $[\Delta b_x]_{N \times M}^{\mathrm{BS}}$ is the superposition of all $[\Delta \widetilde{b}_x]_{N \times M}$ of the different square current loops weighted by the corresponding $I_\mathrm{d}(i,j)$ what can be formulated as a convolution or in vector-matrix-form.

Convolution formulation It is easily comprehensible that the perturbation magnetic flux density component $[\Delta \widetilde{b}_x]_{N \times M}$ from a square current loop with $I_\mathrm{d} = 1\,\mathrm{A}$ outside of the position $x = y = 0$ is similar to the one shown in Fig. 2.17 b just shifted to the center of the current loop. In consequence, the total MFP $[\Delta b_x]_{N \times M}^{\mathrm{BS}}$ viewed as a matrix

with $N \times M$ observation points can be calculated as a convolution by

$$[\Delta b_x]_{N \times M}^{\text{BS}} = [\Delta \widetilde{b_x}]_{N \times M} * [I_{\text{d}}]_{N \times M} \qquad (2.44)$$

where $[\Delta \widetilde{b_x}]_{N \times M}$ is referred to as the kernel (Fig. 2.17 b). The square current loops centers (Fig. 2.17 a) have the same x- and y-distances as the observation points of the MFP. The 2D-discrete Fourier transform (DFT) changes the convolution into a simple point-wise multiplication as:

$$[\Delta \hat{b}_x]_{N \times M}^{\text{BS}} = [\Delta \hat{\widetilde{b}}_x]_{N \times M} \circ [\hat{I}_{\text{d}}]_{N \times M}. \qquad (2.45)$$

An inverse algorithm would operate in this frequency domain and the obtained $[\hat{I}_{\text{d}}]_{N \times M}$ would be transformed back by the inverse DFT.

Vector-matrix-formulation Alternatively, the forward problem can be formulated in a vector-matrix-form in the spatial domain. The MFP that should be calculated for $N \times M$ observation points is arranged into a vector $\Delta \vec{b}_x$. The current amplitudes of the square current loops are also arranged in a vector $\vec{I}_{\text{d}}$ with $A \times B$ elements. The vector-matrix-formulation is defined as

$$\underbrace{\begin{bmatrix} \Delta b_x^1 \\ \vdots \\ \Delta b_x^n \\ \vdots \\ \Delta b_x^{N \cdot M} \end{bmatrix}}_{\Delta \vec{b}_x{}^{\text{BS}}} = \underbrace{\begin{bmatrix} \Delta \widetilde{b_x}^{1,1} & \cdots & & \Delta \widetilde{b_x}^{1,A \cdot B} \\ \vdots & \vdots & & \vdots \\ \Delta \widetilde{b_x}^{n,1} & \Delta \widetilde{b_x}^{n,k} & & \Delta \widetilde{b_x}^{n,A \cdot B} \\ \vdots & \vdots & & \vdots \\ \Delta \widetilde{b_x}^{N \cdot M,1} & \cdots & & \Delta \widetilde{b_x}^{N \cdot M,A \cdot B} \end{bmatrix}}_{[L]} \underbrace{\begin{bmatrix} I_{\text{d}}^1 \\ \vdots \\ I_{\text{d}}^k \\ \vdots \\ I_{\text{d}}^{A \cdot B} \end{bmatrix}}_{\vec{I}_{\text{d}}}, \qquad (2.46)$$

where $[L] \in \mathbb{R}^{N \cdot M \times A \cdot B}$ denotes the lead field matrix. One lead field matrix element $\Delta \widetilde{b_x}^{n,k}$ denotes the contribution of the k-th square current loop to the MFP at the n-th observation point according to (2.43). The number of elements in the perturbation current vector $\vec{I}_{\text{d}}$ do not have to be the same as in $\Delta \vec{b}_x{}^{\text{BS}}$. The vector-matrix-formulation enables further inverse methods as described in section 2.3.2. The determined $\vec{I}_{\text{d}}$ will be reshaped into a $A \times B$ matrix.

Both, the kernel and the lead field matrix are calculated for one setup assuming the defect at a z-distance $d + \delta z$ away from the magnetic field sensor, where d denotes the defect depth and δz the lift-off distance of the GMR sensor. If other possible distances/defect depths should be investigated, they have to be re-calculated. Both forward formulations are valid for the complex valued MFP $[\underline{\Delta b_x}]_{N \times M}$ with corresponding $[\underline{I_{\text{d}}}]_{N \times M}$. The kernel and the lead field matrix stay the same. The description with real numbers was chosen for better comprehensibility.

Post-processing of I_d   If a distribution of current square loops $[I_d]_{A \times B}$ has been determined by solving an inverse problem for a given MFP, some post-processing steps are necessary to investigate the defect characteristics. First, the distribution of current square loops is converted into the eddy current density components Δj_x and Δj_y. Due to the 2D characteristic of the problem, the corresponding unit is A/m. The conversion is defined according to [51] as

$$\Delta j_x(i,j) = \frac{I_d(i+1,j) - I_d(i-1,j)}{2\Delta y}$$
$$\Delta j_y(i,j) = \frac{I_d(i,j+1) - I_d(i,j-1)}{2\Delta x}. \tag{2.47}$$

The indexing is visualized in Fig. 2.18. The central value of $\Delta \vec{j}$ (e.g. $x = y = 0$ in Fig. 2.16, left) is extracted as uniform signal part. At all observation points the corresponding $\Delta \vec{j}$ is subtracted by this uniform value. That leads to a qualitative representation of the total eddy current density distribution j (like in Fig. 2.16, center) that allows the estimation of the defect shape and alternative visualizations for the investigation of defect characteristics.
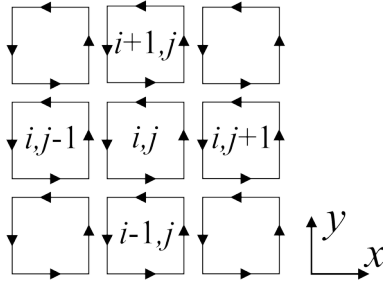

Figure 2.18: Indexing scheme for conversion of determined current square loops I_d into Δj_x and Δj_y [51] according to (2.47).

2.3 Inverse Problem

2.3.1 Characterization of Inverse Problems

In order to determine the defect properties from measurements of an electromagnetic NDE method like LFE or ECE, an inverse problem has to be solved as visualized in Fig. 2.19.

The inverse problem can be defined as a minimization problem

$$\arg\min_{\vec{x}} \left(\vec{y} - \vec{y}^{\,\text{forward}} \right) = \arg\min_{\vec{x}} \left(\vec{y} - \mathcal{G}(\vec{x}) \right). \tag{2.48}$$
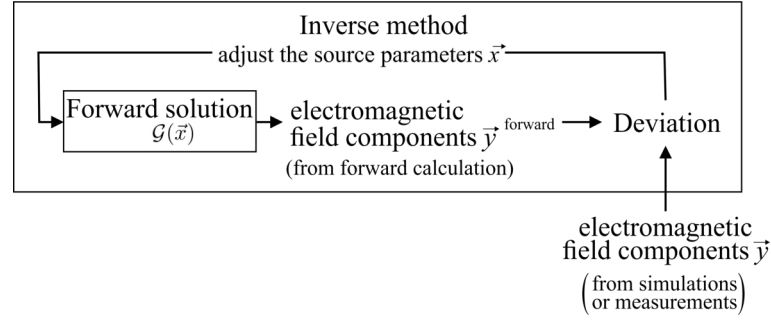
Figure 2.19: Principle of an inverse problem in electromagnetic NDE: An inverse method adjusts the source parameters such that they minimize the deviation between electromagnetic field components from simulations or measurements and the forward calculated one. The source parameters represent the defect properties directly or indirectly.

It is the aim to find a source parameter vector $\vec{x}$ such that it minimizes the deviation between the electromagnetic components $\vec{y}$ obtained from measurements or simulations and the forward calculated one $\vec{y}^{\text{forward}}$. The forward calculation is described by the operator $\mathcal{G}(\vec{x})$ that projects the source parameter vector onto the measurement data. The inverse method adjusts the source parameter vector such that $\vec{y} - \mathcal{G}(\vec{x})$ is minimized. The source parameter vector $\vec{x}$ in NDE could contain the defect properties directly like defect extensions and location. More often measures are used for the source parameter vector $\vec{x}$ that represent the defect properties indirectly. Previous work in LFE used the conductivity distribution [10, 17] or the eddy current density distribution [19]. In this thesis the defect identification vector (sections 2.1.4.2-2.1.4.3) is used as source parameter vector $\vec{x}$ in LFE. The used forward solution for ECE in this thesis also uses an indirect measure with the square current loops as parameter source vector (section 2.2.4).

Inverse problems can be classified according to the used forward solution into linear and non-linear inverse problems. The inverse problem is linear, if the operator $\mathcal{G}(\vec{x})$ can be written in a vector-matrix-form $\mathcal{G}(\vec{x}) = [L]\vec{x}$, where the lead field matrix $[L]$ itself is independent from $\vec{x}$. A non-linear inverse problem is characterized by a more complicated expression of the operator $\mathcal{G}(\vec{x})$. In LFE, the AFS leads to a linear inverse problem. The EAA cannot be written in vector-matrix-form. Thus, the corresponding inverse problem is non-linear. In Chapter 6, a novel forward solution is introduced for LFE referred to as SVA that also leads to a linear inverse problem. The forward solution used for ECE also leads to a linear inverse problem. Thus, this thesis mainly deals with linear inverse problems.

An inverse problem is usually characterized as ill-posed. According to Hadamard [54] a problem can be classified as well-posed if:

1. A solution exists.

2. The solution is unique.

3. The solution is stable.

If at least one of the criteria is violated, the problem is characterized as ill-posed. Usually, the forward problem can be classified as well-posed. Based on Hadamard's uniqueness criterion inverse problems can be further classified into underdetermined and overdetermined problems, where for both no unique solution of the problem might exists. An undetermined problem is characterized by a larger number of source parameters in $\vec{x}$ than measured electromagnetic field components in $\vec{y}$. For an overdetermined problem it is the other way round. A typical example for both situations can be found in medical engineering, where the sources in the brain are determined from electroencephalograms and magnetoencephalograms. For sources that are known to be focal, the number of sensors is larger than the sources (e.g. only one) to be determined, characterizing it as an overdetermined problem. If the sources are known to be distributed in the brain, the number of unknown source parameters in $\vec{x}$ is much larger than the number of sensors, characterizing an underdetermined problem.

The stability criterion of Hadamard states that a continuous change in the input data leads to a continuous change in the solution. Often inverse problems are sensitive to noise, where small changes in the measurement data have a large impact on the estimated source parameter vector. In that case, the inverse problem is characterized as ill-conditioned. The degree of ill-condition of linear inverse problems can be determined by calculation of a condition number of the lead field matrix. The condition number with respect to the L2-norm of the lead field matrix (CN) [55], the Skeel condition number [56] and the figure of merit ϱ [57] are calculated exemplary for a lead field matrix in LFE $[L] \in \mathbb{R}^{7803 \times 2601}$ and for a lead field matrix in ECE $[L] \in \mathbb{R}^{8100 \times 8100}$ (Table 2.2). The different condition numbers are characterized by advantages and disadvantages, where an overview can be found in [58]. However, all revealed values larger than 1, indicating the LFE and the ECE as ill-conditioned problems.

Table 2.2: Exemplary condition numbers with respect to the L2-norm, the Skeel condition number and the figure of merit ϱ for LFE and ECE.

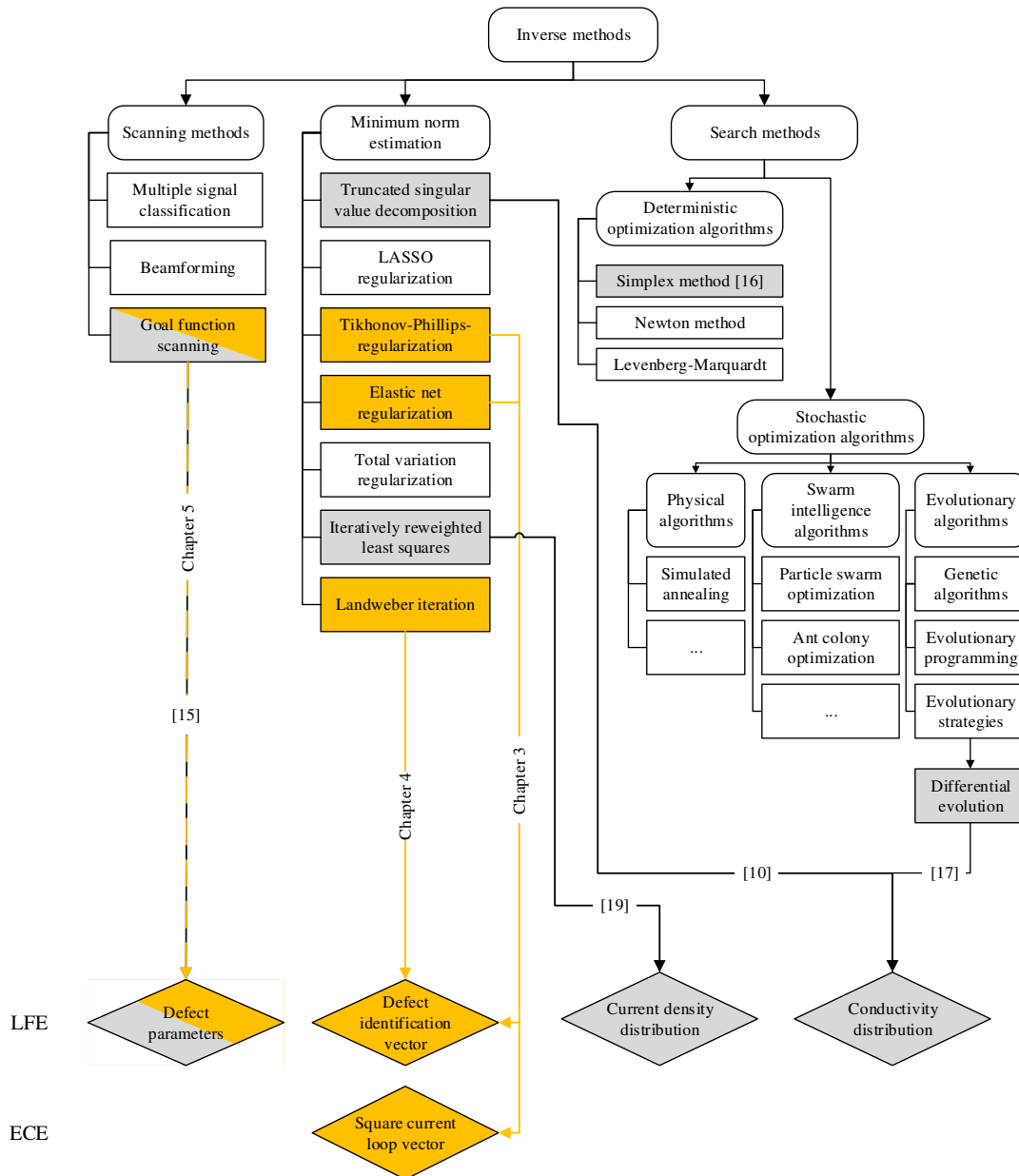| NDE method	Condition number		
	CN	Skeel	ϱ
LFE	$9.15 \cdot 10^{12}$	$2 \cdot 10^{12}$	46.25
ECE	$1.19 \cdot 10^{46}$	$8.96 \cdot 10^{12}$	152.41

Figure 2.20: Overview of selected inverse methods continued from [15]: Used source parameters are shown in rhombuses. Inverse Methods that have been applied for LFE in previous studies [10, 15–17, 19] are marked with light gray, the methods used in this thesis with orange. References to the respective chapters are given at the arrows.

2.3.2 Inverse Calculation Methods

An overview of selected inverse methods is shown in Fig. 2.20. The inverse methods used in previous studies for LFE (Fig. 2.20, gray) and in this thesis for LFE and ECE (Fig. 2.20, orange) are highlighted.

The applicable inverse methods for LFE depend on the used forward solution. If the AFS is used, the forward problem can be written in vector-matrix-form according to

(2.27). This enables the use of scanning methods, MNE and deterministic and stochastic optimization algorithms to solve the inverse problem. The EAA is an iterative forward solution that cannot be written into a vector-matrix-form. Thus, for EAA, scanning methods and stochastic optimization algorithms are applicable. Deterministic optimization algorithms, which often need to evaluate the gradient of the deviation function (2.48), are not applicable as the estimation of the gradient of the deviation function is not straight forward. For the ECE, the forward solution according to (2.46) leads to a linear inverse problem. This allows the use of scanning methods, MNE, deterministic and stochastic optimization algorithms in order to solve the inverse problem.

Scanning methods   The goal function scanning represents the simplest scanning methods. It is optimal for source vectors $\vec{x}$ with very few elements, e.g. the direct defect properties like the defect diameter or length and width. The forward problem is calculated for different source vector element combinations and the deviation to the measured signal is determined. The source vector element combination that belongs to the lowest deviation indicates the estimated source parameters. Previous work applied a length-width-depth scan for the estimation of the defect parameters of a cuboidal defect located in a conducting layer of a GLARE specimen [15]. Goal function scanning methods are beneficial for cases where already many properties of the defect are known in advance or for proof-of-concept studies to test novel forward solutions. In Chapter 5, radius-depth scans and length-width-depth scans are applied for cylindrical and cuboidal defects in aluminum specimens in order to compare the defect reconstruction performance using the two different forward solutions AFS and EAA. Other inverse methods that belong to the scanning methods are e.g. the multiple signal classification (MUSIC) method or beamforming. MUSIC is a method from information theory [59] that is based on the goal function scan, where the goal function (2.48) is divided into subspaces. In each subspace, a scan is performed with a single source, leading to the estimation of multiple sources. Beamforming origins from the field of sound wave localization [60]. The principle idea is to determine the contribution of a source region to the measured signal by spatial filtering [61] and thus, reconstructing multiple sources that contributed to the measured field.

Minimum Norm Estimation   In contrast to the scanning methods, the MNE usually solves an undetermined problem with many more unknown sources than measurement points that can be reformulated from (2.48) to

$$\arg\min_{\vec{x}} \frac{1}{2} \left\| \vec{y} - [L]\,\vec{x} \right\|_2^2 , \tag{2.49}$$

where the lead field matrix $[L] \in \mathbb{R}^{N \times M}$ contains the forward solution that projects

the source vector $\vec{x}$ to the measured data $\vec{y}$. Using the Moore-Penrose inverse a closed solution of this problem can be obtained by

$$\vec{x} = [L]^{+} \, \vec{y} \tag{2.50}$$

However, as this inverse problem is underdetermined and often ill-conditioned (section 2.3.1), a form of regularization has to be applied to obtain a sufficient solution of $\vec{x}$. One possible method is the truncated singular value decomposition (TSVD) [62]. The Moore-Penrose inverse $[L]^{+}$ can be calculated using the singular value decomposition (SVD) of $[L]$ by

$$[L]^{+} = [V] \, [\Sigma]^{+} \, [U]^{*}, \tag{2.51}$$

where $[U]$, $[\Sigma]$ and $[V]$ denote the matrices of the SVD $[L] = [U] \, [\Sigma] \, [V]^{*}$. The superscript '*' denotes the adjoint matrix. The TSVD omits small singular values of $[\Sigma]$ leading to a $[\Sigma]_{\mathrm{TSVD}}$. The source parameter vector $\vec{x}$ by TSVD is then determined by

$$\vec{x} = \left([V] \, [\Sigma]^{+}_{\mathrm{TSVD}} \, [U]^{*} \right) \vec{y}, \tag{2.52}$$

which enables a more stable estimation of the source vector $\vec{x}$. In the TSVD the crucial parameter is the truncation parameter k that decides at which point the singular values are omitted. The TSVD has been used previously in LFE for the reconstruction of the conductivity distribution [10]. The TSVD is also used in other fields of NDE, e.g. in dual-energy computed tomography for ceramics and composite materials [63]. The TSVD is also widely applied in other fields of inverse problems [64], e.g. for the detection of buried ferromagnetic objects based on geomagnetic measurements [65], for source reconstruction in the human brain from magnetoencephalographic measurements [66] or for microwave inverse scattering for breast imaging [67].

Another method to solve the MNE problem depicted in (2.49), is the Landweber iteration. It iteratively solves (2.49) using the gradient descent for updating the solution vector $\vec{x}$. Crucial parameters of the Landweber iteration are the step size or the number of iterations. The Landweber iteration is e.g. used for image processing [68, 69] and is widely applied in various fields of tomography [70–81]. In this thesis, the Landweber iteration is used to estimate the defect properties by reconstructing the defect identification vector from the DRS components of aluminum specimens (Chapter 4).

Another possibility to regularize the problem is by adding a regularization term $\mathcal{R}(\vec{x})$ to (2.49)

$$\arg \min_{\vec{x}} \left(\frac{1}{2} \left\| \vec{y} - [L] \, \vec{x} \right\|_{2}^{2} + \lambda \mathcal{R}(\vec{x}) \right), \tag{2.53}$$

where λ denotes the regularization parameter, which is the crucial parameter. It weights between the data term and the regularization and therefore specifies how much the

determined source vector $\vec{x}$ depends on both terms. Automatic methods to determine λ are e.g. the discrepancy principle [82], the L-curve method [83] or the generalized cross validation [84].

The probably best-known regularization method is the TPR [85, 86] with the L2-norm term $\mathcal{R}(\vec{x}) = ||\,[W]\,\vec{x} - \vec{r}||_2^2$. The *a priori* knowledge is encoded in $\vec{r}$ and $[W]$. The L2-norm leads to a smooth source parameter vector $\vec{x}$ [87]. Using the TPR, the source vector $\vec{x}$ can be determined as a closed solution by

$$\vec{x} = \left([L]^{\mathrm{T}}\,[L] + \lambda\,[W]^{\mathrm{T}}\,[W] \right)^{-1} \left([L]^{\mathrm{T}}\,\vec{y} + \lambda\,[W]^{\mathrm{T}}\,\vec{r} \right). \tag{2.54}$$

In the field of NDE, the TPR has been applied e.g. in ECE [53, 88], for the defect reconstruction from magnetic flux leakage measurement data [89] or magnetic induction tomography [5]. In fields beyond NDE, the TPR is widely used in biomedical engineering for the reconstruction of current source distributions in the human brain [90] and heart [91] or for magnetic nanoparticle imaging [92].

Beside the L2-norm, the L1-norm can be used as regularization term $\mathcal{R}(\vec{x}) = ||\vec{x}||_1$. The corresponding problem is referred to as least absolute shrinkage and selection operator (LASSO) problem [87], which is solved by a coordinate descent method. The reconstructed source vector $\vec{x}$ tends to be sparse [87]. Thus, the L1-norm regularization is a sufficient choice if the source vector $\vec{x}$ can be assumed to contain many zeros. The L1-norm regularization is used in NDE for reconstruction of defects in pipelines based on magnetic flux leakage measurements [89]. In biomedical engineering, it is used for the reconstruction of electromagnetic brain activity [90, 93].

Beside these two norms, p-norms with $1 < p < 2$ can be also applied for regularization $\mathcal{R}(\vec{x}) = ||\vec{x}||_p$. In previous work of LFE [19], an iteratively re-weighted least square algorithm has been used to determine the perturbation eddy current density distribution to characterize the defect, where the $p = 1.5$-norm yielded the best results.

In order to combine the properties of the L1- and the L2-norm, a weighted sum can be applied $\mathcal{R}(\vec{x}) = \left(\dfrac{\gamma - 1}{2} ||\vec{x}||_2^2 + \gamma ||\vec{x}||_1 \right)$, referred to as ENR which origins from statistical regression [87]. Regarding inverse problems, the ENR has been applied e.g. for the reconstruction of the electric activity of the heart [94] or the reconstruction of missing sensor traffic data [95]. In Chapter 3, a defect identification vector (section 2.1.4.2) is reconstructed using MNE with ENR in comparison to TPR for aluminum specimens under investigation from LFE measurements. Further, the MNE with ENR in comparison to TPR is applied to ECE in order to reconstruct the square current loop vector (section 2.2.4) for the estimation of defect properties in aluminum specimens.

Another possible regularization is the total variation (TV) [96]. The TV of a signal is defined as the sum of the absolute gradient of the signal. The idea origins from image denoising [96]. It is based on the fact that an image e.g. with Gaussian noise shows a

high total variation. By minimizing the total variation additionally to minimizing the data term (2.49), unwanted details like noise are suppressed and edges are kept. Beside the denoising of signals, TV regularization was already applied in ECE [51,88].

Deterministic Optimization Algorithms Further, deterministic optimization algorithms can be used to solve the minimization problem (2.48) iteratively. Thus, they require an initial solution source vector $\vec{x}_{\text{initial}}$. Methods like the Newton's [97] or the Levenberg-Marquardt methods [98] require the differentiability of the minimization problem as they are based on the principle of gradient descent. Another deterministic method is the simplex method. Deterministic methods often further assume continuousness and convexity of the problem to be minimized. The quality of the solution vector $\vec{x}$ depends on the initial solution. Due to the local search, deterministic methods tend to drop into local minima. But reproducible solutions of $\vec{x}$ are achieved if the initial solution, the search area and the termination criterion remain unchanged. In the framework of LFE, the simplex method was used for the optimization of the multiple dipoles model (section 2.1.4.1) [16].

Stochastic Optimization Algorithms In contrast to deterministic optimization algorithms, most stochastic optimization algorithms do not require differentiability, continuousness or convexity of the problem. The ability to stuck at local minimal is smaller, e.g. due to multiple initial solutions or due to the ability of accepting a worsening of the solution during the optimization procedure. In consequence, stochastic optimization algorithms require an increased number of evaluations of the goal function (2.48) compared to deterministic algorithms. The obtained solution is not reproducible. Stochastic optimization methods contain intrinsic control parameters that are crucial to adjust. Stochastic optimization methods can be divided into physical algorithms, swarm intelligence algorithms and evolutionary algorithms.

One example for physical algorithms is the simulated annealing that has already been applied for ECE [99–101]. In the field of NDE, the particle swarm optimization [102–104] and the ant colony optimization [105] have been applied for defect reconstruction in ECE. Evolutionary algorithms are based on Darwin's theory. Different solutions form an initial population that evolves by genetic mutation and recombination. The selection of the solution is based on the survival-of-the-fittest principle. Evolutionary algorithms can be subdivided into genetic algorithms, evolutionary programming and evolutionary strategies. In the field of NDE, genetic algorithms and evolutionary programming have been applied for ECE [106]. For LFE, previous work used the Differential Evolution to reconstruct a conductivity distribution from DRS components to determine the defect properties [17].

3 Elastic Net Regularization in Lorentz Force and Eddy Current Evaluation

3.1 Introduction

The described inverse problems in LFE and ECE are unstable as the solutions are sensitive to small changes in the noisy measurement data (section 2.3.1). Thus, regularization is required that represents *a priori* knowledge about the problem.

For that purpose the elastic net regularization (ENR) is used. ENR emerges from statistical regression [87,107] suited for correlated predictors. It is applied for regression problems e.g. in mining [108], food industry [109,110], pharmacology [111,112], medicine [113–115], chemistry [116], or engineering [117]. Further, applications of ENR can be found in image processing [118–120], model order reduction [121,122], neuroinformatics [123–125], or the regularization of a Markov model [126]. The ENR is also used within fault diagnosis of rolling bearings [127] and machinery [79]. Regarding inverse problems, the ENR has been applied for the reconstruction of the electric activity of the heart [94] or the reconstruction of missing sensor traffic data [95].

Considering the widespread application of ENR, it is considered for the inverse problem of LFE and ECE. The minimum norm estimation (MNE) with ENR is defined as [107]

$$\underset{\vec{x}\in\mathbb{R}^{M\times 1}}{\arg\min}\left(\underbrace{\frac{1}{2N}\left\|\vec{y}-[L]\,\vec{x}\right\|_2^2}_{\text{Data term}}+\lambda\underbrace{\left(\frac{1-\gamma}{2}\left\|\vec{x}\right\|_2^2+\gamma\left\|\vec{x}\right\|_1\right)}_{\text{Regularization term}}\right), \qquad (3.1)$$

where $\vec{y}\in\mathbb{R}^{N\times 1}$ describes the electromagnetic field components from measurements of N observation points that act as input for the defect reconstruction. The unknown source parameter vector $\vec{x}$ is obtained by minimizing the sum of the data and the regularization term. The data term contains the deviation between $\vec{y}$ and $[L]\vec{x}$, where the lead field matrix $[L]\in\mathbb{R}^{N\times M}$ contains the forward solution, see sections 2.1.4.2 and 2.2.4. The norm weight parameter γ weights between the L1- and the L2-norm. For $\gamma = 1$ the problem is referred to as the LASSO problem which leads to a sparse solution $\vec{x}$ [87]. If $\gamma \to 0$ the problem converges towards the Tikhonov-Phillips-regularization (TPR),

which prefers the solution $\vec{x}$ to be more smooth [87]. The regularization parameter λ
controls how much the obtained solution depends on the regularization term.

In LFE, the unknown vector $\vec{x}$ equals the defect identification vector $\vec{\theta}$ (section
2.1.4.2). It is known *a priori* that the defect identification vector $\vec{\theta}$ should contain
ones for elements that belong to the defect and zeros otherwise, where the defect voxels
are assumed to be spatially connected. The L2-norm of the ENR term (3.1) enables a
spatially smooth solution $\vec{\theta}$ [87], which implicitly leads to a spatial connection of the
voxels. The L1-norm privileges zero-values in $\vec{\theta}$.

In ECE, the unknown vector $\vec{x}$ equals the square current loop vector $\underline{\vec{I}}_{\mathrm{d}}$. It is char-
acterized by smooth continuous values with surrounding zeros. This *a priori* knowledge
should be mirrored by ENR.

In the remaining chapter the application of ENR to LFE and ECE in comparison to
the widely applied TPR is described in the sections 3.2 and 3.3, respectively. The sub-
sections include the description of the analyzed setup, the methodical description of TPR
and ENR including the parameter studies for determination of the control parameters,
the defect reconstruction results for simulated and measured data, as well as a discussion
and conclusion of the results. In section 3.4 the obtained results from LFE and ECE are
compared, discussed and summarized. Section 3.2 contains methods and results that
have been presented in [21] and are published in [22].

3.2 Lorentz Force Evaluation

3.2.1 Setup

Problem description   A conducting specimen is moved relative to a fixed perma-
nent magnet with a velocity $\vec{v} = 0.1\,\mathrm{m/s}\,\vec{e}_x$ (Fig. 3.1) along multiple parallel scanning
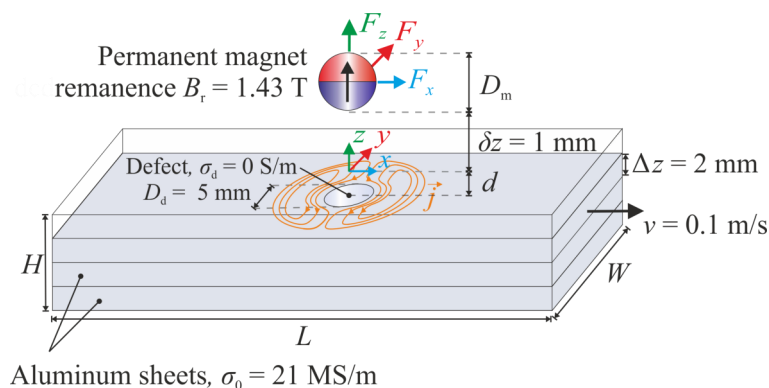

Figure 3.1: Problem setup: A package of aluminum sheets with a cylindrical defect is
moved relative to a permanent magnet. The interaction of the induced eddy currents
(orange lines) with the magnetic field leads to Lorentz forces.

lines. The permanent magnet is located at a lift-off distance $\delta z = 1\,\mathrm{mm}$ above the top surface of the specimen. The homogeneous magnetization $\vec{M} = B_\mathrm{r}/\mu_0\,\vec{e}_z\,(B_\mathrm{r} = 1.43\,\mathrm{T})$ characterizes the magnet, where B_r describes the remanence. The specimen consists of stacked aluminum sheets, each with a thickness $\Delta z = 2\,\mathrm{mm}$ and a conductivity of $\sigma_0 = 21\,\mathrm{MS/m}$. The sheets are separated by thin insulating interfaces. A single cylindrical defect is located at the x-y-center of the specimen at depth d. Three different defect depths $d = 2$, 4 and $8\,\mathrm{mm}$ are analyzed. The defect with a conductivity $\sigma_\mathrm{d} = 0$ is characterized by a diameter $D_\mathrm{d} = 5\,\mathrm{mm}$ and a height $H_\mathrm{d} = 2\,\mathrm{mm}$. The area of the defect cross section is $A_\mathrm{d} = 19.63\,\mathrm{mm}^2$.

Simulations   The numerical simulations use the setup shown in Fig. 3.1 with specimen dimension $L \times W \times H = 400\,\mathrm{mm} \times 400\,\mathrm{mm} \times 100\,\mathrm{mm}$ and a spherical permanent magnet
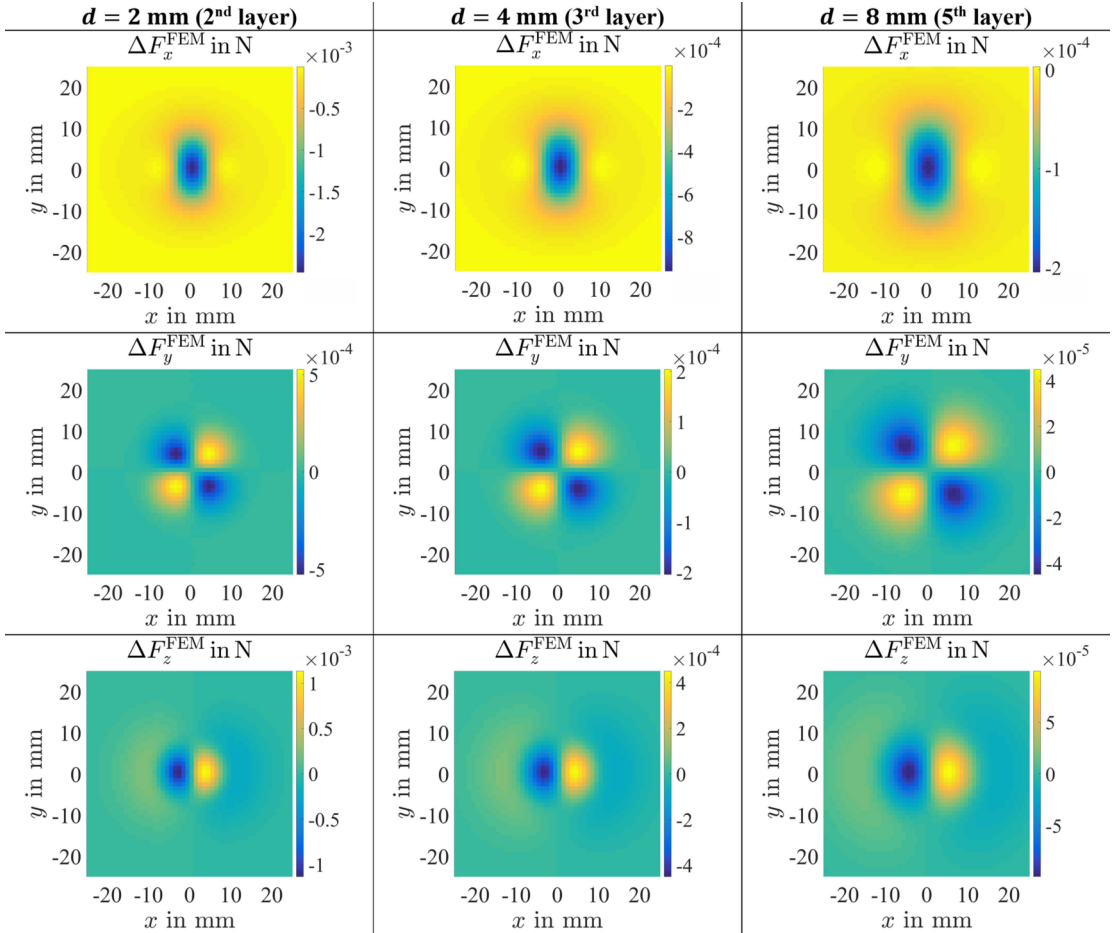
Figure 3.2: Defect response signal components obtained from FEM simulations with ΔF_x^FEM (top), ΔF_y^FEM (middle), ΔF_z^FEM (bottom) at the observation points for defect depths $d = 2$ (left), 4 (middle) and $8\,\mathrm{mm}$ (right). Note the different scaling of the color bars.

with a diameter of $D_\mathrm{m} = 15\,\mathrm{mm}$. The DRS components are computed by FEM simulations using the weak reaction approach as described in section 2.1.2.2. The observation points are equally distributed within $|x| \leq 25\,\mathrm{mm}$ and $|y| \leq 25\,\mathrm{mm}$ at $z = 8.5\,\mathrm{mm}$. The z-position corresponds to the center of the spherical permanent magnet. The distances between these points in x- and y-direction are $d_x = d_y = 1\,\mathrm{mm}$. The obtained DRS components (Fig. 3.2) act as noise free benchmark signals. Consequently, the general properties of novel inverse methods can be assessed before the application to the measurement data.

Measurements   A specimen with dimensions $L \times W \times H = 250\,\mathrm{mm} \times 50\,\mathrm{mm} \times 50\,\mathrm{mm}$ and a cylindrical permanent magnet with a diameter of $D_\mathrm{m} = 22.5\,\mathrm{mm}$ and a height of $H_\mathrm{m} = 17.6\,\mathrm{mm}$ are used for the measurements (Fig. 2.6). The specimen consists of
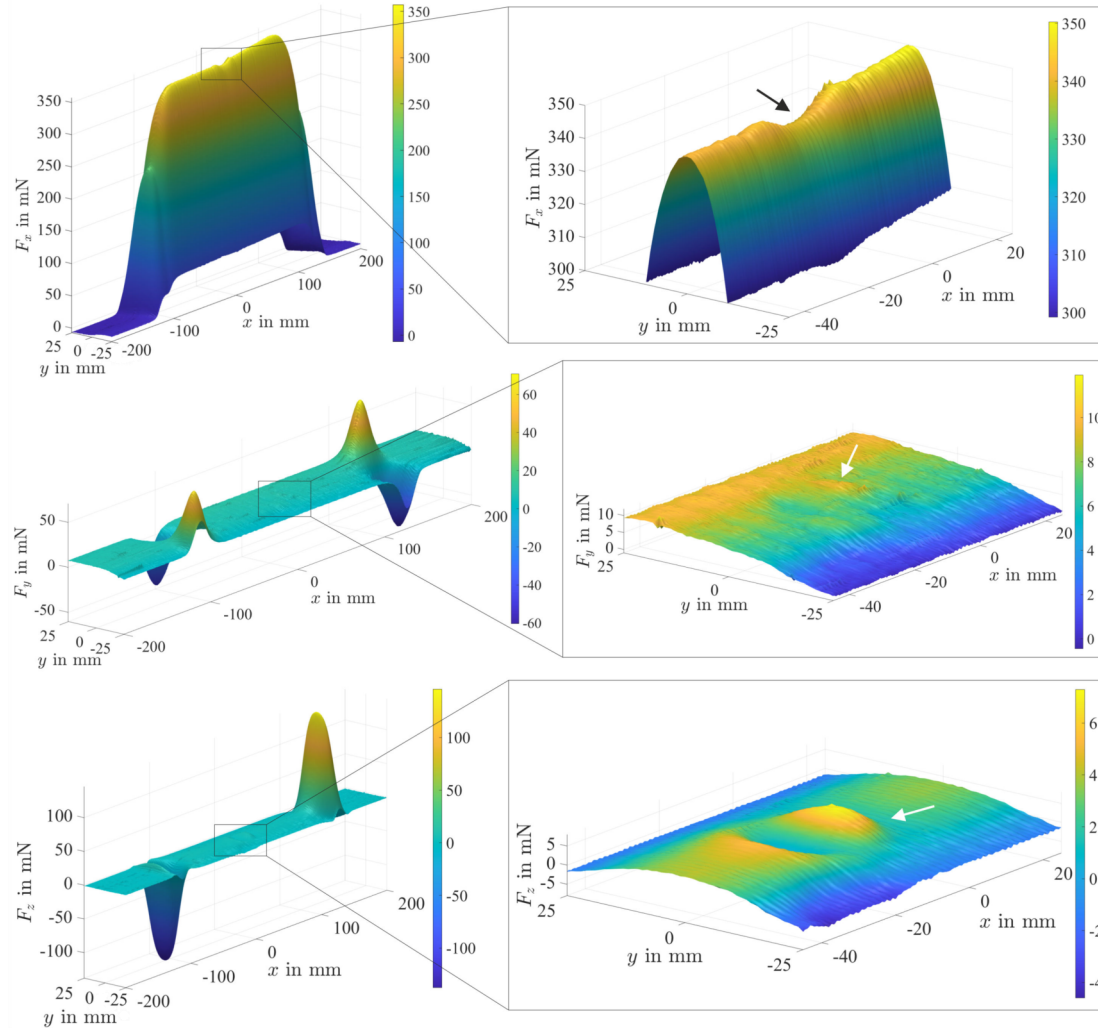
Figure 3.3: Measured raw data of the Lorentz force components F_x (top), F_y (middle), F_z (bottom) for defect depth $d = 2\,\mathrm{mm}$ and trial no. 1 with enlargement of the areas, representing the defect influence (arrows). Note the different scaling of the color bars.

stacked aluminum sheets and is moved by a linear direct drive relative to the fixed perma-
nent magnet with a 3D strain gauge force sensor. The forces have been measured along
51 y-lines that are uniformly distributed in the range of $-25\,\text{mm} \leq y \leq 25\,\text{mm}$. The
force components are derived at each y-line in the range $-208.5\,\text{mm} \leq x \leq 208.6\,\text{mm}$.
The distances between the observation points are $d_x = 0.1\,\text{mm}$ and $d_y = 1\,\text{mm}$. The
measurements were repeated for every y-line 25 times resulting in 25 measurement trials
per defect depth. Exemplary measured Lorentz force components F_x (Fig. 3.3, top), F_y
(Fig. 3.3, middle) and F_z (Fig. 3.3, bottom) are shown for the defect depth $d = 2\,\text{mm}$.
The defect shows noticeable effects in F_x (Fig. 3.3, top, black arrow) and F_z (Fig. 3.3,
bottom, white arrow) and small effects are visible in F_y (Fig. 3.3, middle, white arrow).

In order to extract the DRS from the measured forces, the following preprocessing
steps are carried out:

1. The force profiles F_x, F_y and F_z (Fig. 3.3) are cut from $x = [-80, 70]\,\text{mm}$ to
   remove the influence of left and right specimen edges. This asymmetric cut-out
   roughly centers the force profiles according to the visible influences of the defect
   (Fig. 3.3).

2. A principal component analysis is applied separately to the force profiles F_x, F_y
   and F_z, where the distorted components are removed.

3. A finite impulse response low pass filter with an order of 400 is applied. The
   force signals have a resolution of 10000 samples/m in scanning direction, which
   corresponds to the sampling rate of 1000 Hz at the velocity $v = 0.1\,\text{m/s}$. The
   filter is applied for each scanning line at the spatial cut-off frequencies of $100\,\text{m}^{-1}$
   ($\hat{=}10\,\text{Hz}$) for F_x and F_z and $75\,\text{m}^{-1}$ ($\hat{=}7.5\,\text{Hz}$) for F_y. The same spatial cut-
   off frequencies could be chosen for slightly lower or higher velocities as the main
   spatial frequencies in m^{-1} of the DRS components do not change considerably [19].

4. A detrending is applied along the scanning lines. A linear detrending is used for
   F_y and F_z. A combination of linear and quadratic detrending is applied for F_x.
   The detrending removes the effects of front and back edges of the specimen as well
   as trends from distortions.

5. An average filter is applied line-wise perpendicular to the scanning direction to
   remove further distortions.

6. The coordinate origin is realigned to the minimum of ΔF_x to ensure that the
   center of the defect lies directly below the coordinate origin.

7. A down-sampling from $d_x = 0.1\,\text{mm}$ to $d_x = 1\,\text{mm}$ is applied to reduce the
   computational cost for following defect reconstruction algorithms. The corre-
   sponding observation points are equally distributed within $|x| \leq 25\,\text{mm}$ and

$|y| \leq 19\,\text{mm}$ (Fig. 3.4). The distances between these points in x- and y-direction are $d_x = d_y = 1\,\text{mm}$.

The resulting DRS signal components ΔF_x^{meas}, ΔF_y^{meas} and ΔF_z^{meas} after preprocessing and for the defect depths 2, 4 and 8 mm are shown in Fig. 3.4 for measurement trial no. 1.

In order to evaluate the signal quality, the signal-to-noise-ratio (SNR) in dB of the preprocessed DRS is calculated as the ratio of the power in the region of observation points $P_{\text{Signal+Noise}}$ (Fig. 3.5 a, black rectangle) and the power P_{Noise} of the surrounding region (Fig. 3.5 a, red rectangles) of equal size according to:

$$\text{SNR} = 10 \cdot \log_{10}\left(\frac{P_{\text{Signal+Noise}}}{P_{\text{Noise}}}\right)\ \text{dB} = 10 \cdot \log_{10}\left(\frac{\sum_{s=1}^{N} \Delta F_s^2}{\sum_{n=1}^{N} \Delta F_n^2}\right)\ \text{dB} \qquad (3.2)$$

where ΔF_s and ΔF_n denote the signal components in the region of observation points (Fig. 3.5 a, black rectangle) and the surrounding region (Fig. 3.5 a, red rectangles), respectively. The squared sum in both regions is calculated from N data points. The SNR
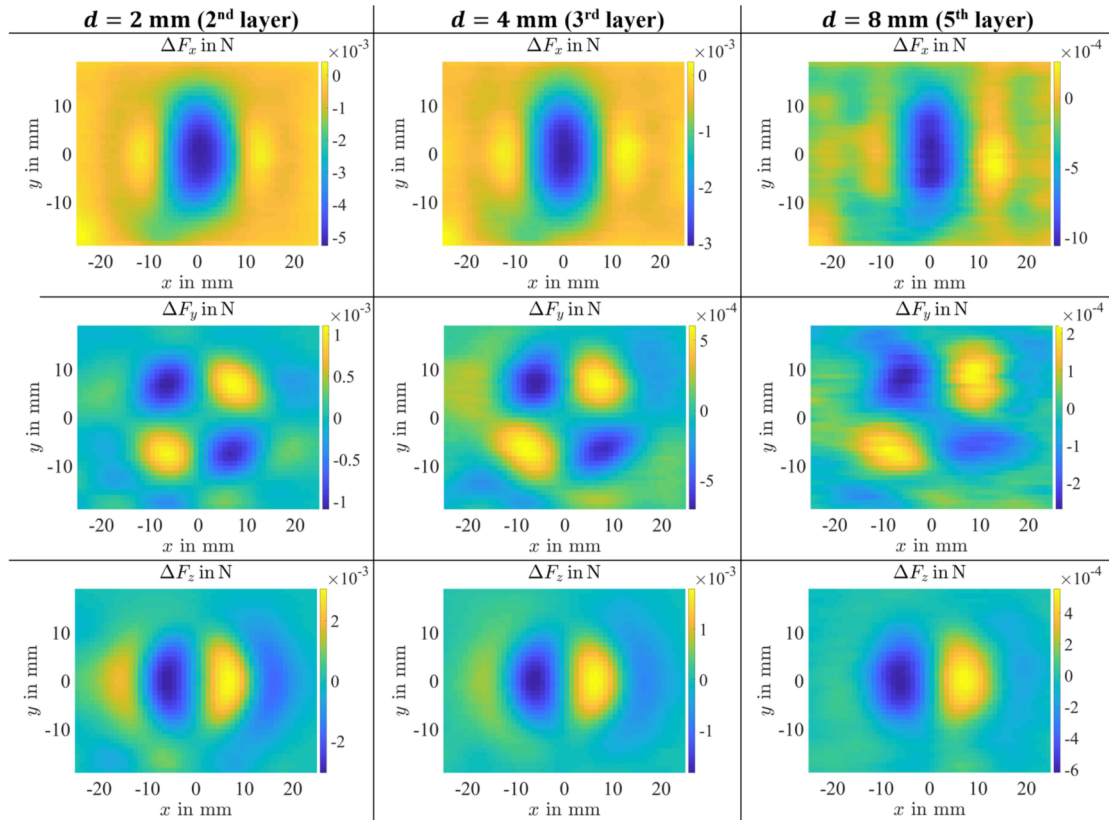
Figure 3.4: Defect response signal components obtained from measurement trial no. 1 with ΔF_x^{meas} (top), ΔF_y^{meas} (middle), ΔF_z^{meas} (bottom) for the defect depths $d = 2$ (left), 4 (middle) and 8 mm (right) after preprocessing. Note the different scaling of the color bars.
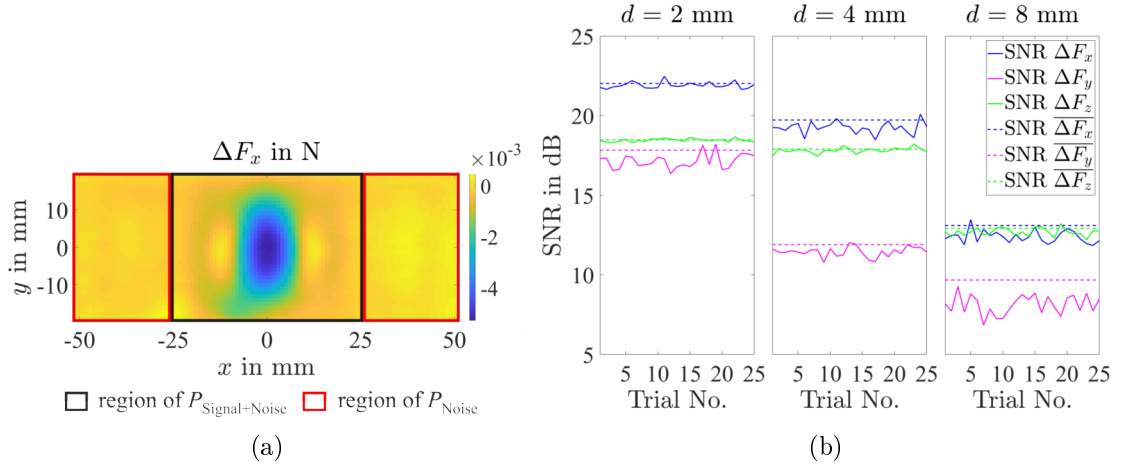
Figure 3.5: SNR of DRS components: (a) Regions for calculation of SNR from DRS components (here: ΔF_x) according to (3.2), (b) SNR in dB of DRS components: ΔF_x^{meas} (solid blue), ΔF_y^{meas} (solid magenta) and ΔF_z^{meas} (solid green) for different trials and defect depths. SNR values of corresponding averaged DRS components are shown by dashed lines.

is calculated for ΔF_x^{meas}, ΔF_y^{meas} and ΔF_z^{meas}, separately. The data points of the surrounding region are extracted from two rectangular regions with $25\,\text{mm} < |x| \leq 50\,\text{mm}$ and $|y| \leq 19\,\text{mm}$ (Fig. 3.5 a, red rectangles). Fig. 3.5 b shows the SNR values of ΔF_x^{meas}, ΔF_y^{meas} and ΔF_z^{meas} for the 25 trials.

Averaging the DRS components of the 25 trials results in $\overline{\Delta F_x^{\text{meas}}}$, $\overline{\Delta F_y^{\text{meas}}}$ and $\overline{\Delta F_z^{\text{meas}}}$ for the defect depths $d = 2\,\text{mm}$, $4\,\text{mm}$ and $8\,\text{mm}$. The SNR values are also calculated for the averaged DRS components (Fig. 3.5 b, dashed lines). It can be observed that the increase of SNR due to averaging is largest for ΔF_y. ΔF_x and ΔF_z show the highest SNR values. The decrease of SNR with increasing defect depth is minimal for ΔF_z.

3.2.2 Minimum Norm Estimation

It is the aim to reconstruct defect properties from the DRS components obtained from simulations (Fig. 3.2) and measurements (Fig. 3.4). For that purpose, the DRS components $\Delta F_x^{\text{FEM/meas}}$, $\Delta F_y^{\text{FEM/meas}}$ and $\Delta F_z^{\text{FEM/meas}}$ with N observation points are arranged in a vector $\Delta \vec{F}^{\text{FEM/meas}} \in \mathbb{R}^{3N \times 1}$.

The inverse problem can be formulated as a MNE problem

$$\underset{\vec{\theta} \in \mathbb{R}^{M \times 1}}{\arg \min} \frac{1}{2} \left\| \Delta \vec{F}^{\text{FEM/meas}} - \underbrace{[L]\vec{\theta}}_{\Delta \vec{F}^{\text{AFS}}} \right\|_2^2, \tag{3.3}$$

where a defect identification vector $\vec{\theta}$ (section 2.1.4.2) has to be found that minimizes

the deviation between $\Delta\vec{F}^{\text{FEM/meas}}$ and the forward calculated $\Delta\vec{F}^{\text{AFS}}$. The lead field matrix $[L] \in \mathbb{R}^{N\times M}$ contains the AFS (section 2.1.4.2).

In order to determine the defect depth and the defect shape, problem (3.3) has to be solved for separate layers. The metal layers 1 ($d = 0\,\text{mm}$) to 11 ($d = 20\,\text{mm}$) are selected as possible layers for a defect location. These sheets are discretized in x-, y- and z-direction by $1\,\text{mm} \times 1\,\text{mm} \times 2\,\text{mm}$ voxels at a region where the possible defect is expected.

Corresponding to the definition of the AFS (section 2.1.4.2), the estimated vector $\vec{\theta}$ should contain ones at the elements that correspond to the defect voxels and zeros at defect-free voxels. For that purpose, a thresholding is introduced to the elements of the continuous $\vec{\theta}$ determined by the MNE

$$
\theta_{\text{th}_m} = \begin{cases} 0 \text{ if } \theta_m \leq t_{\text{h}} \cdot \left(\max\left(\vec{\theta}\right) + \min\left(\vec{\theta}\right) \right) \\ 1 \text{ if } \theta_m > t_{\text{h}} \cdot \left(\max\left(\vec{\theta}\right) + \min\left(\vec{\theta}\right) \right) \end{cases} \quad . \tag{3.4}
$$

The thresholding factor t_{h} has to be chosen in a range of [0.01,0.99]. As the defect reconstruction is carried out layer-wise, a solution $\vec{\theta}_{\text{th}}$ is computed with an error measure for each layer individually.

Error measures   The error measure for the application of the MNE including thresholding is defined as NRMSE

$$
\begin{aligned}
\text{NRMSE} &= \frac{1}{3}\sum_{i=x,y,z}\left[\frac{\sqrt{\frac{1}{N}\sum_{n=1}^{N}\left(\Delta F_{n,i}^{\text{AFS}} - \Delta F_{n,i}^{\text{FEM/meas}}\right)^2}}{\min\left[R^{\text{AFS}}, R^{\text{FEM/meas}}\right]} \right]. \\
&\text{with } R^{\text{AFS}} = \max\left(\Delta\vec{F}_i^{\text{AFS}}\right) - \min\left(\Delta\vec{F}_i^{\text{AFS}}\right) \\
&\text{and } R^{\text{FEM/meas}} = \max\left(\Delta\vec{F}_i^{\text{FEM/meas}}\right) - \min\left(\Delta\vec{F}_i^{\text{FEM/meas}}\right)
\end{aligned} \tag{3.5}
$$

It describes the deviation between the forward calculated DRS $\Delta\vec{F}^{\text{AFS}} = [L]\vec{\theta}_{\text{th}}$ and the DRS obtained from simulations or measurements $\Delta\vec{F}^{\text{FEM/meas}}$. The NRMSE is the mean of the errors of x-, y- and z-components. The layer with the smallest NRMSE indicates the defect depth.

Measures to quantify the defect reconstruction error are the Euclidean distance d_0 to the center of the true defect, the size difference a_{d} in mm^2 as well as the extensions of the reconstructed defect in x- and y-direction, x_{e} and y_{e}, in mm.

The inverse problem (3.3) is unstable, as the solutions are highly sensitive to small changes in the noisy measured data. Thus, regularization methods have to be applied.

3.2.3 Tikhonov-Phillips-Regularization

Principle The TPR [85, 86] is a widely applied regularization method and therefore used for comparison with ENR. The MNE problem (3.3) with TPR can be defined as follows

$$\underset{\vec{\theta} \in \mathbb{R}^{M \times 1}}{\arg\min} \left(\underbrace{\frac{1}{2} \left\| \Delta \vec{F}^{\mathrm{FEM/meas}} - [L]\vec{\theta} \right\|_2^2}_{\text{Data term}} + \lambda \underbrace{\left\| \vec{r} - [W]\vec{\theta} \right\|_2^2}_{\text{Regularization term}} \right). \tag{3.6}$$

In this study the TPR of zero order [128] with $\vec{r} = \vec{0}$ and $[W] = [I]$ is used, where $[I]$ denotes the identity matrix. After some derivations and pre-whitening, $\vec{\theta}$ can be obtained by

$$\vec{\theta} = [L]^{\mathrm{T}} \left[[L][L]^{\mathrm{T}} + \lambda[I] \right]^{-1} \Delta \vec{F}^{\mathrm{FEM/meas}}. \tag{3.7}$$

The regularization parameter λ controls how much the solution $\vec{\theta}$ depends on the regularization term. The obtained vector $\vec{\theta}$ is smooth with continuous values, where elements of zero are unlikely. The optimal regularization parameter λ has to be determined. Additionally, a suitable thresholding factor t_{h} is needed to obtain $\vec{\theta}_{\mathrm{th}}$.

Parameter Studies The specific case of LFE including the thresholding necessitates for searching the optimal parameters with the help of a known reference case. For that purpose, the simulated data set $\Delta \vec{F}^{\mathrm{FEM}}$ with a cylindrical defect at $d = 2\,\mathrm{mm}$ (Fig. 3.2 left) is used. It is assumed that the defect depth is known. Various λ-t_{h} combinations are tested according to the scheme:

1. Determination of continuous $\vec{\theta}$ by (3.7) for one λ;

2. Determination of $\vec{\theta}_{\mathrm{th}}$ by (3.4) for one t_{h};

3. Calculation of $\Delta \vec{F}^{\mathrm{AFS}}$ by (2.27) with $\vec{\theta}_{\mathrm{th}}$;

4. Calculation of NRMSE by (3.5) between $\Delta \vec{F}^{\mathrm{AFS}}$ and $\Delta \vec{F}^{\mathrm{FEM}}$.

The scheme is applied separately to the single aluminum layers. The parameters λ and t_{h} are selected according to the minimal NRMSE.

First, the regularization parameters λ are tested with 500 logarithmically spaced values in the range of $\lambda = \left[10^{-20}, 10^8 \right]$ with a fixed thresholding factor $t_{\mathrm{h}} = 0.5$. For that purpose, the above described scheme is applied only for metal layer 2, where the defect is located. The resulting NRMSEs for different λ are shown in Fig. 3.6 b. A region with a stable minimum is found for λ between $2.52 \cdot 10^{-8}$ and $1.99 \cdot 10^{-7}$. This optimal region of λ cannot be found by using the L-curve method [83] as the corresponding curve (Fig. 3.6 a) is not L-shaped.

The stable region is shifted to lower λ-values in the range of 2 orders of magnitude for $d = 4\,\mathrm{mm}$ and 5 orders of magnitude for $d = 8\,\mathrm{mm}$, respectively. The value of λ with
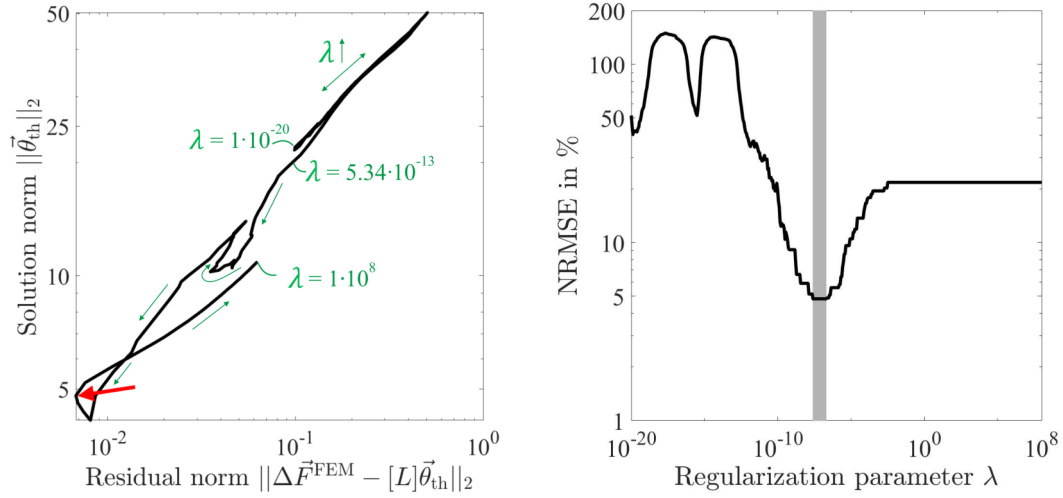
(a) Curve of solution norm in dependence of the residual norm for the investigated λ-values. The minimal residual norm (red arrow) corresponds to minimal NRMSE of Fig. 3.6 b.

(b) A minimum of NRMSE= 4.83 % can be obtained for the interval $\lambda = [2.52 \cdot 10^{-8}, 1.99 \cdot 10^{-7}]$ (vertical bar).

Figure 3.6: Determination of the optimal regularization parameter λ with a fixed thresholding factor $t_h = 0.5$ for TPR.

minimal NRMSE also changes during the layer-wise calculation. These changes do not follow a specific pattern and are in the range of 2 orders of magnitude. It should be added that also the shape of the NRMSE-λ-curve changes. The described behavior leads to the decision to keep the broad range of $\lambda = [10^{-20}, 10^8]$ and to obtain the minimal NRMSE from 500 logarithmically spaced λ-values within that range.

Second, different thresholding factors $t_h = [0.125, 0.25, \ldots, 0.875]$ are tested. For the determination of the optimal thresholding factor t_h, the metal layers 1 to 11 are considered. Further, the simulated data sets with defect depths $d = 4$ and $8\,\mathrm{mm}$ are analyzed. The minimal NRMSE at the correct depth is found for t_h between 0.25 and 0.75 for $d = 2\,\mathrm{mm}$ (Fig. 3.7 a), for t_h between 0.375 and 0.875 for $d = 4\,\mathrm{mm}$ (Fig. 3.7 b) and for t_h between 0.625 and 0.875 for $d = 8\,\mathrm{mm}$ (Fig. 3.7 c). It is concluded that the optimal t_h depends on the defect depth. A compromise for the three defect depths would be $t_h = 0.625$ or 0.75. But it should be also taken into account that regularization with L2-norm leads to smooth vectors $\vec{\theta}$, where a fixed thresholding factor limits the ability of TPR to reconstruct defects of different sizes. Consequently, the thresholding factor t_h is considered as an own regularization parameter of TPR for LFE.
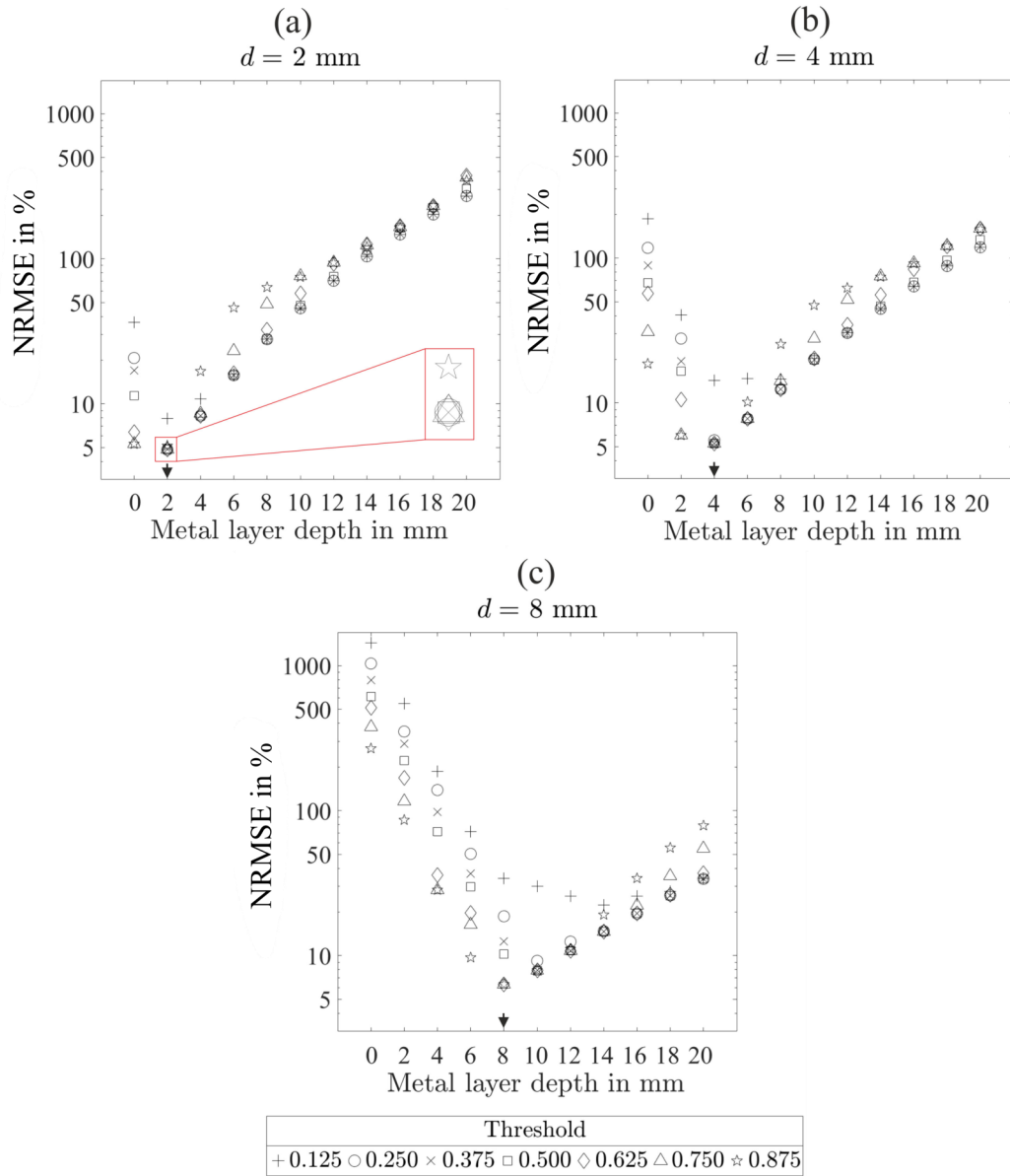
Figure 3.7: Determination of the optimal thresholding factor t_{h} in TPR: NRMSE at different metal layer depths are shown for the defect depths $d = 2$ (a), 4 (b) and 8 mm (c). The optimal t_{h}, indicated by minimal NRMSE at the correct depth (arrows), depends on the depth of the defect.

Reconstruction Scheme The defect reconstruction scheme, described in Algorithm 1 is derived from the parameter studies results. The minimal $\text{NRMSE}_{m,i,t_\text{h}}$ is obtained from this reconstruction scheme. The related layer m indicates the defect depth and the corresponding defect identification vector $\vec{\theta}_{\text{th},m,i,t_\text{h}}$ contains information about location, size and shape of the reconstructed defect.

Algorithm 1: Defect reconstruction scheme for Tikhonov-Phillips-regularization in Lorentz force evaluation in pseudo-code.

---

for $m = 1$ **to** 11 **do**
    Analyze layer m:
    for $i = 1$ **to** 500 **do**
        Determination of continuous $\vec{\theta}_i$ by (3.7) with λ_i
        for $t_\text{h} = 0.01 : 0.01 : 0.99$ **do**
            Determination of:
            $\vec{\theta}_{\text{th},m,i,t_\text{h}}$ by (3.4) with t_h
            $\Delta\vec{F}^{\text{AFS}}_{m,i,t_\text{h}}$ by (2.27) with $\vec{\theta}_{\text{th},m,i,t_\text{h}}$
            $\text{NRMSE}_{m,i,t_\text{h}}$ by (3.5) with $\Delta\vec{F}^{\text{AFS}}_{m,i,t_\text{h}}$
        end
    end
end

3.2.4 Elastic Net Regularization

Principle It is known *a priori* that the defect identification vector $\vec{\theta}$ should contain ones for elements belonging to the defect and zeros otherwise (see section 2.1.4.2). The L2-norm term enables a spatially smooth solution $\vec{\theta}$ [87], which implicitly leads to a spatial connection of the voxels of $\vec{\theta}_{\text{th}}$. To privilege zero-values in $\vec{\theta}$, the L1-norm term is added to the previously described TPR. This principle is referred to as ENR and emerges from statistical regression [87, 107]. The MNE (3.3) with ENR [107] can be formulated as

$$\operatorname*{arg\,min}_{\vec{\theta}\in\mathbb{R}^{M\times 1}}\left(\underbrace{\frac{1}{2(3N)}\left\|\Delta\vec{F}^{\text{FEM/meas}}-[L]\vec{\theta}\right\|_2^2}_{\text{Data term}}+\lambda\underbrace{\left(\frac{1-\gamma}{2}\left\|\vec{\theta}\right\|_2^2+\gamma\left\|\vec{\theta}\right\|_1\right)}_{\text{Regularization term}}\right),\qquad(3.8)$$

where N denotes the number of observation points. The norm weight parameter γ weights between the L1- and L2-norm. For $\gamma = 1$ the problem is equal to the LASSO problem, which leads to a sparse solution [87]. If $\gamma \to 0$ the problem converges towards the TPR, which prefers solutions to be more smooth [87].

Parameter Studies   In order to determine the optimal values of λ, γ and t_h, the same approach as described for TPR (section 3.2.3) is used. Various γ-λ-t_h-combinations are tested. The optimal parameters are chosen according to a minimal NRMSE. First, the norm weight parameter γ is tested for 46 decadal spaced values of $\gamma = \left[1 \cdot 10^{-5}, 2 \cdot 10^{-5}, \ldots, 1 \cdot 10^{-4}, \ldots, 1\right]$. For every single γ, 100 values of λ are equally distributed between λ_min and λ_max. The maximal value λ_max that permits non-zero coefficients of $\vec{\theta}$ [107] is calculated by

$$\lambda_\mathrm{max} = \frac{\max\left(\left|[L]^\mathrm{T}\Delta\vec{F}^\mathrm{FEM/meas}\right|\right)}{3N\gamma}. \tag{3.9}$$

The minimal value of λ is defined by $\lambda_\mathrm{min} = \lambda_\mathrm{max} \cdot 10^{-4}$. The optima of the two parameters λ and γ are searched using the fixed thresholding factor $t_\mathrm{h} = 0.5$. The optimal value of λ cannot be found by using the L-curve method [83] as the corresponding curve is not L-shaped in our application (Fig. 3.8 a). Fig. 3.8 b shows the distribution of NRMSE in dependence of γ and λ for the reference case at the fixed thresholding factor $t_\mathrm{h} = 0.5$. The minimal NRMSE of 4.83 % (Fig. 3.8 b, white markers) can be found for $\gamma < 0.4$ (Fig. 3.8 b, below orange dashed line). As a first consequence, γ should be smaller than 0.4.
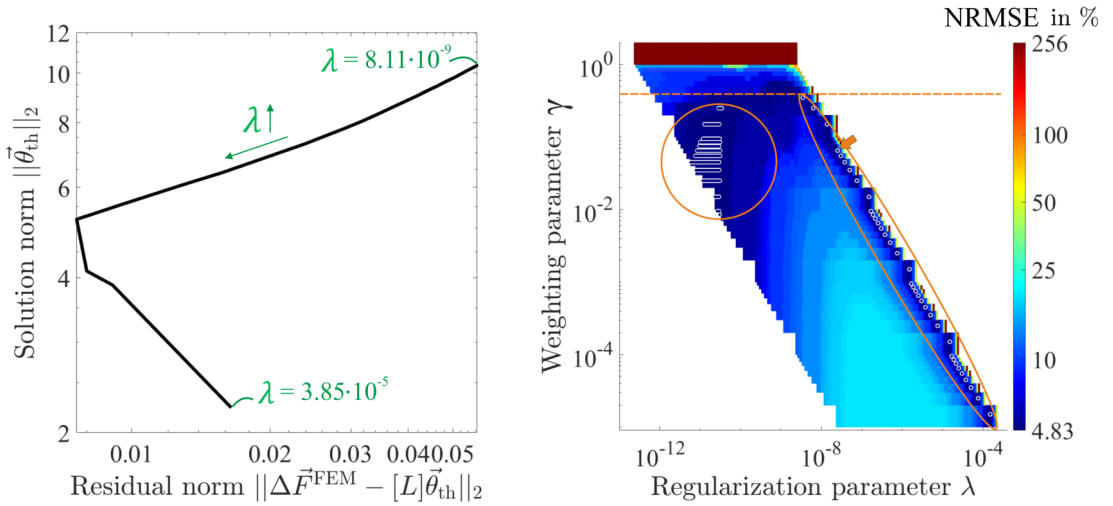
(a) Curve of solution norm in dependence of the residual norm for the investigated λ-values for $\gamma = 6 \cdot 10^{-5}$.

(b) Colors indicate NRMSE values for different γ-λ-combinations. The minimal NRMSE (white markers) can be found for $\gamma < 0.4$ (below orange dashed line). Suitable minima for defect reconstruction are located within the ellipse for $\gamma \leq 6 \cdot 10^{-2}$ (arrow). The orange circle indicates an additional stable region of minimal NRMSE values. The diagonal shape origins from the definition of λ_max, see eqn. (3.9).

Figure 3.8: Determination of optimal γ and λ with a fixed thresholding factor $t_\mathrm{h} = 0.5$ for ENR.

In the upper γ- and lower λ-range a stable region of minimal NRMSE (Fig. 3.8 b, orange circle with white curved rectangles) can be observed. The white curved rectangles show neighboring minima of the same γ. This stable region is shifted towards smaller regularization parameter values λ with increasing defect depth and disappears for deeper defect depths, e.g. $d = 8\,\text{mm}$. It follows that this region is not an appropriate basis for the decision of optimal γ and λ values.

Up to $\gamma = 6 \cdot 10^{-2}$ (Fig. 3.8 b, orange arrow) minimal NRMSE values are reliably obtained close to λ_{max} (Fig. 3.8 b, region within orange ellipse). Within the interval of $\gamma = [1 \cdot 10^{-5}, 6 \cdot 10^{-2}]$ there is no difference regarding the defect reconstruction quality. Therefore, any of the analyzed γ-values of that range can be chosen. The calculation time using a small γ of the order 10^{-5} is 2.7 times smaller than using one of the order 10^{-2}. As a result, a small γ is preferred. In this study, γ is selected with $\gamma = 6 \cdot 10^{-5}$.

The analyzed λ-range cannot be fixed as λ_{max} depends on the DRS $\Delta \vec{F}^{\text{FEM/meas}}$ and on the lead field matrix $[L]$, see (3.9). Additionally, the optimal λ depends on the defect size.

Second, the optimal thresholding factor t_{h} is determined while testing different values of $t_{\text{h}} = [0.125, 0.25, \ldots, 0.875]$. For the determination of optimal t_{h} all metal layers are taken into account. Further, the simulated data sets with defect depths $d = 4$ and $8\,\text{mm}$ are analyzed. For all analyzed thresholding factors the minimal NRMSE can be found at the correct depths (Fig. 3.9 a-c, arrows).

From that point of view, any of the analyzed thresholding factors could be applied. With respect to the measurement data, the DRSs for the defect depth $d = 8\,\text{mm}$ show the lowest SNR values (Fig. 3.5). Assuming that data with lower SNR values are more sensitive to parameter selections, the choice of t_{h} is also based on the results shown in Fig. 3.9 c. We choose the thresholding factor with minimal NRMSE at the correct defect depth and with significantly higher NRMSE values in the neighboring metal layers. For $d = 8\,\text{mm}$, this is fulfilled best by $t_{\text{h}} = 0.125$ (Fig. 3.9 c, symbol plus). As a result, the thresholding factor t_{h} is selected with $t_{\text{h}} = 0.125$.

Reconstruction Scheme The parameter studies resulted in a choice for the weighting factor of $\gamma = 6 \cdot 10^{-5}$ and for the thresholding factor of $t_{\text{h}} = 0.125$. No fixed optimal value can be set for λ as its value depends on λ_{max} (3.9) and on the defect size. The derived reconstruction scheme is separated in a depth and a shape estimation step, see Algorithm 2. If the minimal NRMSE values of two neighboring layers obtained from step 1 (Algorithm 2) are close, i.e. the absolute difference is smaller than $1\,\%$, step 2 of the defect reconstruction regime (Algorithm 2) is applied for both layers in order to improve the depth reconstruction accuracy.
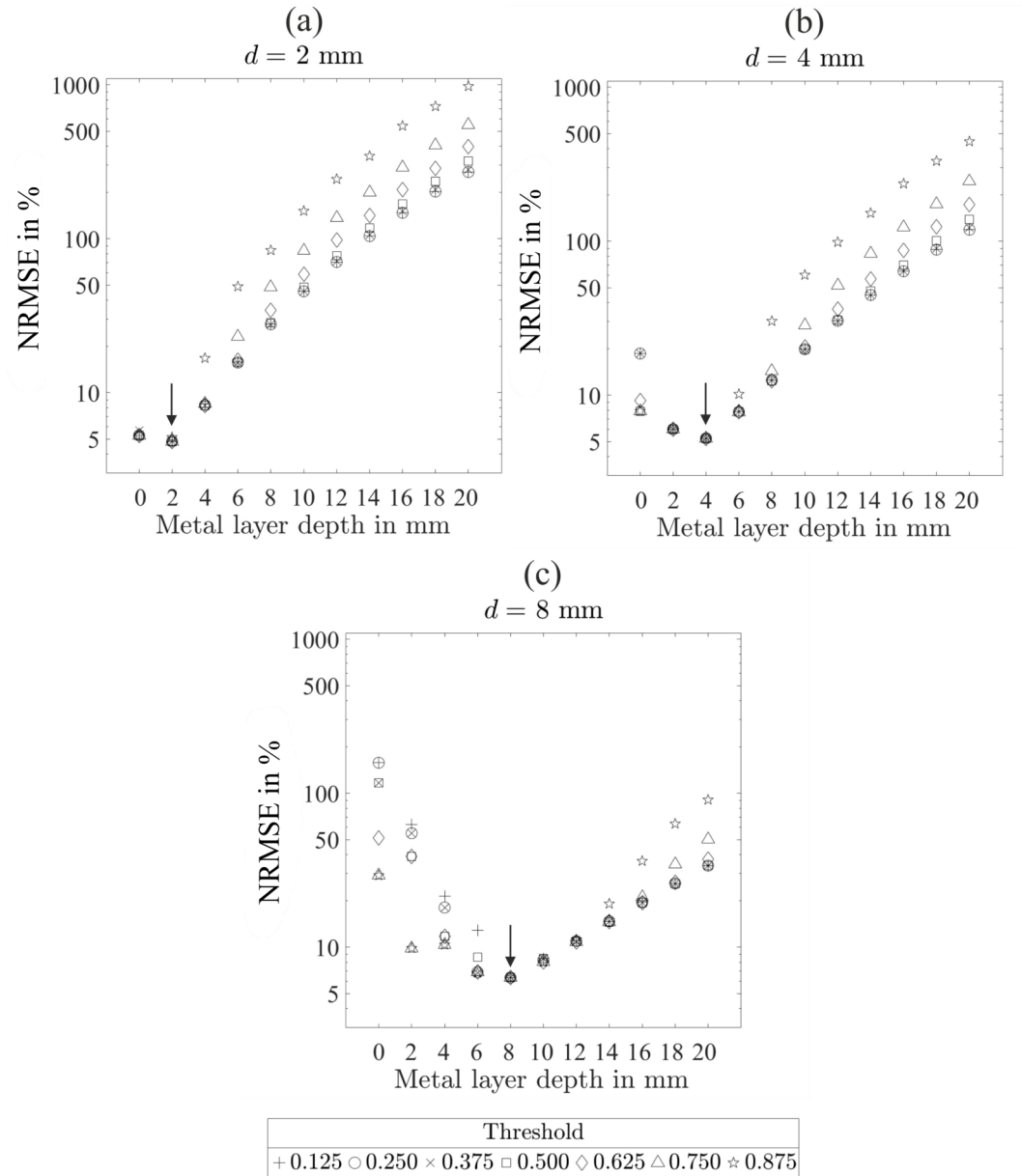
Figure 3.9: Determination of optimal thresholding factor t_h for ENR: NRMSE at different metal layers are shown for defect depths $d = 2$ (a), 4 (b) and 8 mm (c). The minimal NRMSEs of each case and for each thresholding factor are located at the correct defect layers (arrows).

Algorithm 2: Defect reconstruction scheme for Elastic Net Regularization in
Lorentz force evaluation in pseudo-code.

---

1. Defect depth estimation:

for $m = 1$ **to** 11 **do**

    Analyze layer m:

    for $i = 1$ **to** 100 **do**

        Determination of:

        Continuous $\vec{\theta}_{m,i}$ by (3.8) with $\lambda_{m,i}$ and $\gamma = 6 \cdot 10^{-5}$

        $\vec{\theta}_{\mathrm{th},m,i}$ by (3.4) with $t_{\mathrm{h}} = 0.125$

        $\Delta \vec{F}_{m,i}^{\mathrm{AFS}}$ by (2.27) with $\vec{\theta}_{\mathrm{th},m,i}$

        $\mathrm{NRMSE}_{m,i}$ by (3.5) with $\Delta \vec{F}_{m,i}^{\mathrm{AFS}}$

    end

    Determine minimal NRMSE_m of the current layer.

end

coarse λ-range: $\lambda_{m,1} = \lambda_{m,\mathrm{min}}$ and $\lambda_{m,100} = \lambda_{m,\mathrm{max}}$

Minimal NRMSE_m with related $\lambda_{m,i}$ indicates the defect depth by the
corresponding layer m.

2. Defect shape estimation at determined defect layer m:

for $j = 1$ **to** 100 **do**

    Determination of:

    Continuous $\vec{\theta}_j$ by (3.8) with λ_j and $\gamma = 6 \cdot 10^{-5}$

    $\vec{\theta}_{\mathrm{th},j}$ by (3.4) with $t_{\mathrm{h}} = 0.125$

    $\Delta \vec{F}_j^{\mathrm{AFS}}$ by (2.27) with $\vec{\theta}_{\mathrm{th},j}$

    NRMSE_j by (3.5) with $\Delta \vec{F}_j^{\mathrm{AFS}}$

end

fine λ-range: $\lambda_1 = \lambda_{m,i-1}$ and $\lambda_{100} = \lambda_{m,i+1}$

Minimal NRMSE_j with related $\vec{\theta}_{\mathrm{th},j}$ contains information about location, size
and shape of the reconstructed defect.

3.2.5 Reconstruction Results

Simulations   The MNE with ENR and TPR applied to the simulated data sets
yields correct defect depth detection for the depths of 2, 4 and 8 mm (Table 3.1 and
Fig. 3.10). Table 3.1 shows that the defect reconstruction error measures (section 3.2.2)
are identical for ENR and TPR, except for $d = 8$ mm. The four additional voxels for
TPR at $d = 8$ mm are located at the left and right edges of the reconstruction region.

All centers of the defects are correctly reconstructed at $x = y = 0$. The extension x_e in x-direction is correct. The defect extension y_e in y-direction is two voxels too large (Table 3.1), which relates to 3 additional voxels in each positive and negative y-direction. These additional voxels and the mismatch of a round defect and the voxel approximation lead to a size error a_d of $11.37\,\mathrm{mm}^2$.

The regularization parameters λ of ENR (Table 3.1) decrease with increasing defect depth. The determined λ for TPR also decrease with increasing defect depth. While ENR uses the fixed thresholding factor $t_h = 0.125$, the found thresholding factors in TPR are different for the three defect depths (Table 3.1). The NRMSE values for $d = 2$, 4 and $8\,\mathrm{mm}$ increase from $4.83\,\%$, $5.25\,\%$ to $6.32\,\%$ for both ENR and TPR but the defect reconstruction quality reflected by the error measures remains the same for defect depths $d = 2$, 4 and $8\,\mathrm{mm}$, except for TPR and $d = 8\,\mathrm{mm}$ (Table 3.1) .
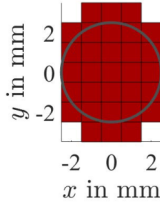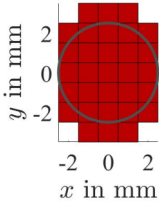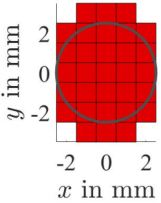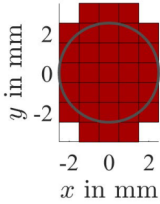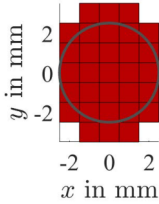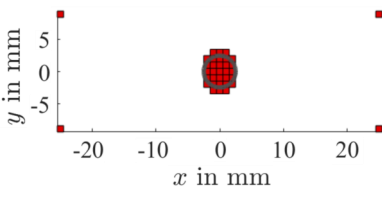
The reconstructed defects of each layer, color-coded according to their NRMSE, are shown in Fig. 3.10. The NRMSE values of the correct layer and the neighboring layers are close to each other.

Measurements   The defect reconstruction results by ENR and TPR of 25 trials are shown in Table 3.2. The visualizations of reconstructed defects show how often one voxel is reconstructed, where a frequency value of 25 represents a reconstruction in all 25 trials.

ENR yields correct depth detection for the defect depths 2, 4 and $8\,\mathrm{mm}$ (Table 3.2 and Fig. 3.11). Whereas TPR shows correct depth estimation for 2 and $4\,\mathrm{mm}$ and in 17/25 cases for $d = 8\,\mathrm{mm}$. The centers of the reconstructed defect are slightly shifted. This shift in mainly negative y-direction is below $1\,\mathrm{mm}$ for both ENR and TPR, reflected by the Euclidean distance d_0. The mean defect extensions x_e (Table 3.2, top) obtained by ENR in x-direction are slightly too small, and slightly too large for TPR (Table 3.2). For both, ENR and TPR, the defect extensions y_e are a bit too large (Table 3.2). This leads to mean size errors a_d between $7.41\,\mathrm{mm}^2$ and $14.01\,\mathrm{mm}^2$ for ENR and TPR. For one trial with $d = 8\,\mathrm{mm}$ TPR reconstructs a larger defect (blue voxels, Table 3.2) compared to the other trials.

The found optimal regularization parameters λ of ENR decrease with increasing defect depth as observed for the simulated data sets (Table 3.1). The corresponding standard deviations are small (Table 3.2). In contrast, the standard deviations of the regularization parameters λ found for TPR are relatively large. This reflects the results of the parameter studies (section 3.2.3) that no optimal region of λ can be found. The found mean thresholding factors are equal for different defect depths at $t_h = 0.99$. In accordance to simulation data, see Table 3.1, the mean NRMSE values increase for increasing defect depth for both ENR and TPR.

Table 3.1: Results of defect reconstruction of simulated data with elastic net regularization and Tikhonov-Phillips-regularization: The correct depth estimation was obtained with both regularization methods, where for $d = 8\,\text{mm}$ and Tikhonov-Phillips-regularization four additional defect voxels are reconstructed. The circle indicates the shape of the true defect. The color-coding corresponds to Fig. 3.10.

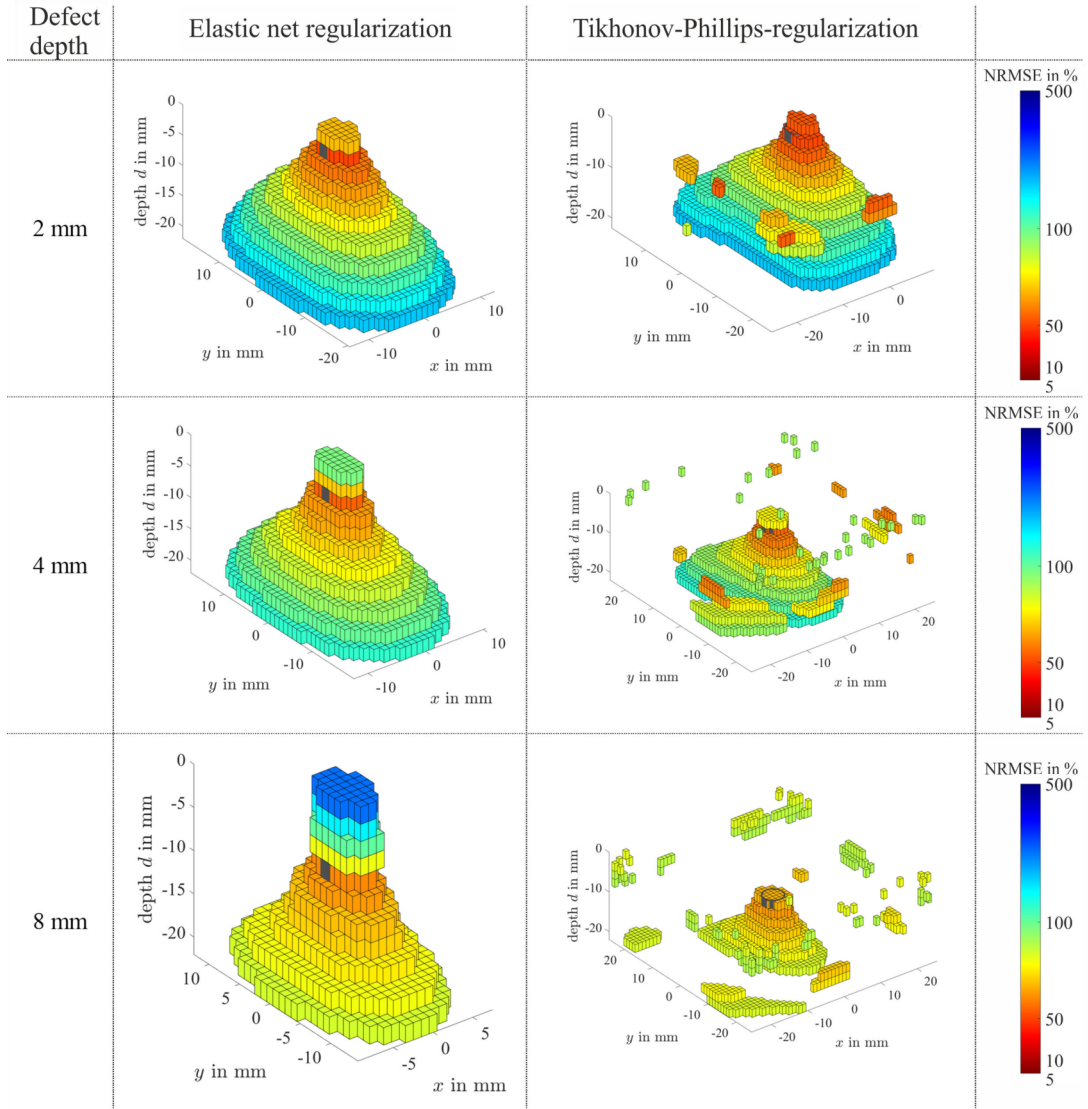|	**Elastic net regularization**		
Defect depth d in mm	2	4	8
Reconstruction at the layer of the defect			
Regularization parameter λ	$3.03 \cdot 10^{-5}$	$6.44 \cdot 10^{-6}$	$4.97 \cdot 10^{-7}$
Reconstructed depth in mm	2	4	8
Euclidean distance d_0 from $[0,0]$ in mm	0	0	0
Size in mm^2	31	31	31
Size difference in mm^2	11.37	11.37	11.37
x-extension x_e in mm	5	5	5
y-extension y_e in mm	7	7	7
NRMSE in %	4.83	5.25	6.35
	Tikhonov-Phillips-regularization		
Defect depth d in mm	2	4	8
Reconstruction at the layer of the defect			
Thresholding factor t	0.29	0.51	0.89
Regularization parameter λ	$1.13 \cdot 10^{-9}$	$1.86 \cdot 10^{-10}$	$1.59 \cdot 10^{-11}$
Reconstructed depth in mm	2	4	8
Euclidean distance d_0 from $[0,0]$ in mm	0	0	0
Size in mm^2	31	31	35
Size difference in mm^2	11.37	11.37	15.37
x-extension x_e in mm	5	5	5
y-extension y_e in mm	7	7	7
NRMSE in %	4.83	5.25	6.32
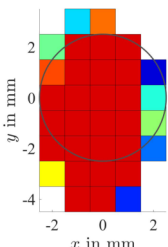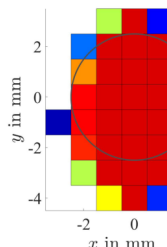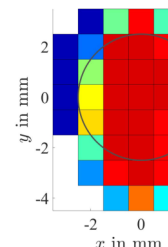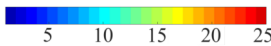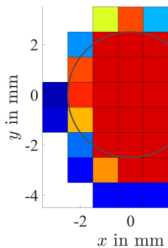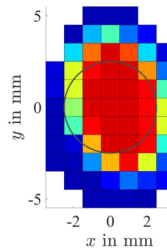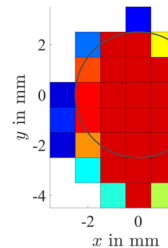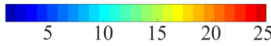
Figure 3.10: Defect reconstruction results color-coded by NRMSE of the analyzed layers for simulated data sets with defects at $d = 2$, 4 and 8 mm depth achieved by elastic net regularization (left column) and Tikhonov-Phillips-regularization (right column). The gray cylinder indicates the position and shape of the true defect. The correct depth can be detected for both regularization methods and all three defect depths. The region around the minimal NRMSE (red hotspot) is represented by similar colors, which illustrates the ill-posed character of the problem. For $d = 8$ mm additional outer voxels are reconstructed with Tikhonov-Phillips-regularization (right column, bottom) for the metal layers 5 and 6. The top views of defect reconstruction results are shown in Table 3.1.

Table 3.2: Results of defect reconstruction of measured data with elastic net regularization and Tikhonov-Phillips-regularization: The reconstructed defect and corresponding defect reconstruction error parameters are shown as mean $\pm$ standard deviation for the correct defect depth. The circle indicates the shape of the true defect. Elastic net regularization detected correct depth for $d = 2$, 4 and 8 mm, whereas Tikhonov-Phillips achieves correct detection for $d = 2$ and 4 mm and for 17/25 cases for $d = 8$ mm. Wrong reconstructed depths and the corresponding NRMSE are indicated by asterisks.

Elastic net regularization			
Defect depth d in mm	2	4	8

Frequency of reconstructed voxels

Regularization parameter λ	$7.08 \cdot 10^{-4} \pm 4.48 \cdot 10^{-6}$	$2.38 \cdot 10^{-4} \pm 1.69 \cdot 10^{-6}$	$2.86 \cdot 10^{-5} \pm 3.21 \cdot 10^{-7}$
Reconstructed depth in mm	2.00 ± 0.00	4.00 ± 0.00	8.00 ± 0.00
Euclidean distance d_0 from $[0,0]$ in mm	0.76 ± 0.08	0.64 ± 0.09	0.62 ± 0.23
Size in mm^2	27.76 ± 0.52	28.36 ± 0.70	27.04 ± 0.61
Size difference in mm^2	8.13 ± 0.52	8.73 ± 0.70	7.41 ± 0.61
x-extension x_e in mm	4.56 ± 0.51	4.80 ± 0.41	4.40 ± 0.50
y-extension y_e in mm	7.88 ± 0.33	8.00 ± 0.00	7.88 ± 0.33
NRMSE in %	10.27 ± 0.14	11.33 ± 0.14	14.34 ± 0.23

Tikhonov-Phillips-regularization			
Defect depth d in mm	2	4	8

Frequency of reconstructed voxels

Thresholding factor t	0.99 ± 0.01	0.99 ± 0.01	0.99 ± 0.00
Regularization parameter λ	$1.92 \cdot 10^{6} \pm 5.47 \cdot 10^{6}$	$8.51 \cdot 10^{6} \pm 2.05 \cdot 10^{7}$	$1.87 \cdot 10^{6} \pm 3.34 \cdot 10^{6}$
Reconstructed depth in mm	2.00 ± 0.00	4.00 ± 0.00	8.72 ± 1.14*
Euclidean distance d_0 from $[0,0]$ in mm	0.88 ± 0.16	0.43 ± 0.28	0.64 ± 0.36
Size in mm^2	27.68 ± 0.56	28.68 ± 1.25	33.64 ± 10.22
Size difference in mm^2	8.05 ± 0.56	9.05 ± 1.25	14.01 ± 10.22
x-extension x_e in mm	5.08 ± 0.40	5.16 ± 0.37	5.40 ± 0.87
y-extension y_e in mm	7.12 ± 0.33	7.00 ± 0.00	7.64 ± 0.99
NRMSE in %	10.37 ± 0.15	11.50 ± 0.20	16.63 ± 4.56 (14.88 ± 0.85)*

Figure 3.11: Defect reconstruction results color-coded by NRMSE of the analyzed layers for measured data sets (trial no. 1) with defects at $d = 2$, 4 and 8 mm depth achieved by elastic net regularization (left column) and Tikhonov-Phillips-regularization (right column). The gray cylinder indicates the position and shape of the true defect. Additional outer voxels are reconstructed for all three defect depths with Tikhonov-Phillips-regularization. The top views of defect reconstruction results are shown in Table 3.2.

The reconstructed defects of each layer for trial 1 are shown in Fig. 3.11, color-coded according to their NRMSE. The ENR (Fig. 3.11, left column) shows connected structures comparable to the results of simulated data sets (Fig. 3.10, left column). In contrast, TPR (Fig. 3.11, right column) shows the reconstruction of additional voxels outside the expected region of the defect as well as the reconstruction of spread single voxels in upper metal layers for defect depths 4 and 8 mm.

In order to investigate the influence of an improved SNR (Fig. 3.5), the defect reconstructions by ENR and TPR were applied for the averaged DRSs with defect depths

$d = 2$, 4 and 8 mm for 25 trials.

ENR detected the correct defect depths for three defect depths. The defect error measures are in accordance with reconstruction results from single trials (Table 3.2).

TPR also detects the correct defect depth for all three depths using the averaged DRSs. The reconstruction results for the defect depths $d = 2$ mm and 4 mm are in accordance with the single reconstruction results (Table 3.2). For $d = 8$ mm the size error $a_{\mathrm{d}} = 7.37 \, \mathrm{mm}^2$ and the NRMSE= 13.94 % are reduced (compared to Table 3.2).

3.2.6 Discussion

The MNE with ENR achieves correct depth and adequate size estimations of cylindrical shaped defects at depths of $d = 2$, 4 and 8 mm for simulations and measurements. The reproducibility of LFE is indicated by stable reconstruction results from single trials (Table 3.2).

The MNE with TPR achieves comparable results with the exception for $d = 8$ mm, where the defect depth is detected correctly only for 17 of 25 trials (Table 3.2). Additionally, TPR partly reconstructs spurious voxels outside the expected region (Fig. 3.10 and 3.11).

Both inverse methods use the AFS as forward solution, which is a simplified model of the DRS. This simplification might partly explain that the defect sizes are estimated slightly too large. However, this forward solution allows the application of the fast MNE with ENR, which achieved reproducible reconstruction results and correct depth estimations. The use of the weak reaction approach, i.e. the neglection of the secondary magnetic field, is not expected to influence the defect reconstruction results considerably. The NRMSE of the DRS calculated by FEM with the weak reaction approach compared to the DRS calculated by FEM with the transient moving magnet approach [32] equals 0.69 % for the simulation setup described in section 3.2.1.

In terms of computational time, the calculation of a single vector of $\vec{\theta}_{\mathrm{th}}$, see (3.4), is between 0.5 and 3 s for TPR and ENR. Calculations have been performed using MATLAB® R2015b with an Intel® Core™ i7-4790K processor and 32 GB of RAM. The performance of ENR and TPR could be improved further by algorithmic enhancements.

In contrast to previous work [10, 17, 19], a correct depth estimation could be achieved for all investigated cases. In this study, LFE was able to reconstruct deep defects at $d = 8$ mm.

In comparison, deep defects in eddy current testing can be detected using a low-frequency setup with highly sensitive magnetic field sensors such as fluxgate [46], SQUID [47], anisotropic magnetoresistive (AMR) [48] or GMR [49] sensors. These setups might be also capable for estimating the size, shape and location of the defect.

In other setups of motion induced eddy current testing [11–14], the secondary mag-

netic field from the induced eddy currents is used to detect surface and sub-surface defects in conducting specimen.

3.2.7 Summary and Conclusions

The MNE with ENR shows correct depth and adequate size estimation of a cylindrical shaped defect for simulation and measurements. The reproducibility of LFE has been shown by the investigation of single measurement trials. TPR shows comparable defect reconstruction results. ENR slightly outperforms TPR in reconstruction of deep defects from single trials.

The derived control parameters as well as the defect reconstruction schemes in TPR and ENR are considered as generalizable for further LFE measurements. Nevertheless, in future work the principles of the sensitivity [129] and the uncertainty analysis [130] could be considered to assess the sensitivity of the selected optimal parameters.

3.3 Eddy Current Evaluation

3.3.1 Setup

Problem description   A planar coil (Fig. 3.12) is excited with a sinusoidal current I_e of frequency f_e. The related magnetic field induces eddy currents in the aluminum specimen under test. The induced eddy currents $\vec{j}$ lead to a secondary magnetic field $\vec{b}_s$. In presence of a defect, the eddy currents and the corresponding secondary magnetic field are perturbed. The excitation coil is located δz above the top surface of the specimen. The total magnetic field in x-direction B_x is measured by a GMR sensor. The probe
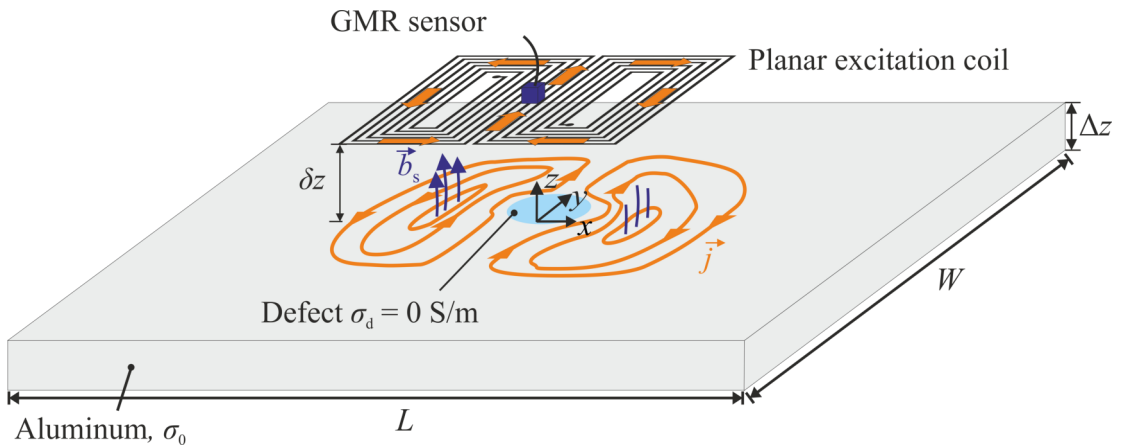
Figure 3.12: Problem setup: A planar coil excited with a sinusoidal current lead to induced eddy currents (orange lines) in the aluminum specimen, generating the secondary magnetic field $\vec{b}_s$. The total magnetic field is sensed by a GMR sensor.

is placed at several observation points in x- and y-direction above the specimen. The
amplitude and the phase shift of the sinusoidal B_x at each position are determined by a
sine fitting algorithm. The obtained magnetic flux density can be represented as complex
number $\underline{B_x}$. In order to get the magnetic field perturbation (MFP) $\underline{\Delta b_x}$ from $\underline{B_x}$, the
uniform offset is subtracted, determined from an area where no perturbation from the
defect is visible (section 2.2.1).

Simulations   The simulations are carried out by FEM as described in section 2.2.2.
The simulated data sets act as noise free benchmark signals to asses the general prop-
erties of the applied inverse methods before the application to measurement data.

In a first setup, a planar coil is located $\delta z = 0.5\,\mathrm{mm}$ above an aluminum plate
with dimensions $L \times W \times \Delta z = 180\,\mathrm{mm} \times 150\,\mathrm{mm} \times 1\,\mathrm{mm}$. The central region of
the coil (Fig. 3.13, blue) is excited with a uniform current density of $270\,\mathrm{A/m}$. The
surrounding regions (Fig. 3.13, orange) are imposed with $500\,\mathrm{A/m}$ such that the current
loop closes. The used sinusoidal excitation frequency is $f_\mathrm{e} = 5\,\mathrm{kHz}$. A star-shaped defect
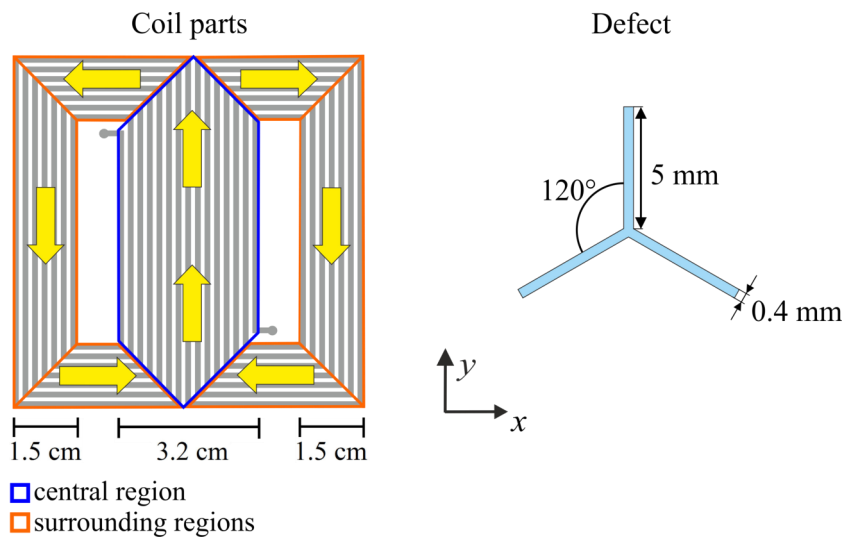
Figure 3.13: Excitation coil parts and star-shaped defect.

(Fig. 3.13) is located in the center region of the aluminum plate, characterized by a defect
height of $h_\mathrm{d} = 1\,\mathrm{mm}$. Two excitation directions are applied, where the excitation in x-
direction is referred to as 0°-excitation, the excitation in y-direction as 90°-excitation.
The observation points are located at $z = 1.7\,\mathrm{mm}$ above the top surface of the specimen
with $|x| \leq 14.4\,\mathrm{mm}$ and $|y| \leq 14.4\,\mathrm{mm}$ around the center of the defect. The distances
between these points in x- and y-direction are $d_x = d_y = 0.4\,\mathrm{mm}$. Fig. 3.14 shows the
real and the imaginary components of the obtained MFP $\underline{\Delta b_x}$ for 0°- and 90°-excitation.

The second simulation setup is used for qualitative comparison to LFE (section 3.2).
A cylindrical shaped defect is located at a depth of $d = 1\,\mathrm{mm}$, where d describes the
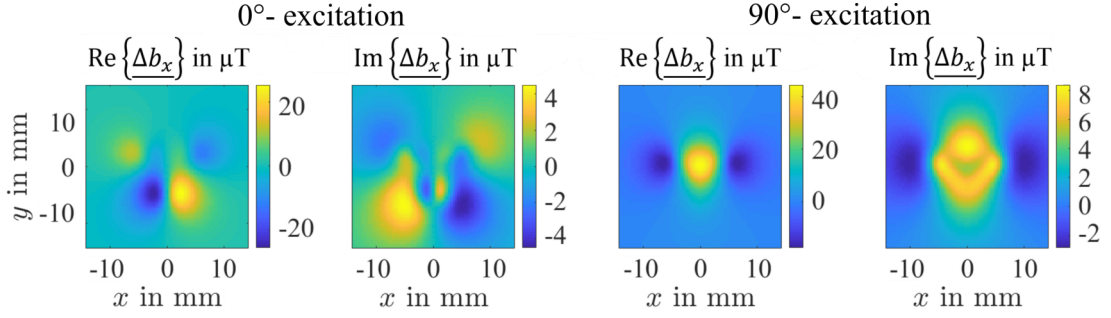
Figure 3.14: Real and imaginary part of the perturbation magnetic flux density component $\underline{\Delta b_x}$ in µT in the vicinity of the star-shaped defect obtained by FEM simulations for 0°- and 90°-excitation.
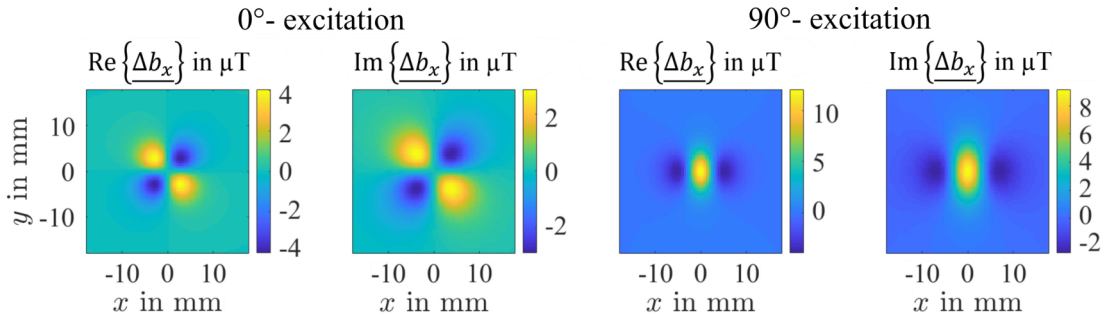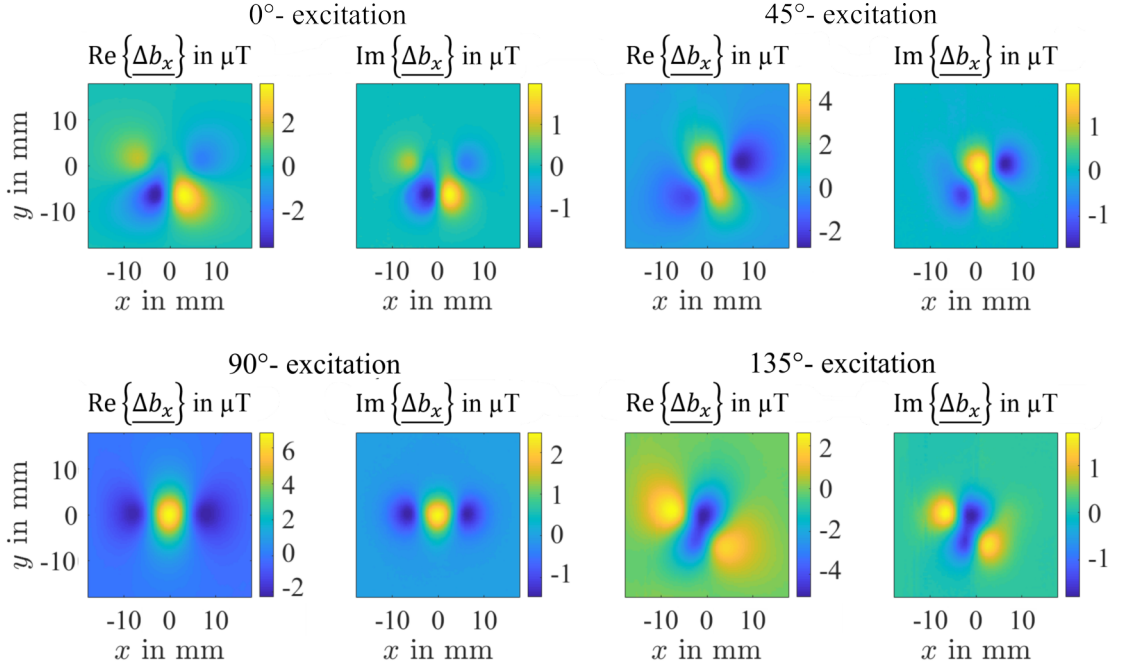

Figure 3.15: Real and imaginary part of the perturbation magnetic flux density component $\underline{\Delta b_x}$ in µT in the vicinity of the cylindrical shaped defect obtained by FEM simulations for 0°- and 90°-excitation.

z-distance of the top surface of the specimen to the top surface of the crack. The defect is characterized by a diameter $D_\mathrm{d} = 5\,\mathrm{mm}$ and a height $H_\mathrm{d} = 1\,\mathrm{mm}$. The aluminum specimen has dimensions of $L \times W \times H = 360\,\mathrm{mm} \times 300\,\mathrm{mm} \times 5\,\mathrm{mm}$. A planar coil is located $\delta z = 0.5\,\mathrm{mm}$ above the top surface of the specimen. The coil is imposed with an excitation current of $I_\mathrm{e} = 2.4\,\mathrm{A}$. The used excitation frequency is $f_\mathrm{e} = 2\,\mathrm{kHz}$. Consecutive observation points have a distance of $d_x = d_y = 0.5\,\mathrm{mm}$ and are located at $z = 2\,\mathrm{mm}$ above the top surface of the specimen with $|x| \leq 18\,\mathrm{mm}$ and $|y| \leq 18\,\mathrm{mm}$. Fig. 3.15 shows the real and the imaginary components of $\underline{\Delta b_x}$ for 0°- and 90°-excitation.

Measurements In a first setup (Fig. 3.16 a), a conducting specimen is scanned with steps of $d_x = d_y = 0.5\,\mathrm{mm}$ over a region of $45\,\mathrm{mm} \times 45\,\mathrm{mm}$ around the position of the star-shaped crack (Fig. 3.16 a). The specimen with dimension $L \times W \times H = 250\,\mathrm{mm} \times 250\,\mathrm{mm} \times 4\,\mathrm{mm}$ consists of four stacked aluminum sheets, each of thickness $\Delta z = 1\,\mathrm{mm}$. One aluminum sheet contains a star-shaped defect (Fig. 3.16 a), similar to the one used in FEM simulations (Fig. 3.13). Four different defect depths are analyzed by changing the position of the plate with the defect from layer 1 (top layer) to layer 2, 3 and layer 4 (bottom layer). The double coil planar probe (section 2.2.3) is used
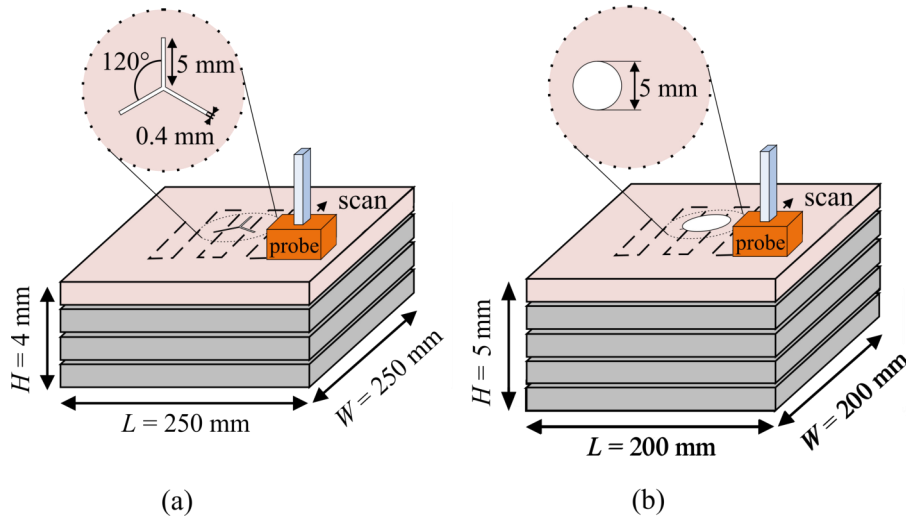
Figure 3.16: Measurement setups: (a) First setup: A scan with the double coil planar ECE probe is performed to evaluate the stack of aluminum sheets with one containing a star-shaped defect [50], (b) Second setup: A scan with the single coil planar ECE probe is performed to evaluate the stack of aluminum sheets with one containing a cylindrical shaped defect.

for inducing eddy current in the specimen. For every probe position 100 periods of the excitation current and the measured output sensor voltages are acquired for each of the four excitation modes 0°, 45°, 90° and 135°. The amplitude and phase are determined by a sine-fitting algorithm. The amplitudes are converted from voltage into Tesla units. Maps of complex numbers are generated using the amplitudes and the phase shift between GMR and excitation signals. In order to obtain the MFP $\underline{\Delta b_x}$, the uniform complex offset is subtracted using an observation point where no influence of the defect is visible. Fig. 3.17 shows the real and the imaginary part of $\underline{\Delta b_x}$ for the excitation angles with the defect located at the top aluminum layer. These signals act as input for the defect reconstruction schemes described in sections 3.3.3 and 3.3.4.

In the second setup (Fig. 3.16 b), that acts for qualitative comparison with the LFE (section 3.2), a specimen of five stacked aluminum sheets, each of thickness $\Delta z = 1 \, \text{mm}$, is investigated. Each aluminum plate is characterized by a size of $L \times W = 200 \, \text{mm} \times 200 \, \text{mm}$. One plate contains a hole, representing the cylindrical shaped defect of diameter $D_\text{d} = 5 \, \text{mm}$ and height $H_\text{d} = 1 \, \text{mm}$. By changing the position of the plate containing the hole, defect depths of $d = 1$, 2 and 4 mm are investigated. The coil of the single planar probe is located $\delta z = 1 \, \text{mm}$ above the top surface of the specimen. The GMR sensor is located 1 mm above. It senses the magnetic field component B_x at several observation points between $|x| \leq 18 \, \text{mm}$ and $|y| \leq 18 \, \text{mm}$. Consecutive measurement points have a distance of $d_x = d_y = 0.5 \, \text{mm}$. Two measurement scans are carried out by the excitation coil oriented for 0°- and 90°-excitation, while the GMR sensor sensitivity axis is kept in

Figure 3.17: Real and imaginary part of the perturbation magnetic flux density component $\underline{\Delta b_x}$ in µT obtained from measurements in the vicinity of the star-shaped defect located in the top aluminum layer for 0°-, 45°-, 90°- and 135°-excitation.

x-direction. It is assumed that the defect depth is known, e.g. determined in advance by a multi-frequency [131] or pulsed [132] eddy current evaluation method. According to [51], the used forward solution in ECE (section 2.2.4) is not capable for estimating the defect depth by solving an inverse problem. As the defect depth is assumed to be known, the used excitation frequency f_e is chosen based on the standard depth of penetration [8]

$$\delta \approx \frac{1}{\sqrt{\pi f_e \mu \sigma_0}} \rightarrow f_e \approx \frac{1}{\delta^2 \pi \mu \sigma_0}, \tag{3.10}$$

where $\mu \approx \mu_0$ denotes the magnetic permeability and $\sigma_0 = 35\,\mathrm{MS/m}$ the conductivity of the aluminum plates. The distance from the top surface of the aluminum specimen to the bottom of the defect is considered as penetration depth δ that should be achieved for getting an appropriate MFP $\underline{\Delta b_x}$. For the analyzed defect depths $d = 1$, 2 and 4 mm, the desired penetration depths are equal $\delta = 2\,\mathrm{mm}$, 3 mm and 5 mm. According to (3.10), the related excitation frequencies are 1809 Hz, 804 Hz and 289 Hz. For the measurement setup, the smooth values of 2 Hz, 800 Hz and 400 Hz have been used for excitation. The excitation frequency at the defect depth $d = 4\,\mathrm{mm}$, was increased to 400 Hz as for 300 Hz no usable MFP signal $\underline{\Delta b_x}$ could be extracted anymore. Fig. 3.18 shows the real and the imaginary component of the MFP $\underline{\Delta b_x}$ for the excitation angles 0° and 90° for the cylindrical defect located at $d = 1$, 2 and 4 mm.
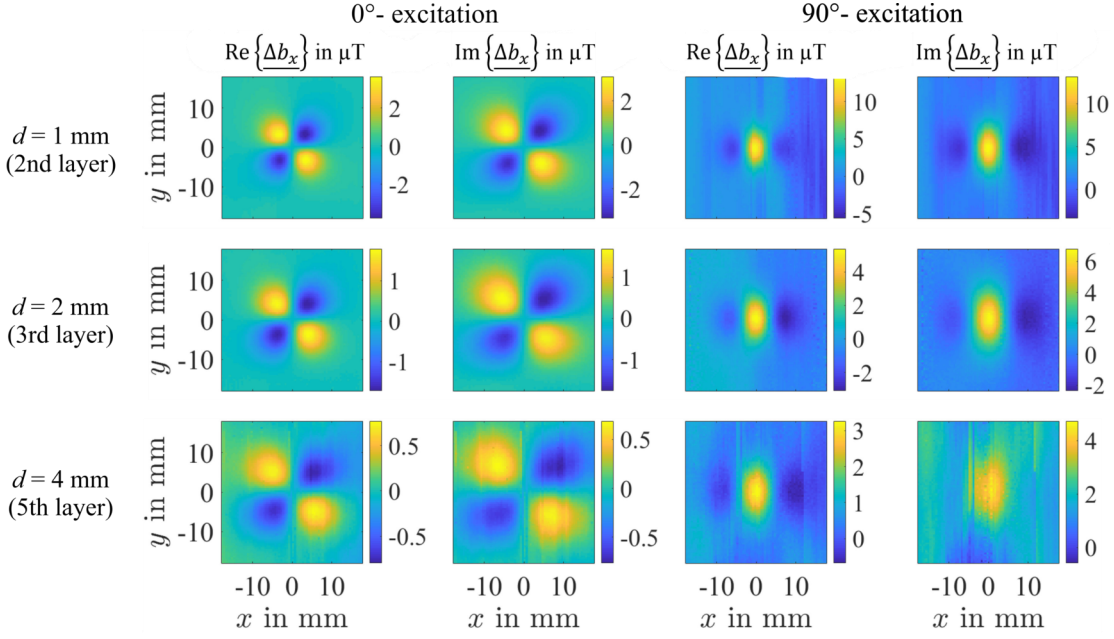
Figure 3.18: Real and imaginary part of the MFP $\underline{\Delta b_x}$ in µT obtained from measurements in the vicinity of the cylindrical shaped defect at the depths $d = 1$, 2 and $4\,\mathrm{mm}$ for 0°- and 90°-excitation.

3.3.2 Minimum Norm Estimation

The defect properties should be reconstructed from the MFP $\underline{\Delta b_x}^{\mathrm{FEM/meas}}$ obtained from simulations (Fig. 3.14 and Fig. 3.15) and measurements (Fig. 3.17 and Fig. 3.18). $\underline{\Delta b_x}^{\mathrm{FEM/meas}}$ with N observation points is arranged in a vector $\underline{\vec{\Delta b}_x}^{\mathrm{FEM/meas}} \in \mathbb{C}^{N \times 1}$.

It is assumed that the defect depth is known, e.g. obtained by another method in advance [131, 132]. The corresponding metal layer is discretized in x- and y-direction within a region of interest (ROI) into M square eddy current loops with center points $[x(i,j), y(i,j)]$. The neighboring currents loops are Δx and Δy apart from each other. The inverse problem in ECE can be formulated as a MNE problem

$$\underset{\underline{\vec{I}_d} \in \mathbb{C}^{M \times 1}}{\arg \min} \frac{1}{2} \left\| \underline{\vec{\Delta b}_x}^{\mathrm{FEM/meas}} - \underbrace{[L]\underline{\vec{I}_d}}_{\underline{\vec{\Delta b}_x}^{\mathrm{BS}}} \right\|_2^2 , \tag{3.11}$$

where a square eddy current loop vector $\underline{\vec{I}_d}$ (section 2.2.4) has to be found that minimizes the deviation between $\underline{\vec{\Delta b}_x}^{\mathrm{FEM/meas}}$ and the forward calculated $\underline{\vec{\Delta b}_x}^{\mathrm{BS}}$. The lead field matrix $[L] \in \mathbb{R}^{N \times M}$ contains the Biot-Savart law (section 2.2.4). The obtained vector $\underline{\vec{I}_d}$ is post-processed as described in section 2.2.4 such that a qualitative estimation of the total 2D eddy current density distribution with $\vec{j}(i,j) = [\underline{j_x}(i,j)\ \underline{j_y}(i,j)]^{\mathrm{T}}$ at the points of the ROI can be used to investigate the defect shape and location. In order to

combine the reconstruction results from measurements of different excitation angles and to increase the comprehensibility, the absolute value $\left|\vec{\underline{j}}(i,j)\right|$ at each point of the ROI is calculated by

$$\left|\vec{\underline{j}}(i,j)\right| = \left|\sqrt{\underline{j_x}(i,j)^2 + \underline{j_y}(i,j)^2}\right|. \tag{3.12}$$

For improved qualitative interpretation, the obtained current density norm map is normalized between 0 and 1. Regions with 0, i.e. without current flow, indicate defect regions. All normalized current density norm maps obtained from several measurements out of different excitation angles are averaged.

Fig. 3.19 illustrates the described post-processing (section 2.2.4) for real valued variables due to visualization purposes. A square current loop amplitude map I_d leads to the planar perturbation eddy current density distribution $\Delta\vec{j}$ according to (2.47). A uniform eddy current density $\vec{j_0}$ is determined from the center between the two vortices and subtracted from the whole distribution. The obtained eddy current density distribution $\vec{j}$ gives a first qualitative impression of the eddy current flow. With the calculation of the
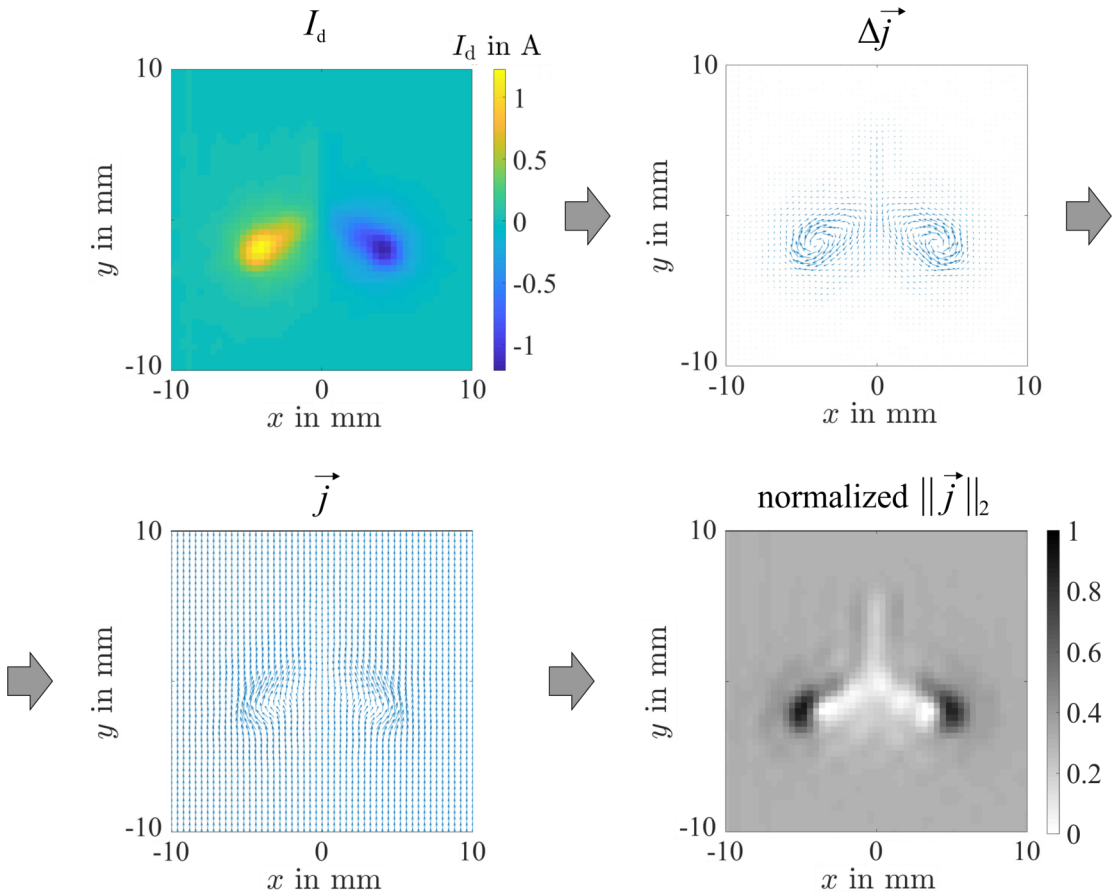
Figure 3.19: Principle of post-processing of a determined square current loop map I_d with the conversion into perturbation eddy current density map $\Delta\vec{j}$ according to (2.47), the estimation of the total eddy current density distribution $\vec{j}$ and the determination of the normalized map $\left\|\vec{j}\right\|_2$ to evaluate the defect shape.

norm map according to (3.12) and the normalization between 0 and 1, the underlying
defect shape becomes visible. White areas belong to the defect where no current flows.
Black areas illustrate the high current density close to defect edges.

3.3.3 Tikhonov-Phillips-Regularization

In comparison to LFE (section 3.2.3), the MNE with TPR of zeroth order [128] is used
for the application in ECE. It is defined as

$$\underset{\underline{\vec{I_d}} \in \mathbb{C}^{M \times 1}}{\arg\min} \left(\underbrace{\frac{1}{2} \left\| \Delta \vec{b}_x^{\,\mathrm{FEM/meas}} - [L]\underline{\vec{I_d}} \right\|_2^2}_{\text{Data term}} + \lambda \underbrace{\left\| \underline{\vec{I_d}} \right\|_2^2}_{\text{Regularization term}} \right). \tag{3.13}$$

This leads to the closed solution for $\underline{\vec{I_d}}$ with

$$\underline{\vec{I_d}} = [L]^{\mathrm{T}} \left[[L][L]^{\mathrm{T}} + \lambda[I] \right]^{-1} \Delta\vec{b}_x^{\,\mathrm{FEM/meas}}. \tag{3.14}$$

The regularization parameter λ controls how much the solution $\underline{\vec{I_d}}$ depends on the regularization term. The obtained vector $\underline{\vec{I_d}}$ is smooth with continuous values, where elements
with zero are unlikely. The optimal regularization parameter λ has to be determined.
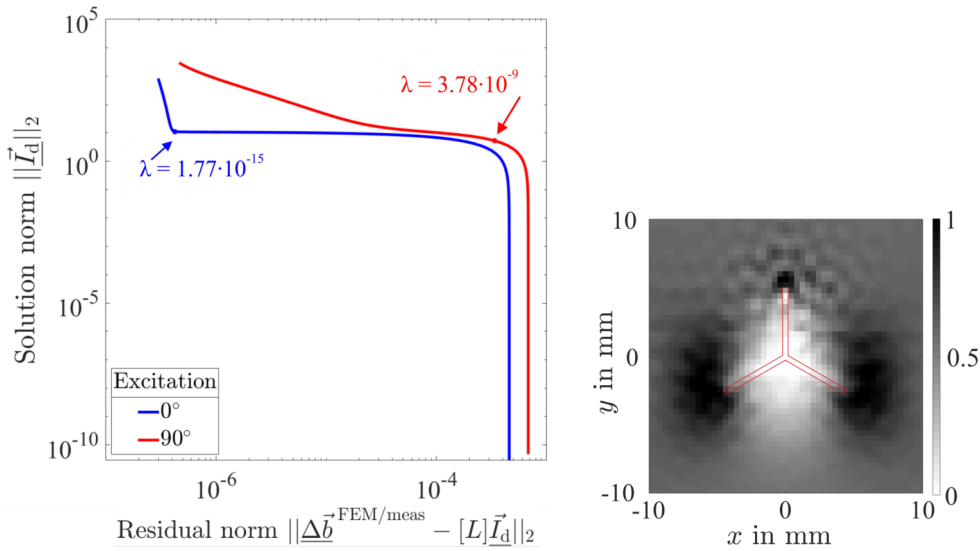
(a) Curves of solution norm in dependence of the residual norm for the investigated λ-values for 0°- (blue) and 90°-excitation (red) for the simulation setup with the star-shaped crack. The curve of 0°-excitation shows a L-shape.

(b) Corresponding normalized current density norm map obtained from the two excitation directions using the λ-values indicated in (a). The red contour indicates the star-shaped crack.

Figure 3.20: Determination of the optimal regularization parameter λ for MNE with TPR in ECE for (3.14).

For that purpose, the L-curve criterion [83] is intended to be used. The simulation setup with the star-shaped crack is chosen as reference setup. Fig. 3.20 a shows the corresponding curves for the two excitation directions 0° and 90° for regularization parameters λ between 10^{-20} to 1000. It can be observed that the curve for 0°-excitation (Fig. 3.20 a, blue) shows a L-curved shape, but the one for 90° does not (Fig. 3.20 a, red). In consequence, the choice of the optimal regularization parameter λ can not be determined by choosing the point with the maximal curvature, i.e. the corner of the L-curve, according to L-curve criterion. Fig. 3.20 b shows the corresponding derived normalized current density norm map if the L-curve criterion is applied anyway. The star-shaped character of the defect is not clearly visible (Fig. 3.20 b).

Auxiliary formulation of the MFP In order to solve this problem, the idea is to reduce the degrees of freedom. For that purpose, instead of the complex valued MFP vector $\underline{\Delta \vec{b}_x}^{\text{FEM/meas}}$, a novel modified MFP vector is created by

$$\Delta \vec{b}_x^{\text{FEM/meas}} = \text{Re}\left\{\underline{\Delta \vec{b}_x}^{\text{FEM/meas}}\right\} + \text{Im}\left\{\underline{\Delta \vec{b}_x}^{\text{FEM/meas}}\right\}. \tag{3.15}$$

This leads to a real valued input for the MNE with TPR. In consequence, the estimated square current loop vector $\vec{I}_d$ contains real valued amplitudes. This means, that the
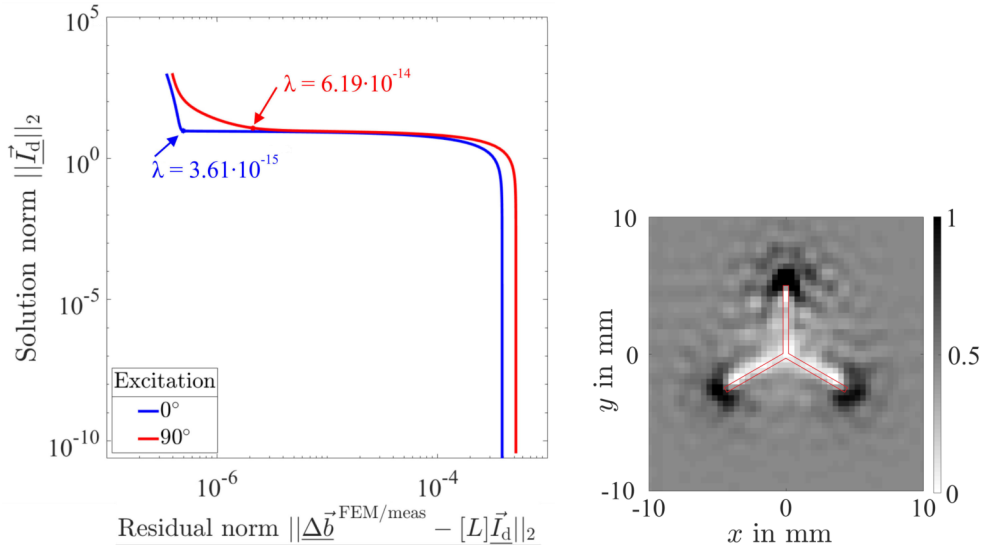
(a) Curves of solution norm in dependence of the residual norm for the investigated λ-values for 0°- (blue) and 90°-excitation (red) for the simulation setup with the star-shaped crack. Both curves show a L-shape.

(b) Corresponding normalized current density norm map obtained from the two excitation directions using the λ-values indicated in (a). The red contour indicates the star-shaped crack.

Figure 3.21: Determination of the optimal regularization parameter λ for MNE with TPR in ECE for the auxiliary formulation (3.16).

degrees of freedom are reduced with the formulation in (3.16) and only one amplitude for
each point in the ROI has to be estimated for $\vec{I}_d$. In contrast, with the formulation (3.14),
a real and an imaginary part have to be estimated for each point of $\vec{I}_d$. Additionally,
the auxiliary $\vec{b}_x^{\mathrm{FEM/meas}}$ is beneficial for the following MNE with ENR (section 3.3.4)
that requires real valued input. The closed solution of (3.14) is modified to the auxiliary
formulation

$$\vec{I}_d = [L]^{\mathrm{T}} \left[[L][L]^{\mathrm{T}} + \lambda[I] \right]^{-1} \Delta\vec{b}_x^{\mathrm{FEM/meas}}. \tag{3.16}$$

Fig. 3.21 a shows the solution norm in dependence of the residual norm for the two
excitation directions $0°$ and $90°$ obtained from (3.16). Now, for both excitation directions
a L-shaped curve is observable. The determined optimal positions with corresponding
λ are marked with arrows. The derived normalized current density norm map is shown
in Fig. 3.21 b. It shows the advantage of the auxiliary formulation in comparison to
(3.14), where the corresponding normalized current density norm map shows a worse
representation of the star-shaped crack (Fig. 3.20 b). In conclusion, the auxiliary MFP
$\Delta\vec{b}_x^{\mathrm{FEM/meas}}$ according to (3.15) is chosen for this study.

3.3.4 Elastic Net Regularization

Principle   It is known *a priori* that the current square loops vector $\vec{I}_d$ contains
several zeros (Fig. 3.19). The regularization with the L2-norm term enables a spatially
smooth solution $\vec{I}_d$ [87]. To privilege zero-values in $\vec{I}_d$, the L1-norm term is added.
This regularization method is referred to as ENR. The MNE with ENR is solved by
a coordinate descent algorithm that requires real valued input. Thus, the auxiliary
formulation of the MFP $\Delta\vec{b}^{\mathrm{FEM/meas}}$ (3.15) is used. In consequence, the MNE (3.11)
with ENR [107] in ECE can be formulated as

$$\underset{\vec{I}_d \in \mathbb{R}^{M \times 1}}{\arg\min} \left(\underbrace{\frac{1}{2N} \left\| \Delta\vec{b}_x^{\mathrm{FEM/meas}} - [L]\vec{I}_d \right\|_2^2}_{\text{Data term}} + \lambda \underbrace{\left(\frac{1-\gamma}{2} \left\| \vec{I}_d \right\|_2^2 + \gamma \left\| \vec{I}_d \right\|_1 \right)}_{\text{Regularization term}} \right), \tag{3.17}$$

where N is the number of measurement points. Similarly to MNE with ENR in LFE
(section 3.2.4), the optimal values for the norm-weighting parameter γ and the regu-
larization parameter λ have to be estimated. The maximal regularization parameter
$\lambda_{\max}$ [107] is defined as

$$\lambda_{\max} = \frac{\max \left([L]^{\mathrm{T}} \Delta\vec{b}^{\mathrm{FEM/meas}} \right)}{N\gamma}. \tag{3.18}$$

For larger regularization parameters λ, the obtained square current loop vector $\vec{I}_d$ will
contain only zeros. The regularization parameter λ is represented using the regulariza-

tion factor λ_{fac} by

$$\lambda = \lambda_{\text{fac}}\lambda_{\text{max}}, \qquad\qquad (3.19)$$

where λ_{fac} can be chosen between 0 and 1. If $\lambda_{\text{fac}} = 0$, no regularization is applied. If $\lambda_{\text{fac}} = 1$, the regularization parameter equals $\lambda = \lambda_{\text{max}}$. The optimal regularization parameter λ is searched indirectly by means of the regularization factor λ_{fac}. This ensures the possibility to choose a similar degree of regularization for varying λ_{max}.

Fig. 3.22 shows the solution norm in dependence of the residual norm exemplary for $\gamma = 0.5$ and λ_{fac} varying between 0 and 1 for the simulation setup with the star-shaped crack. The L-curve method [83] is not applicable as the corresponding curves are not L-shaped.
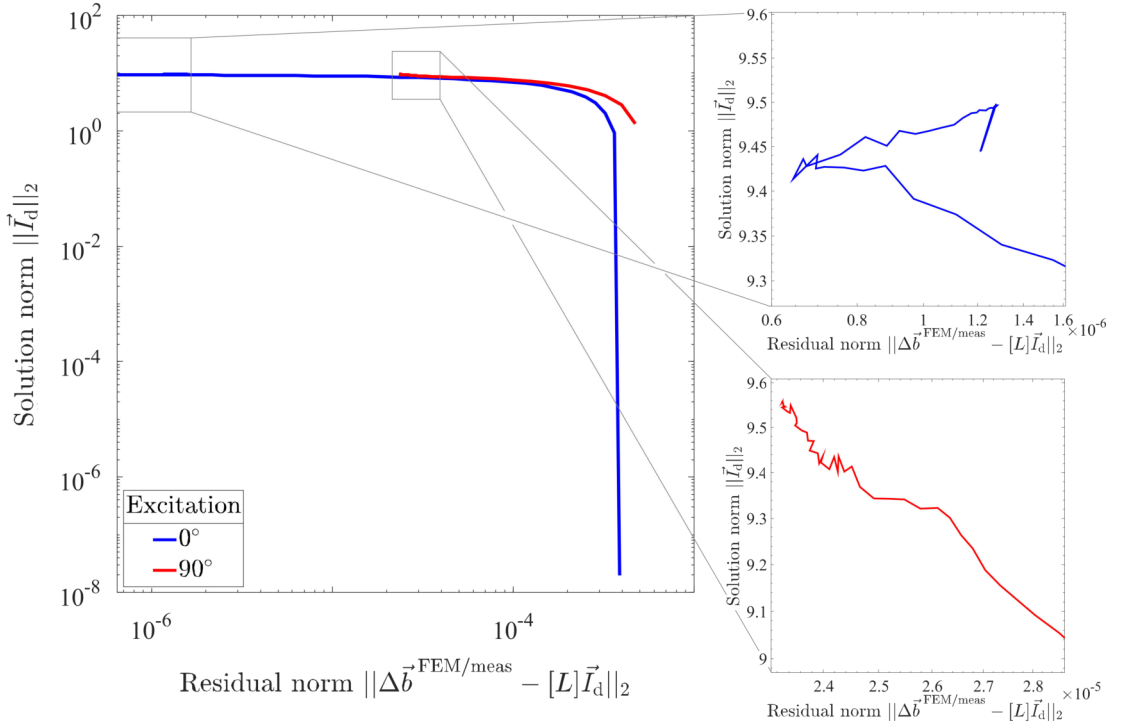
Figure 3.22: Curves of solution norm in dependence of the residual norm for λ_{fac}-values between 0 and 1. The 0°- (blue) and 90°-excitation (red) for the simulation setup with the star-shaped crack are investigated. Both curves do not show a L-shape. Areas with regularization factors λ_{fac} close to zero are shown enlarged (right).

Parameter studies for simulated data   Parameter studies have been conducted to select an appropriate γ-λ_{fac}-combination. The simulation setup with the star-shaped crack acts as reference case. The auxiliary MFPs obtained from the corresponding FEM simulations act as input. The MNE with ENR is performed for the combinations $\gamma = [10^{-10}, 10^{-9}, \cdots, 1]$ with $\lambda_{\text{fac}} = [10^{-10}, 10^{-9}, \cdots, 10^{-1}]$ for the two excitation angles 0° and 90°. The obtained $\vec{I}_{\text{d}}$ are post-processed as described in section 2.2.4 to get normalized current density norm maps $\vec{j}_{\text{abs}} = \left[\|\vec{j}_1\|_2 \ \ \|\vec{j}_2\|_2 \ \ \cdots \ \ \|\vec{j}_m\|_2 \ \ \cdots \ \ \|\vec{j}_M\|_2 \right]^{\text{T}},$
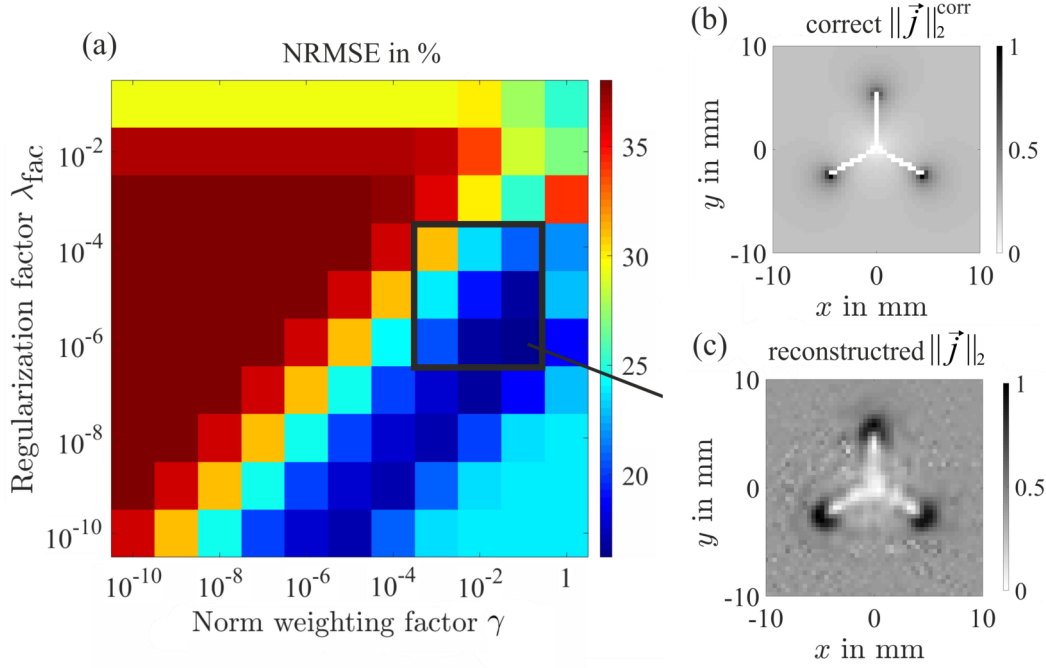
Figure 3.23: Parameter studies for choosing γ and λ_{fac} for ENR in ECE based on simulated data sets of two excitation angles $0°$ and $90°$: The color-coded NRMSE (3.20) (a) between the correct normalized current density norm map (b) and the reconstructed ones for the different γ-λ_{fac}-combinations, shows a minimum (dark blue) for $\gamma = 10^{-1}$ and $\lambda_{\text{fac}} = 10^{-6}$. The corresponding reconstructed normalized current density norm map is shown in (c). The black square indicates the parameter combination subset that is analyzed for measurement data.

where m indicates the observation point. The NRMSE (Fig. 3.23 a) is calculated for each γ-λ_{fac}-combination between the obtained normalized current density norm map $\vec{j}_{\text{abs}}$ (Fig. 3.23 c) and the correct one $\vec{j}_{\text{abs}}^{\text{corr}} = \left[\|\vec{j}_1\|_2^{\text{corr}} \; \|\vec{j}_2\|_2^{\text{corr}} \; \cdots \; \|\vec{j}_m\|_2^{\text{corr}} \; \cdots \; \|\vec{j}_M\|_2^{\text{corr}} \right]^{\text{T}}$ (Fig. 3.23 b) originating from FEM simulations. The NRMSE is defined as

$$\text{NRMSE} = \frac{\sqrt{\frac{1}{M} \sum_{m=1}^{M} \left(j_{\text{abs}}(m) - j_{\text{abs}}^{\text{corr}}(m) \right)^2}}{\left(\max\left(\vec{j}_{\text{abs}}^{\text{corr}} \right) - \min\left(\vec{j}_{\text{abs}}^{\text{corr}} \right) \right)}, \tag{3.20}$$

where M denotes the number of observation points in the ROI. Minimal errors (Fig. 3.23 a, dark blue) can be found for norm weighting factors between $\gamma = 10^{-5}$ and $\gamma = 10^{-1}$ and the regularization factors λ_{fac} between $\lambda_{\text{fac}} = 10^{-10}$ and $\lambda_{\text{fac}} = 10^{-6}$. The normalized current density norm map obtained by MNE with ENR with minimal NRMSE ($\gamma = 10^{-1}$ and $\lambda_{\text{fac}} = 10^{-6}$) is shown in Fig. 3.23 c. Thus, for simulation data the parameter combination of $\gamma = 10^{-1}$ and $\lambda_{\text{fac}} = 10^{-6}$ is chosen.

Parameter studies for measurement data For the application to measurement data, the occurrence of noise is taken into account. Thus, the regularization factor λ_{fac}

needs to be increased. A square of 3×3 parameter combinations (Fig. 3.23, black square) including the found minimum from simulation data is considered. The MNE with ENR is applied for these 9 parameter combinations to the measurement data with the star-shaped crack at the first layer and excitation angle of $0°$. Finally, the combination of $\gamma = 10^{-3}$ and $\lambda_{\text{fac}} = 10^{-5}$ is chosen for measurement data in this study, because it showed the steepest gradient in the obtained normalized current density norm map.

3.3.5 Results and Discussion

Simulations The estimation of the normalized current density norm map for the star-shaped crack by MNE with TPR (Fig. 3.24 a) and ENR (Fig. 3.24 b) shows that the defect shape is visible with both methods. The length of the three branches of the

(a) MNE with TPR using the L-curve criterion.

(b) MNE with ENR using the selected parameters $\gamma = 10^{-1}$ and $\lambda_{\text{fac}} = 10^{-6}$.
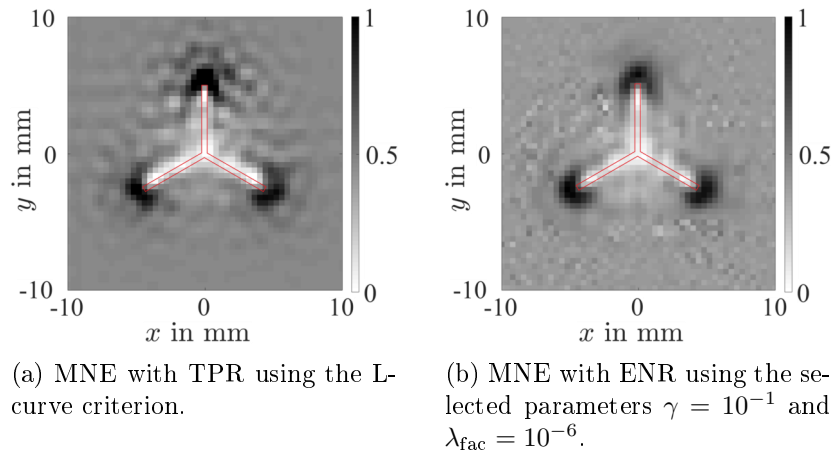
Figure 3.24: Reconstructed normalized current density norm maps from FEM simulations for the star-shaped defect. The red contour indicates the defect.

(a) MNE with TPR using the L-curve criterion.

(b) MNE with ENR using the selected parameters $\gamma = 10^{-1}$ and $\lambda_{\text{fac}} = 10^{-6}$.
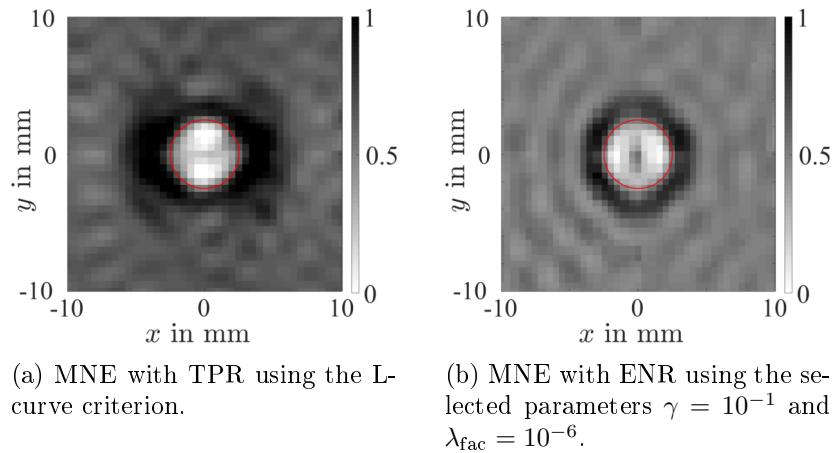
Figure 3.25: Reconstructed normalized current density norm maps from FEM simulations for the cylindrical shaped defect. The red circle indicates the defect.

star is correctly estimated as 5 mm by ENR and TPR. It can be observed that both methods determine the width of the branches too large, roughly between 0.8 - 1.2 mm. Both regularization methods show comparable reconstruction results.

Fig. 3.25 shows the normalized current density norm maps for the simulation setup with the cylindrical shaped crack obtained from the two excitation directions 0° and 90°. The circle indicates the diameter of the true defect. Both MNE with TPR (Fig. 3.25 a) and with ENR (Fig. 3.25 b) estimated the defect diameter of 5 mm correctly.

Measurements   Fig. 3.26 shows the reconstructed normalized current density norm maps as mean of the four excitation directions for the star-shaped crack positioned at the aluminum layers 1 to 4. At layer 1, the L-curve method for TPR selected too small regularization parameters λ leading to a noisy normalized current density norm map. The star shape of the crack is slightly better observable with ENR compared to TPR. Although the shape of the defect is visible, the width of the three branches can not be reliably determined due to a blurring in the determined normalized current density norm maps.
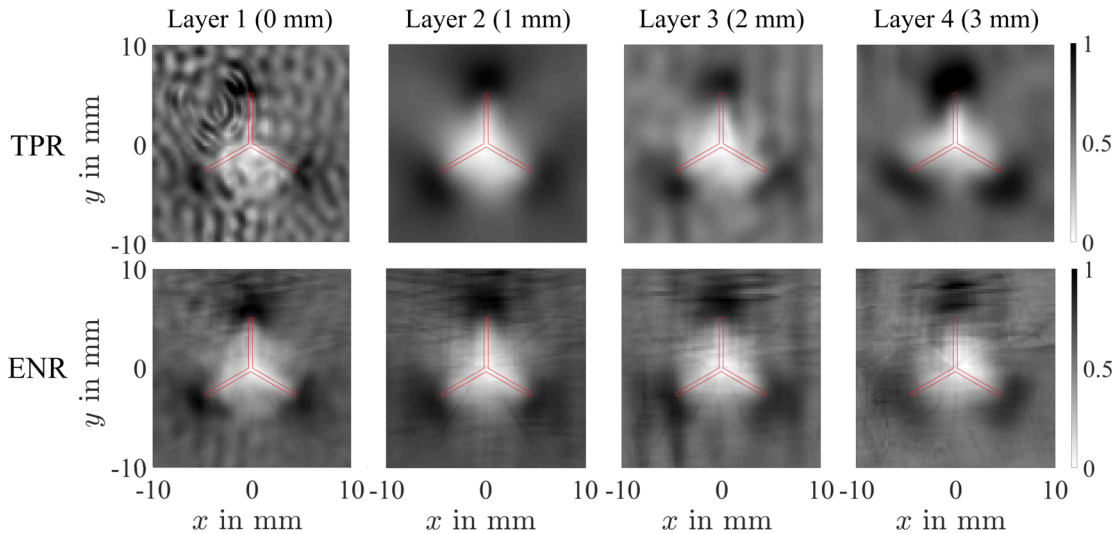
Figure 3.26: Reconstructed normalized current density norm maps for the star-shaped defect from measurements for different defect depths comparing the two regularization methods TPR and ENR.

The MNE with TPR presented in this thesis shows a worse reconstruction result in the first layer compared to the results presented in [50], where the inverse problem was solved in Fourier domain with TPR. But the star-shape of the crack is better to recognize in the MNE with TPR for layers 3 and 4 compared to [50]. The MNE with ENR shows slightly improved visibility of the star shape in comparison to [50].

Fig. 3.27 shows the determined normalized current density norm maps for the cylindrical defect by MNE with TPR (Fig. 3.27, top) and with ENR (Fig. 3.27, bottom) as
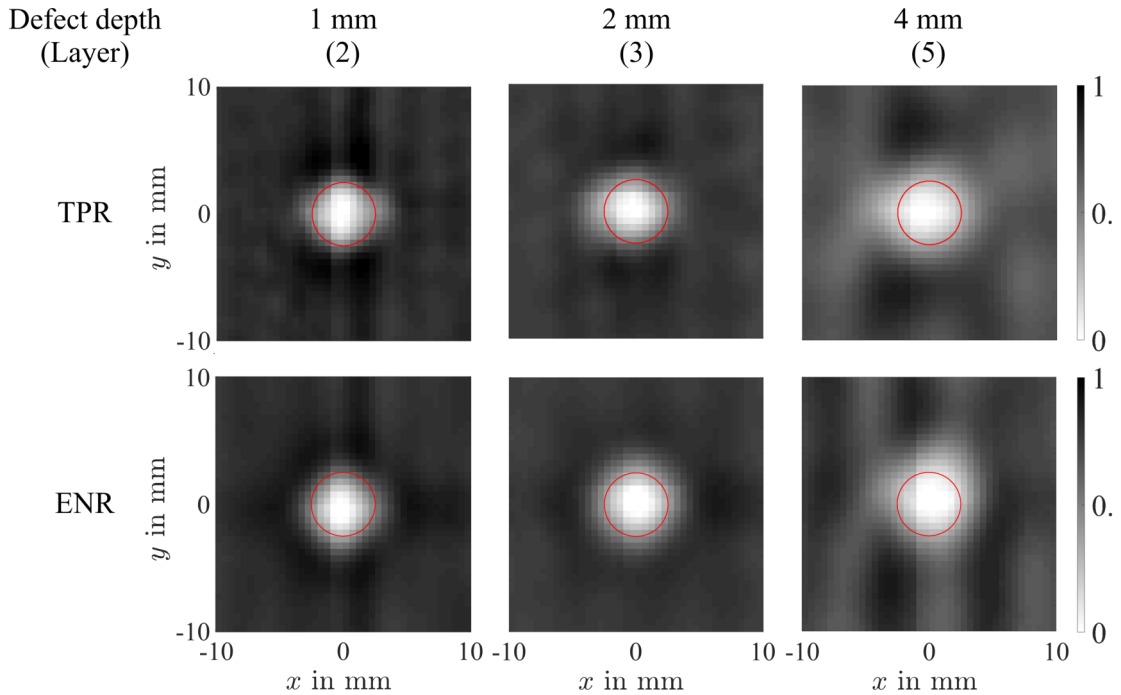
Figure 3.27: Reconstructed normalized current density norm maps for the cylindrical shaped defect from measurements for different defect depths comparing the two regularization methods TPR and ENR. The red circle indicates the defect.

mean value from the two excitation directions 0° and 90°. It can be observed that for both regularization methods the defect dimensions are estimated too large. No differences of the reconstruction results using the regularization methods TPR in comparison to ENR are observable.

3.3.6 Summary and Conclusions

The MNE with ENR in comparison to TPR shows that for the investigation of the star-shaped crack, the ENR slightly outperforms the TPR regarding the visibility of the defect shape. For the analysis of the cylindrical shaped defect, no advantage of one of the two regularization methods can be observed. Future work could focus on optimizing the measurement setup for deeper penetration with increased signal-to-noise ratio, while keeping the uniform excitation as it simplifies the inverse reconstruction scheme [53] and allows for reconstruction of arbitrary shaped defects. Another possible option would be the consideration of a more complex forward solution. The current one (section 2.2.4) assumes a single infinite thin metal plate, which might partly explain the worse reconstruction results with increasing defect depth.

3.4 Discussion and Summary

The MNE in LFE showed repeatable reconstruction results of a cylindrical defect with correct estimation of the defect depth. The results are stable for changing defect depths. The used forward solution AFS is optimized for defects of regular shape with uniform extensions, like a circular or quadratic shape in x- and y-extension. Thus, no complex shaped defects can be reconstructed with this forward solution. In the investigated examples, defects up to 8 mm could be reconstructed.

In contrast, the MNE in ECE is capable to reconstruct arbitrary shaped defects (like the shown star-shape), especially when they are located close to the specimen surface. For ECE, no evaluable measurement signals could be derived for the deeper defects. The corresponding planar excitation coil is not optimized for the evaluation of deep defects. Thus, the ECE setup was different from the LFE, using aluminum plates of thickness 1 mm, with the cylindrical defect located at the layers 2 (1 mm), 3 (2 mm) and 5 (4 mm) for qualitative comparison. Defects could be reconstructed evaluable up to 4 mm with this ECE setup.

Thus, the LFE shows the capability to reconstruct defect characteristics of deeper defects compared to the ECE used in this study.

4 Lorentz Force Evaluation using an Adapted Landweber Algorithm

4.1 Introduction

In the field of inverse problems, the Landweber algorithm [133] is a method that iteratively solves linear inverse problems. It uses the negative gradient of the current residual as search direction. The Landweber iteration has also been extended for solving non-linear problems that involve constraints [134] and is applicable for time dependent inverse problems [135].

The Landweber iteration has been used for image restoration [68] and recovery [69]. Further, it has been applied within the scopes of elastography [71, 136], earth science [137], optics [138] and mathematics [139, 140]. The Landweber iteration is widely applied in various fields of tomography such as magnet resonance imaging [70, 71], electrical resistance tomography [72], electrical impedance tomography [73, 74], electrical capacitance tomography [75–78], absorption tomography methods [141, 142] and further tomography methods [79–81].

In the electrical capacitance tomography, the aim is to reconstruct the permittivity distribution from capacitance measurements within a cross-section or volume. The result is a gray scale image as an estimation of the distribution of dielectric materials. In [75], the Landweber iteration is used together with a fuzzy thresholding operator to suppress low gray-level artifacts. The thresholding acts as regularization. This principle is transferable to the LFE inverse problem. The general Landweber iteration [133] is defined as

$$\vec{\theta}_{i+1} = \vec{\theta}_i - \eta \left[L\right]^{\mathrm{T}} \left(\left[L\right] \vec{\theta}_i - \Delta \vec{F}^{\mathrm{FEM/meas}}\right), \tag{4.1}$$

where $\vec{\theta}_{i+1}$ depends on the step size η and the current defect identification vector $\vec{\theta}_i$. The lead field matrix $[L]$ contains the approximate forward solution (AFS) (section 2.1.4.2). This formulation leads to a continuous $\vec{\theta}_{i+1}$, but it is known *a priori* that the defect identification vector $\vec{\theta}_{i+1}$ should contain ones for elements that belong to the defect and

zeros otherwise. The resulting idea applies a thresholding factor t_{h} to $\vec{\theta}_{i+1}$ such that

$$
\vec{\theta}_{i+1,t_{\mathrm{h}}}(k) = \begin{cases} 0 \text{ if } \vec{\theta}_{i+1}(k) \leq t_{\mathrm{h}} \left(\max\left(\vec{\theta}_{i+1}\right) - \min\left(\vec{\theta}_{i+1}\right) \right) \\ 1 \text{ if } \vec{\theta}_{i+1}(k) > t_{\mathrm{h}} \left(\max\left(\vec{\theta}_{i+1}\right) - \min\left(\vec{\theta}_{i+1}\right) \right) \end{cases} , \qquad (4.2)
$$

where k refers to the elements of $\vec{\theta}_{i+1}$. The thresholded $\vec{\theta}_{i+1,t}$ act as new input for the next iteration step of (4.1).

The aim of this Chapter is to analyze, whether the adapted Landweber iteration can give benefits in terms of reconstruction of the defect depth, size and location. The next section 4.2.1 contains the description of the simulation and measurement setup. Section 4.2.2 describes the adapted Landweber algorithm and the determination of the optimal number of iterations, step size η and thresholding factor t_{h} based on simulated data sets. The defect reconstruction results obtained from simulated and measured data sets are described in section 4.3. Section 4.4 discusses the results and compares them to the previous section about minimum norm estimation (MNE) with elastic net regularization (ENR) and Tikhonov-Phillips-regularization (TPR) (section 3.2). This Chapter contains methods and results that were presented in [23].

4.2 Materials and Methods

4.2.1 Setup

Simulation A conducting specimen of size $L \times W \times H = 400\,\mathrm{mm} \times 400\,\mathrm{mm} \times 100\,\mathrm{mm}$ is moved in x-direction relative to a spherical permanent magnet with a velocity $v = 0.1\,\mathrm{m/s}$. The specimen consists of stacked aluminum sheets with conductivity
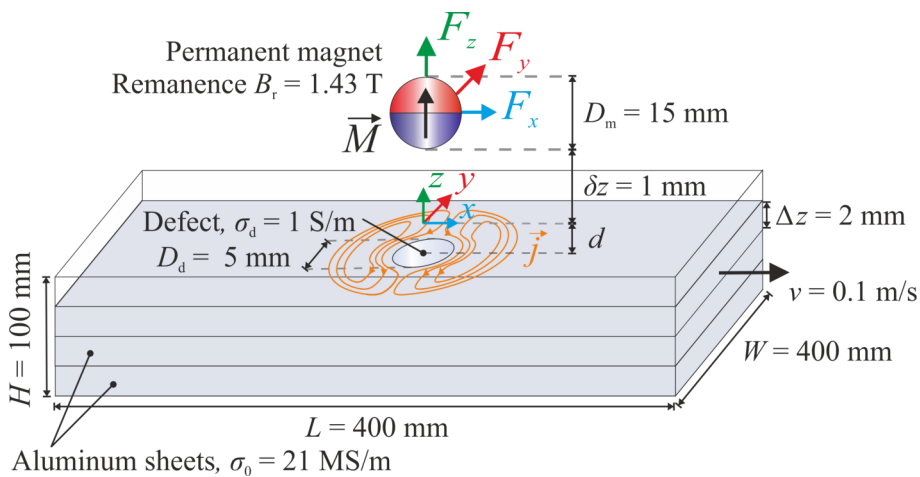
Figure 4.1: Simulation setup: A specimen of stacked aluminum sheets containing a defect is moved relative to a spherical permanent magnet.

$\sigma_0 = 21\,\mathrm{MS/m}$, each of thickness $\Delta z = 2\,\mathrm{mm}$. The spherical permanent magnet is located at the lift-off distance $\delta z = 1\,\mathrm{mm}$ above the top surface of the specimen. The permanent magnet of diameter $D_\mathrm{m} = 15\,\mathrm{mm}$ is characterized by a homogeneous magnetization $\vec{M} = B_\mathrm{r}/\mu_0\,\vec{e}_z$ ($B_\mathrm{r} = 1.43\,\mathrm{T}$), where B_r describes the remanence.

A cylindrical shaped defect with diameter $D_\mathrm{d} = 5\,\mathrm{mm}$ is located at the x-y-origin. Different defect depths of $d = 2, 4$ and $8\,\mathrm{mm}$ are investigated. The DRS components ΔF_x^FEM, ΔF_y^FEM and ΔF_z^FEM are calculated using the weak reaction approach solved by FEM (section 2.1.2.2) at the observation points between $|x| \leq 25\,\mathrm{mm}$ and $|y| \leq 25\,\mathrm{mm}$. The simulation setup is similar to the one described in section 3.2.

Measurement The specimen under test (Fig. 4.2) consists of stacked aluminum sheets, each of thickness $\Delta z = 2\,\mathrm{mm}$. The total size of the specimen compromises $L \times W \times H = 250\,\mathrm{mm} \times 50\,\mathrm{mm} \times 50\,\mathrm{mm}$. It is moved relative to the cylindrical permanent magnet with a velocity $v = 0.1\,\mathrm{m/s}$. The permanent magnet is described by a diameter of $D_\mathrm{m} = 22.5\,\mathrm{mm}$ and a height of $H_\mathrm{m} = 17.6\,\mathrm{mm}$ and homogeneously magnetized by $\vec{M} = B_\mathrm{r}/\mu_0\,\vec{e}_z$ ($B_\mathrm{r} = 1.43\,\mathrm{T}$). It is located $\delta z = 1\,\mathrm{mm}$ above the top surface of the specimen.

A cylindrical shaped defect of diameter $D_\mathrm{d} = 5\,\mathrm{mm}$ and height $H_\mathrm{d} = 2\,\mathrm{mm}$ is located at the x-y-origin (Fig. 4.2). The defect depths $d = 2, 4$ and $8\,\mathrm{mm}$ are analyzed.
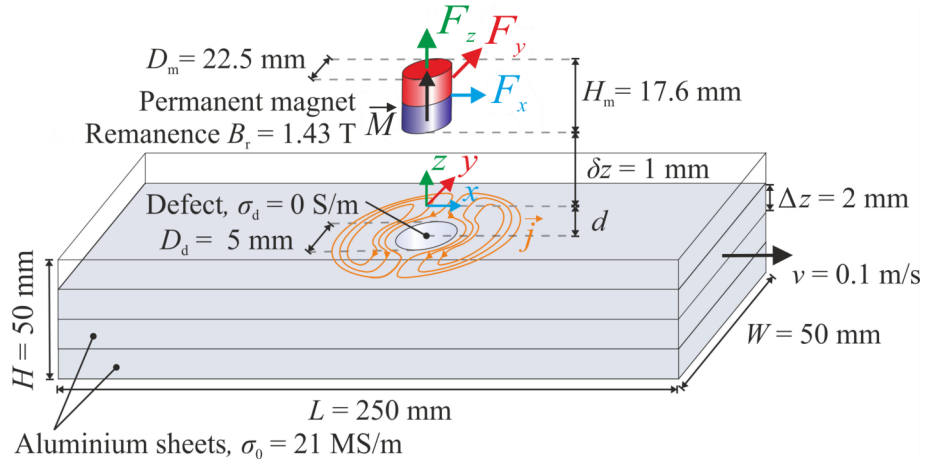
Figure 4.2: Measurement setup: A specimen of stacked aluminum sheets containing a defect is moved relative to a cylindrical permanent magnet.

This measurement setup is similar to the one described in section 3.2.1. Hence the preprocessing steps and the resulting DRS components of the 25 repeated measurements are identical.

4.2.2 Adapted Landweber Algorithm

In order to develop a Landweber algorithm adapted for the application in LFE, a reference case is needed for parameter studies. The simulated data set with the cylindrical defect at depth $d = 2\,\mathrm{mm}$ is selected. It is assumed that the defect depth is known. Thus, only the second aluminum layer is discretized into $1\,\mathrm{mm} \times 1\,\mathrm{mm} \times 2\,\mathrm{mm}$ voxels within a region of interest (ROI) $[-25, -24, \ldots, 25]\,\mathrm{mm}$ in x- and y-direction around the minimum of $\Delta F_x^{\mathrm{FEM}}$. The voxel positions correspond to the elements of the defect identification vector $\vec{\theta}$ that should be determined.

The Landweber algorithm (4.1) including a thresholding (4.2) is defined as

$$\vec{\theta}_{i+1} = \vec{\theta}_{i,t_{\mathrm{h}}} - \eta\,[L]^{\mathrm{T}}\left([L]\,\vec{\theta}_{i,t_{\mathrm{h}}} - \Delta\vec{F}^{\mathrm{FEM/meas}}\right), \tag{4.3}$$

where $\vec{\theta}_{i+1}$ depends on the step size η and the current thresholded defect identification vector $\vec{\theta}_{i,t_{\mathrm{h}}}$. The lead field matrix $[L]$ contains the AFS (section 2.1.4.2). The step size η should be chosen between $0 < \eta < 2/S_1^2$, where S_1 denotes the the largest singular value of $[L]$ [133]. This formulation leads to a continuous valued $\vec{\theta}_{i+1}$. In consequence, $\vec{\theta}_{i+1}$ is thresholded according to (4.2) and inserted into (4.3) as the new current $\vec{\theta}_{i,t_{\mathrm{h}}}$.

The Landweber iteration needs an initial solution $\vec{\theta}_0$. It is chosen as a vector with zeros and one '1' at the element that belongs to the voxel at $x = y = 0$. The 2D visualization of $\vec{\theta}_0$ within the region of interest is shown in Fig. 4.3, bottom left.

In order to find the optimal values for the number of iterations I, step size η and thresholding factor t_{h}, parameter studies are applied. For that purpose $\eta = 1/S_1^2$ and $t_{\mathrm{h}} = 0.5$ are chosen initially and the number of iterations $I = [1, 10, 100, 1000, 10000]$ should be tested. In order to find the optimal thresholding factor t_{h}, the varying $t_{\mathrm{h}} = [0.125, 0.25, \ldots, 0.875]$ should be investigated using the chosen I and the fixed step size $\eta = 1/S_1^2$. Finally, the optimal η should be chosen with obtained I and t_{h} in the range $0 < \eta < 2/S_1^2$. The measure for choosing the optimal parameters is the NRMSE.

$$\begin{aligned} \mathrm{NRMSE} = \frac{1}{3}\sum_{i=x,y,z} &\frac{\sqrt{\frac{1}{N}\sum_{n=1}^{N}\left(\Delta F_{n,i}^{\mathrm{AFS}} - \Delta F_{n,i}^{\mathrm{FEM/meas}}\right)^2}}{\min\left[R^{\mathrm{AFS}}, R^{\mathrm{FEM/meas}}\right]} \\ &\text{with } R^{\mathrm{AFS}} = \max\left(\Delta\vec{F}_i^{\mathrm{AFS}}\right) - \min\left(\Delta\vec{F}_i^{\mathrm{AFS}}\right) \\ &\text{and } R^{\mathrm{FEM/meas}} = \max\left(\Delta\vec{F}_i^{\mathrm{FEM/meas}}\right) - \min\left(\Delta\vec{F}_i^{\mathrm{FEM/meas}}\right), \end{aligned} \tag{4.4}$$

where n indicates the current position of the permanent magnet. The NRMSE describes the deviation between the DRS obtained from FEM simulations or measurements and the forward calculated DRS from the reconstructed defect.

Number of iterations Fig. 4.3 shows $\vec{\theta}_1$ after the first iteration according to (4.3). The thresholding factor $t_\mathrm{h} = 0.5$ has been adapted to the fixed value of $t_\mathrm{h} = 0.02$ as the side minima of $\vec{\theta}_1$ are very small (Fig. 4.3, logarithmic color scale). Otherwise the thresholded solution $\vec{\theta}_{1,t_\mathrm{h}}$ would have been the same as the initial $\vec{\theta}_0$. Fig. 4.3 further shows that $\vec{\theta}_{1,t_\mathrm{h}}$ acts as input for the second iteration. The resulting continuous $\vec{\theta}_2$ is thresholded and the corresponding $\vec{\theta}_{2,t_\mathrm{h}}$ act as input for the third iteration and so on. It can be observed that the same continuous $\vec{\theta}_i$ is determined by (4.3) from the second iteration onwards (Fig. 4.3, top). That means that the same thresholded $\vec{\theta}_{i,t_\mathrm{h}}$ is determined after first iteration (Fig. 4.3, bottom), i.e. the same defect would be reconstructed. Thus, (4.3) has to be applied only once and $I = 1$ is used in the remaining parts of this chapter.
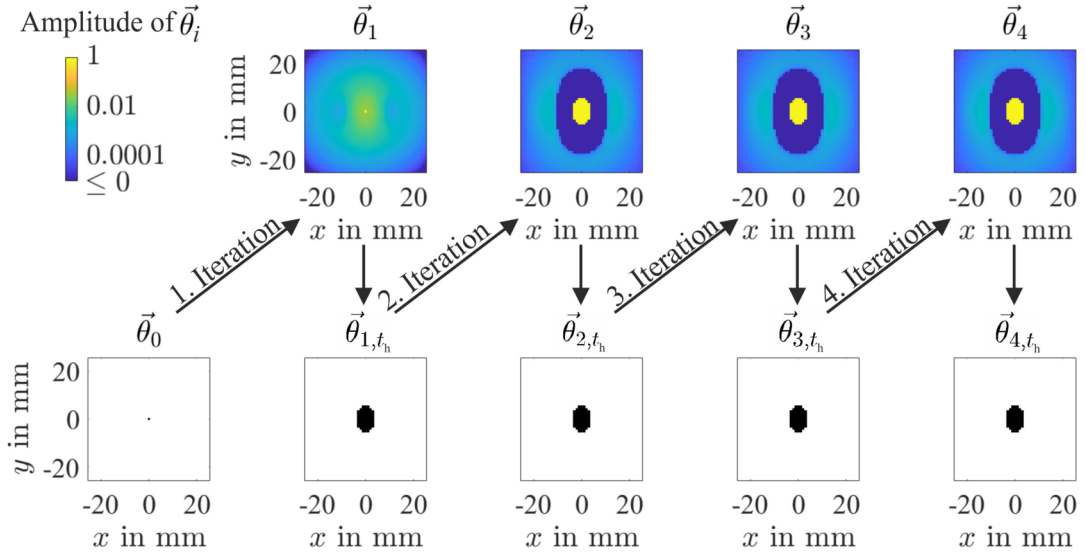
Figure 4.3: Principle of adapted Landweber iteration in LFE: The initial solution $\vec{\theta}_0$ leads to a continuous $\vec{\theta}_1$, the thresholded $\vec{\theta}_{1,t_\mathrm{h}}$ acts as input for the next iteration etc. Continuous values ≤ 0 of $\vec{\theta}_i$ are indicated together by dark blue due to the logarithmic scaling.

Thresholding factor and step size Using the fixed step size $\eta = 1/s_1^2$, it turned out that the optimal t_h depends on the size of the defect. Fig. 4.4 left shows that a small t_h leads to a large reconstructed defect and vice versa. In consequence, none of the envisaged thresholding factors $t_\mathrm{h} = [0.125, 0.25, \dots, 0.875]$ could be selected as fixed thresholding factor if a fixed step size is used at the same time. On the other hand, if the fixed thresholding factor $t_\mathrm{h} = 0.02$ is used and the step size η is changed, a small defect is reconstructed if η is small and a larger one if η is increased (Fig. 4.4, right). In consequence, one of the two parameters has to be fixed. Here, the step size is fixed to $\eta = 1/s_1^2$.
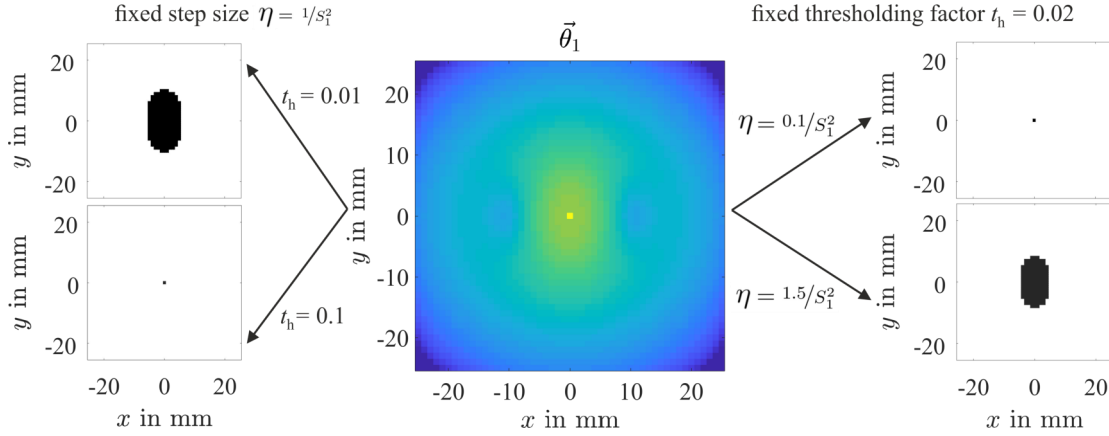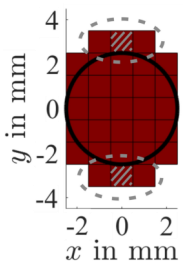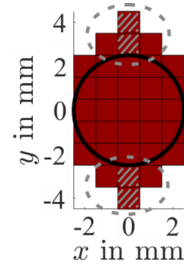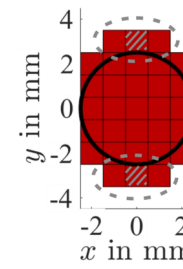
Figure 4.4: Influence of thresholding factor t_h and step size η on the defect identification vector $\vec{\theta}_{1,t_h}$: If the step size η is fixed (left), the reconstructed defect identification vector $\vec{\theta}_{1,t_h}$ depends on the used thresholding factor t_h. If t_h is small (top left) a large defect is reconstructed and vice versa. A fixed thresholding factor t_h (right) with a changing step size η leads to a small reconstructed defect identification vector $\vec{\theta}_{1,t_h}$ if η is small (top right) and vice versa.

Defect reconstruction scheme The derived defect reconstruction scheme is applied layer-wise. It uses a fixed step size $\eta = 1/s_1^2$ and searches the minimal NRMSE by testing different thresholding factors t_h. The singular value S_1 is calculated from the lead field matrix $[L]$ (section 2.1.4.2). The minimal NRMSE is obtained in a four-step approach that reduces the thresholding factor range in every step by searching first for minimal NRMSE by testing t_h values in the range of $[0, 0.01, \ldots, 0.2]$ and then adapting the new finer t_h-range by searching in the surrounding region of the t_h value that belongs to the current minimal NRMSE. This step is repeated three times and the distance between consecutive t_h-values of the current t_h-range is reduced in every step from 0.01, 0.001, to 0.0001 and 0.00001. The layer with the minimal NRMSE indicates the defect depth. The determined corresponding defect identification vector $\vec{\theta}_{t_h}$ represents the reconstructed defect.

4.3 Results

Simulations The defect reconstruction results are shown in Table 4.1 and Fig. 4.5 for the three different defect depths $d = 2, 4$ and $8\,\mathrm{mm}$. The corresponding NRMSE values of $4.83\,\%$, $5.30\,\%$ and $6.35\,\%$ are minimal at the correct defect depths. Fig. 4.5 shows the reconstructed defects for each of the investigated layers, color-coded according to the corresponding NRMSE. The minimal NRMSE becomes less distinct with increasing defect depth (Fig. 4.5 a-c). The defect reconstruction error parameters introduced in section 3.2 show that all centers of the defects are correctly reconstructed at $x = y = 0$.

Table 4.1: Results of defect reconstruction of simulated data using the adapted Landweber algorithm: The correct defect depth was estimated for $d = 2, 4$ and $8\,\mathrm{mm}$. The circle indicates the shape of the true defect. The color-coding corresponds to Fig. 4.5. The gray hatching indicates the number of voxels that the y-extensions are estimated too large. The gray dashed ellipses indicate the additional voxels.

| Defect depth d in mm	2	4	8
Reconstruction at the layer of the defect			
Thresholding factor t_{h}	$2.5 \cdot 10^{-2}$	$5.3 \cdot 10^{-3}$	$4.23 \cdot 10^{-4}$
Reconstructed depth in mm	2	4	8
Euclidean distance d_0 from $[0,0]$ in mm	0	0	0
Size in mm^2	31	33	31
Size difference in mm^2	11.37	13.37	11.37
x-extension x_{e} in mm	5	5	5
y-extension y_{e} in mm	7	9	7
NRMSE in %	4.83	5.30	6.35
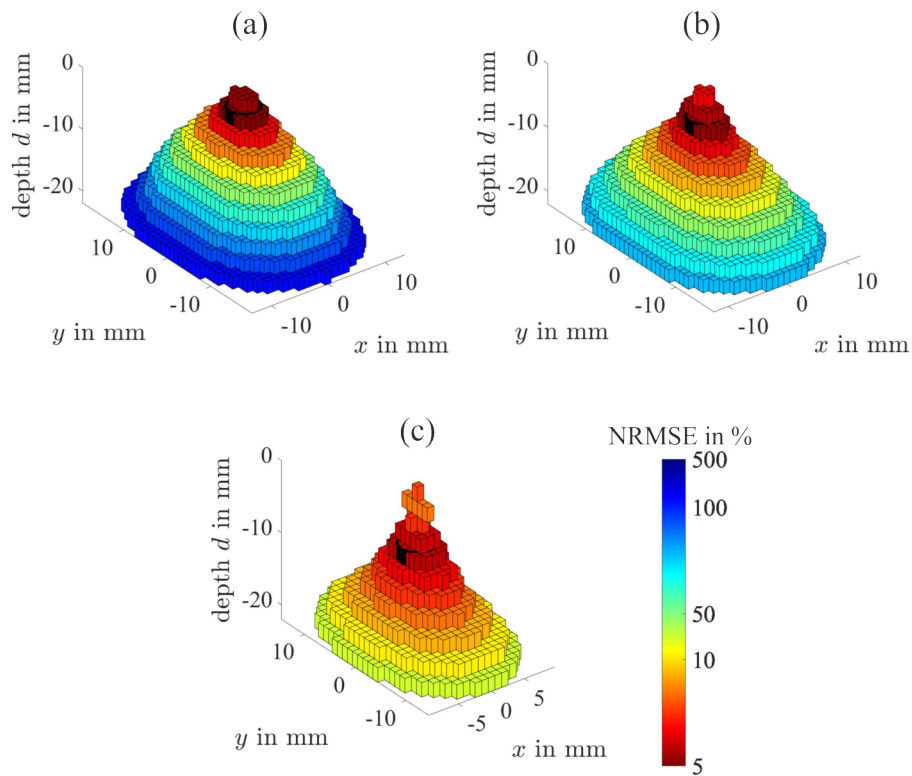
Figure 4.5: Defect reconstruction results from simulated data for the defect depths $d = 2, 4$ and $8\,\mathrm{mm}$ (a-c): Reconstructed defects for the investigated aluminum layers are color-coded according to the corresponding NRMSE. The minimal NRMSE (red) indicates the estimated defect depth. The correct defect is shown as black cylinder.

The extension x_e in x-direction is correct. The defect extension y_e in y-direction is two voxels too large (Table 4.1, gray hatching) for the defects at the depths $d = 2$ and $8\,\text{mm}$. That relates to 3 additional voxels in each positive and negative y-direction (Table 4.1, gray dashed ellipses). For $d = 4\,\text{mm}$, the extension in y_e in y-direction is 4 voxels too large (Table 4.1, gray hatching). The additional voxels and the mismatch of a round defect and the voxel approximation lead to a size errors of $11.37\,\text{mm}^2$ for the defects at $d = 2$ and $8\,\text{mm}$ and of $13.37\,\text{mm}^2$ for the defect at $d = 4\,\text{mm}$, respectively. The thresholding factors t_h decrease with increasing defect depth (Table 4.1).

Measurements   The defect reconstruction results of 25 measurement trials are shown in Table 4.2. The visualizations of the reconstructed defects show how often one voxel is reconstructed, where a frequency value of 25 represents a reconstruction in all 25 trials. The adapted Landweber iteration yielded correct depth detection for $d = 2\,\text{mm}$. For $d = 4\,\text{mm}$, the estimated depth is $2\,\text{mm}$ (Table 4.2). The depth of the defect at $d = 8\,\text{mm}$ is estimated at $4\,\text{mm}$ in $23/25$ cases and at $6\,\text{mm}$ in $2/25$ cases. Table 4.2 shows the defect reconstruction error measures for the correct depth in order to assess the properties like defect shape and location in x-y-plane. The centers of the reconstructed defects are slightly shifted. This shift in mainly negative y-direction is below $1\,\text{mm}$, reflected by the Euclidean distance d_0. The mean defect extensions in x-direction x_e are slightly too

Table 4.2: Results of defect reconstruction of measurement data using the adapted Landweber algorithm: The reconstructed defect and the corresponding defect reconstruction error parameters are shown as mean $\pm$ standard deviation for the correct depth. The circle indicates the shape of the true defect. Wrong reconstructed depths and the corresponding NRMSE are indicated by asterisks.

Defect depth d in mm	2	4	8
Thresholding factor t_h	$2.01\cdot10^{-3}\pm8.59\cdot10^{-5}$	$6.9\cdot10^{-3}\pm3.97\cdot10^{-5}$	$6.9\cdot10^{-3}\pm3.97\cdot10^{-5}$
Reconstructed depth in mm	2	2*	4.24 ± 0.66*
Euclidean distance d_0 from $[0,0]$ in mm	0.82 ± 0.08	0.64 ± 0.08	0.67 ± 0.24
Size in mm^2	27.40 ± 0.50	28.64 ± 0.49	27.04 ± 0.73
Size difference in mm^2	7.77 ± 0.50	9.01 ± 0.49	7.41 ± 0.74
x-extension x_e in mm	4.48 ± 0.51	4.80 ± 0.41	4.60 ± 0.50
y-extension y_e in mm	7.68 ± 0.48	8.00 ± 0	7.84 ± 0.37
NRMSE in %	10.27 ± 0.14	11.33 ± 0.14 (10.68 ± 0.13)*	14.37 ± 0.24 (13.54 ± 0.24)*
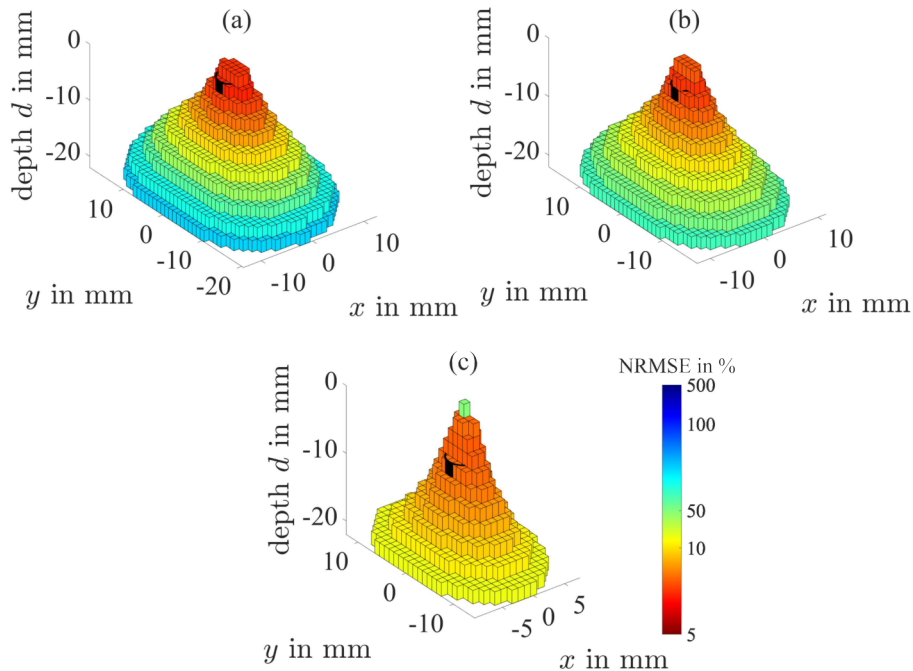
Figure 4.6: Defect reconstruction results from measurement trial no. 1 for the defect depths $d = 2, 4$ and $8\,\text{mm}$ (a-c): Reconstructed defects for the investigated aluminum layers are color-coded according to the corresponding NRMSE. The minimal NRMSE (red) indicates the defect depth. The correct defect is shown as black cylinder.

small whereas the mean y_e are a bit too large (Table 4.2). This leads to mean size errors a_d between $7.41\,\text{mm}^2$ and $9.01\,\text{mm}^2$. In accordance to the simulated data (Table 4.1), the mean NRMSE values increase for increasing defect depth. The reconstructed defects of each layer for trial 1 are shown in Fig. 4.6 color-coded according to their NRMSE. The correct defect depth is found for $d = 2\,\text{mm}$. For the defect depths $d = 4$ and $8\,\text{mm}$ the "hot spots" (e.g. minimal NRMSE) are located above. The corresponding depths are estimated at $2\,\text{mm}$ and $4\,\text{mm}$.

In order to investigate the influence of an improved SNR (Fig. 3.5 b, section 3.2.1), the defect reconstruction by the adapted Landweber algorithm was applied for the averaged DRSs with the defect depths $d = 2, 4$ and $8\,\text{mm}$. The defect error measures are in accordance with the reconstruction results from the single trials.

4.4 Discussion

The adapted Landweber iteration achieves correct depth and adequate size estimation of cylindrical shaped defects at the depths $d = 2, 4$ and $8\,\text{mm}$ for the simulated data sets.

For the DRSs obtained from measurements, adequate size estimations are achieved, but the correct defect depth could be obtained only for $d = 2\,\text{mm}$. For $d = 4$ and $8\,\text{mm}$

the depth has been estimated above. It is known that defects close to the specimen upper surface show smaller NRMSE values. This behavior might occur as the forward solution AFS does not take the eddy current perturbations into account that occur in the metal layers above the defect. Thus, if less metal layers are located above the defect, the NRMSE must be smaller. In consequence, a reconstruction of the defect above the correct one (Table 4.2) might be partly explained by this phenomenon.

The MNE with ENR and TPR described in the previous chapter showed a correct defect depth estimation. That indicates the sensitivity of the depth estimation to the used inverse method if the forward solution AFS is used. Further, the AFS assumes an infinitely extended conductor in x- and y-direction (Chapter 2.1.4.2). That might explain why the reconstructed depth is correct for the simulated data sets, where the extensions of the specimen are larger (Fig. 4.1) in comparison to the measurement setup.

The advantage of the presented adapted Landweber algorithm is the calculation time. Calculations have been performed using MATLAB$^{\circledR}$ 2018b with an Intel$^{\circledR}$ Core $^{™}$ i7-4790K processor an 32 GB of RAM. The calculation of one single defect identification vector $\theta_{t_{\mathrm{h}}}$ needs ≈ 0.35 s in contrast to MNE with TPR or ENR that need between 0.5 s and 3 s (section 3.2.6). For one metal layer under investigation, defect identification vectors $\theta_{t_{\mathrm{h}}}$ are calculated and investigated for 65 different thresholding factors t_{h} by the adapted Landweber algorithm. In contrast, in MNE with TPR (Algorithm 1), defect identification vectors are calculated for 500 different regularization parameters λ and for each of them different thresholding factors t_{h} between 0.01 and 0.99 are evaluated. In MNE with ENR (Algorithm 2), the defect identification vectors are calculated for 200 different regularization parameters λ and a fixed thresholding factor t_{h}. To summarize, the adapted Landweber iteration needs less function calls per investigated metal layer in comparison to MNE with TPR and ENR. However, in order to use the adapted Landweber algorithm for further work, the defect depth has to be estimated with another method or a more accurate forward solution has to be used.

5 Lorentz Force Evaluation with an Extended Area Approach

5.1 Introduction

The defect reconstruction quality depends on the accuracy of the used forward solution. Previous studies [10,17,22] in LFE used the approximate forward solution (AFS). It is known from comparisons to FEM simulations [18] that the AFS shows the best accuracy in forward calculation for defects of uniform shape, e.g. of cylindrical or cuboidal shape, where the edges of the cuboid in x- and y-direction are of equal length. In the fast and simple AFS only the defect is discretized and used for forward calculation of the DRS (section 2.1.4.2). The extended area approach (EAA) represents an extension of the AFS, where an extended area surrounding the defect is discretized and used for the calculation of the DRS (section 2.1.4.3). The EAA shows improved accuracy for the forward calculation of cuboidal defects with non-equal edge lengths or ellipsoidal defects [18]. The EAA is computationally more expensive than the AFS.

The aim of the current study is to compare the defect reconstruction performance of both forward solutions. It should be investigated whether an improved diameter and depth estimation of cylindrical shaped defects is possible with EAA. For that purpose simulated and measured data sets with cylindrical defects at different depths are investigated. Further, it is investigated whether a more accurate length-width estimation of a cuboidal defect is possible with EAA based on a simulated data set.

The remaining chapter contains the description of the simulation setup with cylindrical defects and a cuboidal defect as well as the description of the measurement setup in 5.2.1. The subsections 5.2.2 and 5.2.3 contain the descriptions of the diameter-depth scan and the length-width-depth scan. Both scanning methods aim to avoid that the comparison of the defect reconstruction performance is biased by the properties (e.g. parameter selection) of an inverse method. Subsection 5.3 contains the results and discussion of the scanning methods applied to the investigated simulated and measured data sets. A conclusion is drawn in 5.4. Parts of the methods and results have been published in [24] and presented at [25–27].

5.2 Materials and Methods

5.2.1 Setup

Simulation   A conducting specimen of size $L \times W \times H = 400\,\text{mm} \times 400\,\text{mm} \times 100\,\text{mm}$ is moved in x-direction relative to a spherical permanent magnet with a velocity $v = 0.01\,\text{m/s}$. The specimen consists of stacked aluminum sheets with conductivity $\sigma_0 = 30.61\,\text{MS/m}$, each of thickness $\Delta z = 2\,\text{mm}$. The spherical permanent magnet is located at the lift-off distance $\delta z = 1\,\text{mm}$ above the top surface of the specimen. The permanent magnet of diameter $D_\text{m} = 15\,\text{mm}$ is characterized by a homogeneous magnetization $\vec{M} = B_\text{r}/\mu_0\,\vec{e}_z$ ($B_\text{r} = 1.17\,\text{T}$), where B_r describes the remanence.
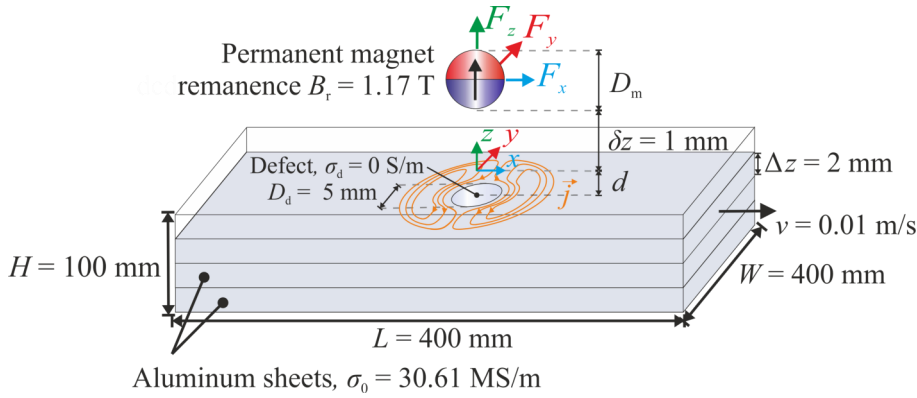
Figure 5.1: Simulation setup: A specimen of stacked aluminum sheets containing a defect is moved relative to a spherical permanent magnet.

Two different defect configurations are investigated. First, a cylindrical shaped defect with diameter $D_\text{d} = 5\,\text{mm}$ is located at the x-y-origin. Different defect depths of $d = 2, 4$ and $8\,\text{mm}$ are investigated. Second, a cuboidal defect of dimensions $L_\text{d} \times W_\text{d} \times H_\text{d} = 12\,\text{mm} \times 2\,\text{mm} \times 2\,\text{mm}$, also located at the x-y-origin, at the depth $d = 2\,\text{mm}$ is analyzed.

The DRS components ΔF_x^FEM, ΔF_y^FEM and ΔF_z^FEM are calculated using the weak reaction approach solved by FEM (section 2.1.2.2) at the observation points between $|x| \leq 25\,\text{mm}$ and $|y| \leq 25\,\text{mm}$ for the cylindrical defect and $|x| \leq 30\,\text{mm}$ and $|y| \leq 30\,\text{mm}$ for the cuboidal defect. The region of observation points is larger for the cuboidal defect as the DRS components, especially the side minima and maxima, are more extended (Fig. 5.2).

Measurement   The specimen under test (Fig. 5.3) consists of stacked aluminum sheets, each of thickness $\Delta z = 2\,\text{mm}$. The total size of the specimen compromises $L \times W \times H = 250\,\text{mm} \times 50\,\text{mm} \times 50\,\text{mm}$. It is moved relative to the cylindrical permanent magnet with a velocity $v = 0.1\,\text{m/s}$. The permanent magnet is described by a diameter

(a)

(b)
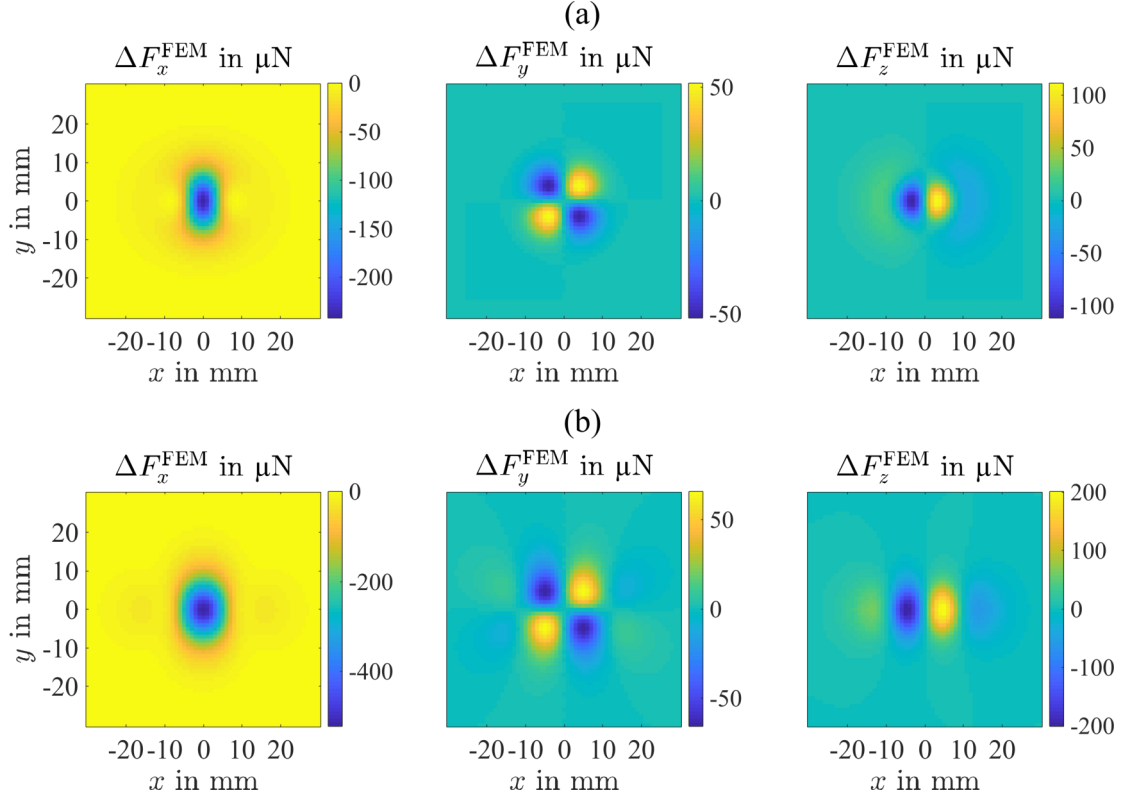
Figure 5.2: DRS components $\Delta F_x^{\mathrm{FEM}}$, $\Delta F_y^{\mathrm{FEM}}$ and $\Delta F_z^{\mathrm{FEM}}$ for the cylindrical shaped defect (a) and the cuboidal shaped defect (b), both at depth $d = 2\,\mathrm{mm}$. The side maxima and minima of the DRS components are more extended in (b).

of $D_{\mathrm{m}} = 22.5\,\mathrm{mm}$ and a height of $H_{\mathrm{m}} = 17.6\,\mathrm{mm}$ and homogeneously magnetized by $\vec{M} = B_{\mathrm{r}}/\mu_0\,\vec{e}_z$ ($B_{\mathrm{r}} = 1.43\,\mathrm{T}$). It is located $\delta z = 1\,\mathrm{mm}$ above the top surface of the specimen. A cylindrical shaped defect of diameter $D_{\mathrm{d}} = 5\,\mathrm{mm}$ and height $H_{\mathrm{d}} = 2\,\mathrm{mm}$ is located at the x-y-origin (Fig. 5.3). The defect depths $d = 2, 4$ and $8\,\mathrm{mm}$ are analyzed. This measurement setup is similar to the one described in section 3.2.1. Hence the
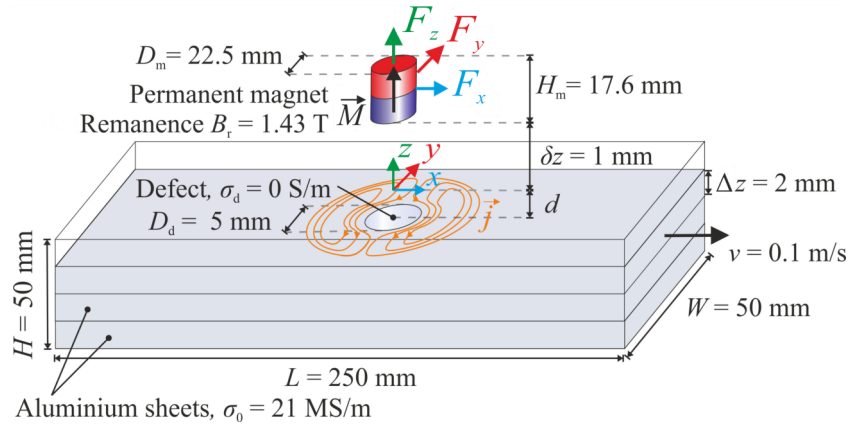
Figure 5.3: Measurement setup: A specimen of stacked aluminum sheets containing a defect is moved relative to a cylindrical permanent magnet.

preprocessing steps and the resulting DRS components of the 25 repeated measurements are identical.

5.2.2 Diameter-Depth Scan (cylindrical defect)

It is assumed that the defect height $H_\mathrm{d} = 2\,\mathrm{mm}$ is known and equal to the aluminum sheet thickness Δz. Further, it is assumed that the defect shape is cylindrical. The DRS is calculated by AFS (section 2.1.4.2) and by EAA (section 2.1.4.3). For the EAA that considers an extended area around the defect for the calculation of the DRS (section 2.1.4.3), an appropriate size of the extended area has to be chosen. The size of the extended area is represented by the extension factor ε (2.32). For that purpose, the DRS components for the cylindrical shaped defect at depth $d = 2\,\mathrm{mm}$ are calculated for $\varepsilon = [0, 1, 2, \ldots, 10]$ and compared to the DRS components obtained by FEM (Fig. 5.2 a) using the NRMSE (2.31). Fig. 5.4 shows the NRMSE for the different extension factors ε.
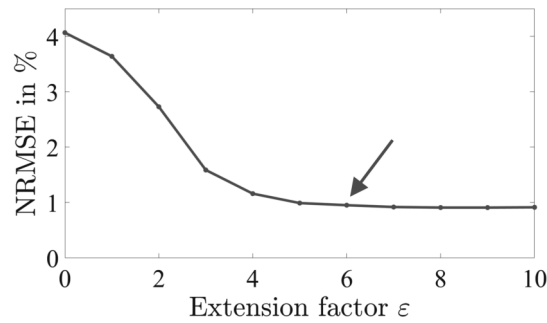
Figure 5.4: Parameter studies of an appropriate extension in EAA for a cylindrical defect: A stable saturation of NRMSE without noticeable further improvement is reached at $\varepsilon \approx 6$ (arrow).

The extension factor is chosen as $\varepsilon = 6$, as the NRMSE starts to saturate at this point (Fig. 5.4, arrow). A further increasing of the extension factor ε only leads to a small further decrease of the NRMSE, but the computational time increases according to (2.33). The cylindrical defect shows a cross-sectional shape in x-y-direction of a circle. In consequence, the main axes lengths c_x and c_y are equal to the defect diameter $D_\mathrm{d} = 5\,\mathrm{mm}$. Thus, the area A_ext that is taken into account for EAA equals $A_\mathrm{ext} = 30\,\mathrm{mm} \times 30\,\mathrm{mm}$ in x- and y-direction around the center of the defect according to (2.32). This area increases according to (2.32) for cylindrical defects of larger diameters.

For the diameter-depth scan, different possible defect diameters $D_\mathrm{d} = 1, 3, 5, \ldots, 50$ mm are used for the calculations. The calculations are performed from metal layer 1 (depth $d = 0\,\mathrm{mm}$) to metal layer 11 (depth $d = 20\,\mathrm{mm}$). For each calculation, the NRMSE between the DRS calculated by AFS or EAA and the DRS obtained from FEM

simulations or measurements is determined as

$$
\mathrm{NRMSE} = \frac{1}{3} \sum_{i=x,y,z} \frac{\sqrt{\frac{1}{N} \sum_{n=1}^{N} \left(\Delta F_{n,i}^{\mathrm{AFS/EAA}} - \Delta F_{n,i}^{\mathrm{FEM/meas}} \right)^2}}{\min\left[R^{\mathrm{AFS/EAA}}, R^{\mathrm{FEM/meas}} \right]}
$$
$$
\text{with } R^{\mathrm{AFS/EAA}} = \max\left(\Delta \vec{F}_i^{\mathrm{AFS/EAA}} \right) - \min\left(\Delta \vec{F}_i^{\mathrm{AFS/EAA}} \right)
$$
$$
\text{with } R^{\mathrm{FEM/meas}} = \max\left(\Delta \vec{F}_i^{\mathrm{FEM/meas}} \right) - \min\left(\Delta \vec{F}_i^{\mathrm{FEM/meas}} \right). \tag{5.1}
$$

The NRMSE is the mean of the errors of x-, y- and z-components for N observation points. At each layer, the diameter, that results in the lowest NRMSE, is determined. The layer with the lowest NRMSE gives the result for the depth and the diameter of the defect determined by the diameter-depth-scan.

5.2.3 Length-Width-Depth Scan (cuboidal defect)

The length-width-depth scan also assumes that the defect height $H_{\mathrm{d}} = 2\,\mathrm{mm}$ is known. The defect shape is assumed to be cuboidal. The DRS is calculated for different length-width-combinations $L_{\mathrm{d}} = 1, 2, \ldots 50\,\mathrm{mm}$ and $W_{\mathrm{d}} = 1, 2, \ldots 50\,\mathrm{mm}$ by AFS (section 2.1.4.2) and by EAA (section 2.1.4.3). Similarly to the diameter-depth scan an appropriate extension factor ε has to be chosen for the EAA. For that purpose, the DRS components are calculated by EAA for varying extension factors $\varepsilon = [0, 1, 2, \ldots, 7]$ for the cuboidal defect of $12\,\mathrm{mm} \times 2\,\mathrm{mm} \times 2\,\mathrm{mm}$ and compared to the DRS components computed by FEM (Fig. 5.2 b) using the NRMSE (2.31). Fig. 5.5 shows the NRMSE for the different extension factors ε.

The extension factor is chosen as $\varepsilon = 5$, as no further decreasing of the NRMSE can be observed (Fig. 5.5, arrow). Thus, for the $12\,\mathrm{mm} \times 2\,\mathrm{mm} \times 2\,\mathrm{mm}$ defect the extended area equals $A_{\mathrm{ext}} = 84\,\mathrm{mm} \times 84\,\mathrm{mm}$ in x- and y-direction around the center of the
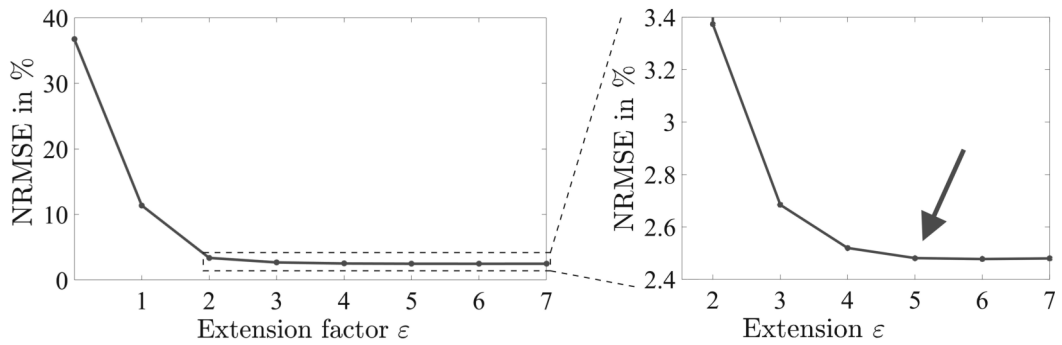
Figure 5.5: Parameter studies of an appropriate extension in EAA for a cuboidal defect: A stable saturation of NRMSE without noticeable further improvement is reached at $\varepsilon \approx 5$ (arrow).

defect according to (2.32). This area changes according to (2.32) for other length-width combinations of cuboidal defects.

For the length-width-depth scan, the calculations are applied from 1$^{\text{st}}$ to 11$^{\text{th}}$ metal layer. The NRMSE is calculated similarly to (5.1), but only the x- and the z-component are used, since including the y-component yielded partly instable reconstruction results. At each layer, the length-width-combination, that results in the lowest NRMSE, is determined. The layer with the lowest NRMSE gives the result for the depth, the length and the width of the defect determined by the length-width-depth-scan.

5.3 Results and Discussion

Simulations   Fig. 5.6 shows the cylindrical defects obtained by diameter-depth scan for each of the investigated aluminum layers. The reconstructed defects are color-coded according to the corresponding NRMSE values. The lowest NRMSE values correspond to the color red, indicating a possible defect position as a hot spot. The diameter-depth scan using the EAA yields correct depth estimation for all three investigated defect depths $d = 2, 4$ and $8\,\text{mm}$ as the minimal NRMSE values can be found at the correct depths (Fig. 5.6, right column, arrows). The diameter-depth-scan with AFS (Fig. 5.6, left column) yields correct depth estimation for $d = 2, 4$ and $8\,\text{mm}$. The diameter-depth scan with EAA determined the correct defect diameter $D_{\text{d}} = 5\,\text{mm}$ (Fig. 5.6, right column, bold circles). A too large defect diameter of $D_{\text{d}} = 7\,\text{mm}$ is determined by the diameter-depth scan with AFS (Fig. 5.6, left column). The diameter-depth scans with both forward solutions show that the minimal NRMSE increase with increasing defect depth. Additionally, the minimal NRMSE values become less distinct. However, the diameter-depth scan with EAA still yields more distinct minimal NRMSE values than the diameter-depth scan with AFS (Fig. 5.6).

The results of the length-width-depth scan based on the AFS are shown in Fig. 5.7 for the aluminum layers 1 to 4. It shows the NRMSE color-coded, where the minimal NRMSE of 6.1 % at the correct depth $d = 2\,\text{mm}$ corresponds to the defect size $L_{\text{d}} \times W_{\text{d}} = 7\,\text{mm} \times 10\,\text{mm}$ (Fig. 5.7, asterisk). The layer-wise minimum (Fig. 5.7, asterisk) further moves from the left bottom corner to the top center for the layers 5 to 11, which are not depicted here.

The results using the forward solution EAA are shown in Fig. 5.8. The lowest NRMSE can be found in layer 2, too. Thus, the correct defect depth is detected. The NRMSE of 1.7 % is smaller compared to AFS and corresponds to a length and width of the defect of $L_{\text{d}} \times W_{\text{d}} = 11\,\text{mm} \times 2\,\text{mm}$, which is closer to the correct extensions of $L_{\text{d}} \times W_{\text{d}} = 12\,\text{mm} \times 2\,\text{mm}$ than achieved by AFS. A larger defect is estimated for deeper metal layers as the layer-wise minimum (Fig. 5.8, asterisk) moves from the bottom left corner to the right center for layers 5 to 11, which are not depicted here.
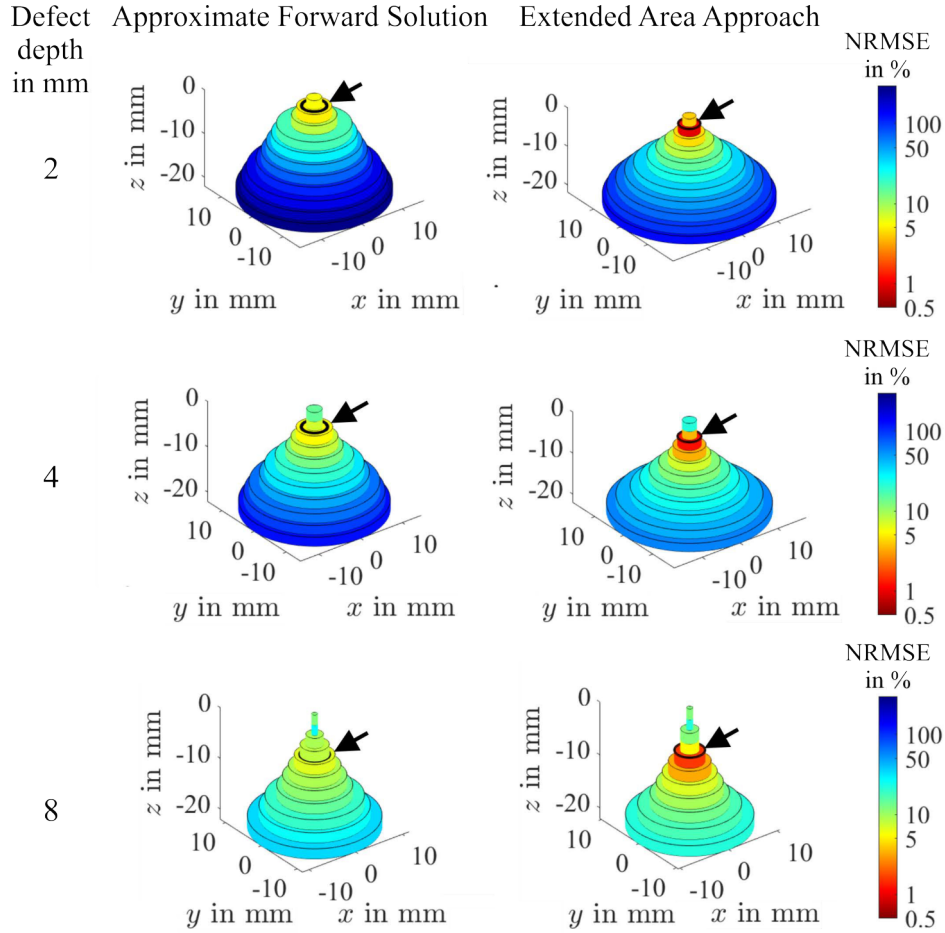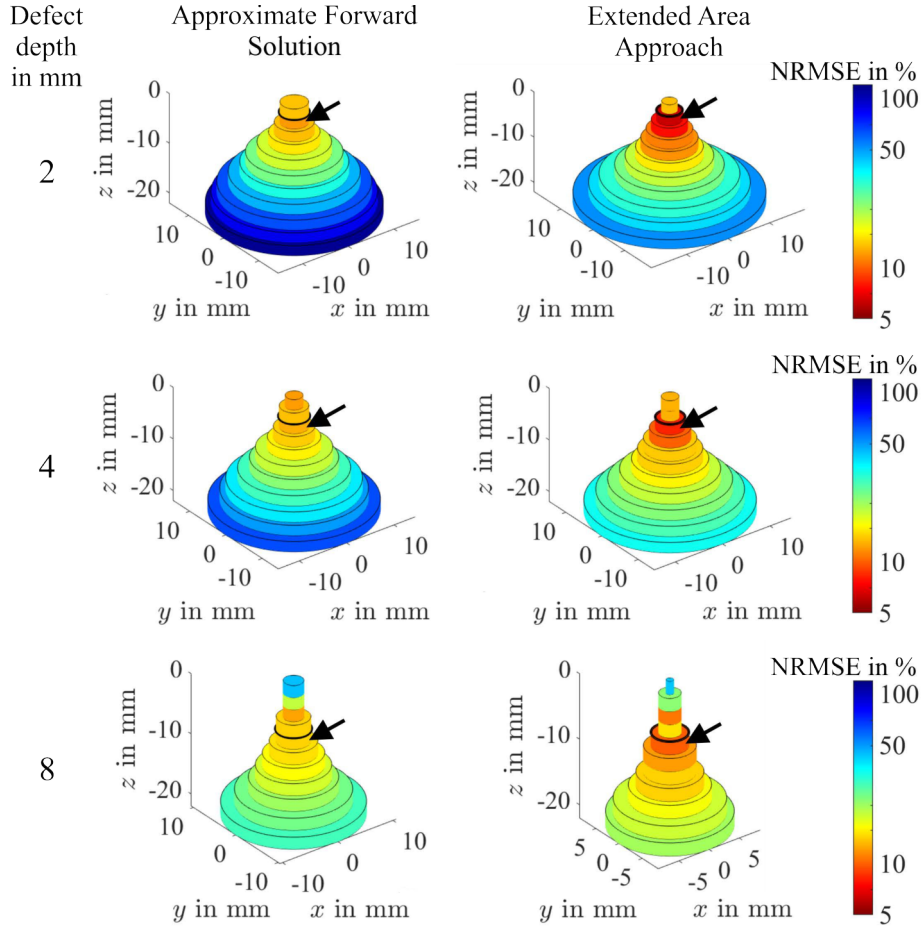
Figure 5.6: Results of diameter-depth scan using AFS (left) and EAA (right) for DRSs obtained from FEM simulations investigating cylindrical defects at the depths $d = 2, 4$ and $8\,\mathrm{mm}$: Determined cylindrical defects for each of the investigated aluminum layers are color-coded according to the corresponding NRMSE values. The defects with the lowest NRMSE values indicate the estimated defect depths. The correct defect depths and diameters are indicated by arrows and bold circles, respectively.

In order to show the direct comparison of AFS and EAA regarding the defect reconstruction performance, the minimal NRMSE values of each metal layer (Fig. 5.7 and Fig. 5.8, asterisks) are visualized in Fig. 5.9 with the corresponding defect extensions. It can be observed that the NRMSE values are larger for AFS compared to EAA. The length-width-depth scan based on EAA shows a steady increase of the estimated defect extensions for deeper metal layers (Fig. 5.9 b). In contrast, the length-width-depth scan based on AFS shows the estimation of much larger defects than expected for the metal layers 6 to 9 (Fig. 5.9 a, side views). This behavior occurs as the corresponding length-width-NRMSE functions show a structure with two minima within the observed parameter range. Fig. 5.10 a shows this behavior exemplary for metal layer 6. In contrast, the length-width-NRMSE functions based on EAA show a structure with only one minimum that is present for all 11 observed metal layers and explains the steady
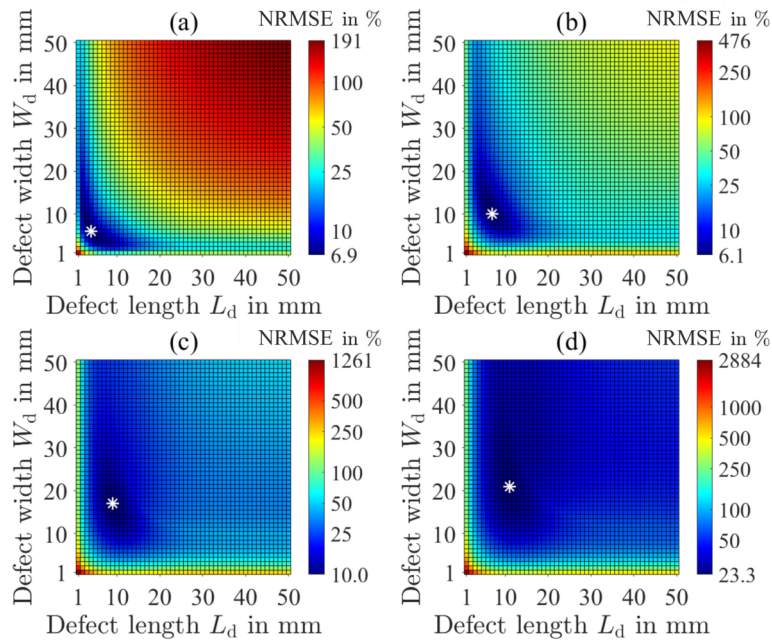
Figure 5.7: Detailed view on length-width-depth scan based on AFS for metal layers 1-4 (a)-(d). NRMSE values for different length-width-combinations of the possible defect are color-coded. The limits of the color bar indicate the minimal and maximal NRMSE of each layer. The white asterisks indicate the length-width combination of each layer with minimal NRMSE.
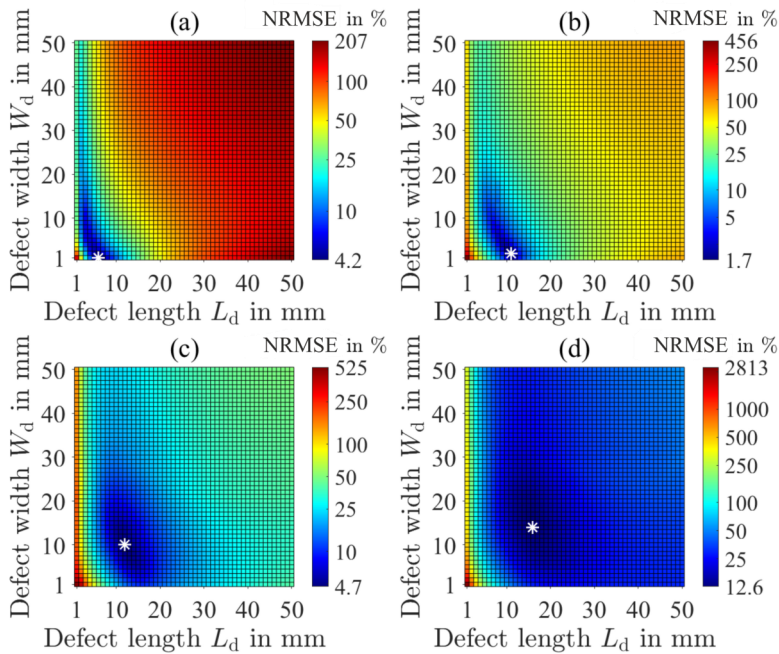
Figure 5.8: Detailed view on length-width-depth scan based on EAA for metal layers 1-4 (a)-(d). NRMSE values for different length-width-combinations of the possible defect are color-coded. The limits of the color bar indicate the minimal and maximal NRMSE of each layer. The white asterisks indicate the length-width combination of each layer with minimal NRMSE.
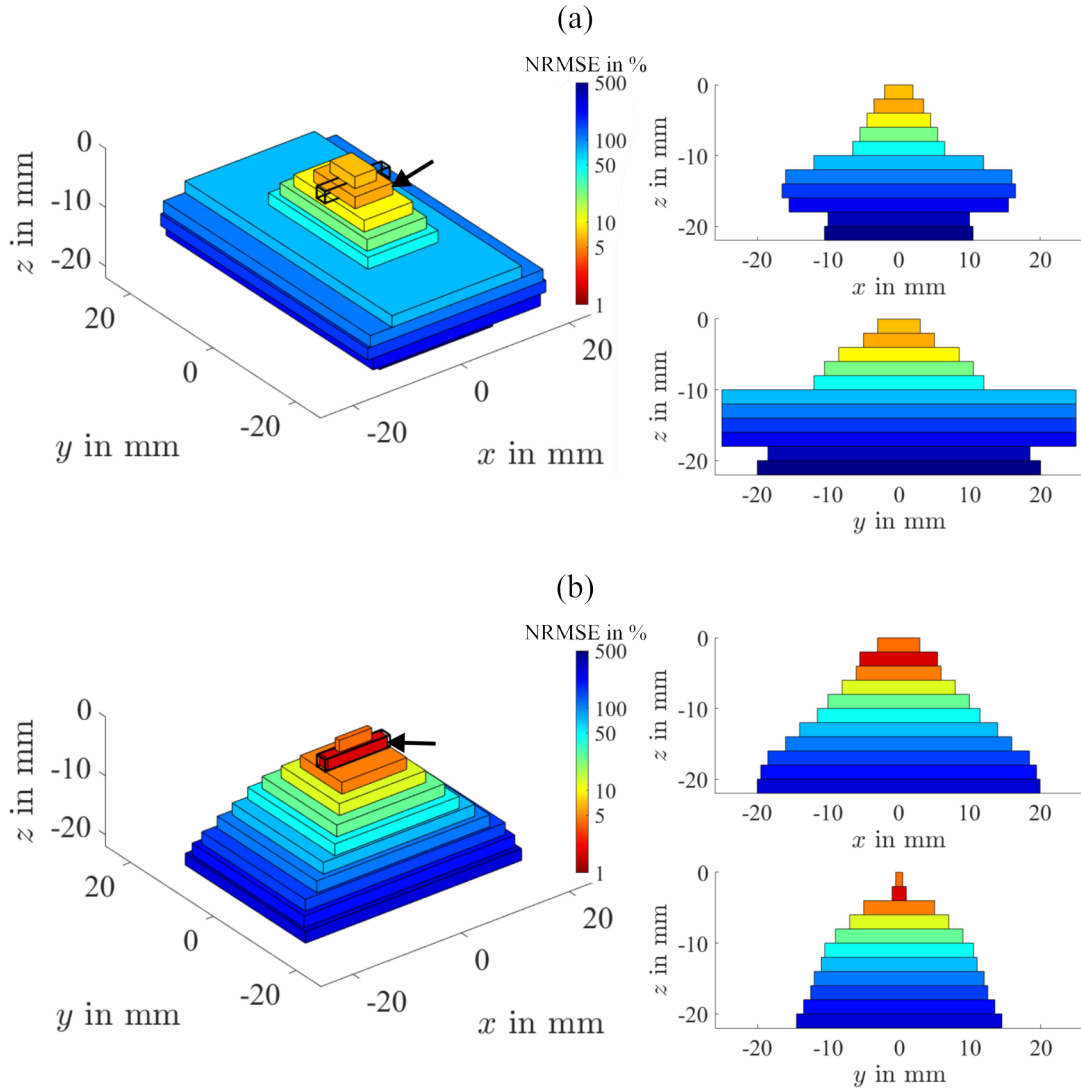
Figure 5.9: Results of length-width-depth scan using AFS (a) and EAA (b) for DRS obtained from FEM simulations at the depth $d = 2\,\text{mm}$: Determined cuboidal defects for each of the investigated aluminum layers are color-coded according to the corresponding NRMSE values. The defects with the lowest NRMSE values indicate the estimated defect depths. The correct defect depth is indicated by an arrow. The correct cuboidal defect is shown by bold black lines.

increase of the defect extensions. Fig. 5.10 b shows the structure with one minimum exemplary for metal layer 6.
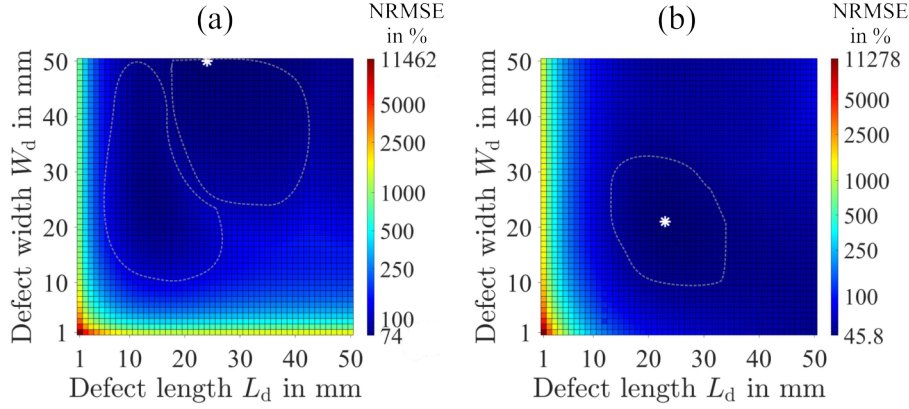
Figure 5.10: Detailed view on the length-width-depth scan for metal layer 6 with two minimum regions (dashed lines) for AFS (a) and one (dashed line) for EAA (b). NRMSE values for different length-width-combinations of the possible defect are color-coded. The asterisks mark the minima.

Measurements   Fig. 5.11 shows the determined defect diameters for each of the investigated aluminum layers color-coded according to the NRMSE for measurement trial no. 1. The correct defect depth is determined by the diameter-depth scan based on the EAA indicated by the minimal NRMSE values at the correct depths (Fig. 5.11, arrows). The diameter-depth scan based on AFS shows that the depth is estimated correctly only for defect at $d = 2\,\mathrm{mm}$. For $d = 4$ and $8\,\mathrm{mm}$ the depth has been estimated at 0 and $4\,\mathrm{mm}$ respectively.

Table 5.1 shows the mean defect depth $\pm$ standard deviation estimated by diameter-depth scan based on AFS and EAA and the corresponding NRMSE values from 25 measurement trials. Additionally, the determined defect diameter at the correct depth is shown as mean value $\pm$ standard deviation. The defect depth and the defect diameter have been determined correctly by the diameter-depth scan based on EAA in all cases for the investigated defect depths $d = 2, 4$ and $8\,\mathrm{mm}$. The diameter-depth scan based on AFS yielded correct defect diameters of $D_{\mathrm{d}} = 5\,\mathrm{mm}$ for the investigated defects at depth $d = 2$ and $8\,\mathrm{mm}$. For $d = 4\,\mathrm{mm}$, in $4/25$ cases the correct diameter has been determined. The correct depth has been estimated for $d = 2\,\mathrm{mm}$ for all 25 measurement trials. For the investigated defect depths $d = 4$ and $8\,\mathrm{mm}$, the defect depths have been estimated at $0.72 \pm 0.98\,\mathrm{mm}$ and $4 \pm 0\,\mathrm{mm}$, respectively. For the investigated depth $d = 4\,\mathrm{mm}$, depths of $0\,\mathrm{mm}$ in $16/25$ cases and $2\,\mathrm{mm}$ in $9/25$ cases have been determined.

The AFS shows lower NRMSE values for defects closer to the upper surface of the specimen, what might partially explain the estimation of the defect depth above the correct ones (Table 5.1).

Figure 5.11: Results of diameter-depth scan using AFS (left) and EAA (right) for DRSs obtained from measurement trial no.1 investigating cylindrical defects at the depths $d = 2, 4$ and $8\,\mathrm{mm}$: Determined cylindrical defects for each of the investigated aluminum layers are color-coded according to the corresponding NRMSE values. The defects with the lowest NRMSE values indicate the estimated defect depths. The correct defect depth and diameter are indicated by arrows and bold circles, respectively.

Table 5.1: Results of diameter-depth scan based on on AFS and EAA of 25 measurement trials: Determined defect depth d, corresponding NRMSE and determined defect diameter D_d at the correct depth are shown as mean $\pm$ standard deviation.

Defect depth	$d = 2\,\mathrm{mm}$		$d = 4\,\mathrm{mm}$		$d = 8\,\mathrm{mm}$	
Forward solution	AFS	EAA	AFS	EAA	AFS	EAA
Determined defect depth d in mm	2 ± 0	2 ± 0	0.72 ± 0.98	4 ± 0	4 ± 0	8 ± 0
NRMSE in %	12.30 ± 0.22	6.38 ± 0.19	12.47 ± 0.17	7.00 ± 0.21	13.62 ± 0.26	10.27 ± 0.35
Determined defect diameter D_d in mm	5 ± 0	5 ± 0	6.68 ± 0.75	5 ± 0	5 ± 0	5 ± 0

5.4 Conclusion

In terms of defect reconstruction performance, the correct defect depths were determined for simulated data sets with cylindrical and cuboidal defects for both forward solutions AFS and EAA. For the analyzed measurement data, the deeper cylindrical defects (depths of 4 and 8 mm) where reconstructed above the correct depths if the forward solution AFS was used. In contrast, the correct depths were estimated with EAA. The AFS assumes an infinitely extended conductor in x- and y-direction (section 2.1.4.2). That might partly explain why the reconstructed depths are correct for the simulated data sets, where the extensions of the specimen are larger (Fig. 5.1) in comparison to the measurement setup (Fig. 5.3). A similar behavior was observable for the adapted Landweber algorithm that also used the AFS as forward solution (Chapter 4). In contrast, the minimum norm estimation with Tikhonov-Phillips-regularization and elastic net regularization determined the correct defect depths for both simulated and measured data (Chapter 3). It also used the AFS as forward solution.

For both simulated and measured data, the diameter-depth scans for cylindrical defects and the length-width-depth scan for the cuboidal defect revealed more accurate diameter and length-width estimations of the defect with EAA compared to AFS.

The more accurate EAA is more expensive than AFS regarding the computational cost. The computation time of one single DRS point ranges [1.1 ms, 232.9 ms] for AFS and [3.1 ms, 7.4 s] for EAA. The computations have been performed with the software MATLAB$^{\circledR}$ R2017a with an Intel$^{\circledR}$ Xeon E5-2697v3 processor and 384 GB of RAM, which is used for the expensive FEM calculations, where the calculation of one single DRS point is in the order of minutes.

However, the EAA is optimized for the symmetry line of the system ($y = 0$) and designed for defects of uniform shape [18]. Additionally, the iterative calculation scheme (section 2.1.4.3) requires non-linear inverse methods for defect reconstruction.

In consequence, a novel forward solution is needed that shows no restrictions regarding the defect shape and allows the application of fast linear inverse methods.

6 Single Voxel Approach

6.1 Introduction

The quality of the defect reconstruction depends on various factors such as the forward solution, the inverse method, the measurement data, et cetera. Previous studies used the approximate forward solution (AFS) [10,17,19,22] and the extended area approach (EAA) [18,24] to model the DRS.

The AFS is a simple and fast forward solution, but restricted to defects of uniform shape, like a square or a circle. The EAA is more accurate than the AFS [18] but is also limited to regular shaped defects, e.g. of rectangular or elliptical shape. Both methods assume a single defect far away from the specimen edges.

The direct application of field computation methods, like FEM, is not considered for forward calculation, as the computation time of the DRS for one observation point is in the order of minutes. Additionally, a new calculation is necessary for every change in the relative position between the permanent magnet and the specimen to implement the relative motion. For the reconstruction of defect properties, several observation points are necessary. Previous work used observation points in the range of 2,000-4,000 [17,19,22,24]. This would lead to an impractically high calculation time for the DRS components.

The current study aims to find a more accurate forward solution that overcomes the limitations of AFS and EAA but is also fast and easy to include in a linear defect reconstruction scheme. For that purpose, the novel single voxel approach (SVA) is introduced. It models the DRS as a superposition of DRSs from $1\,\mathrm{mm} \times 1\,\mathrm{mm} \times 1\,\mathrm{mm}$ defects. The single defect DRSs are calculated in advance using the boundary element source method (BESM) (section 2.1.2.2) [38]. The SVA is compared to the FEM using the NRMSE, for a setup with an isotropic conducting specimen with defects of different shapes and depths. Additionally, the NRMSE values are compared to those of the forward solutions AFS and EAA.

This chapter contains methods and results that have been presented at [28] and are published in [29].
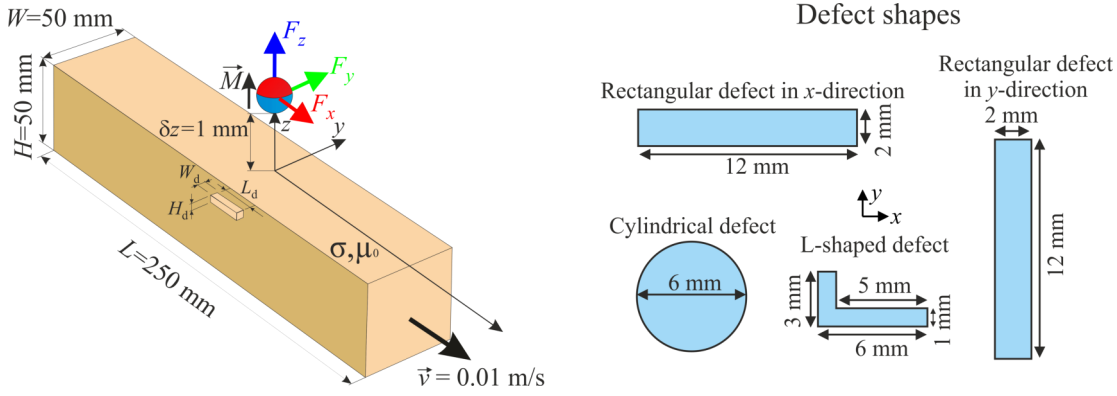
Figure 6.1: Simulation setup and investigated defect shapes.

6.2 Materials and Methods

6.2.1 Setup

The setup (Fig. 6.1) consists of an aluminum specimen of size $L \times W \times H = 250\,\text{mm} \times 50\,\text{mm} \times 50\,\text{mm}$ with an isotropic conductivity of $\sigma_0 = 20.41\,\text{MS/m}$. A spherical permanent magnet is located $\delta z = 1\,\text{mm}$ above the top surface of the specimen. It is characterized by a homogeneous magnetization of $\vec{M} = 9.28 \cdot 10^5\,\text{A/m}\,\vec{e}_z$. The diameter of the magnet is $D_\text{m} = 15\,\text{mm}$. The specimen is moved relative to the permanent magnet in x-direction with a velocity of $\vec{v} = 0.01\,\text{m/s}\,\vec{e}_x$. Defects of conductivity $\sigma_d = 0$, with the shapes depicted in Fig. 6.1, are investigated. All defects have a height H_d of $2\,\text{mm}$, except the L-shaped defect with a height H_d of $1\,\text{mm}$. The defects are placed centrally in the x-y-plane. The two different defect depths $d = 2\,\text{mm}$ and $d = 10\,\text{mm}$ are considered.

The DRS components $[\Delta F_x^\text{FEM}]_{A \times B}$, $[\Delta F_y^\text{FEM}]_{A \times B}$ and $[\Delta F_z^\text{FEM}]_{A \times B}$ are computed at equally distributed permanent magnet positions within $|x| \leq 30\,\text{mm}$ and $|y| \leq 25\,\text{mm}$ at $z = 8.5\,\text{mm}$. The z-position corresponds to the center of the spherical permanent
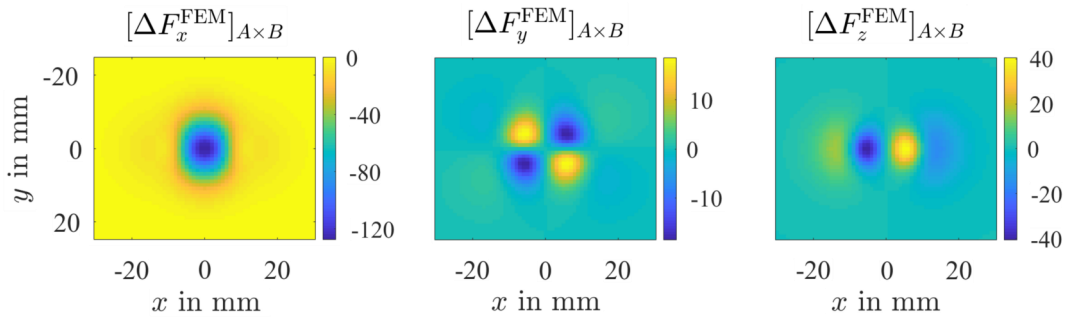
Figure 6.2: Defect response signal components $\left[\Delta F_x^\text{FEM}\right]_{A \times B}$, $\left[\Delta F_y^\text{FEM}\right]_{A \times B}$ and $\left[\Delta F_z^\text{FEM}\right]_{A \times B}$ in µN: obtained by FEM simulations for the rectangular defect in x-direction (Fig. 6.1) at depth $d = 2\,\text{mm}$.

magnet. The distances between the observation points are $d_x = d_y = 1\,\text{mm}$ in x- and y-direction. The weak reaction approach is applied [33] and solved by FEM as described in section 2.1.2.2. Fig. 6.2 shows the DRS components $[\Delta F_x^{\text{FEM}}]_{A \times B}$, $[\Delta F_y^{\text{FEM}}]_{A \times B}$ and $[\Delta F_z^{\text{FEM}}]_{A \times B}$ with $A = 61$ and $B = 51$ for the rectangular defect in x-direction at $d = 2\,\text{mm}$. The DRSs obtained by FEM serve as reference DRSs in this study.

In order to evaluate and compare the accuracy of AFS (section 2.1.4.2), EAA (section 2.1.4.3) and the novel SVA against FEM, the NRMSE between reference DRSs components obtained by FEM and each of the investigated forward solutions is determined by

$$
\begin{aligned}
\text{NRMSE} &= \frac{1}{3} \sum_{i=x,y,z} \frac{\sqrt{\frac{1}{N} \sum_{n=1}^{N} \left(\Delta F_{n,i} - \Delta F_{n,i}^{\text{FEM}} \right)^2}}{\min\left[R, R^{\text{FEM}}\right]} \\
&\text{with } R = \max\left(\Delta \vec{F}_i\right) - \min\left(\Delta \vec{F}_i\right) \\
&\text{with } R = \max\left(\Delta \vec{F}_i^{\text{FEM}}\right) - \min\left(\Delta \vec{F}_i^{\text{FEM}}\right).
\end{aligned}
\tag{6.1}
$$

The NRMSE is the mean of the errors of x-, y- and z-components for $N = A \times B$ observation points.

6.2.2 Single Voxel Approach

The fixed setup given in Fig. 6.1 is considered. Within this setup, a region of interest (ROI) is defined, where a possible defect is expected. This ROI is discretized into K voxels, in this study of size $1\,\text{mm} \times 1\,\text{mm} \times 1\,\text{mm}$. In advance, every single voxel of this ROI is considered as a $1\,\text{mm} \times 1\,\text{mm} \times 1\,\text{mm}$ single defect and the DRS components are calculated for the previously described observation points (section 6.2.1). The main idea is that the DRS components of a defect $[\Delta F_x^{\text{SVA}}]_{A \times B}$, $[\Delta F_y^{\text{SVA}}]_{A \times B}$ and $[\Delta F_z^{\text{SVA}}]_{A \times B}$ can be determined by the superposition of the DRSs from the single voxel defects as

$$
\left[\Delta F_i^{\text{SVA}}\right]_{A \times B} = \sum_{k=1}^{K} \theta_k \left([\Delta F_{k,i}]_{A \times B} \right) \text{ with } i \in \{x, y, z\}.
\tag{6.2}
$$

The variable θ_k depicts whether a single voxel DRS contributes to the DRS components ($\theta_k = 1$) or not ($\theta_k = 0$). Considering the forward problem, only single voxel DRS components from voxels belonging to the defect contribute to the DRS components.

Regarding a defect reconstruction, the DRS components obtained from measurements or FEM simulations $[\Delta F_x^{\text{FEM/meas}}]_{A \times B}$, $[\Delta F_y^{\text{FEM/meas}}]_{A \times B}$ and $[\Delta F_z^{\text{FEM/meas}}]_{A \times B}$ can be arranged in a vector $\Delta \vec{F}^{\text{FEM/meas}} \in \mathbb{R}^{3(A \cdot B) \times 1}$. Additionally, the sums of (6.2) can be arranged in a matrix $[L]_{(3(A \cdot B) \times K)}$ and a defect identification vector $\vec{\theta} \in \mathbb{R}^{K \times 1}$ with entries θ_k is built. With the vector-matrix-form $\Delta \vec{F}^{\text{FEM/meas}} = [L]\vec{\theta}$, linear inverse

methods are applicable. If the single voxel DRS components are calculated for the ROI once in advance by any forward computation method, various defect shapes at different locations can be reconstructed with linear inverse methods. The BESM [38] is chosen as relatively fast and easy method to compute the single voxel DRS components in advance.

The superposition of single voxel DRSs (6.2) represents a linearization. The DRS obtained from the superposition of two neighboring voxels in x-direction is smaller than the DRS obtained by BESM of a corresponding $2\,\text{mm} \times 1\,\text{mm} \times 1\,\text{mm}$ defect. For the neighboring of two voxels in y-direction, it is the other way round. The reason is that the calculated eddy current density distributions vary for the neighboring single voxels and the equivalent defect. The deviation is enhanced if more voxels are neighbored. Consequently, a linearization adjustment is applied as a second step in the SVA method. The adjustment is applied directly to the single voxel DRSs components. The neighborhoods of single defect voxels in x- and y-direction are considered. DRSs components are calculated for defects with the dimensions $a \times 1\,\text{mm} \times 1\,\text{mm}$ by BESM and by SVA for $a = 2, 4$, and $6\,\text{mm}$. Therefore, the linearization adjustment for neighborhood in x-direction is calculated by point-wise division

$$[\alpha_x^a]_{C \times D} = \frac{\left[\Delta F_x^{\text{BESM}(a)}\right]_{C \times D}}{\left[\Delta F_x^{\text{SVA}(a)}\right]_{C \times D}}, \ [\alpha_y^a]_{C \times D} = \frac{\left[\Delta F_y^{\text{BESM}(a)}\right]_{C \times D}}{\left[\Delta F_y^{\text{SVA}(a)}\right]_{C \times D}},$$

$$[\alpha_z^a]_{C \times D} = \frac{\left[\Delta F_z^{\text{BESM}(a)}\right]_{C \times D}}{\left[\Delta F_z^{\text{SVA}(a)}\right]_{C \times D}}. \tag{6.3}$$

The linearization adjustments are calculated for the depths $d = 2\,\text{mm}$ and $10\,\text{mm}$ separately. A 2D median filter of the neighboring values treats the cases where a division by 0 would be present. The defects are placed centrally in the x-y-plane and the adjustment functions are calculated for the area of $C \times D$ points that is larger than the area of the observation points $A \times B$. Equivalently for neighborhood in y-direction, $[\beta_x^b]_{C \times D}$, $[\beta_y^b]_{C \times D}$, $[\beta_z^b]_{C \times D}$ are calculated for defects with the dimensions $1\,\text{mm} \times b \times 1\,\text{mm}$, where $b = 2, 4$, and $6\,\text{mm}$.

The linearization adjustment is applied voxel-wise (Fig. 6.3). The dominant neighborhood for the k-th single voxel of a rectangular defect in x-direction (Fig. 6.3 c, green) is in x-direction, where $a = 6\,\text{mm}$ (Fig. 6.3 c, orange rectangle) is used. The pre-calculated adjustment functions with $C \times D$ elements (Fig. 6.3 b) are shifted such that the position fits the position of the neighborhood (orange rectangle) and cut into $A \times B$ elements (Fig. 6.3 d). In the case where the neighboring voxels are longer than the best fitting neighborhood, the neighborhood is shifted like a moving window (Fig. 6.3 c). The adjustment functions are multiplied point-wise to the single voxel DRS components.
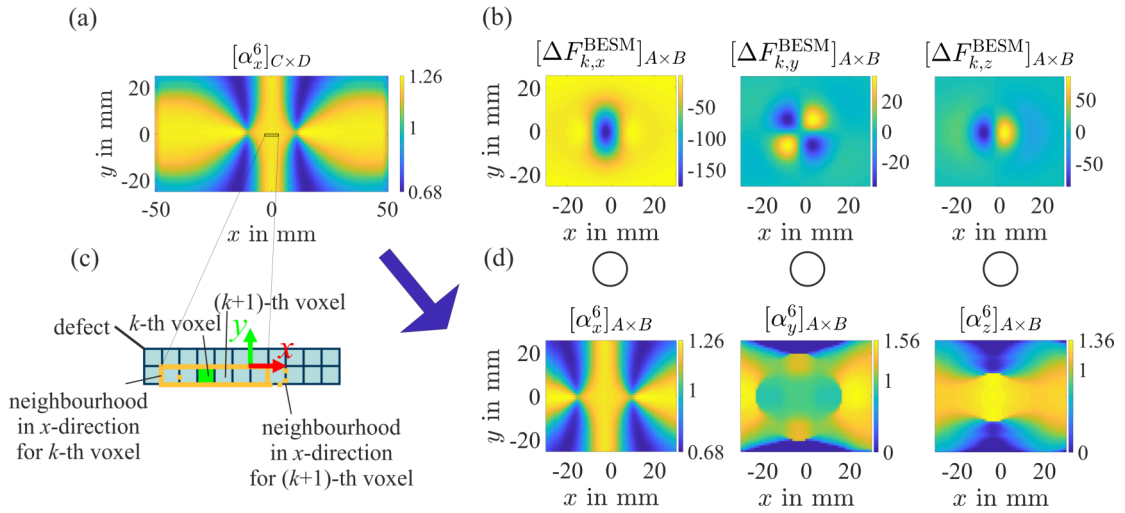
Figure 6.3: Principle of linearization adjustment exemplary for the rectangular defect in x-direction: For the k-th voxel (green, c), the neighborhood in x-direction (6 mm, orange rectangle) is used. The adjustment function components $\left[\alpha_x^6\right]_{C\times D}$, $\left[\alpha_y^6\right]_{C\times D}$ and $\left[\alpha_z^6\right]_{C\times D}$ are shifted such that the position fits to the position of the neighborhood (orange rectangle). The cut adjustment functions (d) are multiplied point-wise with the k-th single voxel DRS components (b), where the color scales are in µN.

6.3 Results

The calculation of the DRSs by AFS, EAA and SVA for different defect shapes leads to the NRMSE values (6.1) in comparison to FEM simulations shown in the Table 6.1 for the defect depths $d = 2\,\text{mm}$ and $10\,\text{mm}$. Fig. 6.4 shows exemplary DRS components for the rectangular defect in x-direction. The NRMSE values are the smallest for SVA in all investigated cases. The improvement is more pronounced for the deep defects at $d = 10\,\text{mm}$. For AFS and EAA, the NRMSE values have a larger increase from $d = 2\,\text{mm}$ to $d = 10\,\text{mm}$ compared to the SVA.

6.4 Discussion

The AFS shows the lowest errors for the cylindrical and the L-shaped defects (Table 6.1), where the relatively low error for the L-shaped defect might be explained by error compensation as the defect consists of two parts, one with extension in x-direction and one with extension in y-direction. The NRMSE values increase for deeper defects, which is in line with previous work [22]. Despite these NRMSEs, appropriate size and depth estimation of cylindrically shaped defects were conducted in [17,19,22]. A correct depth estimation is possible with AFS even if the estimated defect size is not correct [24].
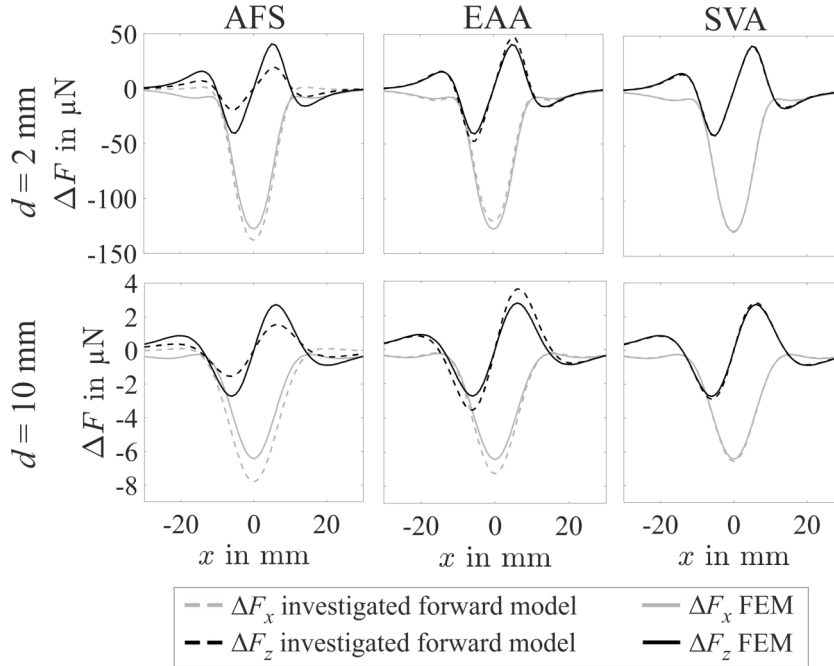
Figure 6.4: DRS components ΔF_x (gray) and ΔF_z (black) modeled by AFS (left), EAA (middle) and SVA (right) in dashed lines compared to FEM (solid lines) for the rectangular defect in x-direction at the depths $d = 2\,\text{mm}$ (top) and $d = 10\,\text{mm}$ (bottom). DRS components are shown for the symmetry line ($y = 0\,\text{mm}$) where ΔF_y vanishes.

Table 6.1: NRMSE in % comparing the DRSs calculated by AFS, EAA and SVA in comparison to FEM for different defect shapes at the depths $d = 2$ and $10\,\text{mm}$.

Defect depth d	2 mm			10 mm		
Forward solution / Defect	AFS	EAA	SVA	AFS	EAA	SVA
Rectangular (x-direction)	6.65	3.60	1.93	7.89	7.86	1.98
Rectangular (y-direction)	6.81	2.81	1.14	11.86	6.90	1.43
Cylindrical	4.13	1.42	0.52	8.92	6.38	1.27
L-shape	4.64	1.57	1.52	7.42	4.46	2.31

The EAA for isotropic conductors shows lower NRMSE values compared to AFS (Table 6.1). Previous work showed this improvement in terms of length and width estimation of a rectangular defect [24]. The increase of the NRMSE values for deeper defects might be partly explained by the fact that the EAA for isotropic conductors is optimized for defects relatively close to the surface [18]. The study shows that for the L-shaped defect at depth $d = 2\,\text{mm}$ low NRMSE values are achieved by EAA. For the example of the rectangular defect (x-direction), Fig. 6.4 visualizes that the EAA (Fig. 6.4, middle column) is optimized for the symmetry line as the difference from SVA (Fig. 6.4, right column) is relatively small. However, the NRMSE values are calculated from all $N = A \times B$ observation points that are necessary for a defect reconstruction.

The novel SVA shows the lowest NRMSE values for all investigated cases. The major

advantage is observed for the deep defects where the NRMSE values are smaller than 2.5 %. If the SVA would be used without the linearization adjustment functions, the NRMSE values could increase up to 9 % in the worst case. The SVA uses the BESM for the calculation of the single voxel DRSs in advance. The BESM is chosen in this particular study because it is relatively fast and easy to compute [38]. Other simulation methods are also conceivable such as FEM or the method of fundamental solutions [143].

The calculations have been performed on an Intel® CoreTM i7-4790K processor and 32 GB of RAM using MATLAB® R2018a. The calculations of the DRS components ΔF_x, ΔF_y and ΔF_z for the analyzed observation points e.g. for the rectangular defect in x-direction require 0.23 s, 165 s and 0.12 s for AFS, EAA and SVA, respectively.

The SVA can be formulated in a vector-matrix form due to the superposition principle. This allows the application of linear inverse methods in future work. The current implementation is defined for defects with low extension in z-direction. The SVA can be expanded easily for defects with high extension in z-direction by introducing a linearization adjustment for consideration of the neighborhood of voxels in z-direction.

6.5 Conclusion

The novel forward solution SVA yields smaller NRMSEs than AFS and EAA for different defect shapes and depths in the calculation of the DRS in LFE. The next step would be the formulation of the SVA in a vector-matrix form and the application of linear inverse methods for defect reconstruction.

7 Velocity Dependent Lorentz Force Evaluation: A Simulation Study

7.1 Introduction

In LFE, the defect properties such as location and shape of the defect are determined by solving an ill-posed inverse problem [10, 17, 19, 22] as also described in section 2.3.1.

The depth estimation is realized by performing the defect reconstruction separately for each conducting layer of the specimen under investigation. The analysis yields a possible defect with a corresponding error for every single layer. This error is defined as the NRMSE between the DRS obtained from measurements or simulations and the forward calculated DRS. The conducting layer with the lowest error indicates the defect depth. In LFE, the DRSs of a small defect near the top surface of the specimen and a larger and deeper defect can be similar. This leads to similar NRMSEs, aggravating the depth estimation. The problem is illustrated in Chapters 3, 4 and 5. This characterizes the LFE as an ill-posed inverse problem and the defect depth estimation as a challenging task.

Thus, the aim of the current study is, to introduce a novel principle, referred to as velocity dependent LFE, to estimate the defect depth. In LFE, the DRS amplitude increases with rising velocity. But due to the motion-evoked skin effect, the DRS of deep defects is at the same time decreased. This effect is comparable to the skin effect appearing in classical ECE, where the response signal increases with rising frequency, while the penetration depth decreases. The velocity dependent LFE uses the defect depth dependent change in DRS signals by applying different velocities.

The remaining chapter shows the investigations how the motion-evoked skin effect can be used to determine the defect depth. For that purpose, simulated data sets of a specimen consisting of stacked aluminum sheets and a cylindrical permanent magnet with different defect shapes and depths at varying velocities are investigated. From the observed behavior of the simulated DRSs, parameters for the defect depth estimation are derived.

This chapter contains methods and results that have been presented at [30] and are published in [31].

7.2 Materials and Methods

7.2.1 Setup

A specimen of stacked aluminum sheets is moved relative to a cylindrical permanent magnet (Fig. 7.1). The specimen is characterized by a size of $L \times W \times H = 250\,\text{mm} \times 50\,\text{mm} \times 50\,\text{mm}$ with each aluminum sheet of thickness $\Delta z = 2\,\text{mm}$. The aluminum sheets are specified by a conductivity of $\sigma_0 = 21\,\text{MS/m}$.
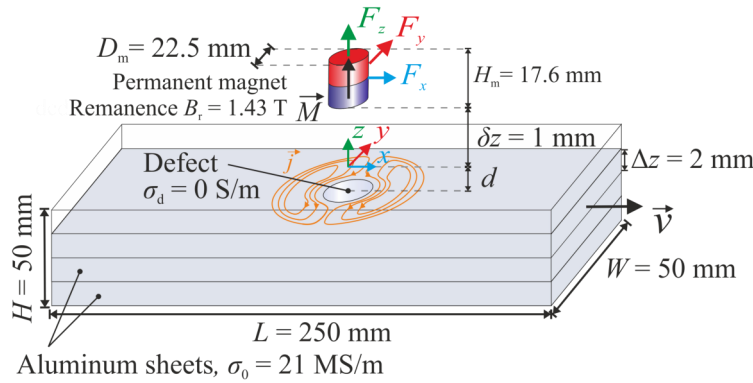
Figure 7.1: Setup: A package of stacked aluminum sheets containing a defect is moved relative to the cylindrical permanent magnet. The interaction of the induced eddy currents (orange lines) with the magnetic field leads to the Lorentz force.

The cylindrical permanent magnet is described by a diameter of $D_\text{m} = 22.5\,\text{mm}$ and a height of $H_\text{m} = 17.6\,\text{mm}$ with homogeneous magnetization $\vec{M} = B_\text{r}/\mu_0\,\vec{e}_x$ ($B_\text{r} = 1.43\,\text{T}$), where B_r describes the remanence. The permanent magnet is located at $\delta z = 1\,\text{mm}$ above the top-surface of the specimen.

Defects with the shapes depicted in Fig. 7.2 with a height of $h_\text{d} = 2\,\text{mm}$ are investigated at different depths $d = 0, 2, 4, 6, 8, 10\,\text{mm}$. The defects are located at the x-y-origin. They are characterized by the conductivity $\sigma_\text{d} = 0$. The behavior of the DRSs is analyzed for the relative velocities $\vec{v} = [0.1, 0.25, 0.5, 1, 2.5, 5, 10, 25]\,\text{m/s}\,\vec{e}_x$.

The Lorentz force components F_x and F_z are calculated along the symmetry line ($y = 0\,\text{mm}$) of the setup, where F_y vanishes. Calculations are performed with the transient moving defect approach (section 2.1.2.4) using the FEM. The consecutive observation points for x between $-30\,\text{mm}$ and $30\,\text{mm}$ have a distance of $d_x = 1\,\text{mm}$. Constant offsets are subtracted from the determined force components. These offsets are related to the force components for the same specimen without a defect. The resulting ΔF_x and ΔF_z are referred to as DRS components. Fig. 7.3 shows examples of ΔF_x (a) and ΔF_z (b) for the long rectangular defect in x-direction.
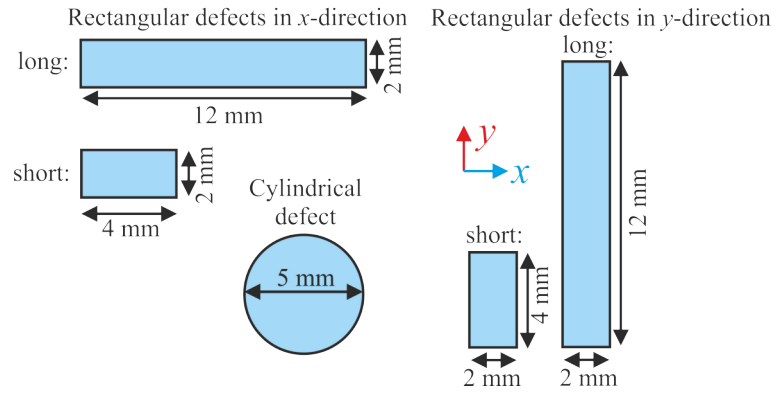
Figure 7.2: Investigated defect shapes.

7.2.2 Defect Depth Estimation Parameters

In LFE, the DRS amplitude increases with rising velocity according to (2.1) and Ohm's law for moving conductors (2.5). An increasing velocity can be considered analogously to an increasing excitation frequency like in classical ECE. An equivalent depth of penetration for LFE, which is called motion-evoked skin depth can be approximated by [20]

$$\delta = \sqrt{\frac{2D_{\mathrm{m}}}{3\pi v \mu_0 \sigma_0}}, \tag{7.1}$$

In consequence, the motion-evoked skin effect reduces the penetration depth of the induced eddy currents. Due to the decreasing penetration depth, the DRS amplitudes are additionally decreased with increasing velocity. The DRS component ΔF_x for the long rectangular defect in x-direction shows that the amplitudes (Fig. 7.3 a, red ranges) increase for the high velocity of $10\,\mathrm{m/s}$ (Fig. 7.3 a, right) compared to the low velocity of $0.1\,\mathrm{m/s}$ 7.3 a, left). This increase is reflected by the amplitude ratio (7.3 a, orange boxes). Due to the motion-evoked skin effect, this increase is smaller at the defect depth $d = 10\,\mathrm{mm}$ (Fig. 7.3 a, bottom) compared to $d = 2\,\mathrm{mm}$ (Fig. 7.3 a, top). A similar behavior can be observed for the DRS component ΔF_z (Fig. 7.3 b).

Comparing the DRS components at the velocities $v = 0.1\,\mathrm{m/s}$ and $v = 10\,\mathrm{m/s}$, a second effect is observable (Fig. 7.3). The increasing velocity leads to a slurring of the eddy current density distributions. In consequence, the DRS components are shifted in x-direction. This shift is for example represented by the position change of the main peaks of ΔF_x and ΔF_z (Fig. 7.3, red arrows). The position shift (Fig. 7.3, green boxes) is increased for the defect depth $10\,\mathrm{mm}$ (Fig. 7.3, bottom) compared to $2\,\mathrm{mm}$ (Fig. 7.3, top).
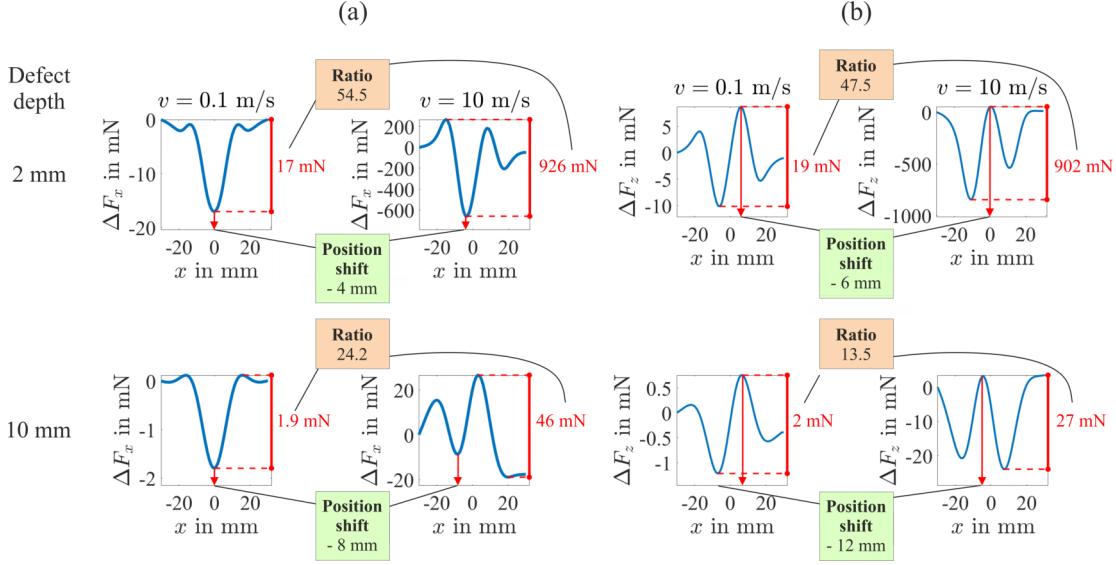
Figure 7.3: Defect response signal components ΔF_x (a) and ΔF_z (b) obtained by FEM simulations for the long rectangular defect in x-direction along the symmetry line ($y = 0\,\mathrm{mm}$) of the system: The DRS component amplitudes (ranges indicated in red) increase with increasing velocity ($v = 0.1\,\mathrm{m/s}$ (left) vs. $v = 10\,\mathrm{m/s}$ (right)), reflected by the amplitude ratio. Due to the motion-evoked skin effect, these ratios are smaller for deeper defect depth 10 mm (bottom) compared to the defect depth 2 mm (top). The increasing velocity also shifts the main peaks (red arrows) of the DRS components.

Based on these observations, the amplitude ratios r_x and r_z are defined as defect depth dependent parameters by

$$r_x = \frac{[\max(\Delta F_x) - \min(\Delta F_x)]^{v_{\mathrm{high}}}}{[\max(\Delta F_x) - \min(\Delta F_x)]^{v_{\mathrm{low}}}}, \tag{7.2}$$

$$r_z = \frac{[\max(\Delta F_z) - \min(\Delta F_z)]^{v_{\mathrm{high}}}}{[\max(\Delta F_z) - \min(\Delta F_z)]^{v_{\mathrm{low}}}}. \tag{7.3}$$

Additionally, the shifts s_x and s_z of the x-position of $\min(\Delta F_x)$ and $\max(\Delta F_z)$, respectively are derived as defect depth dependent parameters by

$$s_x = x^{v_{\mathrm{high}}}_{\min(\Delta F_x)} - x^{v_{\mathrm{low}}}_{\min(\Delta F_x)}, \tag{7.4}$$

$$s_z = x^{v_{\mathrm{high}}}_{\max(\Delta F_z)} - x^{v_{\mathrm{low}}}_{\max(\Delta F_z)}. \tag{7.5}$$

7.2.3 Parameter Studies

The velocity v_{low} is chosen as $v_{\mathrm{low}} = 0.1\,\mathrm{m/s}$. At this velocity, the secondary magnetic field from the induced eddy currents can be neglected. As a result, the DRS components
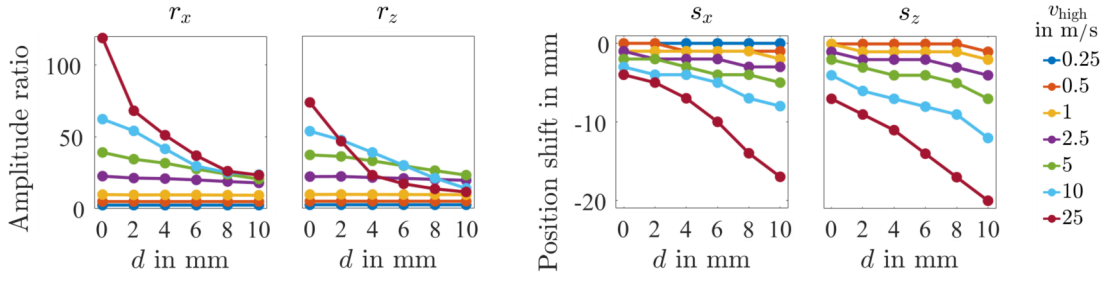
Figure 7.4: DRS amplitude ratios r_x and r_z and position shifts s_x and s_z for the long rectangular defect in x-direction depending on the defect depth d and the velocities v_{high}.
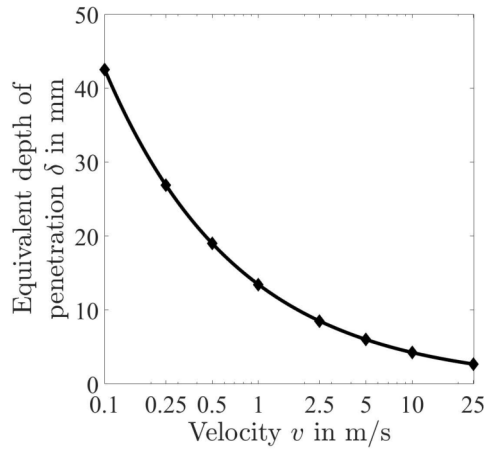
Figure 7.5: Motion-evoked skin depth (7.1) for Lorentz force evaluation depending on the relative velocity v for the setup shown in Fig. 7.1.

(Fig. 7.3 a and b, left) are not shifted relative to the defect location. In consequence, this velocity can be used as reference velocity v_{low}.

The other investigated velocities, see section 7.2.1, act as possible velocities v_{high}. Fig. 7.4 shows the amplitude ratios r_x and r_z as well as the position shifts s_x and s_z for the long rectangular defect in x-direction in dependence of the defect depth d and the varying velocities v_{high}.

It can be observed that for the velocities between 0.25 and 1 m/s no strong dependence from the defect depth is visible (Fig. 7.4). This corresponds to the motion-evoked skin depth (Fig. 7.5), which is $d > 10$ mm for these velocities. For the investigated setup, the motion-evoked skin effect becomes more dominant for velocities $v_{\text{high}} \geq 2.5$ m/s, where the dependence of the derived parameters from the defect depth becomes more clearly visible (Fig. 7.4). The strongest dependence is observed for the velocity $v_{\text{high}} = 25$ m/s (Fig. 7.4). These observations are similar for the other investigated defect shapes (Fig. 7.6). However, the detectability of the main peaks in the DRS components is aggravated at $v = 25$ m/s (Fig. 7.7), especially for ΔF_x.

Further, it has to be considered that a measurement setup with higher velocities is more complicated to construct, as mechanical oscillations have to be taken into account [20]. In consequence, the velocity $v_{\text{high}} = 10\,\text{m/s}$ is chosen as a compromise in this simulation study.
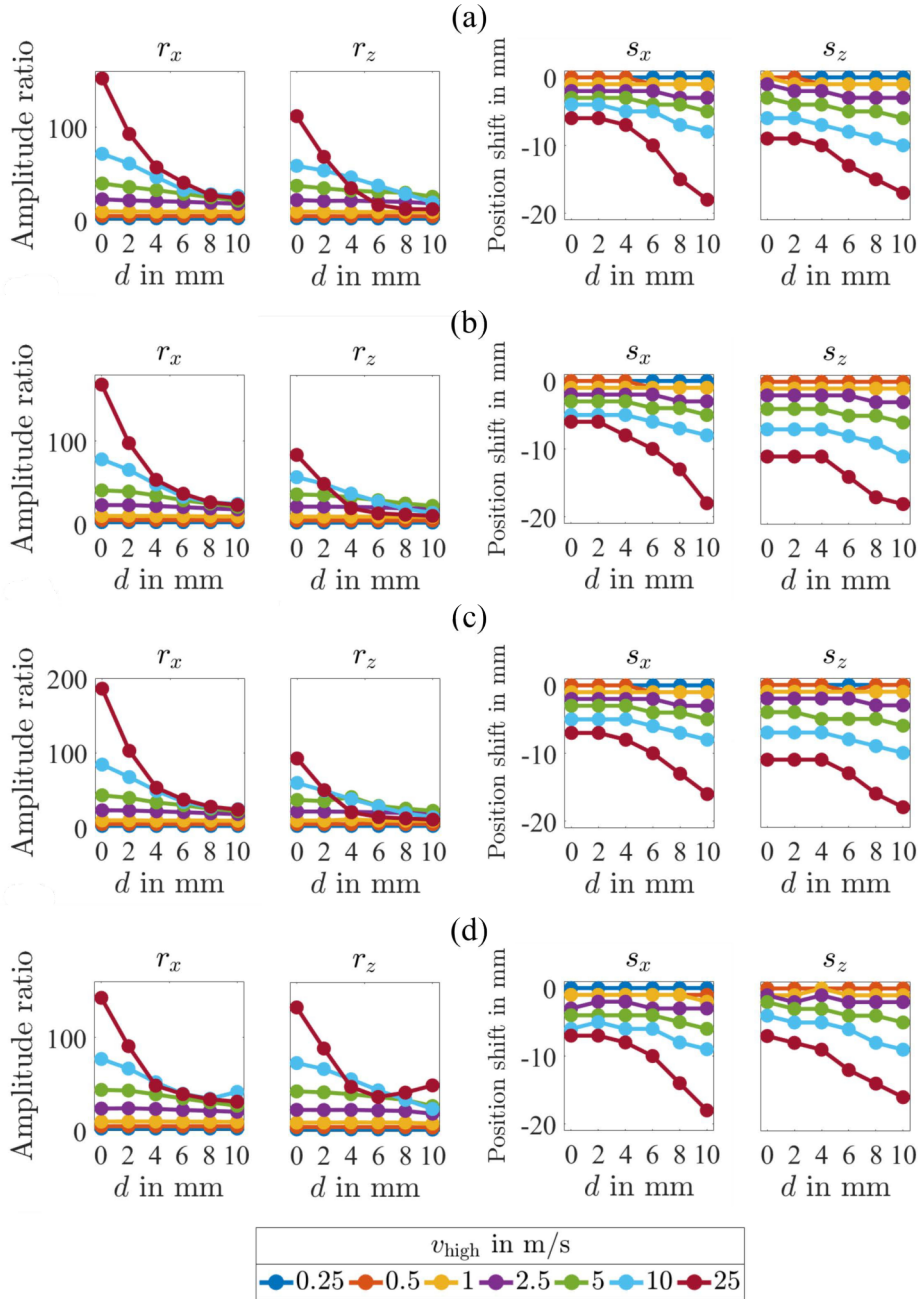
Figure 7.6: DRS amplitude ratios r_x and r_z and position shifts s_x and s_z depending on the defect depth d and the velocities v_{high}: (a) long rectangular defect in y-direction, (b) short rectangular defect in x-direction, (c) short rectangular defect in y-direction, (d) cylindrical shaped defect.
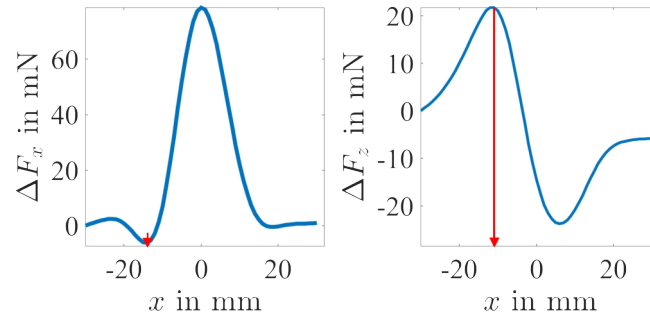
Figure 7.7: DRS components ΔF_x and ΔF_z at velocity $v = 25\,\text{m/s}$ for the long rectangular defect in x-direction at depth $d = 8\,\text{mm}$: The detection of the main peak (red arrow) of ΔF_x (left) is aggravated.

7.3 Results

Fig. 7.8 shows r_x, r_z, s_x and s_z in dependence of the defect depths d and defect shapes. A parameter range (Fig. 7.8, gray tubes) is built from minimal and maximal values at each depth. This parameter range can be used for the depth estimation. For example, a defect with $12\,\text{mm} \times 2\,\text{mm} \times 2\,\text{mm}$ at $d = 6\,\text{mm}$ leads to $r_x = 29.61$, $r_z = 29.96$, $s_x = -5\,\text{mm}$ and $s_z = -8\,\text{mm}$ (Fig. 7.8, stars). From the amplitude ratio r_x a defect depth between $6 - 10\,\text{mm}$ (Fig. 7.8, double arrows) is derived. Equivalently, defect depths between $6 - 8\,\text{mm}$, $0 - 6\,\text{mm}$ and $6 - 8\,\text{mm}$ are determined from r_z, s_x and s_z, respectively (Fig. 7.8, double arrows). Thus, based on the combined information, the depth $d = 6\,\text{mm}$ can be estimated.
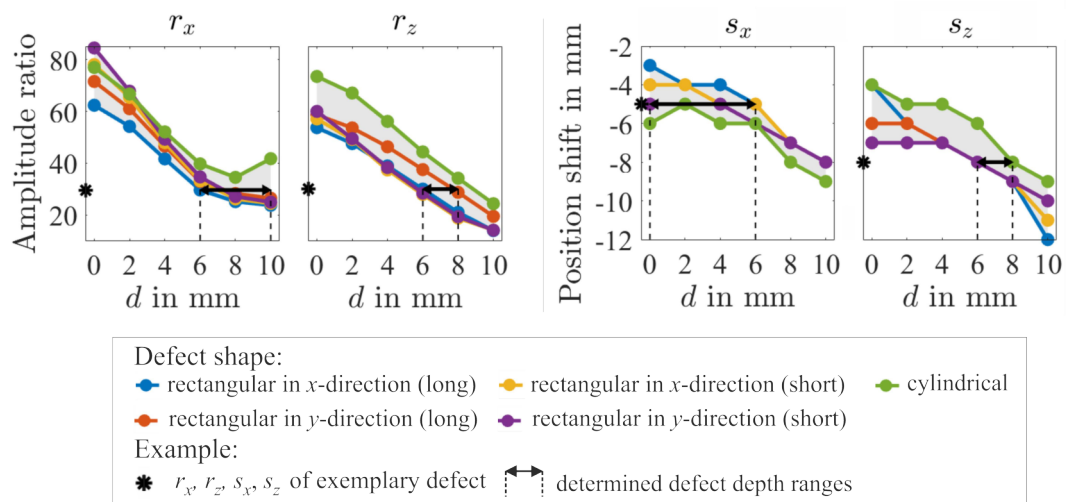
Figure 7.8: DRS amplitude ratios r_x and r_z and position shifts s_x and s_z depending on the defect depth d and the depth shapes with $v_{\text{low}} = 0.1\,\text{m/s}$ and $v_{\text{high}} = 10\,\text{m/s}$. The Grey tubes indicate the derived parameter ranges.

7.4 Discussion

The results of this simulation study indicate some of the requirements for a measurement setup realizing the velocity dependent LFE. The minimal sampling rate of the measurement system is

$$f_\mathrm{s} = \frac{v}{d_x},\qquad(7.6)$$

depending on the relative velocity v and the distance d_x of consecutive measurement points along one scanning line. In order to further improve the accuracy of the introduced defect depth estimation parameters, a smaller d_x, e.g. $d_x = 0.1\,\mathrm{mm}$ is conceivable.

In consequence, for the velocity $v_\mathrm{low} = 0.1\,\mathrm{m/s}$, f_s should be $f_\mathrm{s} \geq 1\,\mathrm{kHz}$ and $f_\mathrm{s} \geq 100\,\mathrm{kHz}$ for $v_\mathrm{low} = 10\,\mathrm{m/s}$, respectively. This high sampling rate might be challenging to realize. Using a small d_x, the defect dependent behavior might be also observable at lower velocities v_high. Thus, lower sampling rates are conceivable. Further, it should be considered that the absolute force increases with rising velocity. The use of two different force sensors is conceivable.

A prospective measurement procedure would first locate the central position of the DRS by a LFE scan of the specimen under test. After that, a relative movement along one scanning line that crosses this center point is realized with the velocities v_low and v_high. The described parameters are calculated to determine the defect depth.

The general idea of using a high velocity relative to a low velocity for the determination of the defect depth is expected to be applicable to other movement patterns of LFE and also other forms of motion-induced eddy current testing.

The principle of the velocity dependent LFE can be related to the multi-frequency eddy current testing [144]. In eddy current testing, the eddy currents are induced by a time changing magnetic field. The sensed secondary magnetic field increases with rising frequency but at the same time the penetration depth decreases due to the skin effect. The depth estimation is based on the idea that a defect close to the surface will give a strong response for a low and a high excitation frequency. In contrast, a deep defect will give an additionally reduced or absent response signal at a high excitation frequency. In the velocity dependent LFE, a low and high velocity are used instead of a low and high excitation frequency.

7.5 Conclusion

The simulation study shows that with the use of two different velocities in LFE a defect depth detection is conceivable. Thus, the depth estimation can be realized before the defect reconstruction procedure using the motion-evoked skin effect and a combined decision based on the extracted parameters.

8 Summary and Outlook

8.1 Summary

The aim of this thesis was to introduce novel inverse methods for the defect reconstruction in Lorentz force evaluation (LFE) and to compare it to the defect reconstruction in eddy current evaluation (ECE). Another objective was to investigate the influence of varying forward solutions in LFE on the reconstructed defect properties. Further, a novel forward solution should be developed that overcomes the limitations from the previous ones regarding defect shape and location. Moreover, a method to improve the depth estimation of defects should be developed.

In this thesis, a minimum norm estimation with elastic net regularization in comparison to Tikhonov-Phillips-regularization was applied in order to determine the defect properties from LFE measurements. For that purpose, defect reconstruction schemes have been developed based on parameter studies of simulated data sets. The concept of the defect identification vector as source parameter has been introduced in this framework, which gives a direct binary information which volume elements (voxels) belong to the reconstructed defect. The experimental analysis by LFE of an aluminum specimen with a cylindrical defect showed comparable results for elastic net regularization and Tikhonov-Phillips-regularization. Varying defect depths have been analyzed. Both methods showed correct defect depth estimation and an appropriate size estimation of the defect. The reproducibility of the reconstruction results within LFE could be shown from repeated measurements. The elastic net regularization slightly outperformed the Tikhonov-Phillips-regularization in this point.

In ECE, for comparison purposes also specimens of stacked aluminum sheets where analyzed with one sheet containing the defect. Various defect depths have been analyzed. Two shapes of defects where analyzed, a star-shaped one and a cylindrical one, where the cylindrical one acts as qualitative comparison to the problem setup of LFE. The minimum norm estimation with elastic net regularization in comparison to Tikhonov-Phillips-regularization applied to ECE showed that the elastic net regularization slightly outperforms the Tikhonov-Phillips-regularization as the reconstructed shape of a star-shaped crack was slightly better visible for deeper defects. For the cylindrical defect

the diameter was estimated too large with both methods, which became worse with increasing defect depth. For both defect shapes and both regularization methods, a blurring of the reconstructed normalized current density norm maps was observable for increasing defect depth.

The qualitative comparison of LFE and ECE showed that the quality of the defect reconstruction with increasing defect depth is more stable in LFE compared to ECE. Additionally, the LFE was able to reconstruct defects up to a depth of 8 mm, whereas the ECE up to 4 mm. However, it should be noted that the planar uniform excitation coil used in this thesis, brings the advantage of the linearization of the inverse problem but is not optimized for the analysis of deep defects. The ECE is able to reconstruct complex defect shapes, like the shown star, whereas the LFE with the used approximate forward solution is optimized for regular defects with a circular or quadratic shape in x-y-direction.

Another inverse method, the Landweber iteration has been adapted for the use of LFE. It also used the approximate forward solution. The same experimental setup as for the minimum norm estimation with Tikhonov-Phillips-regularization and elastic net regularization has been investigated. The estimation of the defect sizes is comparable to the results with the minimum norm estimation, but deeper defects are estimated above the correct depth. The main advantage compared to minimum norm estimation with Tikhonov-Phillips-regularization and elastic net regularization is that the computation time is reduced as only one iteration step was necessary in the adapted Landweber iteration.

Due to the diverging results of defect depth estimation and due to the restriction of approximate forward solution to regular shaped defects with uniform extension, a comparison of the defect reconstruction performance between the approximate forward solution and extended area approach was carried out. It was investigated whether the more computational demanding extended area approach gives better reconstruction results in terms of defect depth and extensions estimation. For that purpose, specimen of stacked aluminum sheets with cylindrical and cuboidal defects have been investigated by the goal-function-scanning methods: diameter-depth scan and length-width-depth scan. It turned out that for experimental LFE data, with approximate forward solution, the defect depth was estimated above the correct one for deeper defects similarly to the results with the adapted Landweber iteration. Further, the defect diameter of the cylindrical shaped defect was partly estimated too large. In contrast, with extended area approach the correct diameter and the correct defect depths have been determined. The investigation of a cuboidal defect with non-uniform extensions showed that the extended area approach gave better estimation of the length and the width of the defect.

In summary, it can be stated that the defect depth estimation showed dependencies on the inverse method and on the accuracy of the forward solution. With the use of

extended area approach as forward solution an improvement in defect reconstruction performance could be achieved. However, the extended area approach is optimized for the symmetry scanning line above a defect. It is also defined for regular shaped defects, despite non-uniform defect extensions are possible. The extended area approach is an iterative forward solution which excludes the fast linear inverse methods. Both forward solutions assume a single defect far away from the specimen edges.

In order to minimize the restrictions regarding the defect shape and location, a novel forward solution approach, referred to as single voxel approach, was developed. The principle idea is to calculate the defect response signal of single defect voxels once in advance by a numerical simulation method. The defect response signal of a defect is then calculated as a superposition of all voxels that belong to the defect. The superposition principle represents a linearization. Thus, the single voxel approach is capable for linear inverse methods. The novel forward solution has been compared to numerical simulations based on the finite element method by the normalized root mean square error (NRMSE). Various defect sizes and shapes at different depths have been investigated. The single voxel approach showed across all simulations NRMSE values $<2.5\,\%$ compared to $<8\,\%$ for the extended area approach and $<12\,\%$ for the approximate forward solution.

The previous work showed that the estimation of the defect depth from a 2D measurement LFE signal remains a challenging task. Previously, the depth was estimated by realizing defect reconstruction separately for each conducting layer of the specimen under investigation. The layer with the smallest corresponding NRMSE indicated the defect depth. In LFE, the defect response signals of a small defect near the top surface of the specimen and a larger and deeper defect can be similar. This leads to similar NRMSEs, aggravating the depth estimation. In consequence, a novel principle, referred to as velocity dependent LFE was developed. It uses the motion-evoked skin effect, which alters the defect response signals of defects at different depths at a high velocity in different ways. The developed principle uses a high velocity ($v = 10\,\text{m/s}$) in comparison to a low velocity ($v = 0.1\,\text{m/s}$). The corresponding shifts and amplitude changes of the defect response signals are used to determine the defect depth. The principle has been successfully tested on simulated data sets with defects of various sizes, shapes and depths.

To conclude, the presented further development of forward solutions and inverse methods within the framework of ECE and LFE contributes to the ongoing development in the field of NDE.

8.2 Outlook

A major upcoming task might be the experimental validation of the velocity dependent LFE, for that purpose the existing experimental setup has to be modified.

The principle of the developed forward solution single voxel approach could be used in further applications of LFE, other fields of nondestructive evaluation or further research areas that require to solve inverse problems and are characterized by high computational demands for an accurate forward solution.

Beside the presented inverse methods, further approaches might be interesting in future investigations. In the field of minimum norm estimation, the total variation regularization [96] could be an appropriate regularization method for LFE. By minimizing the total variation additionally to minimizing the data term unwanted details like noise should be suppressed and edges are kept.

Additionally, the existing methods could be further developed for the reconstruction of multiple defects with similar or varying conductivity values.

Another different direction could be the estimation of the defect properties from LFE measurements by means of artificial neuronal networks and machine learning, which are already used in other fields of nondestructive evaluation, e.g. in ECE [145–148], ultrasonics [149, 150] or thermography [151]. This approach would be of special interest if a LFE setup is brought into industry. The important features of the defect response signals could be determined as input for the neuronal network. It would be trained for the given setup with a wide range of possible defects. After the computational demanding training phase, the actual estimation of defect properties would be in the range of a few seconds.

List of Figures

List of Tables

Acronyms and Symbols

Acronyms

AFS approximate forward solution

BESM boundary element source method

DAQ data aquistion

DFT discrete Fourier transform

DRS defect response signal

EAA extended area approach

ECE eddy current evaluation

ENR elastic net regularization

FEM finite element method

GLARE glass-fiber reinforced aluminum laminate

GMR giant magnetoresistive

GPIB General Purpose Interface Bus

LASSO least absolute shrinkage and selection operator

LFE Lorentz force evaluation

MDA moving defect approach

MDM multiple dipoles method

MMA moving magnet approach

MNE minimum norm estimation

MFP magnetic field perturbation

MUSIC multiple signal classification

NDE nondestructive evaluation

NRMSE normalized root mean square error

PCB printed circuit board

QSA quasi-stationary approach

ROI region of interest

SNR signal-to-noise-ratio

SVA single voxel approach

SVD singular value decomposition

SQUID superconducting quantum interference device

TPR Tikhonov-Phillips-regularization

TSVD truncated singular value decomposition

TV total variation

voxel volume element

Symbols

$\vec{\cdot}$ vector

$[\cdot]$ matrix, tensor

$\underline{\cdot}$ complex number

$[\cdot]^{\mathrm{T}}$ transposed matrix

$[\cdot]^{-1}$ inverse of a matrix

$[\cdot]^{+}$ Moore-Penrose inverse of a matrix

$[\cdot]^{*}$ adjoint matrix

$\hat{\cdot}$ 2D-DFT transformed

α relative z-position of single magnetic dipole in MDM for a cylindrical permanent magnet

β relative radial position of single magnetic dipole in MDM for a cylindrical permanent magnet

γ norm weight parameter in ENR

δ depth of penetration

δz lift-off distance

ε extension factor EAA

η step size of Landweber iteration

$\vec{\theta}$ defect identification vector

Γ_{a} air box surface

Γ_{c} conductor surface

Γ_{d} defect surface

ε_0 electrical permittivity of the free space

μ_0 magnetic permeability of the free space

μ_{r} relative magnetic permeability of a material

μ magnetic permeability

σ electrical conductivity

σ_0 electrical conductivity of the specimen under test

σ_{d} electrical conductivity of the defect

Φ phase shift of the MFP

φ electric scalar potential

Ω_{d} defect-domain

Ω_{m} magnet-domain

ω angular frequency

$\vec{A}$ magnetic vector potential

$\vec{A}^*$ modified magnetic vector potential

A_{d} area of the defect cross section

a_{d} size difference in mm^2

$\vec{B} = \vec{B}_{\mathrm{p}} + \vec{b}_{\mathrm{s}}$ total magnetic flux density

$\vec{B}_{\mathrm{p}}$ primary magnetic flux density of the permanent magnet

$\vec{b}_{\mathrm{s}}$ secondary magnetic flux density of the induced eddy currents

$\Delta b_x(t) = (B_{x,0}(t) - B_x(t))$ MFP in time domain

$\underline{\Delta b_x}$ MFP as complex number

$\underline{\Delta b_x}^{\mathrm{BS}}$ MFP calculated by Biot-Savart law

$B_{x,(0)}(t) = B_{\mathrm{p},x}(t) + b_{\mathrm{s},x,(0)}(t)$ x-component of total time-varying magnetic flux density of a specimen with (without) a defect

$B_{\mathrm{p},x}(t)$ x-component of time-varying primary magnetic flux density of the excitation coil

$b_{\mathrm{s},x,(0)}(t)$ x-component of time-varying secondary magnetic flux density of the induced eddy currents of a specimen with (without) a defect

B_{r} magnetic remanence

C_{d} dipolar correction factor

c_x axis length of the defect in x-direction

c_y axis length of the defect in y-direction

d defect depth

$\vec{D}$ electrical displacement field

D_{d} diameter of the defect

D_{m} diameter of the permanent magnet

d_0 Euclidean distance to the center of the true defect

d_x distance of observation points in x-direction

d_y distance of observation points in y-direction

$\Delta \vec{F} = \vec{F} - \vec{F}_0$ defect response signal (DRS)

$\vec{F}_{(0)}$ Lorentz force for a specimen with (without) a defect

$\Delta \vec{F}^{\mathrm{AFS/EAA/SVA}}$ vector with the x-, y- and z-DRS components at the observation points calculated by AFS/EAA/SVA

$\Delta\vec{F}^{\text{FEM/meas}}$ vector with the x-, y- and z-DRS components at the observation points obtained from FEM simulations or measurements

f_{e} excitation frequency

f_{s} sampling rate

$\mathcal{G}(\vec{x})$ forward solution operator

H height of the specimen

H_{d} height of the defect

H_{m} height of the permanent magnet

$I_{\mathbf{d}}(i,j)$ unitary square current loop at element i,j $I_{\text{d}}(i,j)$

$\Delta\vec{j} = \vec{j} - \vec{j}_0$ perturbation eddy current density

$\vec{j}_{(0)}$ eddy current density for a specimen with (without) a defect

$\underline{\vec{J}}_{\text{e}}$ external eddy current density from the excitation coil as complex number

$[L]$ lead field matrix

L length of the specimen

l_{c} characteristic length of a problem

L_{d} length of the defect

$\vec{M}$ magnetization of the permanent magnet

$\vec{m}$ magnetic dipole moment

$\vec{m}_p$ magnetic dipole moment of a single dipole in MDM

$\vec{n}$ unit vector normal to a surface

N_{d} number of magnetic dipoles of the MDM for a cylindrical permanent magnet

N_{h} number of layers of the MDM for a cylindrical permanent magnet

N_{r} number of rings of the MDM for a cylindrical permanent magnet

q_j surface charge of the j-th element

$\vec{r}$ position vector

R_{m} magnetic Reynolds number

r_x amplitude ratio of ΔF_x

r_z amplitude ratio of ΔF_z

S_i size of i-th surface charge element

s_x x-shift of main ΔF_x peak

s_z x-shift of main ΔF_z peak

t time

$t_\mathbf{h}$ thresholding factor

$\vec{v}$ relative velocity between the permanent magnet and the specimen under test

V volume of the specimen under test

V_d defect volume

V_E volume of a voxel

V_m volume of the permanent magnet

W width of the specimen

W_d width of the defect

$\vec{x}$ source parameter vector

x_e defect extension in x-direction

$\vec{y}$ electromagnetic field components

y_e defect extension in y-direction

Δz thickness of aluminum sheet

Bibliography

[1] Laurence Gonzales , *Flight 232: A story of disaster and survival*. New York City, USA: Norton & Company, 2015. 1

[2] J. L. Blackshire, *Enhanced damage characterization using wavefield imaging methods, 43rd Annual review of progress in QDNE*. Melville, USA: American Institute of Physics, 2017. 1

[3] A. Alaknanda, R.S. Anand, and P. Kumar, "Flaw detection in radiographic weld images using morphological approach," *NDT & E International*, vol. 39, no. 1, pp. 29–33, 2006. 1

[4] N. Montinaro, D. Cerniglia, and G. Pitarresi, "Flying laser spot thermography technique for the NDE of fibre metal laminates disbonds," *Composite Structures*, vol. 171, pp. 63–76, 2017. 1

[5] L. Ma and M. Soleimani, "Hidden defect identification in carbon fibre reinforced polymer plates using magnetic induction tomography," *Measurement Science and Technology*, vol. 25, no. 5, pp. 1–15, 2014. 1, 40

[6] M. Layouni, M. S. Hamdi, and S. Tahar, "Detection and sizing of metal-loss defects in oil and gas pipelines using pattern-adapted wavelets and machine learning," *Applied Soft Computing*, vol. 52, pp. 247–261, 2017. 1

[7] E. K. Oneida, E. B. Shell, J. C. Aldrin, H. A. Sabbagh, E. H. Sabbagh, and R. K. Murphy, "Characterizing surface-breaking cracks through eddy current NDE and model-based inversion," *Materials Evaluation*, vol. 75, no. 7, pp. 915–929, 2017. 1

[8] J. D. Jackson, *Classical Electrodynamics, 3rd Edition*. New York, United States: John Wiley & Sons, Inc., 1998. 1, 12, 13, 69

[9] J. García-Martín, J. Gomez-Gil, and E. Vázquez-Sánchez, "Non-destructive techniques based on eddy current testing," *Sensors (Basel, Switzerland)*, vol. 11, pp. 2525–65, 2011. 1

[10] B. Petković, J. Haueisen, M. Zec, R. P. Uhlig, H. Brauer, and M. Ziolkowski, "Lorentz force evaluation: A new approximation method for defect reconstruction,"

NDT & E International, vol. 59, pp. 57–67, 2013. 1, 2, 20, 21, 35, 37, 39, 64, 91, 103, 111

[11] H. M. G. Ramos, T. Rocha, D. Pasadas, and A. L. Ribeiro, "Velocity induced eddy currents technique to inspect cracks in moving conducting media," in *2013 IEEE International Instrumentation and Measurement Technology Conference (I2MTC) Proceedings*, pp. 931–934, 2013. 2, 64

[12] H. G. Ramos, T. Rocha, A. L. Ribeiro, and D. Pasadas, "GMR versus differential coils in velocity induced eddy current testing," in *2014 IEEE International Instrumentation and Measurement Technology Conference (I2MTC) Proceedings*, pp. 915–918, 2014. 2, 64

[13] T. Rocha, H. Ramos, A. L. Ribeiro, and D. Pasadas, "Sub-surface defect detection with motion induced eddy currents in aluminium," in *2015 IEEE International Instrumentation and Measurement Technology Conference (I2MTC) Proceedings*, pp. 930–934, 2015. 2, 64

[14] T. Rocha, H. Ramos, A. Ribeiro, and D. Pasadas, "Magnetic sensors assessment in velocity induced eddy current testing," *Sensors and Actuators A: Physical*, vol. 228, pp. 55–61, 2015. 2, 64

[15] J. Mengelkamp, *Forward and inverse calculation methods for Lorentz force evaluation applied to laminated composites.* Technische Universität Ilmenau, Ilmenau, Germany: Ph.D. dissertation, 2016. 2, 3, 19, 37, 38

[16] J. Mengelkamp, M. Ziolkowski, K. Weise, M. Carlstedt, H. Brauer, and J. Haueisen, "Permanent magnet modeling for Lorentz force evaluation," *IEEE Transactions on Magnetics*, vol. 51, no. 7, pp. 1–11, 2015. 3, 18, 19, 20, 37, 41

[17] J. Mengelkamp, D. Lattner, J. Haueisen, M. Carlstedt, K. Weise, H. Brauer, M. Ziolkowski, and R. Eichardt, "Lorentz force evaluation with differential evolution," *IEEE Transactions on Magnetics*, vol. 52, no. 5, pp. 1–10, 2016. 3, 11, 35, 37, 41, 64, 91, 103, 107, 111

[18] M. Ziolkowski, *Modern methods for electromagnetic field problems.* Szczecin, Poland: West Pomeranian University of Technology College Publisher, 2015. 3, 22, 23, 24, 25, 91, 102, 103, 108

[19] J. Mengelkamp, M. Carlstedt, K. Weise, M. Ziolkowski, H. Brauer, and J. Haueisen, "Current density reconstructions for Lorentz force evaluation," *Research in Nondestructive Evaluation*, vol. 28, no. 2, pp. 76–100, 2016. 3, 35, 37, 40, 47, 64, 103, 107, 111

[20] J. M. Otterbach, R. Schmidt, H. Brauer, M. Ziolkowski, and H. Töpfer, "Comparison of defect detection limits in Lorentz force eddy current testing and classical eddy current testing," *Journal of Sensors and Sensor Systems*, vol. 7, no. 2, pp. 453–459, 2018. 4, 17, 113, 116

[21] E.-M. Dölker, D. Strohmeier, B. Petković, J. Mengelkamp, K. Weise, R. Schmidt, H. Brauer, and J. Haueisen, "Lorentz force evaluation with elastic net regularization," in *Proceedings of the 14th International Workshop on Optimization and Inverse Problems in Electromagnetism (OIPE 2016)*, pp. 54–55, 2016. 4, 44

[22] E.-M. Dölker, R. Schmidt, S. Gorges, J. M. Otterbach, B. Petković, D. Strohmeier, R. Eichardt, H. Brauer, and J. Haueisen, "Elastic net regularization in Lorentz force evaluation," *NDT & E International*, vol. 99, pp. 141 – 154, 2018. 4, 44, 91, 103, 107, 111

[23] E.-M. Dölker, N. F. B. Baharuddin, E. Supriyanto, R. Schmidt, H. Brauer, and J. Haueisen, "Lorentz force evaluation using an adapted Landweber algorithm," in *Proceedings of the International PhD Seminar on Computational Electromagnetics and Bioeffects of Electromagnetic Fields (CEMBEF 2017)*, pp. 25–28, 2017. 5, 82

[24] E.-M. Dölker, R. Schmidt, K. Weise, B. Petković, M. Ziolkowski, H. Brauer, and J. Haueisen, "Assessment of two forward solution approaches in Lorentz force evaluation," *IEEE Transactions on Magnetics*, vol. 54, no. 3, pp. 1–5, 2018. 5, 91, 103, 107, 108

[25] E.-M. Dölker, R. Schmidt, K. Weise, B. Petković, M. Ziolkowski, H. Brauer, and J. Haueisen, "Lorentz force evaluation with an extended area approach," in *Proceedings of the 2017 International Applied Computational Electromagnetics Society Symposium - Italy (ACES)*, pp. 1–2, 2017. 5, 91

[26] E.-M. Dölker, R. Schmidt, K. Weise, B. Petković, M. Ziolkowski, H. Brauer, and J. Haueisen, "Comparison of two forward solution approaches in Lorentz force evaluation," in *Proceedings of the 21st International Conference on the Computation of Electromagnetic Fields (COMPUMAG 2017)*, pp. 1–2, 2017. 5, 91

[27] E.-M. Dölker, S. Gorges, J. M. Otterbach, R. Schmidt, B. Petković, M. Ziolkowski, H. Brauer, and J. Haueisen, "Lorentz force evaluation with extended area approach," in *XIX International Symposium on Theoretical Electrical Engineering (ISTET) - Book of Abstracts*, p. 36, 2017. 5, 91

[28] E.-M. Dölker, B. Petković, R. Schmidt, H. Brauer, and J. Haueisen, "Single voxel boundary element source method: A novel forward solution approach for Lorentz

force evaluation," in *Proceedings of the 15th International Workshop on Optimization and Inverse Problems in Electromagnetism (OIPE 2018)*, pp. 30–31, 2018. 5, 103

[29] E.-M. Dölker, B. Petković, R. Schmidt, M. Ziolkowski, H. Brauer, and J. Haueisen, "Single voxel approach for Lorentz force evaluation," *COMPEL - The international journal for computation and mathematics in electrical and electronic engineering*, vol. 38, no. 3, pp. 943–952, 2019. 5, 103

[30] E.-M. Dölker, R. Schmidt, H. Brauer, and J. Haueisen, "Velocity dependent Lorentz force evaluation: A simulation study," in *Proceedings of the 18th Biennial IEEE Conference on Electromagnetic Field Computation (CEFC 2018)*, one-page abstract, 2018. 5, 111

[31] E.-M. Dölker, R. Schmidt, H. Brauer, and J. Haueisen, "Velocity-dependent Lorentz force evaluation: A simulation study," *IEEE Transactions on Magnetics*, vol. 55, no. 6, pp. 1–4, 2019. 5, 111

[32] K. Weise, *Advanced modeling in Lorentz force eddy current testing.* Technische Universität Ilmenau, Ilmenau, Germany: Ph.D. dissertation, 2016. 10, 11, 12, 14, 15, 16, 64

[33] M. Zec, R. P. Uhlig, M. Ziolkowski, and H. Brauer, "Fast technique for Lorentz force calculations in non-destructive testing applications," *IEEE Transactions on Magnetics*, vol. 50, no. 2, pp. 133–136, 2014. 10, 11, 105

[34] M. Carlstedt, K. Porzig, R. P. Uhlig, M. Zec, M. Ziolkowski, and H. Brauer, "Application of Lorentz force eddy current testing and eddy current testing on moving nonmagnetic conductors," *International Journal of Applied Electromagnetics and Mechanics*, vol. 45, no. 1-4, pp. 519–526, 2014. 11

[35] N. Derby and S. Olbert, "Cylindrical magnets and ideal solenoids," *American Journal of Physics*, vol. 78, pp. 229–235, 2010. 12, 18

[36] P. Davis and P. Rabinowitz, *Methods of numerical integration.* Dover Books on Mathematics Series, Dover Publications, 2007. 12

[37] J. M. Borwein and P. B. Borwein, *Pi and the AGM: A study in the analytic number theory and computational complexity.* New York, NY, USA: Wiley-Interscience, 1987. 12

[38] B. Petković, K. Weise, and J. Haueisen, "Computation of Lorentz force and 3-D eddy current distribution in translatory moving conductors in the field of a permanent magnet," *IEEE Transactions on Magnetics*, vol. 53, no. 2, pp. 1–9, 2017. 12, 13, 103, 106, 109

[39] M. Zec, *Theory and numerical modelling of Lorentz force eddy current testing*. Technische Universität Ilmenau, Ilmenau, Germany: Ph.D. dissertation, 2013. 15

[40] C. Emson and J. Simkin, "An optimal method for 3-D eddy currents," *IEEE Transactions on Magnetics*, vol. 19, no. 6, pp. 2450–2452, 1983. 15

[41] K. Weise, R. Schmidt, M. Carlstedt, M. Ziolkowski, H. Brauer, and H. Töpfer, "Optimal magnet design for Lorentz force eddy-current testing," *IEEE Transactions on Magnetics*, vol. 51, pp. 1–15, 2015. 17

[42] R. Ravaud, G. Lemarquand, S. Babic, V. Lemarquand, and C. Akyel, "Cylindrical magnets and coils: Fields, forces, and inductances," *IEEE Transactions on Magnetics*, vol. 46, no. 9, pp. 3585–3590, 2010. 18

[43] H. A. Haus and J. R. Melcher, *Electromagnetic fields and energy*. NJ: Prentice-Hall: Englewood Cliffs, 1989. 18, 19

[44] J. A. Nelder and R. Mead, "A simplex method for function minimization," *Computer Journal*, vol. 7, pp. 308–313, 1965. 19

[45] S. Tumanski, "Modern magnetic field sensors - a review," *Przeglad Elektrotechniczny*, vol. 89, pp. 1–12, 2013. 25

[46] M. v. Kreutzbruck, K. Allweins, and C. Heiden, "Wirbelstromprüfsystem mit integriertem Fluxgate-Magnetometer," *DACH-Jahrestagung DGZfP, ÖGfZP, SGZP, Innsbruck*, pp. 871–881, 2000. 25, 64

[47] R. Hohmann, D. Lomparski, H. J. Krause, M. v. Kreutzbruck, and W. Becker, "Aircraft wheel testing with remote eddy current technique using a HTS SQUID magnetometer," *IEEE Transactions on Applied Superconductivity*, vol. 11, no. 1, pp. 1279–1282, 2001. 26, 64

[48] D. F. He and M. Shiwa, "Deep defect detection using eddy current testing with AMR sensor," in *Proceedings of the Progress In Electromagnetics Research Symposium*, pp. 493–495, 2013. 26, 64

[49] J. Bailey, N. Long, and A. Hunze, "Eddy current testing with giant magnetoresistance (GMR) sensors and a pipe-encircling excitation for evaluation of corrosion under insulation," *Sensors (Basel, Switzerland)*, vol. 17, no. 10, pp. 1–21, 2017. 26, 64

[50] D. J. Pasadas, A. L. Ribeiro, H. G. Ramos, and T. J. Rocha, "Inspection of cracks in aluminum multilayer structures using planar ECT probe and inversion problem," *IEEE Transactions on Instrumentation and Measurement*, vol. 66, no. 5, pp. 920–927, 2017. 27, 28, 30, 31, 68, 78

[51] D. J. L. Pasadas, *Characterization of defects by eddy current image constructions*. Universidade de Lisboa, Instituto Superior Técnico, Lisbon, Portugal: Ph.D. dissertation, 2016. 27, 29, 30, 32, 34, 41, 69, 123

[52] COMSOL Multiphysics™ v. 5.4., *AC/DC Module User's Guide,*. Stockholm, Sweden: COMSOL AB, 2018. 28

[53] D. Pasadas, A. L. Ribeiro, H. Ramos, and T. Rocha, "Automatic parameter selection for Tikhonov regularization in ECT inverse problem," *Sensors and Actuators A: Physical*, vol. 246, no. 1, pp. 73–80, 2016. 28, 29, 30, 40, 79

[54] J. Hadamard, "Sur les problemes aux derivees partielles et leur signification physique," *Princeton university bulletin*, pp. 49–52, 1902. 35

[55] A. Deif, *Sensitivity analysis in linear systems*. Springer-Verlag, 1986. 36

[56] J. W. Demmel and N. J. Higham, "Improved error bounds for underdetermined system solvers," *SIAM Journal on Matrix Analysis and Applications*, vol. 14, no. 1, pp. 1–14, 1993. 36

[57] R. Eichardt, D. Baumgarten, B. Petković, F. Wiekhorst, L. Trahms, and J. Haueisen, "Adapting source grid parameters to improve the condition of the magnetostatic linear inverse problem of estimating nanoparticle distributions," *Medical & Biological Engineering & Computing*, vol. 50, no. 10, pp. 1081–1089, 2012. 36

[58] B. Petković, *Assessment of linear inverse problems in magnetocardiography and Lorentz force eddy current testing*. Technische Universität Ilmenau, Ilmenau, Germany: Ph.D. dissertation, 2013. 36

[59] J. C. Mosher, P. S. Lewis, and R. M. Leahy, "Multiple dipole modeling and localization from spatio-temporal MEG data," *IEEE Transactions on Biomedical Engineering*, vol. 39, no. 6, pp. 541–557, 1992. 38

[60] J. Billingsley and R. Kinns, "The acoustic telescope," *Journal of Sound and Vibration*, vol. 48, no. 4, pp. 485 – 510, 1976. 38

[61] M. Brandstein and D. Ward, eds., *Microphone arrays: signal processing techniques and applications*. Springer, 1 ed., 2001. 38

[62] P. C. Hansen, "The truncated SVD as a method for regularization," *BIT Numerical Mathematics*, vol. 27, no. 4, pp. 534–553, 1987. 39

[63] C. Robert, J. M. Dinten, and P. Rizo, *Dual-energy computed tomography for ceramics and composite materials*, pp. 481–488. Boston, MA: Springer US, 1996. 39

[64] P. Xu, "Truncated SVD methods for discrete linear ill-posed problems," *Geophysical Journal International*, vol. 135, pp. 505 – 514, 1998. 39

[65] R. Eichardt, D. Baumgarten, L. D. Rienzo, S. Linzen, V. Schultze, and J. Haueisen, "Localisation of buried ferromagnetic objects based on minimum-norm-estimations: A simulation study," *COMPEL - The international journal for computation and mathematics in electrical and electronic engineering*, vol. 28, no. 5, pp. 1327–1337, 2009. 39

[66] M. S. Hämäläinen and R. J. Ilmoniemi, "Interpreting magnetic fields of the brain: minimum norm estimates," *Medical & Biological Engineering & Computing*, vol. 32, no. 1, pp. 35–42, 1994. 39

[67] J. D. Shea, B. D. Van Veen, and S. C. Hagness, "A TSVD analysis of microwave inverse scattering for breast imaging," *IEEE Transactions on Biomedical Engineering*, vol. 59, no. 4, pp. 936–945, 2012. 39

[68] X. Lv, Z. Zuo, Z. Wang, L. Li, and J. Huang, "Remote sensing image restoration based on an improved Landweber iterative method for forest monitoring and management," in *Proceedings of the 2018 International Workshop on Renewable Energy and Development (IWRED 2018)*, 2018. 39, 81

[69] K. Q. Dinh and B. Jeon, "Iterative weighted recovery for block-based compressive sensing of image/video at a low subrate," *IEEE Transactions on Circuits and Systems for Video Technology*, vol. 27, no. 11, pp. 2294–2308, 2017. 39, 81

[70] R. S. Mathew and J. S. Paul, "Sparsity promoting adaptive regularization for compressed sensing parallel MRI," *IEEE Transactions on Computational Imaging*, vol. 4, no. 1, pp. 147–159, 2018. 39, 81

[71] S. Hubmer, A. Neubauer, R. Ramlau, and H. U. Voss, "On the parameter estimation problem of magnetic resonance advection imaging," *Inverse Problems and Imaging*, vol. 12, no. 1, pp. 175–204, 2018. 39, 81

[72] Z. Xu, Y. Jiang, B. Wang, Z. Huang, H. Ji, and H. Li, "Image reconstruction performance of a 12-electrode CCERT sensor under five different excitation patterns," *IEEE Access*, vol. 6, pp. 65783–65795, 2018. 39, 81

[73] Y. Yang and J. Jia, "An image reconstruction algorithm for electrical impedance tomography using adaptive group sparsity constraint," *IEEE Transactions on Instrumentation and Measurement*, vol. 66, no. 9, pp. 2295–2305, 2017. 39, 81

[74] B. S. Kim and K. Y. Kim, "Resistivity imaging of binary mixture using weighted Landweber method in electrical impedance tomography," *Flow Measurement and Instrumentation*, vol. 53, pp. 39–48, 2017. 39, 81

[75] H. Yan, Y. F. Wang, and Y. G. Zhou, "Three-dimensional electrical capacitance tomography reconstruction by the Landweber iterative algorithm with fuzzy thresholding," *IET Science, Measurement Technology*, vol. 8, no. 6, pp. 487–496, 2014. 39, 81

[76] J. Zhao, L. Xu, and Z. Cao, "Direct image reconstruction for electrical capacitance tomography using shortcut D-bar method," *IEEE Transactions on Instrumentation and Measurement*, vol. 68, no. 2, pp. 483–492, 2019. 39, 81

[77] S. Liang, J. Ye, H. Wang, M. Wu, and W. Yang, "Influence of the internal wall thickness of electrical capacitance tomography sensors on image quality," *Measurement Science and Technology*, vol. 29, no. 3, pp. 1–13, 2018. 39, 81

[78] C. Yan, D. Zhang, G. Lu, and J. Dong, "An improved algorithm based on Landweber-Tikhonov alternating iteration for ECT image reconstruction," in *Proceedings of the 3rd Annual International Conference on Information System and Artificial Intelligence (ISAI)*, pp. 1–5, 2018. 39, 81

[79] Y. Zhang, D. Ye, and Y. Liu, "Robust locally linear embedding algorithm for machinery fault diagnosis," *Neurocomputing*, vol. 273, pp. 323–332, 2018. 39, 43, 81

[80] P. Stefanov and Y. Yang, "Multiwave tomography with reflectors: Landweber's iteration," *Inverse Problems and Imaging*, vol. 11, no. 2, pp. 373–401, 2017. 39, 81

[81] A. Desmal and H. Bagci, "Sparse nonlinear electromagnetic imaging accelerated with projected steepest descent algorithm," *IEEE Transactions on Geoscience and Remote Sensing*, vol. 55, no. 7, pp. 3810–3822, 2017. 39, 81

[82] G. Vainikko, "The discrepancy principle for a class of regularization methods," *USSR Computational Mathematics and Mathematical Physics*, vol. 22, no. 3, pp. 1 – 19, 1982. 40

[83] P. C. Hansen and D. P. O'Leary, "The use of the L-curve in the regularization of discrete ill-posed problems," *SIAM Journal on Scientific Computing*, vol. 14, no. 6, pp. 1487–1503, 1993. 40, 51, 55, 73, 75

[84] G. Wahba, "Practical approximate solutions to linear operator equations when the data are noisy," *SIAM Journal on Numerical Analysis*, vol. 14, no. 4, pp. 651–667, 1977. 40

[85] A. N. Tikhonov, "Solution of incorrectly formulated problems and the regularization method," *Soviet Mathematics - Doklady*, vol. 4, pp. 1035–1038, 1963. 40, 51

[86] D. L. Phillips, "A technique for the numerical solution of certain integral equations of the first kind," *Journal of the ACM*, vol. 9, no. 1, pp. 84–97, 1962. 40, 51

[87] H. Zou and T. Hastie, "Regularization and variable selection via the elastic net," *Journal of the Royal Statistical Society: Series B (Statistical Methodology)*, vol. 67, no. 2, pp. 301–320, 2005. 40, 43, 44, 54, 74

[88] A. Pirani, M. Ricci, A. Tamburrino, and S. Ventre, "3D reconstruction of flaws in metallic materials by eddy currents inspections," *Studies in Applied Electromagnetics and Mechanics*, vol. 31, pp. 109–116, 2008. 40, 41

[89] J. Haueisen, R. Unger, T. Beuker, and M. E. Bellemann, "Evaluation of inverse algorithms in the analysis of magnetic flux leakage data," *IEEE Transactions on Magnetics*, vol. 38, no. 3, pp. 1481–1488, 2002. 40

[90] M. Fuchs, M. Wagner, T. Köhler, and H.-A. Wischmann, "Linear and nonlinear current density reconstructions," *Journal of Clinical Neurophysiology*, vol. 16, no. 3, pp. 267–295, 1999. 40

[91] U. Leder, J. Haueisen, M. Huck, and H. Nowak, "Non-invasive imaging of arrhythmogenic left-ventricular myocardium after infarction," *The Lancet*, vol. 325, no. 9143, p. 1825, 1998. 40

[92] D. Baumgarten, M. Liehr, F. Wiekhorst, U. Steinhoff, P. Münster, P. Miethe, L. Trahms, and J. Haueisen, "Magnetic nanoparticle imaging by means of minimum norm estimates from remanence measurements," *Medical & Biological Engineering & Computing*, vol. 46, no. 12, p. 1177, 2008. 40

[93] M. Wagner, H.-A. Wischmann, M. Fuchs, T. Köhler, and R. Drenckhahn, "Current density reconstructions using the L1 norm," in *Biomag 96: Proceedings of the Tenth International Conference on Biomagnetism*, pp. 393–396, 2000. 40

[94] M. Cluitmans, J. Karel, P. Bonizzi, P. Volders, R. Westra, and R. Peeters, "Wavelet-promoted sparsity for non-invasive reconstruction of electrical activity of the heart," *Medical & Biological Engineering & Computing*, vol. 56, no. 11, pp. 2039–2050, 2018. 40, 43

[95] X. Chen, C. Chen, Y. Cai, H. Wang, and Q. Ye, "Kernel sparse representation with hybrid regularization for on-road traffic sensor data imputation," *Sensors*, vol. 18, no. 9, pp. 1–20, 2018. 40, 43

[96] L. I. Rudin, S. Osher, and E. Fatemi, "Nonlinear total variation based noise removal algorithms," *Physica D: Nonlinear Phenomena*, vol. 60, no. 1, pp. 259 – 268, 1992. 40, 122

[97] P. Deuflhard, *Newton methods for nonlinear problems: Affine invariance and adaptive algorithms.* Springer Publishing Company, Incorporated, 2011. 41

[98] J. J. Moré, *The Levenberg-Marquardt algorithm: Implementation and theory*, pp. 105–116. Berlin, Heidelberg: Springer Berlin Heidelberg, 1978. 41

[99] R. De Oliveira Bohbot, D. Lesselier, and B. Duchêne, "Mapping defects in a conductive half-space by simulated annealing with connectivity and size as constraints," *Journal of Electromagnetic Waves and Applications*, vol. 10, no. 7, pp. 983–1004, 1996. 41

[100] B. Wang, J. P. Basart, and J. C. Moulder, *Linear and nonlinear image restoration methods for eddy current nondestructive evaluation*, pp. 791–798. Boston, MA: Springer US, 1998. 41

[101] G. Berthiau, B. de Barmon, B. de Benoist, and A. Masia, "Inversion process driven by global optimization heuristics coupled with MESSINE, a fast-running forward model," in *Proceedings of the Electromagnetic Nondestructive Evaluation (IV)*, pp. 175–180, IOS Press, 2000. 41

[102] A. Duca, M. Rebican, L. Janousek, M. Smetana, and T. Strapacova, "PSO based techniques for NDT-ECT inverse problems," in *Proceedings of the Electromagnetic Nondestructive Evaluation (XVII)*, pp. 1–8, 2013. 41

[103] M. Kermadi, S. Moussaoui, A. T. Brahimi, and M. Feliachi, "Comparison of efficient global optimization and particle swarm optimization for eddy current nondestructive evaluation," in *Proceedings of the 2016 International Conference on Electrical Sciences and Technologies in Maghreb (CISTEM)*, pp. 1–6, 2016. 41

[104] M. Kashani and J. Karimi, "Analysis and sizing of fatigue cracks in metallic structures from eddy current probe signals," in *Proceedings of the 5th Iranian International NDT Conference (IRNDT 2018)*, pp. 1–5, 2018. 41

[105] B. Ye, M. Li, G. Qiu, J. Dong, F. Zeng, T. Yang, and B. Bai, "Quantitative estimating size of deep defects in multi-layered structures from eddy current NDT signals using improved ant colony algorithm," *Frattura ed Integrita Strutturale*, vol. 8, pp. 32–41, 2014. 41

[106] F. Kojima, N. Kubota, F. Kobayashi, and T. Takagi, "Shape recovery of natural crack using evolutionary programming related to eddy current testing," *International Journal of Applied Electromagnetics and Mechanics*, vol. 15, no. 1–4, pp. 243–247, 2002. 41

[107] J. Friedman, T. Hastie, and R. Tibshirani, "Regularization paths for generalized linear models via coordinate descent," *Journal of Statistical Software*, vol. 33, no. 1, pp. 1–22, 2010. 43, 54, 55, 74

[108] E. Ibrahim, P. Barnabe, E. Ramanaidou, and E. Pirard, "Mapping mineral chemistry of a lateritic outcrop in new Caledonia through generalized regression using Sentinel-2 and field reflectance spectra," *International Journal of Applied Earth Observation and Geoinformation*, vol. 73, pp. 653–665, 2018. 43

[109] Y. Hung and W. Verbeke, "Sensory attributes shaping consumers' willingness-to-pay for newly developed processed meat products with natural compounds and a reduced level of nitrite," *Food Quality and Preference*, vol. 70, pp. 21–31, 2018. 43

[110] M. N. Çiftsüren and S. Akkol, "Prediction of internal egg quality characteristics and variable selection using regularization methods: ridge, LASSO and elastic net," *Archives Animal Breeding*, vol. 61, no. 3, pp. 279–284, 2018. 43

[111] A. Basu, R. Mitra, H. Liu, S. L. Schreiber, and P. A. Clemons, "RWEN: response-weighted elastic net for prediction of chemosensitivity of cancer cell lines," *Bioinformatics*, vol. 34, no. 19, pp. 3332–3339, 2018. 43

[112] A. Cesar-Razquin, E. Girardi, M. Yang, M. Brehme, J. Saez-Rodriguez, and G. Superti-Furga, "In silico prioritization of transporter-drug relationships from drug sensitivity screens," *Frontiers in Pharmacology*, vol. 9, pp. 1–10, 2018. 43

[113] J. Liu, G. Liang, K. D. Siegmund, and J. P. Lewinger, "Data integration by multi-tuning parameter elastic net regression," *BMC Bioinformatics*, vol. 19, pp. 1–9, 2018. 43

[114] H. M. van Loo, S. H. Aggen, C. O. Gardner, and K. S. Kendler, "Sex similarities and differences in risk factors for recurrence of major depression," *Psychological Medicine*, vol. 48, no. 10, pp. 1685–1693, 2018. 43

[115] A. McDermaid, X. Chen, Y. Zhang, C. Wang, S. Gu, J. Xie, and Q. Ma, "A new machine learning-based framework for mapping uncertainty analysis in RNA-seq read alignment and gene expression estimation," *Frontiers in Genetics*, vol. 9, pp. 1–11, 2018. 43

[116] C. Giglio and S. D. Brown, "Using elastic net regression to perform spectrally relevant variable selection," *Journal of Chemometrics*, vol. 32, no. 8, pp. 1–14, 2018. 43

[117] P. Chen, S. Tao, X. Xiao, and L. Li, "Uncertainty level of voltage in distribution network: An analysis model with elastic net and application in storage configu-

ration," *IEEE Transactions on Smart Grid*, vol. 9, no. 4, pp. 2563–2573, 2018. 43

[118] H. Wang, J. Pan, Z. Su, and S. Liang, "Blind image deblurring using elastic-net based rank prior," *Computer Vision and Image Understanding*, vol. 168, pp. 157–171, 2018. 43

[119] D. Karimi, G. Samei, C. Kesch, G. Nir, and S. E. Salcudean, "Prostate segmentation in MRI using a convolutional neural network architecture and training strategy based on statistical shape models," *International Journal of Computer Assisted Radiology and Surgery*, vol. 13, no. 8, pp. 1211–1219, 2018. 43

[120] Y. Sui, G. Wang, and L. Zhang, "Correlation filter learning toward peak strength for visual tracking," *IEEE Transactions on Cybernetics*, vol. 48, no. 4, pp. 1290–1303, 2018. 43

[121] M. H. R. Khan, "On the performance of adaptive preprocessing technique in analyzing high-dimensional censored data," *Biometrical Journal*, vol. 60, no. 4, pp. 687–702, 2018. 43

[122] H. S. Sidhu, A. Narasingam, P. Siddhamshetty, and J. S.-I. Kwon, "Model order reduction of nonlinear parabolic PDE systems with moving boundaries using sparse proper orthogonal decomposition: Application to hydraulic fracturing," *Computers & Chemical Engineering*, vol. 112, pp. 92–100, 2018. 43

[123] H. Guo, Y. Li, Y. Xu, Y. Jin, J. Xiang, and J. Chen, "Resting-state brain functional hyper-network construction based on elastic net and group lasso methods," *Frontiers in Neuroinformatics*, vol. 12, pp. 1–18, 2018. 43

[124] S.-B. Chen, Y. Zhang, C. H. Q. Ding, Z.-L. Zhou, and B. Luo, "A discriminative multi-class feature selection method via weighted l(2,1) -norm and extended elastic net," *Neurocomputing*, vol. 275, pp. 1140–1149, 2018. 43

[125] O. K. Oyedotun, A. E. R. Shabayek, D. Aouada, and B. Ottersten, "Improving the capacity of very deep networks with maxout units," in *Proceedings of the 2018 EEE International Conference on Acoustics, Speech and Signal Processing (ICASSP)*, pp. 2971–2975, 2018. 43

[126] S. Huang, C. Hu, M. L. Bell, D. Billheimer, S. Guerra, D. Roe, M. M. Vasquez, and E. J. Bedrick, "Regularized continuous-time Markov model via elastic net," *Biometrics*, vol. 74, no. 3, pp. 1045–1054, 2018. 43

[127] Z. Meng, X. Zhan, J. Li, and Z. Pan, "An enhancement denoising autoencoder for rolling bearing fault diagnosis," *Measurement*, vol. 130, pp. 448–454, 2018. 43

[128] A. Y. Ng, "Feature selection, L1 vs. L2 regularization, and rotational invariance," in *Proceedings of the Twenty-first International Conference on Machine Learning (ICML '04)*, pp. 78–85, 2004. 51, 72

[129] A. Saltelli, "Global sensitivity analysis: An introduction," in *Proceedings of the 4th international conference on sensitivity analysis of model output (SAMO 2004)*, pp. 27–43, 2004. 65

[130] K. Weise, M. Carlstedt, M. Ziolkowski, and H. Brauer, "Uncertainty analysis in Lorentz force eddy current testing," *IEEE Transactions on Magnetics*, vol. 52, no. 3, pp. 1–4, 2016. 65

[131] A. Bernieri, G. Betta, L. Ferrigno, and M. Laracca, "Multi-frequency ECT method for defect depth estimation," in *2012 IEEE Sensors Applications Symposium Proceedings*, pp. 1–6, 2012. 69, 70

[132] C. Mandache, I. Zainal Abidin, G. Y. Tian, and Y. Li, "Defect depth estimation using pulsed eddy current with varied pulse width excitation," in *Proceedings of Insight: Non-Destructive Testing and Condition Monitoring*, pp. 69–72, 2009. 69, 70

[133] L. Landweber, "An iteration formula for Fredholm integral equations of the first kind," *American Journal of Mathematics*, vol. 73, pp. 615–624, 1951. 81, 84

[134] M. Hanke, A. Neubauer, and O. Scherzer, "A convergence analysis of the Landweber iteration for nonlinear ill-posed problems," *Numerische Mathematik*, vol. 72, no. 1, pp. 21–37, 1995. 81

[135] B. Kaltenbacher, "All-at-once versus reduced iterative methods for time dependent inverse problems," *Inverse Problems*, vol. 33, no. 6, pp. 1–31, 2017. 81

[136] G. Bao, G. Hu, Y. Kian, and T. Yin, "Inverse source problems in elastodynamics," *Inverse Problems*, vol. 34, no. 4, pp. 1–31, 2018. 81

[137] M. Goli, I. Foroughi, and P. Novak, "On estimation of stopping criteria for iterative solutions of gravity downward continuation," *Canadian Journal of Earth Sciences*, vol. 55, no. 4, pp. 397–405, 2018. 81

[138] V. Hutterer and R. Ramlau, "Nonlinear wavefront reconstruction methods for pyramid sensors using Landweber and Landweber-Kaczmarz iterations," *Applied Optics*, vol. 57, no. 30, pp. 8790–8804, 2018. 81

[139] Y.-K. Ma, P. Prakash, and A. Deiveegan, "Optimization method for determining the source term in fractional diffusion equation," *Mathematics and Computers in Simulation*, vol. 155, pp. 168–176, 2019. 81

[140] A. Lerma and D. Hinestroza G, "Coefficient identification in the Euler-Bernoulli equation using regularization methods," *Applied Mathematical Modelling*, vol. 41, pp. 223–235, 2017. 81

[141] Q. Qu, Z. Cao, L. Xu, C. Liu, L. Chang, and H. McCann, "Reconstruction of two-dimensional velocity distribution in scramjet by laser absorption spectroscopy tomography," *Applied Optics*, vol. 58, no. 1, pp. 205–212, 2019. 81

[142] T. Yu and W. Cai, "Benchmark evaluation of inversion algorithms for tomographic absorption spectroscopy," *Applied Optics*, vol. 56, no. 8, pp. 2183–2194, 2017. 81

[143] B. Petković, E. Dölker, R. Schmidt, and J. Haueisen, "Method of fundamental solutions applied to 3-D velocity induced eddy current problems," *IEEE Transactions on Magnetics*, vol. 54, no. 8, pp. 1–10, 2018. 109

[144] A. Bernieri, G. Betta, L. Ferrigno, and M. Laracca, "Crack depth estimation by using a multi-frequency ECT method," *IEEE Transactions on Instrumentation and Measurement*, vol. 62, no. 3, pp. 544–552, 2013. 118

[145] L. Udpa and S. Udpa, "Eddy current defect characterization using neural networks," *NDT International*, vol. 23, no. 6, p. 358, 1990. 122

[146] A. Bernieri, L. Ferrigno, M. Laracca, and M. Molinara, "Crack shape reconstruction in eddy current testing using machine learning systems for regression," *IEEE Transactions on Instrumentation and Measurement*, vol. 57, no. 9, pp. 1958–1968, 2008. 122

[147] A. Bernieri, G. Betta, L. Ferrigno, M. Laracca, and S. Mastrostefano, "Multifrequency excitation and support vector machine regressor for ECT defect characterization," *IEEE Transactions on Instrumentation and Measurement*, vol. 63, no. 5, pp. 1272–1280, 2014. 122

[148] L. S. Rosado, F. M. Janeiro, P. M. Ramos, and M. Piedade, "Defect characterization with eddy current testing using nonlinear-regression feature extraction and artificial neural networks," *IEEE Transactions on Instrumentation and Measurement*, vol. 62, no. 5, pp. 1207–1214, 2013. 122

[149] F. Cau, A. Fanni, A. Montisci, P. Testoni, and M. Usai, "Artificial neural networks for non-destructive evaluation with ultrasonic waves in not accessible pipes," in *Fortieth IAS Annual Meeting. Conference Record of the 2005 Industry Applications Conference, 2005.*, vol. 1, pp. 685–692, 2005. 122

[150] X. Jian, N. Guo, H. Du, M. X. Li, and H. L. Zhang, "Automatic defect characterization using artificial neural networks and deconvolution techniques," *Journal of Intelligent Material Systems and Structures*, vol. 17, pp. 713–720, 2006. 122

[151] S. Vallerand and X. Maldague, "Defect characterization in pulsed thermography: a statistical method compared with kohonen and perceptron neural networks," *NDT & E International*, vol. 33, no. 5, pp. 307 – 315, 2000. 122

Erklärung

Ich versichere, dass ich die vorliegende Arbeit ohne unzulässige Hilfe Dritter und ohne Benutzung anderer als der angegebenen Hilfsmittel angefertigt habe. Die aus anderen Quellen direkt oder indirekt übernommenen Daten und Konzepte sind unter Angabe der Quelle gekennzeichnet.

Bei der Auswahl und Auswertung folgenden Materials haben mir die nachstehend aufgeführten Personen in der jeweils beschriebenen Weise unentgeltlich geholfen:

1. *Unterstützung bei der Interpretation der Ergebnisse in der gesamten Arbeit.*
   Prof. Dr.-Ing. habil. Jens Haueisen, Technische Universität Ilmenau, Fakultät für Informatik und Automatisierung, Deutschland

2. *Durchführung der Lorentzkraft-Wirbelstrom-Prüfung zur Untersuchung von geschichteten Aluminiumplatten, sowie Bereitstellung der gemessenen Lorentzkraft-Signale in den Abschnitten 3.2.1, 4.2.1 und 5.2.1*
   M. Sc. Stephan Gorges, IMMS Institut für Mikroelektronik- und Mechatronik-Systeme gemeinnützige GmbH, 98693 Ilmenau, Deutschland

3. *Durchführung der numerischen Simulationen des Lorentzkraft-Wirbelstrom-Prüfverfahrens mittels eines Finite-Elemente-Modelles, sowie Bereitstellung der simulierten Lorentzkraft- Signale in den Abschnitten 3.2.1, 4.2.1, 5.2.1, 6.2.1 und 7.2.1.*
   M. Sc. Reinhard Schmidt, Technische Universität Ilmenau, Fakultät für Elektrotechnik und Informationstechnik, Deutschland

4. *Durchführung der numerischen Simulationen des Wirbelstrom-Prüfverfahrens mittels eines Finite-Elemente-Modelles und Durchführung der Wirbelstromprüfung zur Untersuchung von geschichteten Aluminiumplatten, sowie Bereitstellung der simulierten und gemessenen Signale der magnetischen Flussdichte im Abschnitt 3.3.1.*
   PhD Dário Jerónimo Pasadas, Universidade de Lisboa, Instituto Superior Técnico, Portugal

Weitere Personen waren an der inhaltlich-materiellen Erstellung der vorliegenden Arbeit nicht beteiligt. Insbesondere habe ich hierfür nicht die entgeltliche Hilfe von Vermittlungs bzw. Beratungsdiensten (Promotionsberater oder anderer Personen) in Anspruch

genommen. Niemand hat von mir unmittelbar oder mittelbar geldwerte Leistungen für Arbeiten erhalten, die im Zusammenhang mit dem Inhalt der vorgelegten Dissertation stehen.

Die Arbeit wurde bisher weder im In- noch im Ausland in gleicher oder ähnlicher Form einer Prüfungsbehörde vorgelegt.

Ich bin darauf hingewiesen worden, dass die Unrichtigkeit der vorstehenden Erklärung als Täuschungsversuch angesehen wird und gemäß §7 Abs. 10 der Promotionsordnung den Abbruch des Promotionsverfahrens zur Folge hat.

Ilmenau, den 26. Juni 2019   Eva-Maria Dölker